

Application of Mixed and Virtual Reality in Geoscience and Engineering Geology

**by
Omar Chang**

B. Sc., Simon Fraser University, 2018

Thesis Submitted in Partial Fulfilment of the
Requirements for the Degree of
Master of Science

in the
Department of Earth Sciences
Faculty of Science

© Omar Chang 2021
SIMON FRASER UNIVERSITY
Summer 2021

Copyright in this work rests with the author. Please ensure that any reproduction or re-use is done in accordance with the relevant national copyright legislation.

Declaration of Committee

Name: Omar Chang

Degree: Master of Science

Title: Application of Mixed and Virtual Reality in
Geoscience and Engineering Geology

Committee: **Chair: Gwenn Flowers**
Professor, Earth Sciences

Doug Stead
Supervisor
Professor, Earth Sciences

Glyn Williams-Jones
Committee Member
Professor, Earth Sciences

Bernhard Rabus
Committee Member
Professor, Engineering Science

Erik Eberhardt
Examiner
Professor, Earth, Ocean and Atmospheric Sciences
University of British Columbia

Abstract

Visual learning and efficient communication in mining and geotechnical practices is crucial, yet often challenging. With the advancement of Virtual Reality (VR) and Mixed Reality (MR) a new era of geovisualization has emerged. This thesis demonstrates the capabilities of a virtual continuum approach using varying scales of geoscience applications.

An application that aids analyses of small-scale geological investigation was constructed using a 3D holographic drill core model. A virtual core logger was also developed to assist logging in the field and subsequent communication by visualizing the core in a complementary holographic environment. Enriched logging practices enhance interpretation with potential economic and safety benefits to mining and geotechnical infrastructure projects.

A mine-scale model of the LKAB mine in Sweden was developed to improve communication on mining induced subsidence between geologists, engineers and the public. GPS, InSAR and micro-seismicity data were hosted in a single database, which was geovisualized through Virtual and Mixed Reality.

The wide array of applications presented in this thesis illustrate the potential of Mixed and Virtual Reality and improvements gained on current conventional geological and geotechnical data collection, interpretation and communication at all scales from the micro- (e.g. thin section) to the macro- scale (e.g. mine).

Keywords: Virtual Core, Geovisualization, Subsidence, Mixed Reality, Virtual Reality

Dedication

I would like to dedicate this thesis to my family: Luis Alberto Chang (father), Soledad Chang (mother), Andre Chang (brother), and Cindy Chang (sister) for supporting me throughout my career and providing me with amazing guidance.

Acknowledgements

I would like to express my most sincere appreciation to my supervisor Doug Stead for his assistance and advice throughout the course of this research. I would also like to thank my committee members Glynn-Williams Jones, Bernhard Rabus, and Erik Eberhardt for their help.

Thank you to every single person in the Engineering Geology and Resource Geotechnics Research Group especially Emre Onsel, Davide Donati and Jesse Mysiorek for all the great times in the lab, coffee breaks, and butter chicken lunches. I would also like to thank the whole Simon Fraser University Earth Science faculty and graduate students for the great experience at Simon Fraser University. Particularly Dan Marshall and his whole research group Megan Binner, Bill Fischer and Carol-Anne Nicol for also assisting with data.

I would also like to acknowledge Grant Sanders, Enersoft CEO, for helping us scan core with their apparatus. Lastly, but surely not last, thank you to all Kiruna LKAB group particularly Britt-Mari Stöckel, Karola Mäkitaavola, and Jimmy Toyra for assisting with data and making my stay at Kiruna outstanding.

Table of Contents

Declaration of Committee	ii
Abstract	iii
Dedication	iv
Acknowledgement	v
Table of Contents	vi
List of Tables	ix
List of Figures	x
List of Acronyms	xviii

Chapter 1. Introduction

1.1. Statement of Problem	1
1.2. Research Objectives	1
1.3. Thesis Structure	2

Chapter 2. Literature Review

2.1. The Virtual Continuum	4
2.2. Virtual Reality (VR)	6
2.3. Augmented Reality (AR)	8
2.4. Mixed Reality (MR)	9
2.4.1. HoloLens 2	12
2.5. Geovisualization	13
2.6. Applying the Virtual Paradigm within Geoscience	14
2.6.1. Using the Virtuality Paradigm for Improved Geovisualization	16
2.6.2. Using the Virtual Paradigm beyond Visualization	19
2.7. Developing and Integrating Models into the Virtual Continuum	24
2.8. The Future of the Virtual Paradigm	24

Chapter 3. Improved Core Characterization using Holographic Logging Procedures and 3D Core Geovisualization

3.1. Introduction	27
3.2. Background Information	29
3.2.1. Diamond Drilling	29
3.2.1.1 Surveying and Depth Registration	30
3.2.1.2 Orientation Bias associated with Drilling	31
3.2.1.3 Storage of Drill Core	32
3.2.1.4 Canadian Mining Law and Role of NI 43-101	34
3.2.2. Conventional Geotechnical Logging Practices	35
3.2.2.1 The Q-System	36
3.2.2.2 Rock Mass Rating (RMR)	38
3.2.2.3 Geologic Strength Index (GSI)	39
3.2.2.4 RQD uncertainties and misguidance	40
3.2.3. Core Logging Software	42
3.3. CoreLogger MR	42

3.3.1.	CoreLogger MR: Initiation of New Geological and Geotechnical Logging Sheets	44
3.3.2.	Geotechnical Logging Sheet	46
3.3.2.1	The Holographic Q-System and Holographic RMR	48
3.3.2.2	Holographic GSI	50
3.3.3.	Lithological Logging Sheet	52
3.4.	Preliminary 3D Core Scanning Model	52
3.5.	Improved 3D Core Scanning.....	55
3.6.	Discussion	61
3.7.	Summary and Conclusion.....	63

Chapter 4. Virtual Core Logging for Resource Assessment

4.1.	Introduction.....	66
4.2.	Background Information.....	68
4.2.1.	One-Dimensional Drill Data	68
4.2.1.1	Destructive and Geochemical Tests	68
4.2.1.2	Non-Destructive Point Data	69
4.2.2.	Two-Dimensional Drill Data	69
4.2.2.1	Hyperspectral Scanning	69
4.2.2.2	Thin Section Analysis for Petrographic Investigation	71
4.2.3.	Three-Dimensional Drill Data	72
4.2.3.1	Imaging of Borehole Walls Through Televiewer and Full Micro Imager (FMI)	72
4.3.	Preliminary Complex Virtual Core Model	76
4.3.1.	2.5 D Core Scan Model	76
4.3.2.	Thermal Reading Acquisition	77
4.3.3.	Laser Reading Acquisition	80
4.3.4.	Hyperspectral Reading Acquisition	81
4.3.5.	Final XR Core Model	81
4.4.	Ore Deposit Virtual Core Model	83
4.4.1.	Hyperspectral Differentiation Along Mining Exploration Core	83
4.4.2.	Thin-Section Analysis	84
4.5.	Borehole Imagery in Conjunction with Virtual Core	88
4.6.	XRCoreShack.....	91
4.6.1.	XRCoreShack in MR	92
4.6.2.	XRCoreShack in VR	98
4.7.	Discussion and Conclusion.....	98

Chapter 5. Geovisualization of Induced Subsidence at LKAB Kiirunavaara Mine, Sweden

5.1.	Introduction.....	102
5.2.	Background Information.....	105
5.2.1.	Sublevel Caving	105
5.2.2.	Subsidence	106
5.2.2.1	Continuous Deformation Zone	107

5.2.2.2 Discontinuous Deformation Zone	109
5.3. Geological and Structural Characteristics Within Kiirunavaara Mine	110
5.3.1. Geology of Kiirunavaara and Current Mine Works	110
5.3.2. Major Discontinuities along Kiirunavaara	112
5.4. Monitoring Mining Induced Subsidence at LKAB Kiruna	115
5.4.1. Ground Surface Monitoring GPS	115
5.4.2. Ground Surface Monitoring via InSAR	119
5.4.3. Underground Monitoring using Microseismic Analysis	126
5.5. A New Visualization Approach for Mine Induced Subsidence Results	128
5.5.1. GPS visualization	130
5.5.2. InSAR visualization	135
5.5.3. Civil and Mining Infrastructure at LKAB Kiirunavaara	138
5.5.4. Microseismic Analysis	140
5.6. Additional Visualization Capabilities	143
5.7. Potential of MineViz MR	144
5.8. Summary and Conclusion	148
Chapter 6. Conclusions and Recommendations for Future Work	
6.1. Introduction	150
6.2. Overall Conclusions	150
6.3. Research Contributions	152
6.4. Current Challenges	155
6.4.1. Overall Challenges within the Virtual Paradigm	155
6.4.2. Challenges in Virtual Core Development	156
6.4.3. Challenges within the Kiruna MineViz MR Model	157
6.5. Recommendations for Future Work	158
References	163
Appendix A. Rock Quality Designation (RQD)	185
Appendix B. Q-System.	186
Appendix C. Rock Mass Rating System (RMR)	194
Appendix D. Geologic Strength Index (GSI)	195
Appendix E. Flysch Geologic Strength Index (Marinos and Hoek, 2001)	196
Appendix F. Composite Geologic Strength Index	198
Appendix G. RMQ in respect to GSI (Kaiser, 2019)	199
Appendix H. Field Estimate of Uniaxial Compressive Strength	200

List of Tables

Table 2-1: Summary of various industry MR applications.	12
Table 2-2: Advantages and disadvantages of VR and MR.....	15
Table 3-1: Broad grouping of rock mass classification system (after Wickman et al., 1972).....	35
Table 5-1: General characteristic of Kiruna type ore setting (Apatite Iron Ore) after Edfelt (2007).	111
Table 6-1: Examples of possible XR geoscience/engineering applications.....	162

List of Figures

Figure 1.1: Flow chart showing thesis structure.....	3
Figure 2.1: Virtual continuum after Milgram and Kishino (1994).	4
Figure 2.2: Comparison of a core sampled in Conventional Reality (CR), Virtual Reality (VR), Augmented Reality (AR), and Mixed Reality (MR).....	5
Figure 2.3: Different controller methodologies used in VR. (A) Leap Motion device that can be attached to VR headset for accurate finger input (Ultraleap, 2021). (B) Optional scanning by Oculus Quest Headset to allow finger input (Oculus, 2021). (C) Valve Index VR controller which scans finger interaction (Valve Corporation, 2021).	7
Figure 2.4: Some uses of AR (A) WayRay AR windshield which is to be implemented into Hyundai car windows by 2020 (WayRay, 2021). (B) Popular phone application known as Pokemon GO which is able to emplace a Pokemon within a cellular view (Ninantic, 2020).	9
Figure 2.5: Examples of occlusion that can be observed in MR (Microsoft, 2021b).	10
Figure 2.6: Microsoft HoloLens 1. The first MR headset that discretized physical environments through a similar technology to the Xbox Kinect (Microsoft, 2021a).	10
Figure 2.7: Hand gesture recognized by Microsoft HoloLens 1 (Microsoft, 2021b).	11
Figure 2.8: HoloLens 2 has a more ergonomic fitting and the lenses can be flipped up to rapidly disengage the user from MR (Microsoft, 2021b).	13
Figure 2.9: Trimble (2021) HoloLens 1 hard hat that complies with safety requirements (Onsel et al., 2019) [Used with permission].....	15
Figure 2.10: Masaya Volcano located in Nicaragua seen as an AR model. The user has the option to change to VR within the HoloLens 1 to observe the model in more detail (Onsel et al., 2018) [Used with permission].	17
Figure 2.11: Hawkesbury slope, BC DEM model combined with the bathymetry model (A) Model with bathymetry results being covered by water (B) Textured with slope orientation, overlain by 2D geological map and cross-sections (C) Spatially anchored cross-sections can be extracted from the slope at the users convenience for in depth analysis (Onsel et al., 2018) [Used with permission].....	17
Figure 2.12: Palabora block cave mine, South Africa model being observed by two individuals at the same time showing the propagation of block caving, open pit model, and underground mine layout (Onsel et al., 2019) [Used with permission].	18
Figure 2.13: DFN model transferred from 3DEC for VR application (A) Cylinders were added to represent drill cores (B) Drill cores can be removed by the user, rotated, and scaled. Core only intersected three of the nine discontinuities.	18
Figure 2.14: Vancouver, BC, Canada model of downtown area made by the author and Jesse Mysiorek; SFU MSc student (A) 3D buildings along Vancouver DEM model visualized through HoloLens (B) Selected RS2 results from the various scenarios modelled.....	19

Figure 2.15: EasyMap MR Application developed by SRK Vanocuver and Simon Fraser University (A) Delineating lithological contacts in the field with X,Y and Z coordinates (B) Underground mining delineation of a normal fault (after Onsel et al., 2019).	20
Figure 2.16: EasyMap MR used in an office setting to map a remotely-sensed outcrop from the Jure Landslide, Nepal, to obtain real-time structural orientation and measurements (Mysiorek, 2019a) [Used with permission].	20
Figure 2.17: EasyMap in VR with a high resolution UAV photogrammetry model (Onsel et al., 2019) [Used with permission].	21
Figure 2.18: Mesh generated from the HoloLens without any postprocessing nor preprocessing (Onsel et al., 2018) [Used with permission].	22
Figure 2.19: Discontinuity can be measured by simply viewing a surface using Hololens 1. Once the user clicks, the measurement is plotted as a defined discontinuity sets (Onsel et al., 2019) [Used with permission].	23
Figure 2.20: EasyMap MR tools (A) Take desired charts to the field as holograms (B) Photographic acquisition of line of sight taken during video recording within the HoloLens (Modified after Onsel et al., 2018) [Used with permission].	23
Figure 2.21: Qualcomm announcement chart of XR2 in comparison to Qualcomm Snapdragon 835 which is currently used in the HoloLens 2 (Fink, 2019).....	26
Figure 2.22: New projected MR and AR aesthetic glasses for the consumer market (A) Apple AR glasses set to be released on 2020 (B) Qualdrom new XR glasses which uses seven cameras to allow improved mesh discretization.	26
Figure 3.1: Anonymized example of drill rock core (CanadaMines, 2019).	29
Figure 3.2: Intersection of joints with respect to drill hole or scanline direction. Weighted joint density (wJd) adjusts joint density by considering joints relative to the diamong drill hole (After Palmström, 1995).	32
Figure 3.3: Core samples from a 1972-1982 mine located on Bear Mountain, Harrison Lake, British Columbia, Canada (Hudson Institute of Mineralogy, 2020). Samples have been mixed, broken, altered, and misplaced. Adjacent active exploration within the region are unable to refer to these boxes as they are unsalvageable due to poor storage.	33
Figure 3.4: Measurement of core for RQD calculation (A) Centerline: Correct method to measure length (B) Tip to Tip: Incorrect method because it is dependent on core diameter (C) Fully circular: Incorrect method to measure as length is dependent on core diameter (Modified after Deere & Deere, 1989).	41
Figure 3.5: CoreLogger data can either be input using the holographic keyboard inbuilt Mixed Reality Toolkit (MRTK) or by connecting to any Bluetooth compatible keyboard.	43
Figure 3.6: CoreLogger MR initial menu.	43

Figure 3.7: User interface (UI) of CoreLoggerMR when a new file is initiated. The user is prompted to fill important parameters such as georeferencing.	44
Figure 3.8: Second step of initiation. Two red markers are placed beside Elevation and Depth as they were not assigned properly. The elevation parameter was constrained to be above 500 m elevation due to project specifications. The depth parameter was marked by a cross as it was left blank.	44
Figure 3.9: CoreLogger MR (A) Parameter summary UI displayed prior to completing model initiation. Any parameters left blank will be displayed as “N/A” and potential erroneous fields will be followed by the string “...Verify”. (B) Menu allowing user to select the type of logging in CoreLogger MR.	45
Figure 3.10: Geotechnical holographic logging sheet in CoreLogger MR showing both the GSI and RMR built-in UI.	47
Figure 3.11: Built-in CoreLogger MR ruler compared to a conventional ruler measuring the length of a core piece that is 26.2 cm long.	48
Figure 3.12: RMR Holographic table based on Bieniawski (1989) [Used with permission]. If a user looks at an unselected quadrant a slightly transparent shader is overlain on top of the observed quadrant. Once clicked the value is assigned and the shader is emplaced permanently.	49
Figure 3.13: Guideline for discontinuity classification (After Bieniawski, 1989) [Used with permission].	50
Figure 3.14: RMR Adjustor relative to type of site and strike/dip direction (After Bieniawski, 1989) [Used with permission].	50
Figure 3.15: Geotechnical holographic logging in CoreLogger MR. (A) Holographic GSI that quickly assigns respective values that were clicked virtually (After Hoek & Marinos, 2000). (B) Holographic RMR summary table that updates as a user classifies RMR parameters.	51
Figure 3.16: Preliminary 3D core scanning results. Roughness of each core end piece was accurately captured. Core is HQ3 (63.5 mm) diameter. Box dimensions are 121 cm x 26 cm x 8 cm.	54
Figure 3.17: MR 3D Holographic Core can be scaled, moved, and rotated freely.	54
Figure 3.18: Core scanner table observed from the point of view of an anchored camera. Multiple view points enable easy meshing, texturing, background masking, and automization.	56
Figure 3.19: TH03 core box 1 scanned. (A) Original Core box (B) 2.5D model that can be observed in VR and MR (C) Virtual 3D core in which each core piece can be moved, scaled, and rotated freely in both MR and VR. Red cylinders are representative of areas with low RQD value (fragmented rock) which cannot be adequately scanned in 3D.	57
Figure 3.20: Scanned HQ3 core can digitally show grain size distribution within the fine lower grain size (>0.125 mm).	58
Figure 3.21: Scanning resulted in a highly detailed mesh. For improved rendering the mesh was selectively reduced to only hold 100 times less than	

the original results (e.g. 1%) without compromising texture or overall model shape.	59
Figure 3.22: TH03 physical and virtual core piece with a slight angle difference (A) Photograph of physical core taken from in-house core scanner (B) 3D model results when three different cameras were used. Differences in camera settings resulted in large contrast difference between the top and the sides of the core. (C) 3D model results when camera settings were homogeneous throughout.....	59
Figure 3.23: 4x4 rectangle matrix used to calculate centre line length of each core piece. A matrix was used because calculation errors were generated along sharp boundaries.....	60
Figure 3.24: 3D digitized core sample (A) Without texture enhancement (B) With texture enhancement. Structures such as brecciated clasts, nodules, and veins are clearly evident (C) False colour.	61
Figure 4.1: Proposed future core module that allows a user to see core data spatially along the core using the virtual paradigm.	67
Figure 4.2: 3D hyperspectral cube with spectral data in the z-dimension for a x and y 2D image (Qin, 2012).	70
Figure 4.3: Final FMI results seen in both azimuthal and 3D view (Schlumberger, 2021a).....	74
Figure 4.4: Common ways to display borehole imaging. Structures that are observed in 3-D view will appear sinusoidal in azimuthal view (Hurley & Zhang, 2017).....	74
Figure 4.5: Sinuous acoustic image results (A) Original (B) Grayscale filtered (C) Automated marks using machine learning, where red show false positive and green are true positives (D) Manually marked by geologist (Cruz et al., 2017).	75
Figure 4.6: Core selected for preliminary 2.5D Core Model. Unit 1: Melanocratic equigranular amphibole biotite phyric granite. Unit 2: Biotite phyric granodiorite. Unit 3: Granite with abundant chloritized veins.	77
Figure 4.7: Preliminary 2.5D model of a core box. Unlike other 3D core models, individual cores cannot be moved, rotated, or scaled freely.	77
Figure 4.8: Five lines drawn to quantify core heat dissipation per pixel after 33 minutes of cooling. Dips and darker shades show discontinuities or lithological differences.	79
Figure 4.9: Riegl VZ-4000 noisy results of core box.	80
Figure 4.10: 1052.63 nm- 18135.57 nm – 2375.77 nm tiff file used to overlay 3D core box model (1) Unit 1 is clearly distinct (2) Bright pixel within the Unit 2 due to large phenocryst (3) Discrepancy within Unit 2 that was not evident during geological analysis (4) Unit 2 gradual change modal mineralogical change (5) Chloritized veins in Unit 3.....	81
Figure 4.11: Single archive that hosted all the datasets for preliminary core model study (A) Photogrammetry 2.5D model made with a Menu that allows selective overlays (B) Hyperspectral results with RGB value of 15-151-252 on 2.5D model.....	82

Figure 4.12: Rainbow 24 contour which shows contrast along different rock types and discontinuities. Unit 3 cooled the slowest, while Unit 2 was the fastest.	82
Figure 4.13: Graphical heat dissipation along Line 1 spatially anchored along the core.	82
Figure 4.14: Half core run of early halo Cu-Mo-Ag porphyry. Virtual core is floating on the background while physical core is held by the user.	83
Figure 4.15: Grayscale Enersoft Inc results overlain along the virtual core. (A) Compared to physical core. Virtual core box with (B) raw results versus (C) grayscale overlay.	84
Figure 4.16: Plain polarized light thin section and respective cross polarized region at (A) 0° (B) 30° (C) 60° (D) 90°	85
Figure 4.17: Designed thin section broken into a 4x4 grid for cropping purposes	86
Figure 4.18: Row 3 Column 3 zoomed in and then broken into a 2x2 grid for even more detailed analysis.	87
Figure 4.19: Thin section seen through the HoloLens that can be freely rotated by moving the scroller.	88
Figure 4.20: Observing borehole imagery in 3D view in (A) MR and (B) VR.	89
Figure 4.21: 3D FMI MR model (A) Unaltered, (B) Discontinuities with metre breaks, (C) Bitumen content [Light green = No Bitumen; Yellow = Moderate Bitumen], and (D) Lithologies.	90
Figure 4.22: Analysis of 1 metre FMI segment in MR through Microsoft HoloLens 1.	90
Figure 4.23: 3D FMI model with half core inside it. FMI can be visually toggled.	91
Figure 4.24: XRCoreShack MR automatic UI interlinked to every core box imported into module. (A) Shows how hologram can be moved at a user's discretion. (B) List of sites that were available for scanning. (C) User is notified if the specific core box was not scanned or imported.	92
Figure 4.25: XRCoreShack required flowchart.	93
Figure 4.26: Low RQD value regions that were unable to be scanned are represented by red cylinders. If the user clicks on the cylinder it will show a representative 2.5D of the region and collection of representative images that can be scrolled through.	94
Figure 4.27: Automatic UI interface assigned to every single box in XRCoreShack toggled through setting button. (A) Observe the core box as a single continuity that takes into account surveying, each sample can still be grabbed individually. (B) Hand draggable enables rotation, movement and scaling of the whole model. Scaling degree is stated adjacent to the box. (C) Extract all rows to a predetermined height and rotation. (D) Observe model as a 2.5D model. (E) Toggle box.	95
Figure 4.28: XRCoreShack MR (A) Examination of selected samples at the same time at different core box locations without potential misplacement (B) Description tab shown once submenu description is clicked. Information shown is derived from a CSV file and can be flagged for future QAQC.	96

Figure 4.29: Physical core while dry does not display textures effectively. Once wet some textures become prominent but not as clear as when using virtual core texture enhancers such as false positive. Texture enhancers can be applied to all digitized samples.....	97
Figure 4.30: Contemporaneous assesment of physical and digital core allows more in-depth analysis of the physical core through standard logging practices.....	97
Figure 4.31: XRCoreShack in VR. Core boxes can be scanned and imported into the platform. Samples from different boxes can be directly compared to each other.	98
Figure 5.1: Location of LKAB Kiruna mine (Extracted from Google Earth (2021b)).....	102
Figure 5.2: Kirunavaara drastic topographic change from 1920 to 2005 (after Hämäläinen & Furbeck, 2011) [Used with permission].	103
Figure 5.3: Kiruna city observed from mine site lookout point on 2018.	104
Figure 5.4: Standard Sublevel Caving layout (Atlas Copco, 2007).....	106
Figure 5.5: Sketch of discontinuous and continuous deformation zone expected in sublevel caving mines (Villegas, 2008) [Used with permission].	107
Figure 5.6: Continuous subsidence sketch with diagnostic portions (Modified after Harrison, 2011; Holla & Barclay, 2000). (A) Subcritical profile showing horizontal displacement, stress, and tilt proportional to the extraction amount. (B) Supercritical profile showing the same parameters proportional to a larger extraction width.	108
Figure 5.7: Simplified progressive sequence of failure as depth of SLC increases: (a) Initial open pit mine walls fails through bi-planar or wedge failure (b) Failure surfaces and tension cracks develop (c) Continuous development of tension cracks and failures surfaces as mine depth increases. Steeply dipping subparallel discontinuities along the hanging wall strata fail through toppling (Modified after Brady & Brown, 2006; Hoek, 1974).....	109
Figure 5.8: Geological map of Kiruna Region with NW structures (blue lines) and NE (red lines) (Magnor & Mattsson, 2000) [Used with permission].....	113
Figure 5.9: Interpreted structural map at LKAB Kiruna (Mattsson et al., 2010) [Used with permission].	114
Figure 5.10: GPS lines across the Kiruna mine. The blue and yellow lines outline the limits of the discontinuous zone and continuous deformation, resepectively (Töyrä, 2013) [Used with permission].	117
Figure 5.11: Example of cumulative displacement plots for GPS hub C17. Red= total horizontal displacement, Black = Deformation along x-axis direction, Green = Deformation in the y-axis direction, and Blue = Vertical Deformation (Töyrä, 2013) [Used with permission].	117
Figure 5.12: Measured horizontal deformation in the x-axis direction for a line roughly perpendicular to the orebody strike (Mäkitaavola, 2012) [Used with permission].	118
Figure 5.13: Environmental criterion calculation using strain percentage, after Stöckel et al. (2012) [Used with permission].	119

Figure 5.14: Topographic interferogram obtained from SRTM over Mount Etna, Italy (a) Post topographic interferogram after fringes were eliminated (b) mean amplitude image (Massonnet & Souyris, 2008) [Used with permission].	120
Figure 5.15: Corner reflector (CR) distribution installed in Kiruna with a corresponding image of the reflector (Stöckel et al., 2013) [Used with permission].	122
Figure 5.16: Example of InSAR measurements at LKAB Kiruna, colour bar shows the line of sight (LoS) deformation in mm/year (Stöckel et al., 2013) [Used with permission].	123
Figure 5.17: Cumulative InSAR deformation measurement for CR03 and CR08, compared to adjacent GPS measurements (C8 and M8), in the east-west direction (Mäkitaavola et al., 2016) [Used with permission]. Jumps are evident in the InSAR data points during every winter period.	124
Figure 5.18: Comparison of GPS Benchmarks L10 and CR6, after Mäkitaavola et al. (2016) [Used with permission].	125
Figure 5.19: MR model of the LKAB Kiruna site observed on MineViz MR. Size of the model can be scaled at the user's discretion.	129
Figure 5.20: Georeferenced GPS hubs along a 3D virtual model. (A) All GPS recorders diaplyed. (B) Only line B displayed. While a user gazes at a GPS hub the specific hub name is displayed. If clicked, the respective displacement-time graph is displayed dependent on coordinate system.	131
Figure 5.21: Hodograph results observed within the Unity interface in various angles (A) Top view (B) 50° angle and (C) 5° angle.	131
Figure 5.22: Z-Movement mesh derived from Surfer Version 16 imported into Unity. 2009 to 2011 has an evident large rebound but it was not caused geologically, but rather by issues within the data base. Some GPS such as F42 and B9 have repeated acquisition of movement within a year while others such as F2, F5, and B10, became lost due to large offsets. Other data such as B11, stopped being recorded. Losing sources of data caused skewing within the final meshing results.	134
Figure 5.23: InSAR CR-CTM Vertical deformation 2010/05/11 - 2014/05/14 overlain and georeferenced along 3D MineViz MR model.	136
Figure 5.24: InSAR CR-CTM Horizontal deformation 2010/05/11 - 2014/05/14 overlain and georeferenced along 3D MineViz MR model.	137
Figure 5.25: Birds-eye view of different textures of map used on Kiruna region that are easily interchangeable between (A) Bing (B) Google Earth (2021b) (C) OpenStreetMap Standard View and (D) Image provided by LKAB	138
Figure 5.26: 3D model of Kiruna's (A) Road/pathways and (B) infrastructures retrieved from OSM.	139
Figure 5.27: LKAB buildings (blue infrastructures) has representative detailed models while OSM models provide satisfactory models but not detailed.	140

Figure 5.28: Microseismic readings on October 2010 observed with (A) no range limit and (B) with a range limit from 0 – 3 magnitude scale	142
Figure 5.29: Flowchart of MineViz MR with LKAB Kiruna data as an example.....	145
Figure 5.30: MineViz MR with various datasets: (A) GPS hubs, civil infrastructures and InSAR data. (B) Roads, railways, GPS hubs and M2 SWEREF GPS movement. (C) Mattsson et al. (2010) structural map with 3D interpolation. (D) GIS Map retrieved from OSM	146
Figure 5.31: MineViz MR with Kiruna datasets. (A) GPS hubs overlaid on a more modern satellite imagery of Kiruna retrieved from Google Earth (2021b) (B) Kiruna observed from a different angle prior to selecting any underground data sets. (C) Once underground data is selected the model expands slowly allowing users to observe underground works clearly. (D) Same point of view as (C) after a few seconds.	147

List of Acronyms

VR	Virtual Reality
AR	Augmented Reality
MR	Mixed Reality
XR	Extended Reality
DFN	Discrete Fracture Network
AI	Artificial Intelligence
UI	User Interface
CSV	Comma Separated Values
SoC	System on a Chip
QA/QC	Quality Assurance and Quality Check
RSS	Rotary Steerable System
HDD	Horizontal Directional Drilling
DDH	Diamond Drill Hole
CSA	Canadian Securities Administration
NI 43-101	National Instrument 43-101 Standard of Disclosure for Mineral Projects
RQD	Rock Quality Designation
J_n	Joint Set Number
J_r	Joint Roughness Number
J_a	Joint Alteration Number
J_w	Joint Water Reduction Factor
SRF	Stress Reduction Factor
UCS	Uniaxial Compressive Strength
MBR	Modified basic Rock Mass Rating
MRMR	Modified Rock Mass Rating
SMR	Slope Mass Rating
GSI	Geologic Strength Index
CGSI	Composite Geologic Strength Index
RMQ	Rock Mass Quality
RMR	Rock Mass Rating
SAR	Synthetic Aperture Radar
InSAR	Interferometric Synthetic Aperture Radar

Chapter 1.

Introduction

1.1. Statement of Problem

New methodologies of acquiring, modelling, and interpreting data are being introduced by the continuous advancement of technology. Some of these include complex numerical modelling, machine learning, multi-sensor scanning and unmanned vehicles.

Such an extensive array of computational and software innovations has led to large comprehensive data sets that are visually challenging to fully observe. Advancement in Virtual (VR), Augmented (AR) and Mixed Reality (MR) has initiated a new era of data visualization. Various hardware and software have undergone intensive research and have proven to be an asset both in the field and office space. However, limited research has been conducted on how extended realities (XR) can improve data collection, interpretation, and communication within geoscience. The principal focus of this research is to demonstrate that superior visualization can greatly enhance current available data. With new conceptual models, current geological problems will be more manageable increasing project safety, profit and productivity.

1.2. Research Objectives

The primary research objectives are:

- Develop new methodologies to improve current geotechnical and geological practice during core analysis.
- Prove that VR/MR platforms are not only useful qualitatively but also quantitatively by analysing data from the core to mine scale.

1.3. Thesis Structure

This thesis consists of six chapters. Chapter 1 presents the objectives of the research, and the thesis structure. Chapter 2 provides a summary of new visualization hardware, defines selected components of the virtual continuum (VR/MR/AR), and described their current scientific applications.

Chapters 3 and 4 show how altering reality has the potential to revolutionize core logging practice in resource assessment and geotechnical investigation. Chapter 3 presents a holographic interface that can aid core logging in both geotechnical and geological practice. Since companies have different core logging standards, the interface can be readily modified to specified requirements. Chapter 4 describes virtual reality/mixed reality visualisation of drill core resource modelling in the mining industry through a variety of platforms including both petrological thin-sections and borehole imagery positioned along virtual core models. All the models were then organized in a single platform, demonstrating the feasibility of a virtual core shed.

Chapter 5 presents geovisualization applied to LKAB Kiruna Mine, Sweden. A major MR/VR holographic database was developed consisting of GPS, tensiometers, InSAR, current mine workings, civil infrastructure, DEM, micro-seismicity, geological structures, and previous mine development. Kiruna is an active mine; therefore, the model was designed to be readily updated.

Chapter 6 provides a discussion and conclusion of the thesis research in addition to recommendations for future work. A summary of each chapter is graphically represented in Figure 1.1. Since this thesis is heavily focused toward geovisualization, short films of the results are available as a supplementary digital data file.

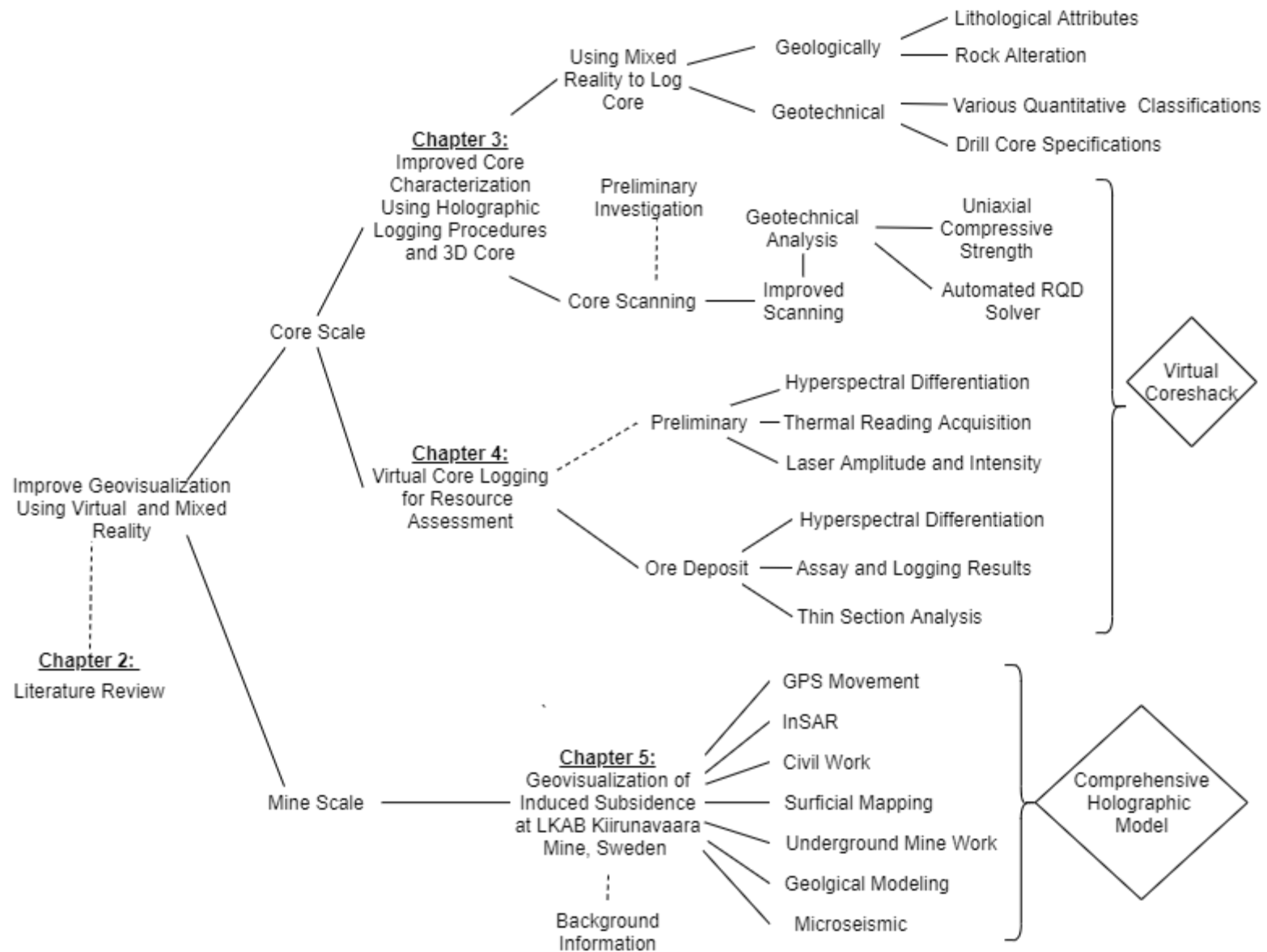


Figure 1.1: Flow chart showing thesis structure.

Chapter 2.

Literature Review

2.1. The Virtual Continuum

Advances in hardware have now allowed the once fictional concept of being able to immerse a person into a different world to become a reality. Milgram and Kishino (1994) state that realities can be separated into a virtual continuum (Figure 2.1).

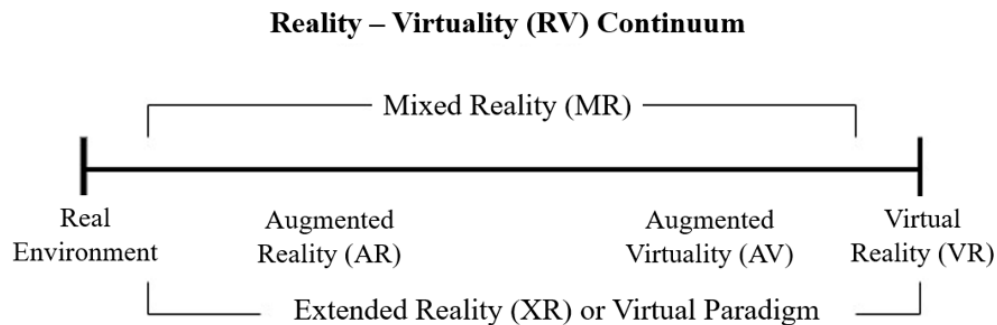


Figure 2.1: Virtual continuum after Milgram and Kishino (1994).

The virtual continuum has been sub-divided by Gownder (2016) and Milgram and Kishino (1994) into:

- Conventional reality (the real environment), is represented by one end member.
- Virtual reality (VR), is representative of the other end member, where conventional reality is completely occluded (e.g. through visual and hearing responses) and replaced by a preprogrammed virtual environment (Section 2.2).
- Augmented reality (AR), enhances a person's view by overlaying data sets within their field of view, and thus, remains close to conventional reality (Section 2.3).
- Augmented virtuality (AV), refers to the emplacement or projection of real objects within a computer-generated realm (e.g. metallurgist on a weather forecast map).

- Mixed reality (MR) includes everything that falls within AR and AV, and thus, virtual and physical objects can coexist in the same dominion (Section 2.4).
- Extended realities (XR) refers to all altered realities within the virtual paradigm.

Terms within the continuum are often used interchangeably and simplified in commercial practice. The inconsistent and incorrect use of terms has led to confusion and misunderstanding of their definition.

The visual range of the virtual paradigm can also be explained using any pre-processed model (Figure 2.2). To place this into perspective, VR would position a computer-generated model (i.e. a core sample) within a virtual world. AR, would place the sample as a simple overlay in the real world, without considering occlusion or orientation. Within MR, the virtual objects would become anchored to the real world allowing them to become occluded, and directly interact with other physical objects adjacent to them. Thus, MR provides the most realistic scenario in which real and virtual objects coincide with one another.

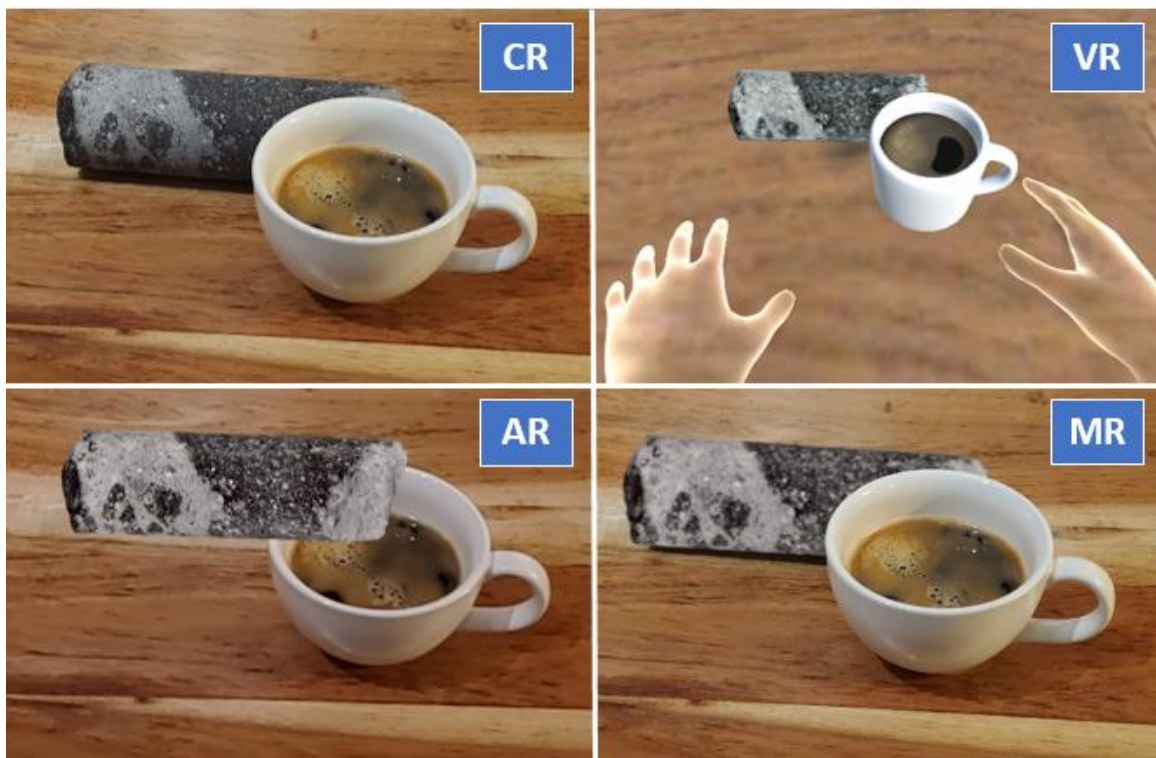


Figure 2.2: Comparison of a core sampled in Conventional Reality (CR), Virtual Reality (VR), Augmented Reality (AR), and Mixed Reality (MR).

2.2. Virtual Reality (VR)

Virtual Reality (VR) is defined as a computer generated interactive immersive environment that stimulates sensory traits such as sight and sounds (Merriam-Webster, 2021). An enveloping reality can be achieved by a head-mounted display (i.e. headset) which completely occludes a person's perspective and replaces it with a pre-programmed ambiance.

The idea of VR remained fictional for many years. It was only when the first stereoscope was constructed in 1838 that it finally started to move beyond science fiction to reality as 2D projections became representative of 3D models. The concept was revolutionized in 1956 when the first VR machine was developed (The Franklin Institute, 2021). Currently the same stereographic approach is used in VR glasses to immerse the user into a 3D world. Rapid advances in software and hardware have permitted semi- to fully- portable VR headsets to become industrialized. Built-in accelerometer, gyroscope, magnetometer and proximity sensors help detect the user's motion. Due to safety and space limitation, locomotion is primarily limited to either joysticks or button inputs.

To make movement more natural, companies such as Virtuix (2021) have created 360° walking platforms. In the past, virtual movement was mostly controlled by teleportation or flyby-effect rather than representative walking. This approach was used since mimicking the action of walking without the physical response had nauseating effects on consumers. Within a year, movement via joystick has been improved significantly and can now mimic walking and running (Boneworks, 2021). However, the abnormal effects of moving without the physically response can still nauseate for some users, and thus, sensation accommodation is still required.

Major companies such as Facebook (Oculus, 2021), Sony Interactive Entertainment (2021), and Microsoft (2021a) have all created their own VR headsets. Latency, frame rate, and authenticity to natural behaviour are key in making VR headsets effective. Thus, most headsets are tethered to a computer to ensure optimum responsive feedback and have compatible controllers that ensure fast response.

Companies such as Leap Motion owned by Ultraleap (2021) revolutionized immersive interaction by detaching from a physical controller and solely focusing on the player's physical hands as the input manager (Figure 2.3.A). As of 2019, more companies are

resorting to this methodology as it is a more natural input. For instance, the Oculus Quest has compatible controllers but can also use its built-in camera to allow the user's hands as input, providing input versatility (Figure 2.3.B) (Oculus, 2021). Other headsets, such as Valve Index VR have resorted to a hybrid methodology in which the user's hand are actively scanned via the controllers (Figure 2.3.C) (Valve Corporation, 2021).



Figure 2.3: Different controller methodologies used in VR. (A) Leap Motion device that can be attached to VR headset for accurate finger input (Ultraleap, 2021). (B) Optional scanning by Oculus Quest Headset to allow finger input (Oculus, 2021). (C) Valve Index VR controller which scans finger interaction (Valve Corporation, 2021).

VR carries a preconceived notion that it is purely for entertainment, however, it is being increasingly adapted for scientific purposes. Some geological applications in which VR has been adapted include, but are not limited to, geological field trips in virtual reality (Onsel et al., 2018; Hopkins, 2019) and mining safety simulations (Smit, 2013). Other applications that are also beneficial to geoscience and other industries include (1) Accurate piloting of drones (DJI, 2021) (2) Improved online pedagogy (Allcoat and von Mühlenen, 2018) (3) Safety enforcement (Rossler et al., 2019) and (4) Innovative driving simulations (Brunner, 2020). Training modules brought to VR have major implications as the user is placed in an environment that may be too expensive, inefficient, unfeasible or too hazardous to be physically experienced.

2.3. Augmented Reality (AR)

Unlike VR, Augmented Reality (AR) does not fully immerse the user in a fictional environment. This reality has been defined as the superimposition of computer-generated image onto a user's view, to generate a composite or "augmented" view (Heimgartner, 2016). Both synthetic and natural light intersect the user's perspective, preventing loss of focus on conventional reality.

AR has shown to be useful by many companies such as RideOn (2019) and WayRay (2021), which display navigation paths on Ski goggles and car windshields, respectively. WayRay have publicly demonstrated the implementation of AR windshields in a Genesis G80 by Hyundai and a Mercedes-Benz E-Class. Currently WayRay has contracts with Porsche, Hyundai and Pininfarina and hopes to revolutionize the automotive industry by the end of 2021 (Figure 2.4A) (WayRay, 2021). Their aim is to implement their interface on boats, planes and building windows providing the potential future implications of AR in everyday use.

AR can alternatively be displayed through a cellular device rather than glasses. Companies such as Facebook, Microsoft, Samsung, Apple, Snapchat and Ninantic (owners of Pokemon Go app) have already executed and introduced AR to a wide variety of users (Figure 2.4B). Furniture companies such as IKEA (2021) and Lowe's (2021) have also introduced AR applications which allows consumers to emplace simulated merchandise at on their selected environment. This helps consumers and interior designers decide what product is most suited to their needs.

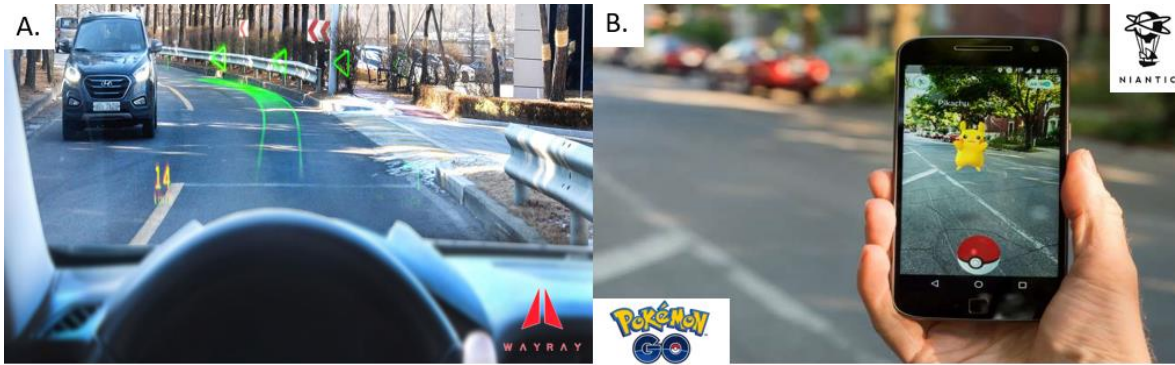


Figure 2.4: Some uses of AR (A) WayRay AR windshield which is to be implemented into Hyundai car windows by 2020 (WayRay, 2021). (B) Popular phone application known as Pokemon GO which is able to emplace a Pokemon within a cellular view (Niantic, 2020).

In 2013, Google attempted to implement AR widely via Google glasses. These glasses were thought to be futuristic and revolutionary but were discontinued in 2015 due to lack of consumer interest. The reasons for this include a lack of consensus over where they could be implemented, questionable value, slow development, and privacy concerns (CBInsight, 2016; Yoon, 2018). With the exponential growth of interest in XR, Google has reopened the project and will progress to its second edition known as Google Enterprise. These glasses have yet to be released to consumers, due to continued privacy concerns (Google, 2021a).

Applications of AR within geoscience has remained limited to research or concepts which have yet to be effectively executed in the field. The most well-known AR geological platform is the AR Sandbox which has been used to teach geology students how contouring, topographic profiling, and fluvial processing work (Woods et al., 2016). Despite the name, this module is a MR platform, as it requires active 3D scanning to operate.

2.4. Mixed Reality (MR)

Mixed Reality (MR) uses objects within our conventional reality as an input. The environment is discretized into an interactable mesh, permitting digital and physical artefacts to co-exist within the same environment (Müller et al., 2007). This differs from

AR as virtual objects are not simply overlain but rather become correctly anchored to an environment and either partially or fully occluded by their imminent setting (Figure 2.5).

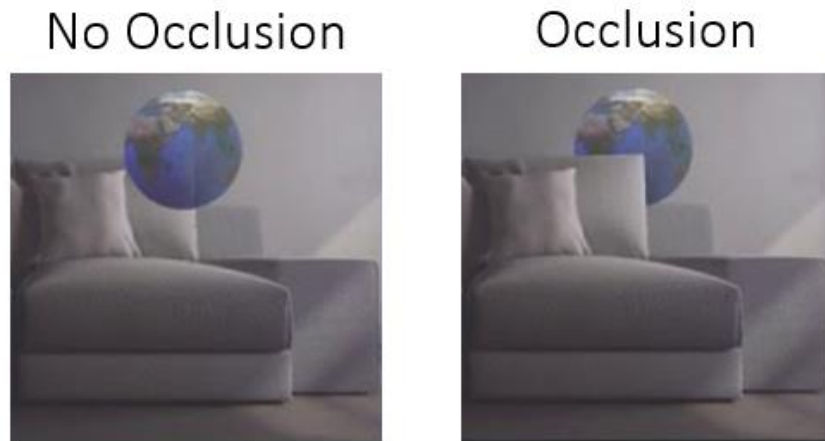


Figure 2.5: Examples of occlusion that can be observed in MR (Microsoft, 2021b).

MR headsets allow AR and limited VR settings within a restricted field of view. In 2016, the only MR headset commercially available was the Microsoft HoloLens. Today several alternatives exist including Magic Leap One (Magic Leap Inc, 2021), Project North Star (Ultraleap, 2021), and the HoloLens 2 (Microsoft, 2021b).



Figure 2.6: Microsoft HoloLens 1. The first MR headset that discretized physical environments through a similar technology to the Xbox Kinect (Microsoft, 2021a).

The HoloLens 1 specification includes a built-in scanner with an operative range between 0.8 to 3.1 metres from the headset. The limited close-range input is due to processing limitations and to prevent unnecessary acquisition. The viewing window is a cone of $34^{\circ} \times 16.9^{\circ}$, making it non-immersive and restricted (Davies, 2019).

Virtual objects fade once the user is less than 40 cm away. Conventional reality is always visible as a rough base to promote spatial awareness. Cross platform display can be interlinked with other HoloLens, VR headsets, and cellular devices. Team viewing data enhances both communication and data interpretation between multiple disciplines.

Limitation of the HoloLens 1 included:

- A 2GB RAM and storage capabilities of 64 GB with only 54.09 GB available space, limiting the processing power required for complex computational algorithms.
- Complex data can make the HoloLens 1 crash or significantly decrease its frame rate.
- Spatial mapping may fail due to lighting, motion, featureless walls, or the camera being obscured.
- Anchoring of an image might not be perfect in a changing environment.
- Lack of accurate controllers restricts input to the user's gaze, voice commands, a clicker and two hand gestures known as Air Tap and Bloom (Figure 2.7) (Microsoft, 2021b).
- Battery life is 2 to 3 hours depending on the processing and brightness.

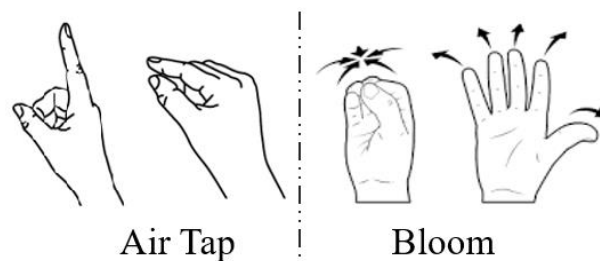


Figure 2.7: Hand gesture recognized by Microsoft HoloLens 1 (Microsoft, 2021b).

Anchoring errors have been corrected using image processing. Vuforia, an add-on software, allows holograms to be instantly placed in a predefined position, orientation and scaling with respect to an image (Vuforia, 2021). These powerful standalone MR glasses have led various companies to start investing and developing numerous applications (Table 2-1).

Table 2-1: Summary of various industry MR applications.

MR Applications		
Application	Company	Benefits
Communication	Autodesk	Designers and engineers can compare CAD models with the physical world and highlight discrepancies (Stocking, 2018).
Assembly and Manufacturing	ThyssenKrupp	Elevator service technician application that helps proactively identify problems. User can show his perception to experts offsite for verification. Proved to increase productivity by 4x (O'Brien, 2017).
Medicine	Harvard Medical School, University of Munich, Washington University, etc.	Various institutes and universities have conducted research to use MR to help future doctors undertake complicated procedures such as radio-frequency ablation of myocardial scar (Jang et al., 2018), near infrared fluorescence guidance (Cui et al., 2017), X-ray free endovascular interventions (Kuhlemann et al., 2017), and vascular localization (Jiang et al., 2020)
Engagement	Ford	Demonstrate new models that can be customized to the consumer's taste. Substitution of clay models with holographic models saves manufacturers time and money (Bardeen, 2017; Galeon, 2017).
Interaction	NASA	MR application known as ProtoSpace. It helps visualize hardware in real space to find discrepancies which might be overlooked. This was designed in hope to enable space stations with rapid assistance, reducing crew training requirements and increasing efficiency (Chan et al., 2019)
Warfare and Surveillance	US Army	Modified HoloLens 2 to displays relative positioning on a virtual map, emplace a virtual reticule for aim assistance and use FLIR camera mounted on-top of the lenses for both thermal and night vision (Haselton, 2019)

2.4.1. HoloLens 2

The HoloLens 2 was introduced in 2019 albeit in limited quantities. The specifications include (Microsoft, 2021b):

- Field of view of view more than doubled compared to the HoloLens 1 (52° compared to 30°).
- Finger recognition and eye tracking provide further input capabilities.
- Hardware has significantly improved allowing better and faster discretization of the environment.
- Built-in artificial intelligence (AI) known as Azure, allows more efficient processing.
- Better ergonomic, design, and leisured dismounting of glasses.
- USB-C Charging port.



Figure 2.8: HoloLens 2 has a more ergonomic fitting and the lenses can be flipped up to rapidly disengage the user from MR (Microsoft, 2021b).

Furthermore, the HoloLens 2 platform now allows the user to observe the same model and interact with it in different localities using Microsoft Mesh (Langston, 2021). This enables collaborative computation for various applications through interlinking of models with other hardware devices such as VR headsets. With Azure's enterprise security, privacy of cloud information being breached is at a minimum, providing security and versatility for holograms in cloud space.

2.5. Geovisualization

Geovisualization is a multidisciplinary field that utilises geographically restricted information such as geological, geohazard, image analysis, and exploratory data analysis (EDA) to provide improved methodologies, tools, analysis, synthesis and presentations (MacEachren & Kraak, 2001; Andrienko et al., 2007; Cartwright & Peterson, 2007; Çöltekin et al., 2017). This field originated from the high demand on visualization required in cartography, and spatial data (i.e. maps). With advances in techniques and technology, mediums to geovisualize procedures and interaction have become more readily available (Keim et al., 2005). Issues that are encountered within all geovisualization platform include:

1. **Multi-disciplinary work representation and design:** Ensuring a multi-user telecommunication system that is effective, readily available, and public is challenging as it requires various mediums, tests and inputs (Andrienko et al., 2007).

2. **Data Handling and analysis:** The large computational capabilities and sophisticated methodologies used to acquire data have resulted in encoding of terabytes of information which may not be easily visualized (Çöltekin et al., 2017).
3. **Experimental and multi-modal “maps”:** There must be major adjustment from traditional maps, which are flat and static to convert to 3D. Virtual realism, multi-sensory representation and modes of interaction are required to improve insight (MacEachren & Kraak, 2001).
4. **Human Centred approach:** Integration between theory, practice, realism, abstract views and human decision must coexist for geovisualization to be effective (MacEachren & Kraak, 2001; Laramée & Kosara, 2007; Virrantaus et al., 2009).

Appropriate visualization can bridge data-driven machine learning and theoretical research, ensuring optimum results (Turkay et al., 2017). Once both human and machine driven data are integrated effectively the removal of skewed/noisy data, intuitive conclusions, and qualitative overviews can be achieved (Keim et al., 2005; Piringer et al., 2010).

2.6. Applying the Virtual Paradigm within Geoscience

The use of Extended Reality (XR) for geovisualization, to date, has been very limited. Some XR applications include (1) Geological education (HoloGroup, 2020), (2) Geovisualization of BIM, CAD and GIS files in real time (vGIS, 2021), and (3) Understanding applied geosciences on multiple projects (BGC, 2021). However, the ability to improve data interpretation and analysis have yet to be investigated in depth.

Geoscience and geotechnics are inherently a practical industry. Thus, MR is the preferred conduit to conduct geological XR research as it does not remove on site field work but rather enhances it. Advantages and limitations of MR and VR are compared and summarized in Table 2-2. It is clear that MR is currently more applicable for on-site geoscience especially since the HoloLens 1 and 2 are now compatible with approved hard hats thereby allowing the headsets to be used in construction and mining sites

while still complying with safety protocols (Trimble, 2021) (Figure 2.9). VR, however continues to remain superior for lab and office-based work as it surpasses MR in memory, processing, and resolution definition. Greater processing power and the VR immersive experience can be used to visualize areas that are inaccessible due to safety or time. Knowing the limitation of each hardware is key for prospecting XR software.

Table 2-2: Advantages and disadvantages of VR and MR.

	Advantages	Disadvantages
Virtual Reality (VR)	<ul style="list-style-type: none"> • Fully immersive • High computational capabilities • Price range low • Responsive controllers 	<ul style="list-style-type: none"> • Motion sickness • Eye straining • Tethered • Fish-eye effect • Specific to setting • Safety
Mixed Reality (MR)	<ul style="list-style-type: none"> • Spatial Awareness • Untethered • Standalone • Scanning capabilities 	<ul style="list-style-type: none"> • Computational limitations • Battery life • Limited user input • Price range high



Figure 2.9: Trimble (2021) HoloLens 1 hard hat that complies with safety requirements (Onsel et al., 2019) [Used with permission].

2.6.1. Using the Virtuality Paradigm for Improved Geovisualization

The integration of visual, computation methodologies, adequate interface, and cognitive usability is required for an effective geovisualization application (Keim et al., 2005).

Research on potential improvements in geological, geotechnical and engineering visualization applications using the HoloLens has been conducted by several companies. BGC Engineering for example, has developed the ADA Platform to help understand and communicate geoscience problems with terrain, survey data, and engineering designs to experts and stakeholders (BGC, 2021). Other companies, such as Finger Food, worked with Goldcorp Inc. to promote operational efficiency, and safety by implementing AR/MR to improve shovel operator precision for different material types. This project was still within the testing phase, but the proof of concept was successful (Facey, 2019).

The Simon Fraser University Engineering Geology and Geotechnics Research Group has also conducted several MR/VR based projects to help investigate the potential for improved interpretation and communication within various engineering/geology areas. Some of these include (Onsel et al., 2018):

- VR and MR imaging of the Masaya Volcano, Nicaragua for educational purposes (Figure 2.10).
- Geotechnical representation of a fjord slope failure with combined terrestrial and bathymetric data (Figure 2.11).
- Propagation of block caving beneath the Palabora Mine Pit, South Africa (Figure 2.12).

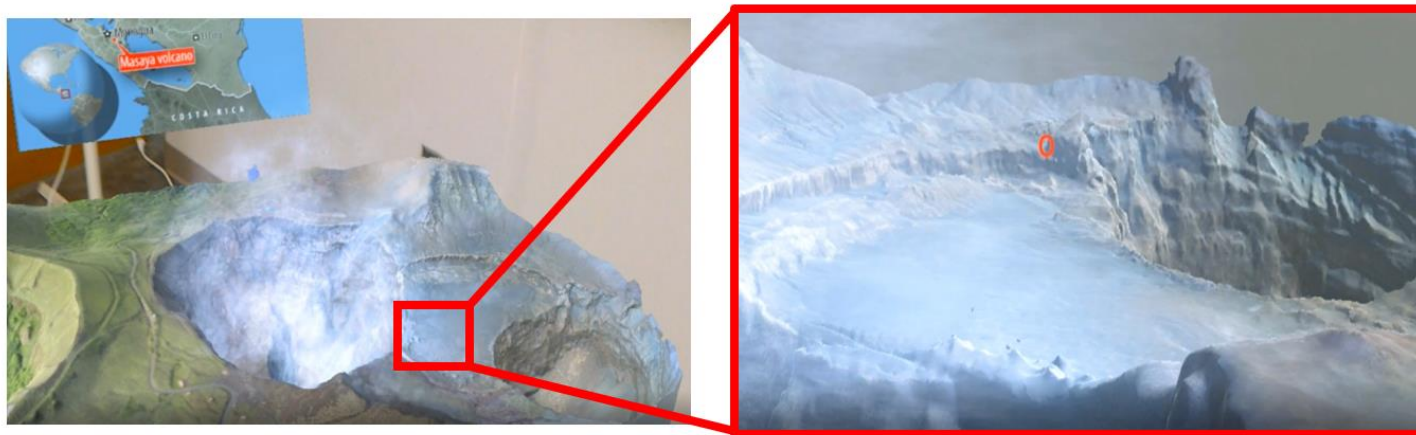


Figure 2.10: Masaya Volcano located in Nicaragua seen as an AR model. The user has the option to change to VR within the HoloLens 1 to observe the model in more detail (Onsel et al., 2018) [Used with permission].

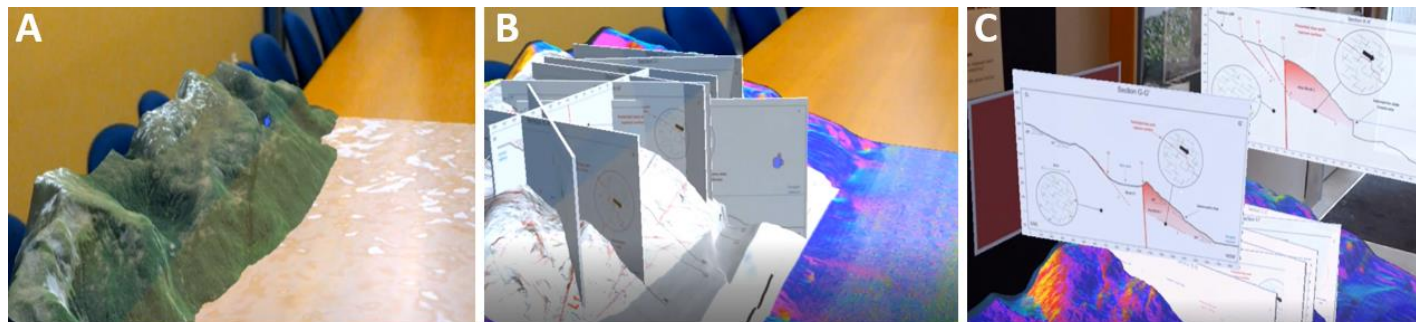


Figure 2.11: Hawkesbury slope, BC DEM model combined with the bathymetry model (A) Model with bathymetry results being covered by water (B) Textured with slope orientation, overlain by 2D geological map and cross-sections (C) Spatially anchored cross-sections can be extracted from the slope at the users convenience for in depth analysis (Onsel et al., 2018) [Used with permission].

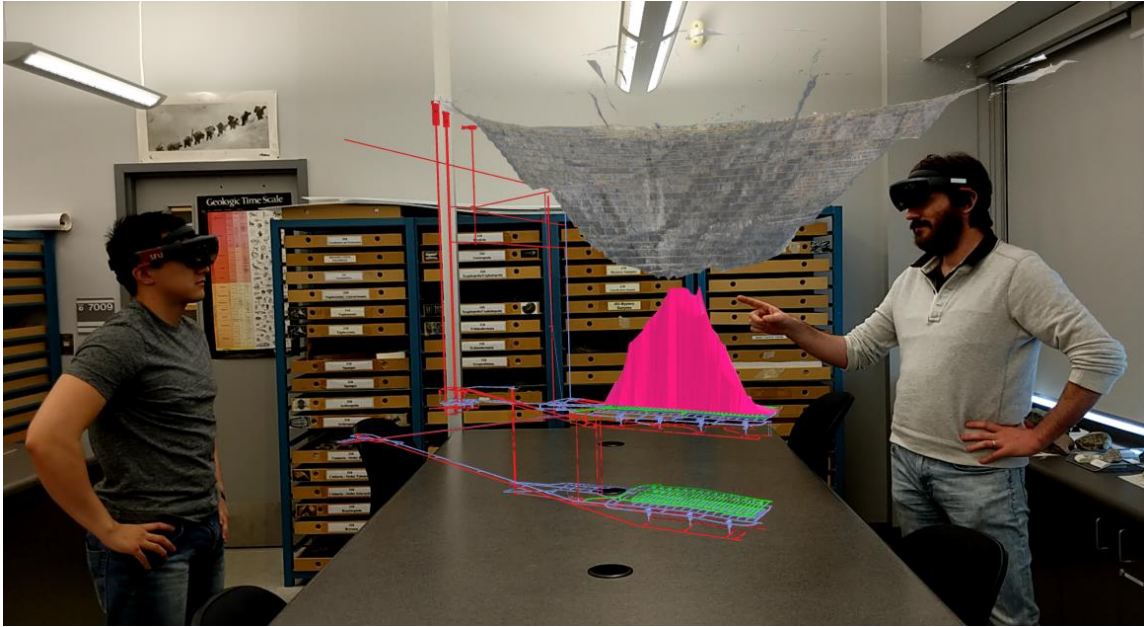


Figure 2.12: Palabora block cave mine, South Africa model being observed by two individuals at the same time showing the propagation of block caving, open pit model, and underground mine layout (Onsel et al., 2019) [Used with permission].

Various other trial projects were conducted during this thesis research. In one project, a discrete fracture network (DFN) was visualised. A model with nine major discontinuities was created using the three-dimensional distinct-distinct element geotechnical modelling software 3DEC (Itasca, 2021). A VR approach was then used to explain how cores can sometimes miss important discontinuities (Figure 2.13).

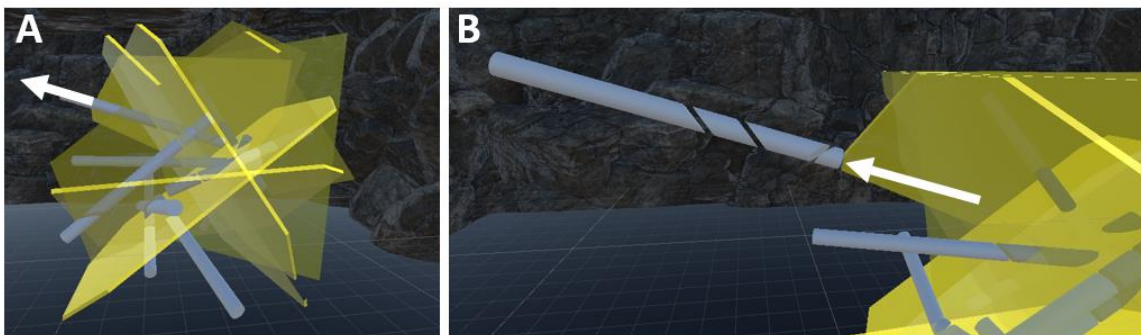


Figure 2.13: DFN model transferred from 3DEC for VR application (A) Cylinders were added to represent drill cores (B) Drill cores can be removed by the user, rotated, and scaled. Core only intersected three of the nine discontinuities.

A second application of MR/VR involved the TransLink Skytrain in Vancouver, British Columbia from Stadium-Chinatown to Waterfront Station. This sector takes the train underground, and thus, knowing the stress distribution around the tunnel is important for assessing the opening stability. The induced stresses were analysed using the finite element software RS2 and RS3 (RocScience, 2021a). The RS2 results were then imported into the HoloLens 1 to communicate with clients, professors, and students. Many scenarios were tested and easily visualized within the model (Figure 2.14). The RS3 results were not imported as compatible export was unavailable.

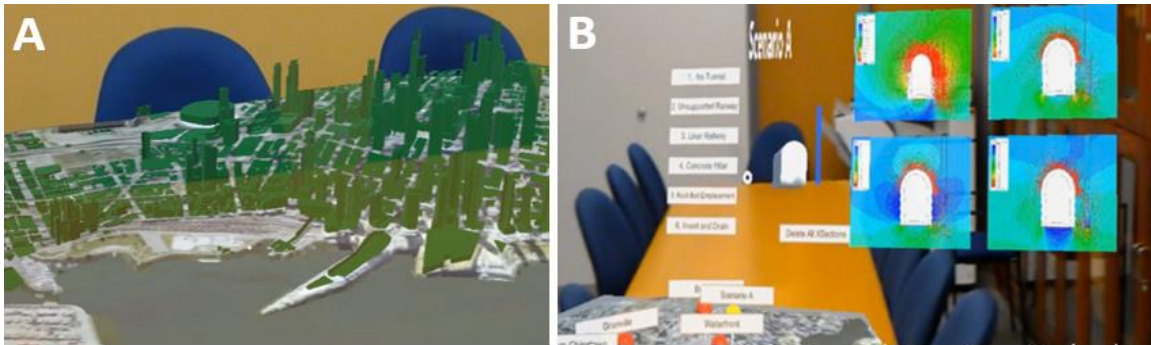


Figure 2.14: Vancouver, BC, Canada model of downtown area made by the author and Jesse Mysiorek; SFU MSc student (A) 3D buildings along Vancouver DEM model visualized through HoloLens (B) Selected RS2 results from the various scenarios modelled.

2.6.2. Using the Virtual Paradigm beyond Visualization

Most researchers and companies have used the virtual paradigm solely as a visualization tool. MR/VR however, also has significant potential for use in both data collection and analysis.

Simon Fraser University Engineering Geology and Geotechnics Research Group, and SRK Vancouver, through a joint Mitacs Accelerate Project, developed a field application which allows 3D mapping in the field using both MR and VR (Figure 2.15, Figure 2.16). This application is known as EasyMap MR/VR and has proven successful for mapping underground and surficial outcrops (Onsel et al., 2019).

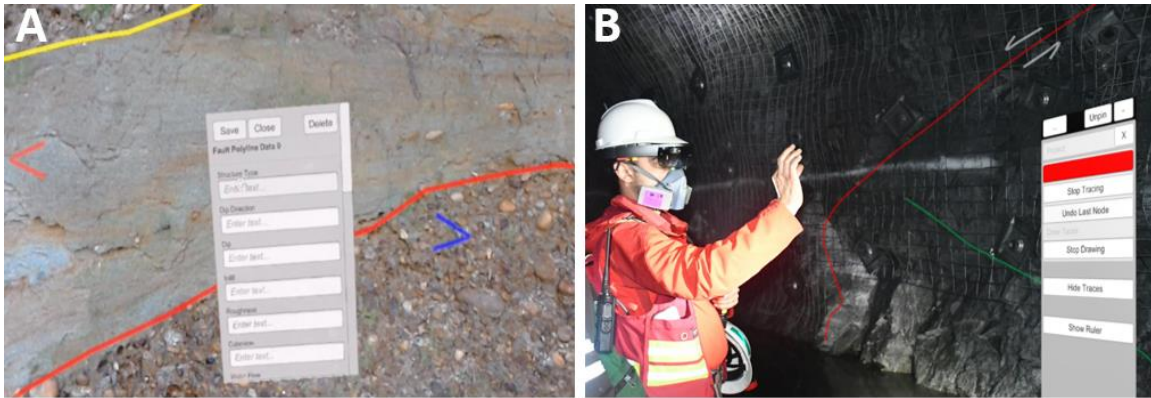


Figure 2.15: EasyMap MR Application developed by SRK Vanocuver and Simon Fraser University (A) Delineating lithological contacts in the field with X,Y and Z coordinates (B) Underground mining delineation of a normal fault (after Onsel et al., 2019) [Used with permission].

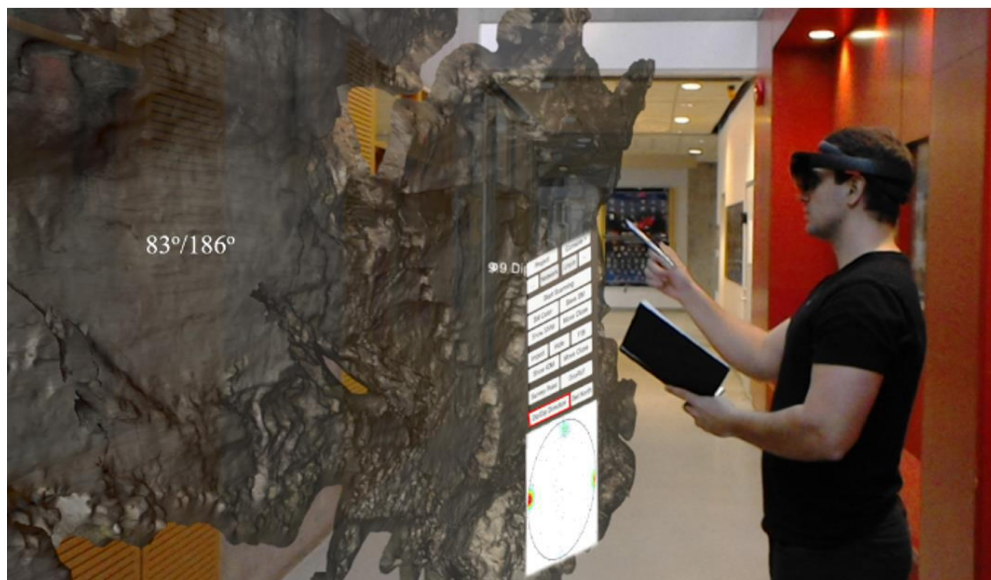


Figure 2.16: EasyMap MR used in an office setting to map a remotely-sensed outcrop from the Jure Landslide, Nepal, to obtain real-time structural orientation and measurements (Mysiorek, 2019a) [Used with permission].

When using EasyMap in VR, higher resolution point clouds and meshes can be imported and analysed in an office environment. Complex meshes can be retrieved from terrestrial/UAV laser scanning (TLS), photogrammetry or other remote sensing methodologies (Figure 2.17).

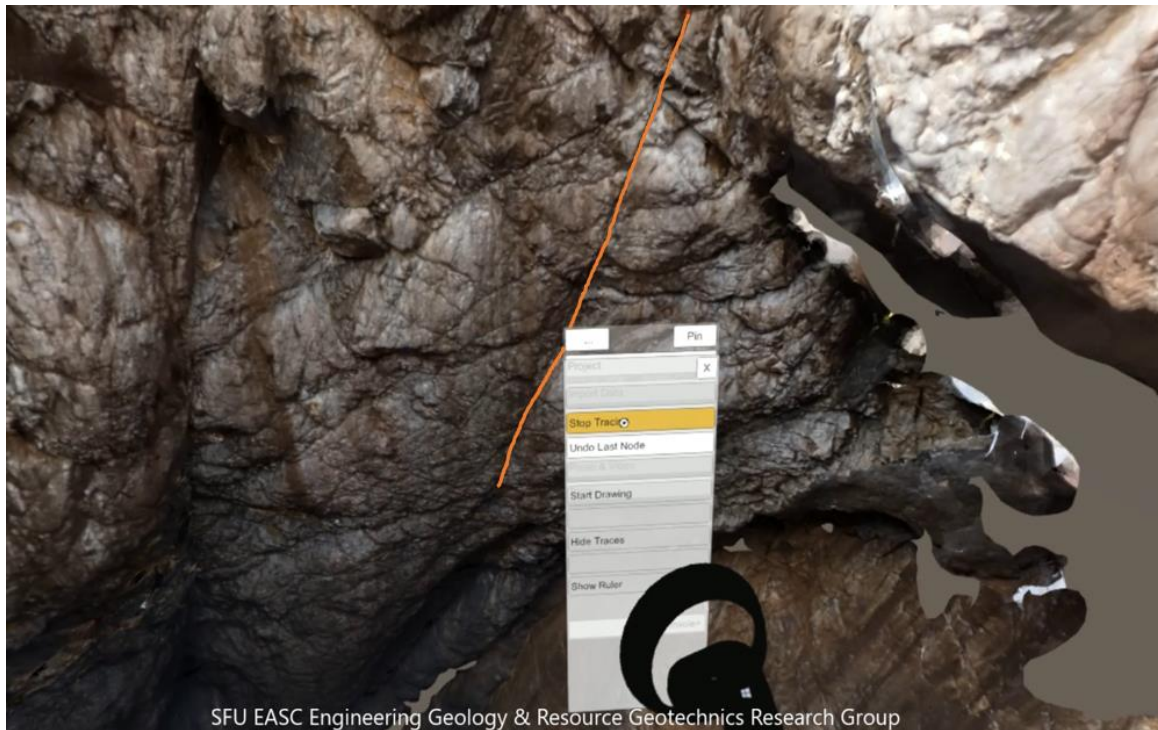


Figure 2.17: EasyMap in VR with a high resolution UAV photogrammetry model (Onsel et al., 2019) [Used with permission].

The ability of HoloLens MR to scan surfaces enables using EasyMap MR to generate a mesh of a rock face in quasi-real time which can then be georeferenced. The registration allows local data to be imported for on-site visualization (Onsel et al., 2019). To ensure an acceptable scan has been completed, the user can observe the quality of the mesh on a small-scale model which can be scaled, rotated, and freely moved in real-time (Figure 2.18).

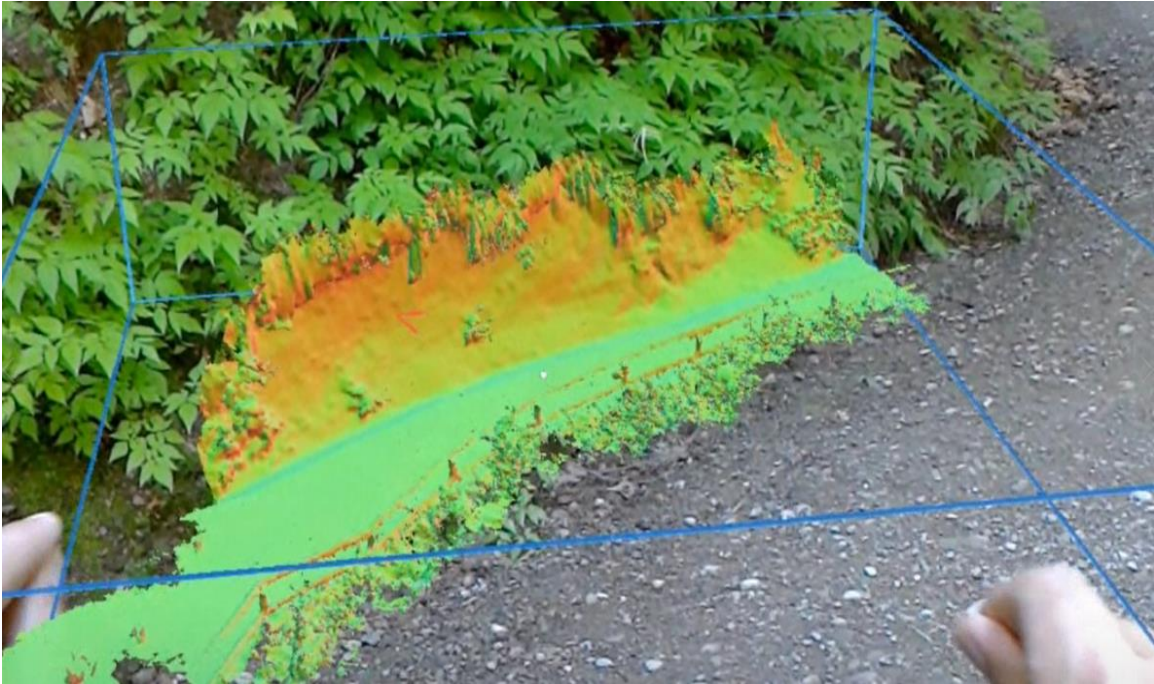


Figure 2.18: Mesh generated from the HoloLens without any postprocessing nor preprocessing (Onsel et al., 2019) [Used with permission].

Whether it is generated in MR or VR, a user can collect geological, structural, and geomechanical mapping data by either drawing traces or polygons on the provided surface. Each mapping feature can then be annotated with specific parameters. All polygons and polylines can be exported as georeferenced comma separated values (CSV) files, removing any post-processing requirements.

An integrated tool which remotely determines dip and dip direction has been incorporated within the EasyMap MR/VR software allowing point data to be rapidly collected compared to manual collection. Safety is increased as the user does not have to be directly on the outcrop surface or under a steep rock face to retrieve a measurement but instead can approach it virtually when necessary. The rapid collection of data allows a better statistical analysis, improving representative attributes such as joint surfaces. Collected data is plotted on a virtual stereonet in real time (Figure 2.19).

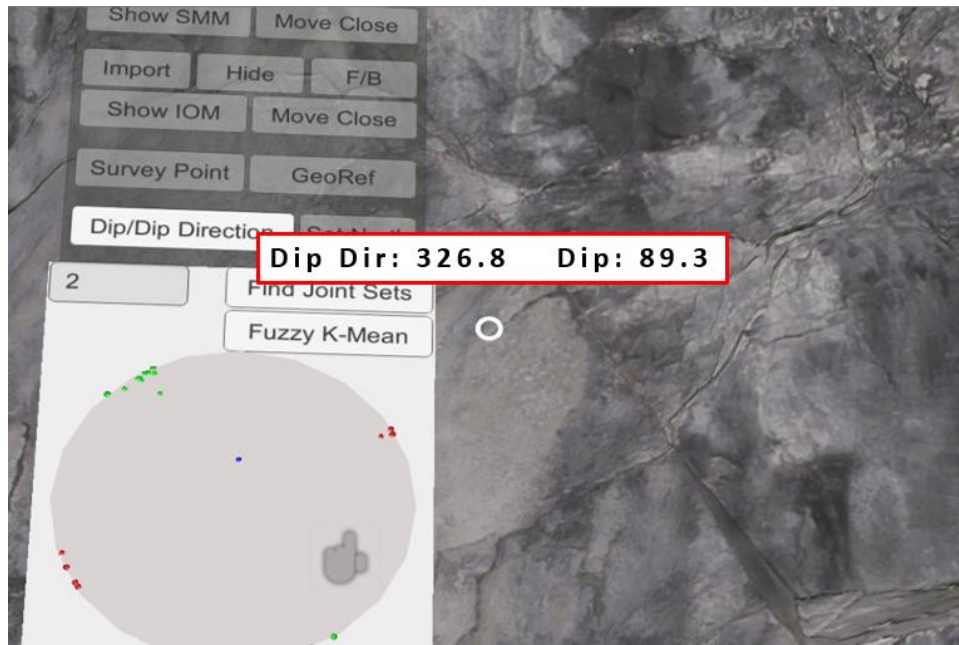


Figure 2.19: Discontinuity can be measured by simply viewing a surface using Hololens 1. Once the user clicks, the measurement is plotted as a defined discontinuity sets (Onsel et al., 2019) [Used with permission].

EasyMap MR/VR also has a ruler tool that allows rapid acquisition of the persistence and length of material. Numerous holographic charts formats, which are commonly taken in the field as hard copies, are also readily available for holographic viewing. A user can also take photographs and record videos for additional documentation (Figure 2.20).

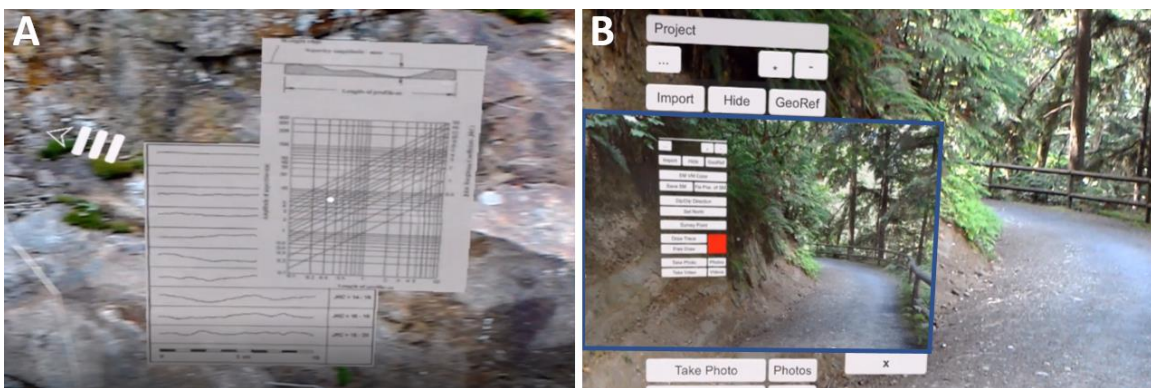


Figure 2.20: EasyMap MR tools (A) Take desired charts to the field as holograms (B) Photographic acquisition of line of sight taken during video recording within the HoloLens (Modified after Onsel et al., 2018) [Used with permission].

The use all these tools within EasyMap MR/VR software can significantly speed up conventional geomechanical, geological and structural mapping practice. With the addition of the Trimble HoloLens helmet, safety requirements on engineering sites are met. As the scanning resolution of the HoloLens is improved, the accuracy and potential EasyMap MR increases proportionally.

2.7. Developing and Integrating Models into the Virtual Continuum

Developments within VR, AR, and MR to date are mostly restricted to two distinct game-engines known as Unity (Unity Technologies, 2021) or Unreal Engine (Epic Games, 2021). Both development engines have been adopted by industry as they provide a user-friendly, versatile user interface (UI) and interactable 3D space. Both can import and interact with an array of complex file formats.

Unity has become the dominant engine within the Augmented and Virtual Reality community hosting approximately 60% of all VR/AR content (Unity Technologies, 2021). In this thesis, Unity was used as the main hub to host all the models as Microsoft freely provided a compatible Mixed Reality Toolkit to promote VR, MR and AR development (GitHub, 2021).

It is important to note that Unity was used as the final hub for many datasets that were retrieved from other complex software such as ArcMap Version 10.5 (ESRI, 2020), Blender Version 2.81 (Blender, 2021), Leapfrog Geo 4.5 (Seequent, 2021), Microsoft Excel 2019 (2021c), MeshLab Version 2016.12 (MeshLab, 2021), CloudCompare 2019 (CloudCompare, 2021), Agisoft Metashape (Agisoft, 2021) and Google Earth Pro (Google, 2021b). Unity's scripting language is C#; however, Python scripts were used for several backend batch processing of research data refinement. The MR headsets used in this research were the HoloLens Versions 1 and 2 (Microsoft, 2021b). The VR headset used was the HP Mixed Reality Headset (HP Development Company, 2019).

2.8. The Future of the Virtual Paradigm

With various major companies such as Google, Apple, Intel, Facebook, and Sony releasing their own XR platform devices, we are entering an era where visualization will

play an increasingly important role in the coming years. As technology continues to advance, hardware will inevitably become more practical and with fewer limitations. The computational capabilities of cellular devices grew exponentially within a 15-year time span and it is to be expected that the same will occur within XR. Being at the forefront of evolving technology will secure applications that will proportionally advance as the hardware and software improve.

To place this into further context, many XR platforms use the Snapdragon XR1 and Snapdragon 835 as their system on a chip (SoC). A SoC is an integrated circuit that can include components such as CPU, GPU, memory, analog, digital and wireless modems embedded in a single system (Keating and Bricaud, 2002). Currently, headsets such as the Oculus Quest and HoloLens 2 have a Qualcomm Snapdragon 835 (Microsoft, 2021b; and Oculus, 2021).

At the end of 2019, Qualcomm announced their new processor Snapdragon XR2, which will be the world's first 5G XR SoC (Horwitz, 2019; Fink, 2019) (Figure 2.21). The capabilities of this new processor include:

- 3K display with 90 frame per second (FPS) in each eye.
- Supports 4K video at 120 FPS.
- 5G will allow incorporation of the cloud for better performance.
- Superior discretization of computer vision within MR headsets.
- The AI engine delivers 15 trillion operations per second (TOPS) compared to the 1.3 TOPS in Snapdragon 835 model which is used in the HoloLens 2.
- Able to operate seven different cameras, rather than four, which promotes better head tracking, eye tracking, hand tracking, and even lip tracking.

The compressible high potency and capabilities of this new SoC represents the next major leap in XR platforms. Concepts involving more natural appearing MR and AR glasses have been also discussed by and Qualcomm (Fink, 2019) (Figure 2.22).

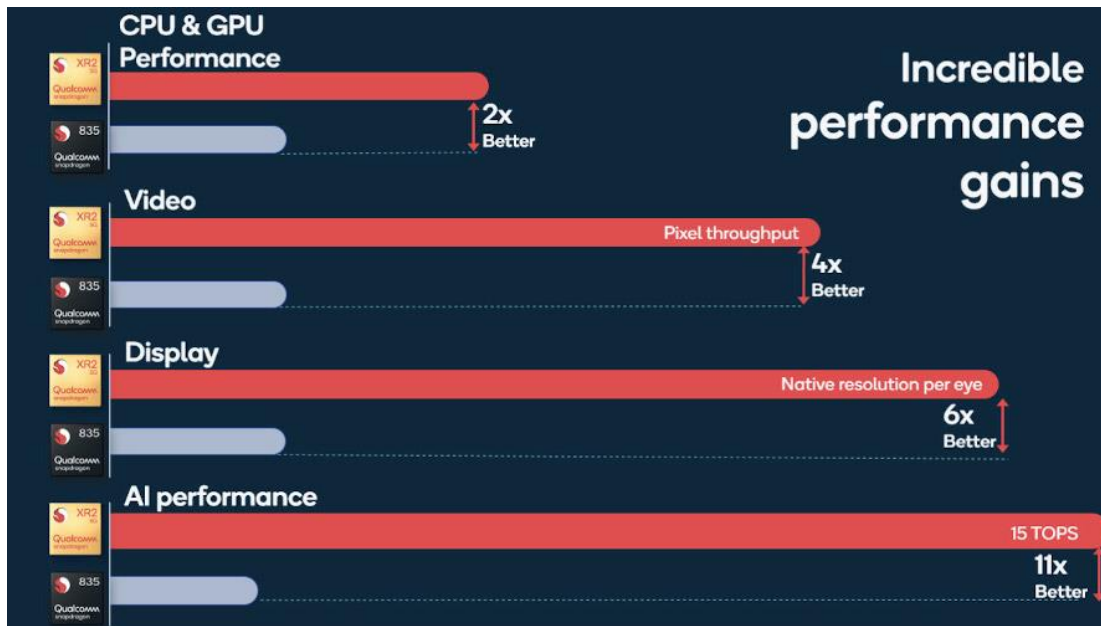


Figure 2.21: Qualcomm announcement chart of XR2 in comparison to Qualcomm Snapdragon 835 which is currently used in the HoloLens 2 (Fink, 2019).

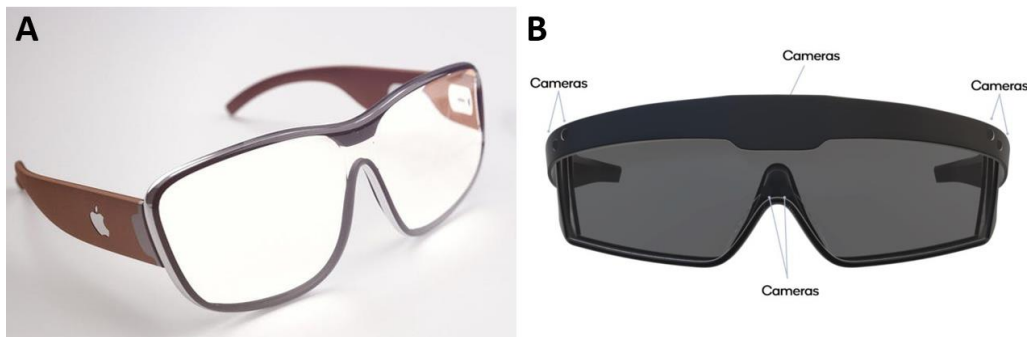


Figure 2.22: New projected MR and AR aesthetic glasses for the consumer market (A) Apple AR glasses set to be released on 2020 (B) Qualcomm new XR glasses which uses seven cameras to allow improved mesh discretization.

Both Apple and Android have continued to make all their devices compatible with AR since 2018. With available iOS package ARKit and Android package ARCore, greater possibilities for integrating AR Applications into cellular devices now exist. Additionally, iPhone 12 Pro and iPad Pro now gathers depth information through LiDAR scanning, allowing MR capabilities within cellular platforms (Apple, 2021).

Chapter 3.

Improved Core Characterization using Holographic Logging Procedures and 3D Core Geovisualization

3.1. Introduction

Yearly, billions of dollars are spent on core drilling for improved subsurface interpretation and locating new mineral resource prospects (Huntington et al., 2010). Despite major investment, such cores are commonly left in remote storage locations or sometimes disposed of.

Logging procedures vary depending on the industry and field of application. In engineering practice, stability of the surface is vital, and thus, significant efforts are spent in the characterization of the rock mass (Wickham et al., 1974). In contrast, porosity, permeability, total organic content, structures and grain size distribution are essential for the petroleum industry because they aid in defining reservoirs and cap rocks extension (Abay, 2017). In mineral exploration, outlining the mineralogical and geochemical composition of rock is essential for constraining the orebody and alteration zones qualifying resource confinement, estimation, and economical revenue of the mine (Roonwal, 2018).

Core logging is an essential and required process in subsurface modelling that is critical for ensuring safe and economic engineering/mining projects. By necessity, this activity is commonly assigned to junior geologists and engineers with limited experience, due to the significant time requirements. This can catalyse ineffective or sometimes unwarranted simplistic observations. Moreover, conventional logging practices are inherently susceptible to human bias and errors that can induce unnecessary costs or deletion of unclear data (McPhee et al., 2015). Logging requires a significant degree of quality assessment and control, which can be challenging when the original core is stored remotely or no longer available.

To ensure collection of reliable information, industries have applied different norms and classifications to constrain geotechnical and geological rock core observations. In engineering practice, classification systems are employed to categorize mechanical

characteristics and behaviour. Some examples specific to rock masses include: Rock Quality Designation (RQD) (Deere, 1963), Q-System (NGI, 2015), Rock Mass Rating (RMR) (Bieniawski, 1976; Bieniawski, 1989) and Geologic Strength Index (GSI) (Hoek et al., 2013). Standardization, however, cannot eliminate or invalidate human bias. Collaborative assessment has also been proven to make core logging more warrantable (Fresia et al., 2017). However, peer evaluation is not always promptly available.

Logging can sometimes be undertaken using a two-step procedure: recording all the observations on a logging sheet and then digitizing them. A multi-step procedure has larger error predisposition as data can be mistyped. To date, discrepancies in rock core observations do not have a complete corrective procedure, unless the physical core is re-examined. Since samples are usually stored near site or in remote areas, additional travel time and rigorous labour is required in core box retrieval.

To avoid mistakes, associated with activities carried out in core sheds and handling of core boxes (i.e. poor core handling, labour, and misplacement), some companies are resorting to re-logging or solely logging via photographic imagery (Imago, 2021). This procedure does not provide a complete three-dimensional (3D) analysis as a single two-dimension (2D) image will possess occluded portions.

In this chapter, innovative MR methods for improved rock core data logging and management are presented and described in detail. The first application developed is aimed to reduce errors due to incorrect digitization, assist with quality assurance/quality control (QA/QC), and accelerate data acquisition. With the assistance of MR, data such as RQD, length of core, and other parameters can be calculated computationally, limiting bias and subjectivity. The secondary application developed enhances and improves the collection and analysis of fully three-dimensional rock core datasets. Through a constructed in-house 3D core scanner, complete 3D digitization of samples was retrieved. By integrating the results into the virtual paradigm, the potential for an innovative remote core revising medium that can help minimize syntax and logical misconception was investigated.

3.2. Background Information

Drilling/boring is the process of using drills to extract subsurface material for geological, geochemical, geotechnical, or engineering purposes (CanadaMines, 2019). In mining, drilling is essential for finding and defining the ore body. The extent of drilling is dependent on the cost of exploration, time constraints, topography of the area, target location, conformity with the mineralization and the marketability of the target (Roonwal, 2018). In geotechnical and civil engineering, drilling is crucial for risk of failure assessment, economics, and construction design.

3.2.1. Diamond Drilling

Diamond drilling uses a cylindrical core bit impregnated with diamonds connected to a hollow tube that is actively rotated by a diesel or pneumatic engine. As the bit rotates, it recovers cylindrical rock (i.e. drill cores) as it transverses and penetrates along its' subsurface trajectory (Roonwal, 2018) (Figure 3.1).

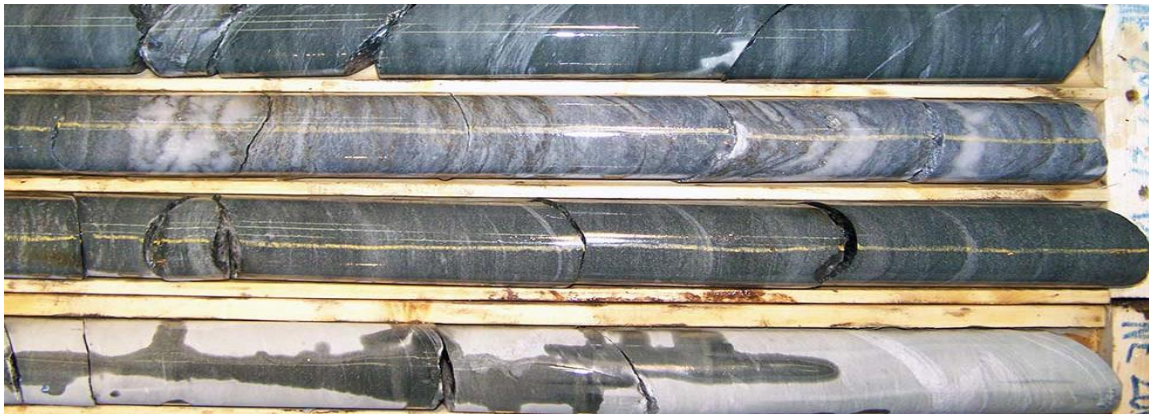


Figure 3.1: Anonymized example of drill rock core (CanadaMines, 2019).

The extracted rock samples allow subsurface characterization of discontinuities, structures, competency, fabrics, lithology and mineralization. Polymers are added as flushing fluids during drilling to prevent overheating, reduce torque development, enhance perforation rate, reduce chipping, and minimize mechanical breaks (Bhatnagar et al., 2011; Lv & Zhang, 2018).

There are various bit sizes that determine the diameter of the core. Larger diameter bits extract larger samples and have lower susceptibility of target deviation. However, drilling is slower, cores are heavier, and it is more expensive, compared to smaller core diameters (CanadaMines, 2019).

Torque associated with drilling unavoidably causes the core to rotate, making it impossible to infer true orientation data (Holcombe, 2013). Techniques exist that allow extraction of “orientated cores” from which “true” strike and dip can be measured by minimizing rotation of the sample while retaining a reference line (Llewelyn et al., 2018). This procedure is slower and more expensive than standard drilling, and thus, is only implemented in required drill holes. Moreover, recent research has shown that such proclaimed orientated core may not always be as accurate as previously suggested (Holcombe, 2013; Llewelyn et al., 2018).

Many well-distributed directional drill holes are required to obtain an acceptable representation of the subsurface body (Roonwal, 2018). Numerous software (e.g. Leapfrog (Seequent, 2021) and Petrel (Schlumberger, 2021)) can demarcate regions with high concentration of mineralization and help determine best processing/mining procedure. If unrepresentative core data is collected, misleading models can be developed.

3.2.1.1 Surveying and Depth Registration

Core extraction is rarely flawless. The drill bits sustains induced instability from: (i) bit/rock interacting forces and moment as it perforates the rock; (ii) unbalanced stresses due to competency inhomogeneity of rock type, hydraulic forces, gravity, and discontinuities; and (iii) poor equipment and/or improper machinery (Perneder et al., 2017). Poor monitoring can cause drastic deviation or oscillation of boreholes which has multiple consequences including (Marck et al., 2014; Prensky, 2010; Sugiura & Jones, 2008)

- Borehole instability
- Reduced target accuracy
- Difficult insertion of borehole casing or post drilling apparatus (e.g. televewers)
- Induced drag which promotes reduced efficiency and drilling speed reduction

Accurately hitting the target and spatially understanding the core location is fundamental for each diamond drill hole (DDH). Some software packages can help predict deviation of DDH by considering expected forces acting on the drill bit (Perkins et al., 2009; Kremers et al., 2016). Drill trajectory, however, is mostly dependent on the onsite drillers and geologists' skills, as they must actively gauge pressure changes, forecast lithological/structural sequence, and anticipate drill response (Perneder et al., 2017).

DDH rarely has 100% recovery. Pieces are lost due to discontinuities, flush out, or vibration from the drill rig (Kremers et al., 2016). Unsuccessful recovery can lead to improper depth registration, orientation errors, and can form omission/misidentification of major structures (Orpen, 2014). Depth discrepancies can arise from cable stretching, irregular tool movement, core losses, and misplaced core (Rider & Kennedy, 2011). Regardless of depth estimation inaccuracy, an approximation of the 3D location of the core is indispensable. An estimate of the position is made by calculating the amount of tubes inserted, inclinometer readings, and accounting extracted core (Perneder et al., 2017). This procedure is known as surveying.

More accurate subsurface alignment can be completed by correlating lithological breaks with gamma ray (GR) data, drilling responses, borehole imagery, and rock density (Cannon, 2016). Proper depth estimation requires several compulsory evaluations, making depth a dynamic measurement that locally shifts with progressive subsurface comprehension (Tavakoli, 2018). Core boxes are recognized both by depth and identification keys, which can significantly alter once re-evaluated. If the physical core must be re-analysed, issues can arise if the person re-logging the core bases their work on outdated depths.

3.2.1.2 Orientation Bias associated with Drilling

DDH has directional bias as it is a subsurface demarcation that will under-sample geological structures parallel or subparallel to the borehole. Conversely, perpendicular structures to the borehole will be intersected more frequently (Terzaghi, 1965) (Figure 3.2). This phenomenon causes the existence of a "blind zone", where fracture frequency is underestimated, potentially leading to inaccurate geological interpretations.

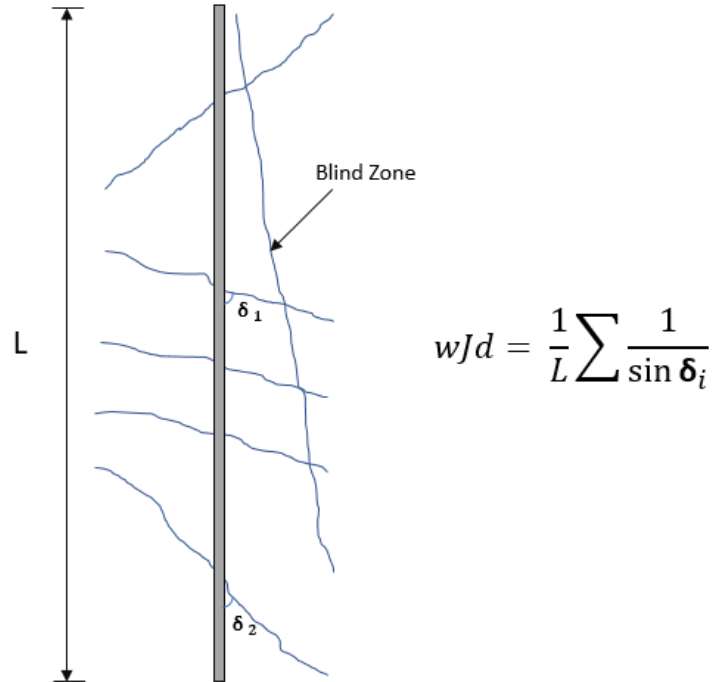


Figure 3.2: Intersection of joints with respect to drill hole or scanline direction. Weighted joint density (wJd) adjusts joint density by considering joints relative to the diamond drill hole (After Palmström, 1995).

Various formulae have been updated and produced to “weight” joint density relative to the orientation of the fracture and the scanline/borehole (Terzaghi, 1965; Wang & Mauldon, 2006; Palmström, 1995). To avoid major bias errors, which cannot be corrected by formulae, the best approach is to drill multiple DDHs with different orientations and locality. A suite of DDHs also advances underground modelling justifications and characterization.

3.2.1.3 Storage of Drill Core

Cores are usually stored in sturdy wooden or plastic boxes that are labelled for continuity and referral between boxes (K7, 2019). Safe transportation, handling and storage is critical, yet costly. Sometimes safe infrastructures known as core sheds or shacks are constructed to preserve cores (McPhee et al., 2015). Conserving, cataloguing, and preventing core mismanagement is an essential prerequisite for reliable core revaluation and referral (Roonwal, 2018). Conversely, poor storage of core, can prevent future analysis of samples (Figure 3.3).



Figure 3.3: Core samples from a 1972-1982 mine located on Bear Mountain, Harrison Lake, British Columbia, Canada (Hudson Institute of Mineralogy, 2020). Samples have been mixed, broken, altered, and misplaced. Adjacent active exploration within the region are unable to refer to these boxes as they are unsalvageable due to poor storage.

Proper core conservation has permitted new methodologies, such as hyperspectral analysis, to retrieve unreported observations on previously drilled cores (MacLagan et al., 2020; Schodlok et al., 2016; Tusa et al., 2019). Core integrity is also important because it serves as a company's asset. If a company's property or the company itself is sold, pristine core greatly benefits the buyer as they might require referral to physical subsurface information or decide to re-log samples using their own protocols.

Storage, labelling, organization and core box retrieval require personnel. Since hiring designated workers for this task can be expensive, professional geologists and geo-technicians have been tasked to complete these responsibilities (Rathi, 2015), resulting in loss of productivity and resources in qualitative studies.

Logistics of disposing of rock samples can be challenging due to environmental issues (American Petroleum Institute, 1998). If storage is full and budget is low, companies

sometimes must resort to core disposal. Such actions force core data to be reliant on previously made logs, which might host ineffective or inaccurate information.

Portions of core can also be lost from local jurisdiction. Some governments prevent private sample retention, requiring half of the core to be provided via core splitting (Newfoundland Labrador Canada, 2019; Alberta Energy Regulator, 2021). These regulations were emplaced to help governments promote mineral and oil prospecting, public research, and secure investors safety. To date, there are limited methodologies to refer to the pristine core samples prior to any altercations.

3.2.1.4 Canadian Mining Law and Role of NI 43-101

In 1995, Bre-X Minerals, a Canadian-based mineral exploration company, claimed that they discovered a deposit that was worth between 11.5 and 25.5 billion US Dollars in Indonesia. The site supposedly hosted approximately 30 and 70 million ounces of gold (Lehman, 1999). Such claims caused the company's stock value to exponentially grow as many investors capitalized stakes. Further testing and drilling, however, proved that it was all a hoax, prompting several investors to lose millions of dollars (Lehman, 1999).

Due to this incident, the Canadian Securities Administration (CSA) has now emplaced a regulation known as the National Instrument 43-101 Standards of Disclosure for Mineral Projects (NI 43-101) to increase the integrity and security towards investors (Ontario Securities Commission, 2021). The NI 43-101 guarantees assurance by setting minimum qualifications for a technical report and requires a third-party declaration. The regulation has been adopted as a Canadian federal requirement for mineral exploration (Newman, 2018).

Both financial analysts and investors use these technical reports as investment validation analysis (Fox, 2017). The report requires minimum jargon, to diminish confusion within the intended audience – investors, advisors and the public (Ontario Securities Commission, 2021). A qualified person (QP) with good standing in a professional association, a minimum of five years of experience in the field, ethical qualification, and university degree or equivalent accreditation must always confirm that the data is accurate (Ontario Securities Commission, 2021).

3.2.2. Conventional Geotechnical Logging Practices

Subsurface material retrieval and professional reports are meaningless if they lack quantitative and qualitative data. Quantification of rock mass characteristics can be broken down into three main subgroups: geology, geometry, and engineering parameters (Wickham et al., 1972) (Table 3-1). Each parameter can be subdivided into larger subgroups that address key findings.

Table 3-1: Broad grouping of rock mass classification system (after Wickman et al., 1972).

Parameter	Description	Main Groups
Geology	General geological structures and parameters	1. Lithology 2. Rock Hardness 3. Geological Structures 4. Ore 5. Porosity 6. Geochemistry
Geometry	Effect of discontinuity pattern related to the site of interest	1. Joint Spacing 2. Joint Orientation 3. Direction of slope or tunnel
Engineering Parameter	Effect of groundwater and joint conditions	1. Rock Mass Quality 2. Joint Condition 3. Water Inflow

Geologic core logging provides more qualitative descriptive information such as rock colour, lithology, pore type, mineralogy, alteration, depositional environment and structures (American Petroleum Industry, 1998). In comparison, geotechnical data is more quantitative.

By quantifying geotechnical parameters, specific classifications can determine the rock mass quality. These parameters can be derived from either outcrop observations or core logging. For instance, Rock Quality Designation (RQD) quantifies rock mass fracturing within a core run or scanline by summing the total length distance of competent rock that is greater than 10 cm (Deere et al., 1967) (Appendix A).

Common rock mass classification systems: Q-System (Barton et al., 1974; NGI, 2015) (Section 3.2.2.1), Rock Mass Rating (RMR) (Bieniawski, 1976; Bieniawski, 1989) (Section 3.2.2.2), and Geologic Strength Index (GSI) (Hoek, 1994; Hoek, 2007; Marinos et al., 2007). Each of these classifications systems have been continuously modified as explained in detail by Hoek (2007). Geotechnical numerical modelling software which are used in practice to assess instability use rock mass strength input parameters derived from to these systems classifications (Itasca, 2021; RocScience, 2021a). By understanding and emplacing representative input parameters, a modeller can significantly improve their results.

Other parameters help estimate intact rock strength by physically breaking competent rock samples in laboratory tests. These measurements are known as destructive tests and include: Uniaxial Compressive Strength (UCS), Tensile Strength, and Triaxial Compressive Strength. By acquiring such measurements, deformability, strength, and rock mass support can be estimated through the appropriate rock mass classification systems.

3.2.2.1 The Q-System

The Q-System was first developed in the early 1970s to quantify rock mass quality and serve as a guideline for estimating adequate rock support design, and systematic documentation (Barton et al., 1974). The system was intended for underground opening assessments but can cautiously be used in borehole analysis, slope assessment and field mapping (Bar & Barton, 2017). The NGI (2015) handbook has been widely used as the modern basis for the Q-System classification (Appendix B). The rock mass quality is based on six parameters:

1. Rock quality designation (RQD)
2. Joint set number (J_n)
3. Joint roughness number (J_r)
4. Joint alteration number (J_a)
5. Joint water reduction factor (J_w)
6. Stress Reduction factor (SRF)

The Q-value equation is:

$$Q = \frac{RQD}{J_n} * \frac{J_r}{J_a} * \frac{J_w}{SRF} (1)$$

This equation is comprised of three quotients which are respectively: degree of jointing or block size (i.e. RQD/J_n), joint friction or inter-block shear strength (i.e. J_r/J_a), and active stress (i.e. J_w/SRF).

The degree of jointing depicts the joint orientation and spacing. Stability decreases as the joint spacing decreases and the joint set number increases. RQD can be calculated through core/scanline analysis (Appendix A) or estimated from the number of discontinuities per unit volume (Palmström, 2005). RQD is heavily directionally dependent, making outcrop exposure the preferable methodology. If outcrop mapping is used to calculate volumetric joint count, a mapper must be vigilant about anthropogenically induced fractures because they should not be considered (NGI, 2015). Once the RQD value is known, dividing it by the number of joints sets (J_n) gives a relative degree of blocking within the rock mass.

The second quotient in Equation (1) represents the inter-block shear strength, which characterizes the discontinuity contribution to the rock mass behaviour by considering roughness and level of alteration. Joint roughness number (J_r) is a quantitative value that measures the roughness profile. Joint alteration number (J_a) quantifies the thickness and strength of joint infill, which is highly dependent on the mineral composition.

The third quotient in the equation is representative of active stresses acting on the rock mass. Joint water can soften or washout minerals, resulting in reduction of friction along discontinuities. Additionally, water pressure reduces the normal stress along the surface, causing a decrease in shear strength. SRF describes the relationship between stress and rock mass performance that can be observed around underground openings including spalling, deformation, dilatancy and other physical responses of the rock mass (NGI, 2015). Defining the third quotient can be challenging during the preliminary design phase because it is highly dependent on the rock mass exposure time

If the Q-system is based on drill core assessment, the following issues should be considered (NGI, 2015):

- Not all the joint surfaces will be captured due to drilling orientation bias, affecting RQD and the joint number (J_n) assessment.
- It will overlook large to medium scale surface undulations, indirectly affecting the roughness coefficient (J_r).
- Water pumping during drilling can wash out weak infill material, affecting the joint alteration (J_a) assessment.
- Assessing stress reduction factor (SRF) and joint water reduction factor (J_w) is nearly impossible solely from drill cores.
- Rating the confidence in how representative the core is in assessing the Q-value should be provided.

By assessing multiple cores, Q-values for specific regions can be statistically assessed, allowing delineation of unstable or competent areas. By plotting Q value distribution, an estimation of high-risk regions can be delineated.

3.2.2.2 Rock Mass Rating (RMR)

The Rock Mass Rating (RMR), also known as the Geomechanics Classification, was developed by Bieniawski (1976) to classify rock mass quantitatively and estimate support requirements. The 1989 RMR version (Bieniawski, 1989) is commonly used, however, the RMR 1976 still remains in use by some practitioners (Appendix C). The main parameters for RMR 1989 include:

1. Uniaxial compressive strength (UCS) of the intact rock.
2. Rock Quality Designation (RQD) (Appendix A).
3. Spacing of discontinuities.
4. Condition of discontinuities.
5. Groundwater condition.
6. Orientation of discontinuities.

The system works by selecting appropriate rating values from provided tables. The system has undergone several different modifications catered to specific applications including: Modified Basic RMR (MBR) (Cummings et al., 1982; Kendorski et al., 1983),

Laubscher's Mining RMR (MRMR) (Laubscher & Jakubec, 2001), and slope mass rating (SMR) (Romana, 1985; Romana et al., 2015). These modifications were introduced as the primordial rating proved to be too conservative which can promote unnecessary expenses (Rehman et al., 2018). Errors emerge from the empirical sharp boundaries between large intervals that inevitably overrates or undervalues parameters (Romana et al., 2015). For instance, 250 MPa and 100 MPa UCS are both given a 12-point rating, despite a significant 150 MPa difference in strength.

Correcting for the sharp breaks within this classification imposes challenges since they are nonlinear and were empirically derived. Recent research has tried using fuzzy clustering to permit a more flexible relationship between values and the rock parameters (Rad & Jalali, 2019). However, such approaches have not been adapted in engineering practice and more research needs to be conducted prior to justifying new assumptions and modifications.

3.2.2.3 Geologic Strength Index (GSI)

The Geological Strength Index (GSI), describes the intrinsic damage within a jointed rock mass (Hoek, 1994). The GSI value (or range) is obtained by comparing the investigated outcrop with a chart that relates rock mass blockiness and the condition of discontinuities (Hoek & Marinos, 2000) (Appendix D). If the rock mass is heavily heterogeneous and lithologically varied, such as siltstone, shale and limestone, a modified GSI for flysch-like material should be adopted (Marinos & Hoek, 2000; Marinos, 2019) (Appendix E).

GSI values should always be recorded as a range to accommodate heterogeneity of the rock mass (e.g. GSI 40- 50) (Hoek & Marinos, 2000). However, a simple range cannot fully represent the rock's diversity because it cannot account for mineral, geometric, and microcracking differentiation. Rock mass heterogeneity contributes to brittle fracturing across a wide range of scales which can then be naturally healed over time from fluid inclusion planes during isobaric cooling, foreign material filling, isothermal decompression process and/or tectonic activity (Day, 2016).

Q-system, RMR, and GSI do not account for any healed fractures (i.e. intrablock planes of weakness), and thus, only considers interblock properties. Recent work by Day (2016) has proven healed fractures serve as a conduit for complex stresses that significantly

influence rock mass behaviour and mechanical properties. Some infilling materials such as quartz and sulphide minerals can strengthen the rock. While other materials such as anhydrite, epidote, calcite, biotite, sericite or clay can significantly reduce the strength (Day, 2016).

The composite geologic strength index (CGSI) was developed by Day (2016) to address overlooking intrablock surfaces (Appendix F). By focusing on mesoscale healed structures, a more representative value of rock mass quality can be identified. Required parameters include infill mineralogy, Moh's hardness, alteration, thickness, persistence and orientation (Day, 2016). However, obtaining all required datasets for CGSI increases core logging time, making it rarely feasible.

In engineering practice it has been observed that underestimation of rock mass strength occur from the inability to capture intact rock failure, strengthening effect of interblock, and geometric bulking (Kaiser, 2019). The continuous use of various classification (e.g. RMR and GSI) has also oversighted the overall behaviour of the rock mass and its evolution. This was observed by Kaiser (2019) through field practices of GSI as it should only be used where blocks are able to freely move and rotate (Hoek, 1994) but is commonly applied to every rock mass quality. Thus, he has proposed a new GSI modification that observes larger subgroups that account rock mass quality (RMQ) to help anticipate the overall behaviour of the rock mass (Appendix G).

3.2.2.4 RQD uncertainties and misguidance

RQD is a fundamental element for many classification systems but is influenced by several uncertainties, including (Forster, 2005; Pells et al., 2017; Palmström, 2001; and Deere & Deere, 1989):

- Measurements are made post-boxing of the core, permitting incipient fractures to open and thereby compromising the in-situ rock mass representation.
- Coverage can be limited as only sound core are considered.
- Proper measuring techniques are not always followed. Measurement should be taken from the mid-tip to mid-tip point of the core piece to prevent dependency on core diameter and minimizes penalization of underestimating fractures parallel to the borehole (Figure 3.4).

- Some people measure RQD for a whole core run rather than the recommended practice of per lithological breaks.
- Directional bias associated with drilling practice.
- Confusion arising from mechanical breakage, schistosity, or planes of weakness in phyllites or shales.

Automated RQD measurement from core box photography has been investigated by various authors in attempts to provide a more consistent and effective methodology than conventional ruler measurements (Lemy et al., 2001; Olson, 2013; Imago, 2021). The problem with this methodology is that it captures RQD in a “Tip to Tip” or “Fully circular” approach (Figure 3.4). Additionally, classifying whether a fracture is anthropogenic or natural cannot be derived from a single image acquisition.

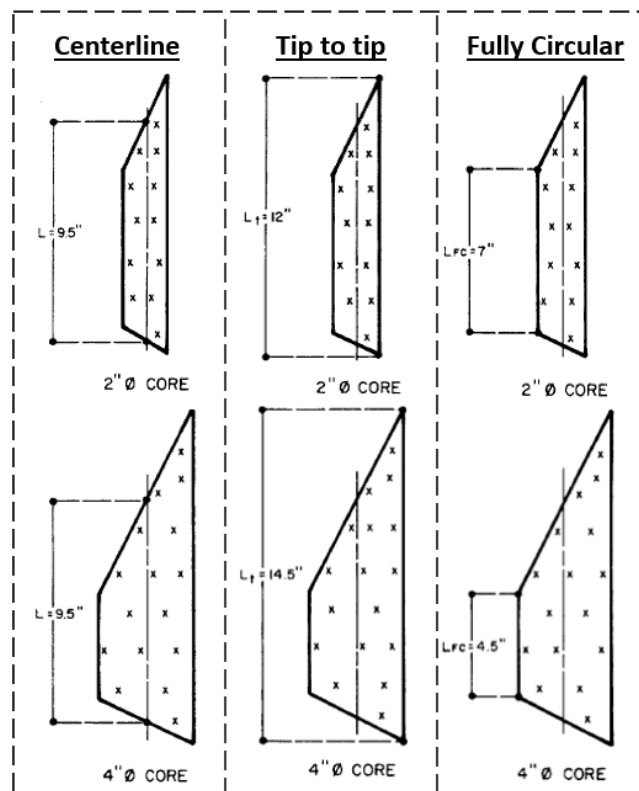


Figure 3.4: Measurement of core for RQD calculation (A) Centerline: Correct method to measure length (B) Tip to Tip: Incorrect method because it is dependent on core diameter (C) Fully circular: Incorrect method to measure as length is dependent on core diameter (Modified after Deere & Deere, 1989).

RQD issues have led to some classifications, such as the Mining Rock Mass Rating (MRMR) (Laubscher & Jakubec, 2000), resorting to measuring fracture frequency. By removing RQD it removes mismeasurements and inaccuracy associated with outdated practices (Pells et al., 2017). Yet, the most common classification systems remain formulate to RQD.

3.2.3. Core Logging Software

Conventional logging software tools such as LogPlot (RockWare, 2021), Excel (Microsoft, 2021c) and Stater (GoldenSoftware, 2021) have helped core loggers digitize core observations in a systematic manner where tables are continuously filled in with appropriate observations.

More advanced applications have enabled logging via core photographs such as Imago (2021), and StereoCore Photolog (2021). These software packages host an array of accessories such as rapid RQD measurements, defining lithological breakpoints, and rapid comparison of similar sample properties.

Other software packages like WellCAD (Mount Sopris, 2020) have integrated a multisensory approach where quantitative data acquired during drilling can be imported. Companies such as Enersoft and CoreScan have taken this functionality a step further by implementing machine learning textural mapping, mineralogical distribution, type of alteration, bitumen content and total organic content via photography in conjunction with hyperspectral scanning and laser profilometry.

Reliance on digitizing core data has proven to be useful for auditable supervision, depth adjustment via downhole geophysics, and rock parameter segregation via multi-disciplinary assessment (Orpen, 2014). Furthermore, restraining loggers from a multi-step logging procedure reduces uncertainty and errors associated with digitizing information from paper records.

3.3. CoreLogger MR

Mixed reality was observed by the author as a tool that could assist both geological and geotechnical loggers by providing a holographic logging sheet. A new application called CoreLogger MR was developed as part of this research by the author

using the Microsoft HoloLens. This application permits values for any parameter to be assigned using either a holographic or Bluetooth keyboard input. New logging sheets can be created freely, or imported from pre-existing files (Figure 3.6).

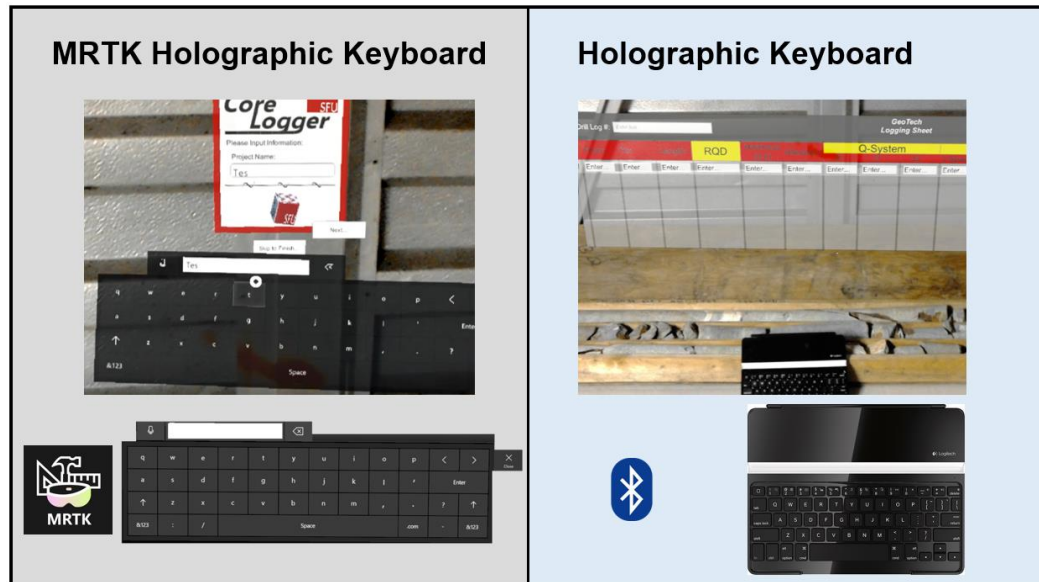


Figure 3.5: CoreLogger data can either be input using the holographic keyboard inbuilt Mixed Reality Toolkit (MRTK) or by connecting to any Bluetooth compatible keyboard.

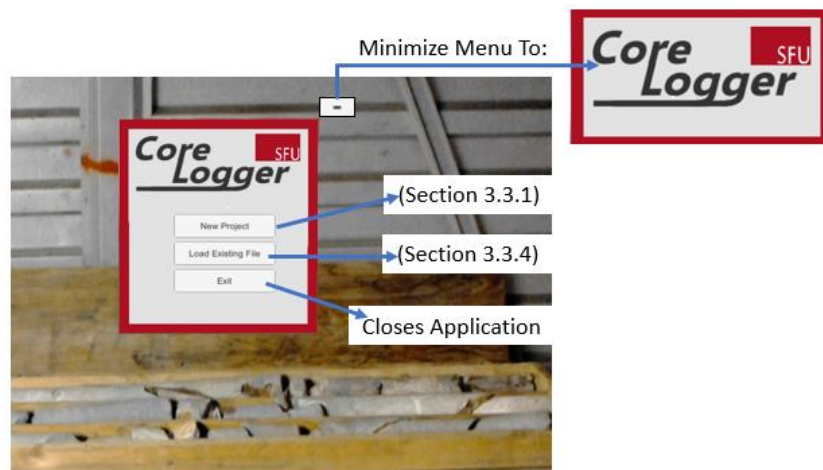


Figure 3.6: CoreLogger MR initial menu.

3.3.1. CoreLogger MR: Initiation of New Geological and Geotechnical Logging Sheets

If a new logging sheet in CoreLogger MR is initiated, the user is prompted to name the project. After naming the project, essential parameters such as project location, logger's name, azimuth of the borehole, elevation, depth and core size need to be annotated (Figure 3.7). The date which the project was initiated will automatically be recorded. If parameters are not entered correctly or do not meet predefined specifications, they are marked with a red cross (Figure 3.8).

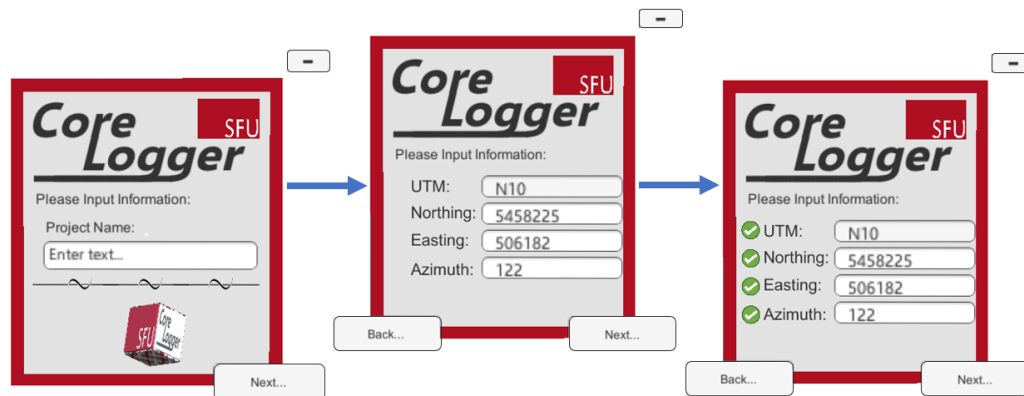


Figure 3.7: User interface (UI) of CoreLoggerMR when a new file is initiated. The user is prompted to fill important parameters such as georeferencing.

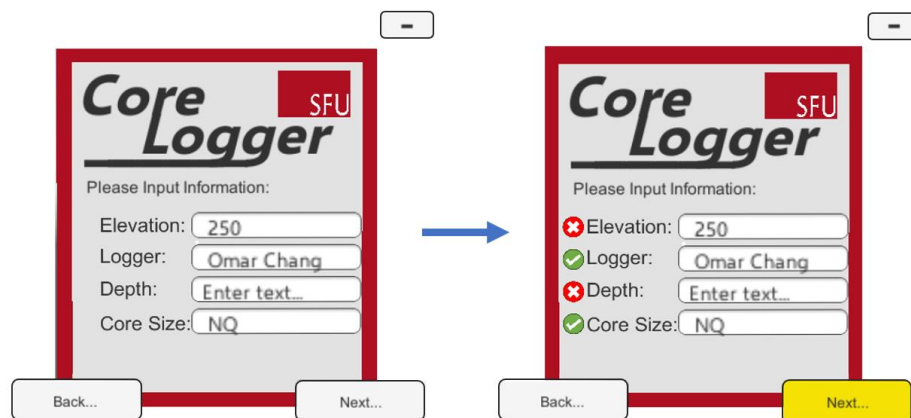


Figure 3.8: Second step of initiation. Two red markers are placed beside Elevation and Depth as they were not assigned properly. The elevation parameter was constrained to be above 500 m elevation due to project specifications. The depth parameter was marked by a cross as it was left blank.

Prior to finalizing the parameters, a summary sheet will be displayed holographically. If data was left blank, it will automatically be labelled as “N/A”. If entered incorrectly, a “...Verify” string will be added to the end of the parameter (Figure 3.9a). If errors are found, the user can either correct them or ignore the warnings and continue. Once finalized, the user must select which type of logging sheet they want to construct (Figure 3.9b)

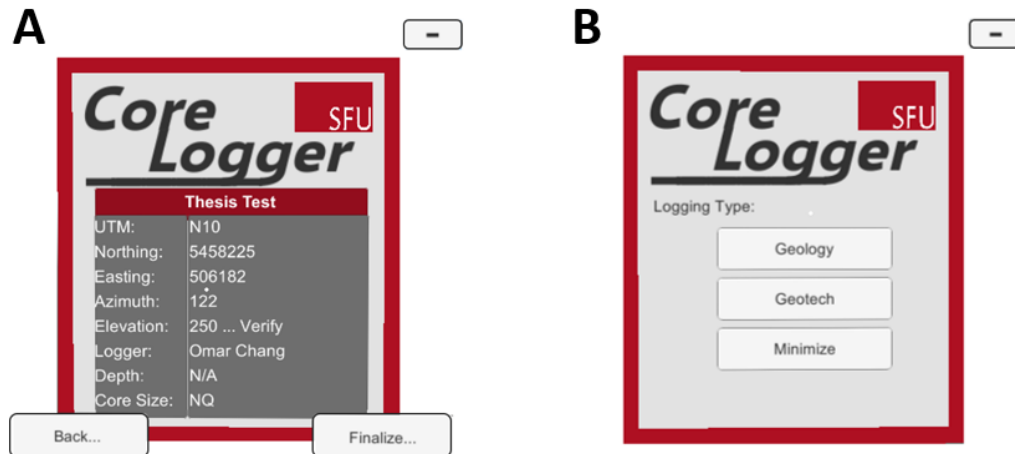


Figure 3.9: CoreLogger MR (A) Parameter summary UI displayed prior to completing model initiation. Any parameters left blank will be displayed as “N/A” and potential erroneous fields will be followed by the string “...Verify”. (B) Menu allowing user to select the type of logging in CoreLogger MR.

Note that the geotechnical logging sheet was investigated in greater detail as it has more quantitative parameters than standard geological logs. Since users have different applications in which different parameters need to be entered; a dynamic and adjustable interface was built.

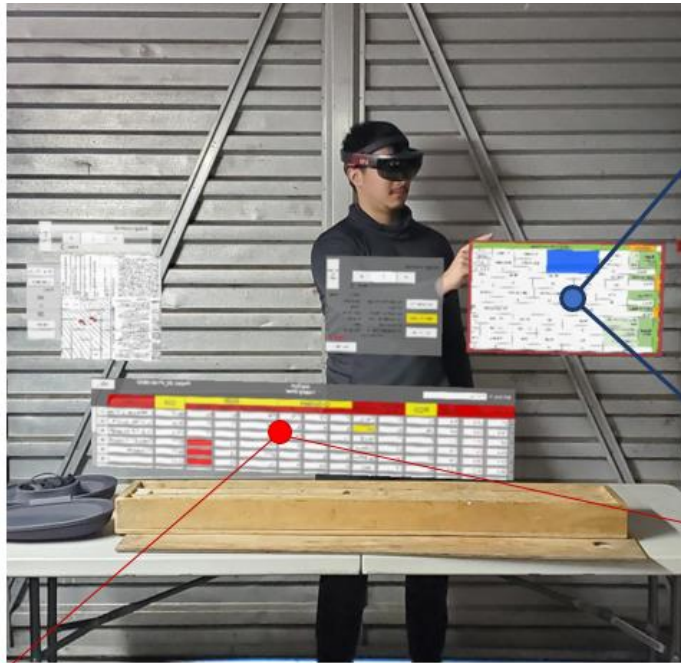
3.3.2. Geotechnical Logging Sheet

The default geotechnical logging sheet is broken down to:

- | | |
|------------------|--|
| 1. Line number | 9. RMR |
| 2. From distance | a. Joint Spacing (J-Spacing) |
| 3. To distance | b. Joint Condition (J-Con) |
| 4. Total Length | c. RMR Value |
| 5. RQD | 10. GSI |
| 6. Hardness | a. Jointed Rock (Hoek and Marinos, 2000) |
| 7. Alteration | b. Heterogeneous Rock (Marinos and Hoek, 2001) |
| 8. QSystem | 11. Extra footnotes |
| a. Jn | 12. Add an extra line KAKA |
| b. Jr | |
| c. Ja | |

Filling only two parameters of either “from distance”, “to distance” or “total distance”, automatically computes the missing parameter. Once a new line is added, the user can depict whether it is a continuation from the previous segment or if there was core loss (Figure 3.10). Each line is meant to represent an interval.

RQD can be calculated by taking advantage of MR’s spatial mapping capabilities. A similar approach to EasyMap (Onsel et al., 2019) was initially applied in which the MR spatial map was used to acquire length measurements. Due to the inability of the Microsoft HoloLens to accurately scan dark colours and reflective surfaces, another approach was investigated that used the HoloLens 2 ability of accurately track the user’s hands. By using the index fingers as an anchoring point, respective lengths could be measured (Figure 3.11). The accuracy of this new MR hand ruler was compared to a conventional metre ruler and it was noted that there was an error of ± 8 mm. By comparison, the conventional ruler remain the superior measuring tool. However, this was a proof of concept and such MR measuring system could be emplaced in improved future hardware. To ensure optimum RQD values, the user can also manually input them. Any systems that are embedded in the application and reliant on RQD, take the respective computed or typed value into account.



W Linear Fit

Parameter	Range of Value and Rating					
1 Strength of Intact Rock	PL	>10 MPa	10-4 MPa	4-2 MPa	2-1 MPa	Universal Compressive test is preferred
	UCS	>250 MPa	250-100 MPa	100-50 MPa	50-25 MPa	PL > 1 MPa, UCS > 10 MPa
Rating	15	12	7	4	2	1 0
2 Drill Core RQD	100-90	90-75	75-50	50-25	<25%	
Rating	20	17	13	8	3	
3 Spacing of	>2 m	2-0.6 m	600-200 mm	200-60 mm	<60 mm	
Rating	20	15	10	8	5	
4 Joint Condition	Detailed Solver					Value: 22
Rating						
5 Ground Water	Inflow per 10m tunnel length	None	<10	10-25	25-125	125 <
	Joint water press./major principal	0	<0.1	0.1-0.2	0.2-0.5	0.5 <
	General Condition	Dry	Damp	Wet	Dripping	Flows
Rating	15	10	7	4	0	

GeoTech Logging Sheet											Project: SV_RT-93-08653				Info...
Drill Log #:	Enter text...														
#	From	To	Length	RQD	Hardness (0-6)	Alteration	Q-System			RMR			GSI	Extra	
							Jr	Ji	Ja	J-Spacing (mm)	J-Con	Value			
1	13	18.3	5.3	91	54	Chlorite	2	1.5	0.75	800	27	52	82-78	Chlorite veining ranges	+
2	18.3	23.1	4.8	100	57	N/A	1	4	1	2000	28	92	90-85	No evident alteration	+
3	23.1	28.2	5.1	7	12	Heavily	12	1	15	20	5	27	44-58	Portions of the sample	+
4	28.2	32.7	4.5	73	33	Oxidation	2	3	6	150	13		55-58	Oxidization is focused	+
5	32.7	35.5	2.8	92	50	Epidotizati	3	1	8	1500	21		84-88	Epidotization	+
6	35.5	47.7	12.2	82	43	Heavy	6	0.5	4	750	22		79-83		+

Figure 3.10: Geotechnical holographic logging sheet in CoreLogger MR showing both the GSI and RMR built-in UI.



Figure 3.11: Built-in CoreLogger MR ruler compared to a conventional ruler measuring the length of a core piece that is 26.2 cm long.

The hardness parameter was based on Hoek's field estimation of uniaxial compressive strength (Appendix H) (Brown, 1981). The "Alteration" column was designed for loggers to populate any crucial lithological changes within the unit. Since the RMR, Q-System and GSI are quantitative classifications, separate UIs were constructed for each system.

3.3.2.1 The Holographic Q-System and Holographic RMR

The Q-System (Appendix B) and RMR (Appendix C) systems had similar interfaces that encourage users to click respective values within designated holographic tables. Only the holographic RMR will be explained in detail, to avoid redundancy.

RMR holographic values are segregated into several tables based on the Bieniawski (1989) RMR table (Appendix C) (Figure 3.12 -Figure 3.14). The newly developed CoreLogger MR table has different dimensions compared to original RMR table to allow the choice to be made between a linear fit approach (i.e. "W/ Linear Fit") or use of the recommended standard RMR table values. The suggested linear fit approach allows values that are near the sharp break points to be adjusted to closer values (e.g. 240 MPa is normally assigned a 12 rating, but with a linear fit a value of 14 can be assigned

since 250 MPa is rated 15). An option to assign the same RMR value for a range of data input is also constructed (i.e. “Convert to Range”). It is emphasized that the new linear fit approach is for research only and the standard RMR table are the default format as more research must be conducted in what the best fit line for each RMR parameter is. These new approaches allow the sensitivity of the RMR rating and equivalent recommended support categories to the use of empirical sharp RMR table boundaries to be assessed for a particular engineering project.

As a user gazes into a quadrant with the HoloLens, a transparent shader is initiated as a visual response. Once clicked, the shader becomes a lower transparent blue and the value is assigned (Figure 3.12).

W/ Linear Fit

Parameter		Range of Value and Rating					
1	Strength of Intact Rock	PL	>10 MPa	10-4 MPa	4 ~ 2 MPa	2-1 MPa	Uniaxial Compressive test is preferred
	UCS	>250MPa	250 – 100 MPa	100-50 MPa	50-25 MPa	25 – 5 MPa	5 – 1 MPa
	Rating	15	12	7	4	2	1
2	Drill Core RQD	100 – 90	90-75	75 - 50	50-25	<25%	
	Rating	20	17	13	8	3	
3	Spacing of	>2 m	2 – 0.6 m	600 – 200 mm	200 – 60 mm	< 60 mm	
	Rating	20	15	10	8	5	
4	Joint Condition	Detailed Solver				Value: 22	
	Rating						
5	Ground Water	Inflow per 10m tunnel length	None	<10	10 – 25	25 – 125	125 <
		Joint water press/major principal	0	< 0.1	0.1 – 0.2	0.2 – 0.5	0.5 <
		General Condition	Dry	Damp	Wet	Dripping	Flows
	Rating	15	10	7	4	0	

Figure 3.12: RMR Holographic table based on Bieniawski (1989) [Used with permission]. If a user looks at an unselected quadrant a slightly transparent shader is overlain on top of the observed quadrant. Once clicked the value is assigned and the shader is emplaced permanently.

Joint condition is considered as a separate table as it can be either manually input or graphically derived through another holographic table (Figure 3.13). The RMR adjustor for orientation of the excavation relative to geological structure are toggled by the “RMR Adjustor” button in the main RMR UI (Figure 3.14).

Guideline for classification of discontinuities					
Persistence (Discontinuity Length)	< 1 m 6	1 – 3 m 4		3 – 10 m 2	10 – 20 m 1
Aperture	None 6	<0.1 mm 5	0.1 – 1.0 mm 4	1 – 5 mm 1	5 m < 0
Roughness	Very Rough 6	Rough 5	Slightly Rough 3	Smooth 1	Slickensided 0
Infilling	None 6	Hard Filling < 5mm 4		Hard Filling > 5mm 2	Soft Filling < 5mm 2
Weathering	Unweathered 6	Slightly Weathered 5	Moderately Weathered 3	Highly Weathered 1	Decomposed 0

Figure 3.13: Guideline for discontinuity classification (After Bieniawski, 1989) [Used with permission].

Rating Adjustment for Orientation					
Strike and Dip Orientation	Very Favorable	Favorable	Fair	Unfavorable	Very Unfavorable
Tunnels and Mines	0	-2	-5	-10	-12
Foundation	0	-2	-7	-15	-25
Slope	0	-5	-25	-50	N/A

Figure 3.14: RMR Adjustor relative to type of site and strike/dip direction (After Bieniawski, 1989) [Used with permission].

Once all the values are entered, the final RMR value will be calculated and the rock mass is classified (Figure 3.15). If the user is satisfied with the results, they must click “Save/Next” button to assign the value to the respective interval or range before continuing to the next interval.

3.3.2.2 Holographic GSI

A holographic GSI for jointed rock (Hoek & Marinos, 2000) (Appendix D) and heterogeneous rock masses (Marinos & Hoek, 2000; Marinos et al., 2007; Marinos, 2019) (Appendix E) was also built into CoreLogger MR. Similar to the other systems, the user must first specify the specific interval or range to assign the respective value to. Since GSI should always be set as a range (Hoek & Marinos, 2000), the user must choose two points along the table (Figure 3.15). The user can switch between GSI charts by clicking “Change to flysch/jointed rock” button. Once the user is satisfied with the selected value, the GSI range can be assigned to the specific interval by clicking the “Record...” button.

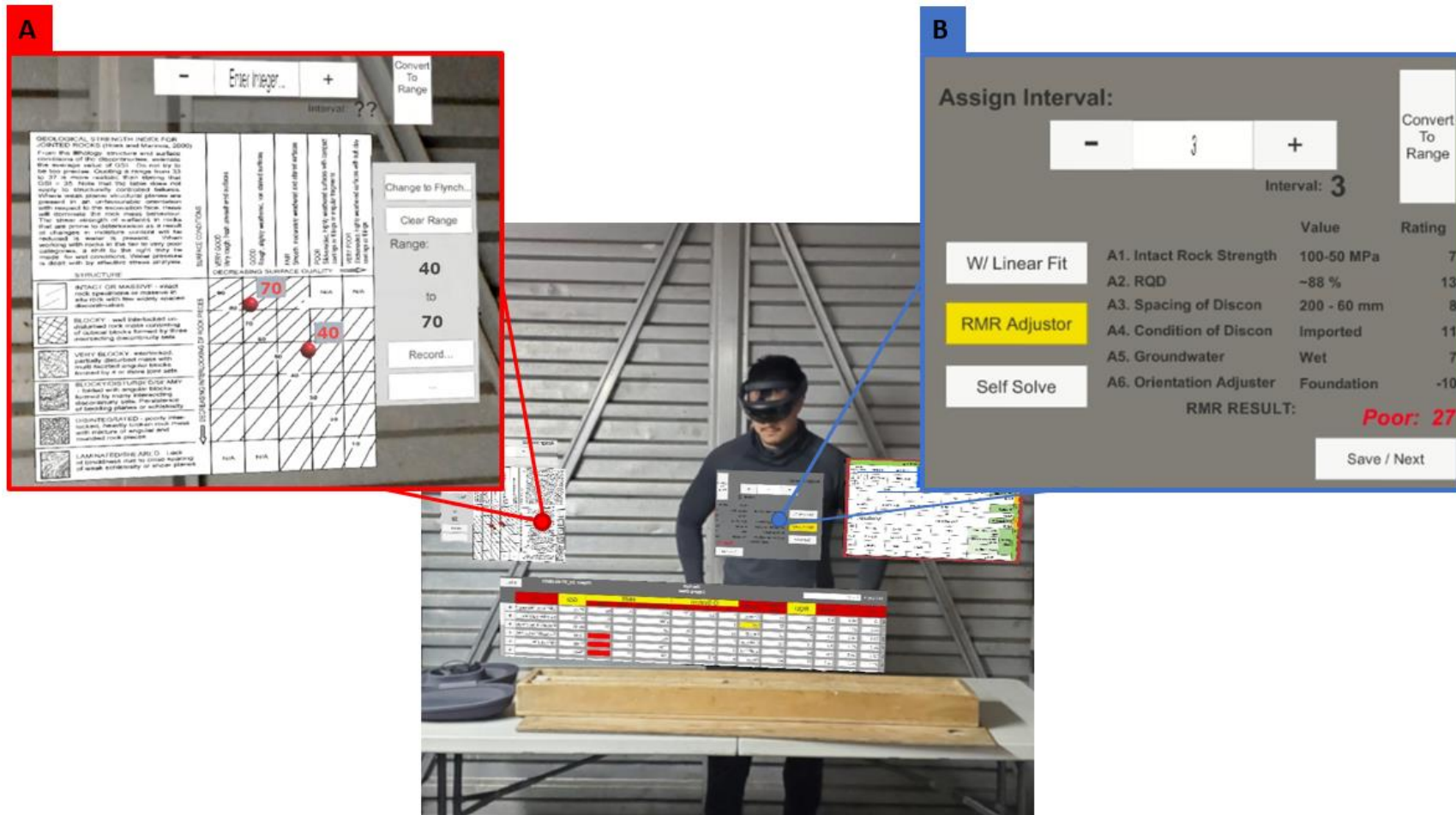


Figure 3.15: Geotechnical holographic logging in CoreLogger MR. (A) Holographic GSI that quickly assigns respective values that were clicked virtually (After Hoek & Marinos, 2000). (B) Holographic RMR summary table that updates as a user classifies RMR parameters.

3.3.3. Lithological Logging Sheet

The geological logging sheet was dominantly based on visual observations rather than quantitative values. The UI contains basic parameters such as to, from, unit, lithological structures, alteration, and geological description. Any previously completed logging sheet can also be scanned and brought into the application as a 2D image. Since the geological logging interface uses the same structure as the geotechnical logging sheet, it is not explained in detail.

The potential for drop down menus to select possible lithological units was investigated. Due to the high variability of lithological characteristic, options that pigeonholed results was disregarded as giving the user qualitative freedom was more appropriate.

Both holographic sheets are saved and exported as a comma-separated values (CSV) file. CSV files can also be imported into CoreLogger MR to continue working on specified logging sheets. If the file is successfully loaded, the user is prompted to the same primary interface (Figure 3.7, Figure 3.8, and Figure 3.9) and any improper data input will be flagged for suggestive editing.

3.4. Preliminary 3D Core Scanning Model

Core logging using photographs has various benefits, but basing observations solely on a 2D image inevitably neglects occluded data. Additionally, if lighting is inadequate or image quality is poor, information along the physical core can be compromised (e.g. mineral alteration colour, fine texture details, etc.), potentially leading to misinterpretation during assessment 2D imagery.

Challenges resulting from existing post core logging procedures, include (McPhee et al., 2015; Roonwal, 2018; Esmaili, 2020; Olson, 2013):

1. Transportation cost and issues accompanied with relocating samples.
2. Improper preservation that leads to reduced data quality and increased cost.
3. Unorganized archiving and cataloguing of core data.
4. Restricted and challenging access to samples stored at remote locations or stacked beneath numerous core boxes.

5. Careful planning of security, economic, and environmental impact associated within core shack and sample maintenance.
6. Employees that move core are susceptible to injury from wood splinters, oxidized nails, rocks fallings, heavy lifting, and uneven weight distribution.
7. 2D images cannot account for 3D features in the core.

A feasibility study to scan core in 3D was completed by the author to address the challenges associated with current core examination and handling procedures (Olson, 2013; Esmaili, 2020). Novel integration of the 3D core logging results to improve data access is demonstrated, with the results unified through XR platforms.

In this thesis, the practicality of core scanning using photogrammetric techniques (e.g. Structure from Motion (SfM)) is investigated using Agisoft Metashape (2021). A core box with high RQD from Stave Falls, Alouette Lake, British Columbia is used to develop and test the core imaging procedures.

The photographs were taken using a Samsung Galaxy S7 smartphone, to investigate the potential of a low cost device to perform SfM drill core reconstruction. The developed procedure was successful, adequately capturing both the texture and discontinuity roughness within each piece of core (Figure 3.16). The model was then exported to Unity. Scripts were subsequently incorporated to allow the user to freely move, scale, and rotate each virtual core using MR and VR capabilities (Figure 3.17).

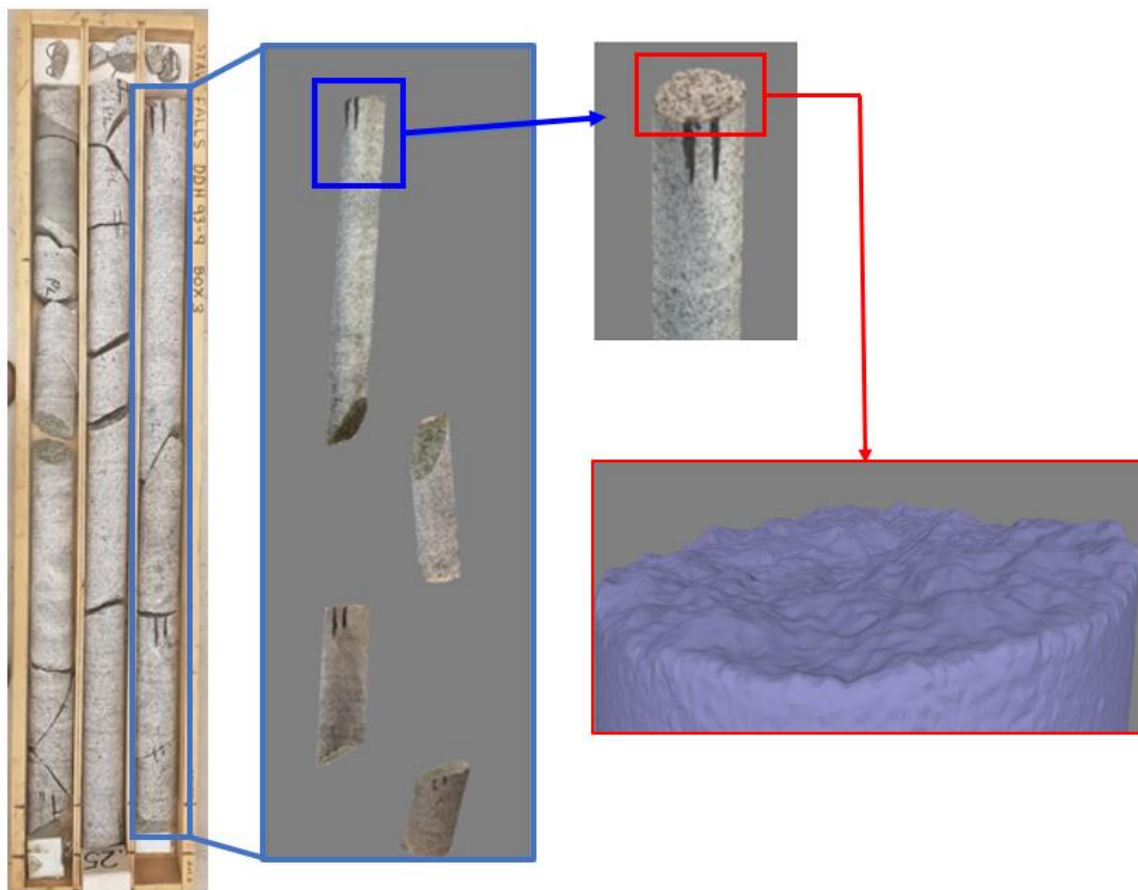


Figure 3.16: Preliminary 3D core scanning results. Roughness of each core end piece was accurately captured. Core is HQ3 (63.5 mm) diameter. Box dimensions are 121 cm x 26 cm x 8 cm.

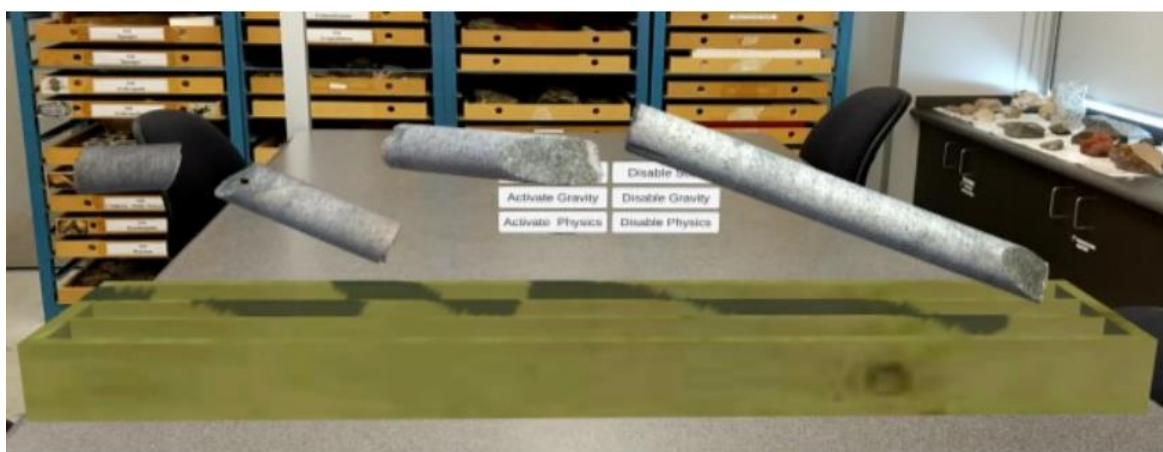


Figure 3.17: MR 3D Holographic Core can be scaled, moved, and rotated freely.

The core scanning test using a smartphone device revealed some limitations and challenges that needed to be addressed to improve automation and the overall quality of the results. These include:

1. Inconsistent lighting, focal length, exposure, International Organization for Standardization (ISO), and camera aperture may result in unrepresentative and inconsistent texturing.
2. Non-mechanical procedures (e.g. physically holding the sample in place) results in time-consuming scanning.
3. A consistent background is required for effective automated masking.
4. Consistently moving the smartphone location, rather than restraining acquisition to a single anchor point resulted in blurry and skewed models.

3.5. Improved 3D Core Scanning

A table with rollers that rotates along a single axis was built to improve core scanning procedures and address these issues. Three different Digital Single Lens Reflex (DSLR) cameras are synchronized and placed at different locations along the table. Each camera was anchored and configured to manual settings to retain consistency throughout the procedure (Challenge 4). To ensure consistent lighting, two 3 feet long 3000 lumens spotlights are used to illuminate the samples (Challenge 3) (Figure 3.18). The table and rollers are painted fluorescent pink to improve the automated masking in MetaShape (Challenge 3). Fluorescent pink paint was dulled to minimize sheen and light reflection along the table. The setup was first painted green to mimic green screen masking, however this obscured abundant green mineral grains such as chlorite. The unnatural fluorescent pink colour ensured minimum improper masking.

A full core run with an HQ3 (63.5 mm) diameter with varied RQD and textures was scanned (Figure 3.19A). A 2.5D model of the core run was also constructed for further analysis (Figure 3.19B). Each core piece longer than 2 cm was scanned. Any regions comprising of fragments smaller than 2 cm were substituted by red cylinders (Figure 3.19C).



Figure 3.18: Core scanner table observed from the point of view of an anchored camera. Multiple view points enable easy meshing, texturing, background masking, and automization.

The core scanning table improved the quality of all scanned virtual cores. High-resolution photography captured by the DSLR cameras allowed compiled textures to display material coarser than “fine lower” grain size (>0.125 mm) (Figure 3.20). The meshing resolution of each scan was extremely detailed causing high vertices count. To avoid latency within the application and reduce hardware demands, the mesh quality was carefully reduced without distorting texture or skewing the structural integrity of the model by “baking” the texture and retaining the normal map. Additionally, by confining the simplifying process to known flat regions, meshes were reduced to 1% of their parent counterpart without affecting the overall model representation (Figure 3.21).

The improved core scanning procedures required several iterations to allow optimization. Hardware differentiation from different camera models and focal length lenses caused severe anchoring errors. Additionally, slight aperture and exposure differentiation between cameras resulted in significant model differences (Figure 3.22). Once the set up was controlled (i.e. same camera and lens), the processing time was significantly shorter, and 3D model quality was superior.

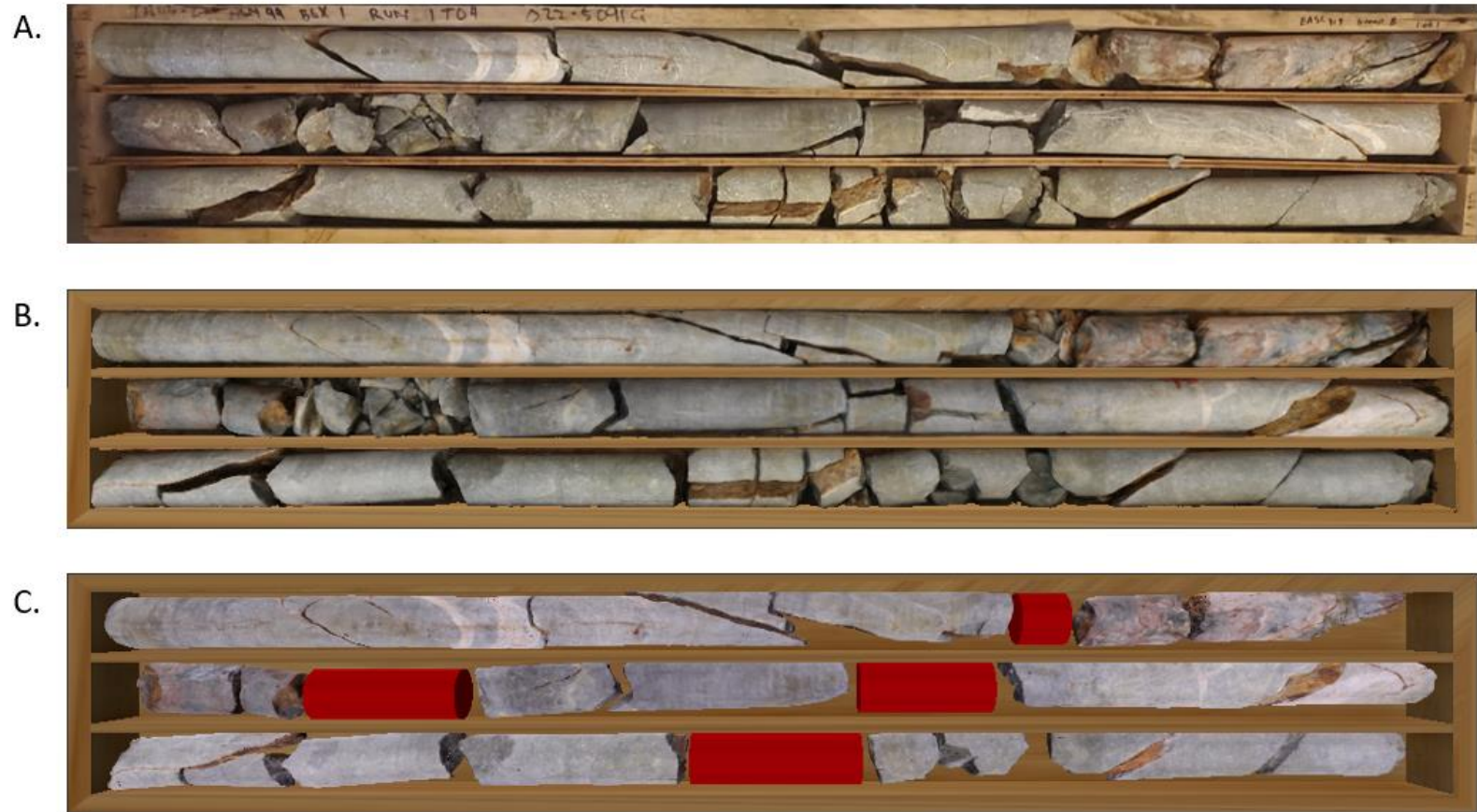


Figure 3.19: TH03 core box 1 scanned. (A) Original Core box (B) 2.5D model that can be observed in VR and MR (C) Virtual 3D core in which each core piece can be moved, scaled, and rotated freely in both MR and VR. Red cylinders are representative of areas with low RQD value (fragmented rock) which cannot be adequately scanned in 3D.

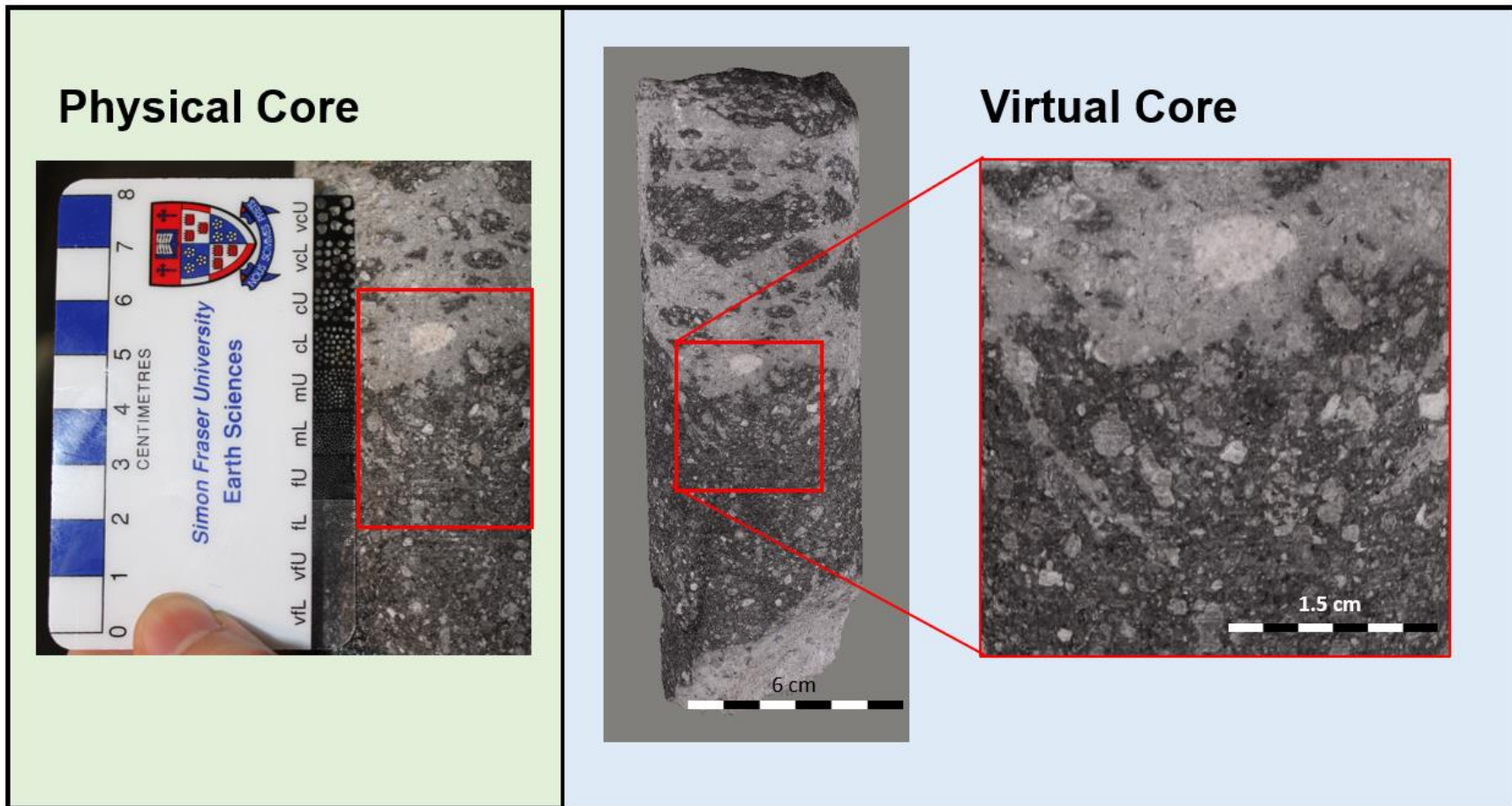


Figure 3.20: Scanned HQ3 core can digitally show grain size distribution within the fine lower grain size (>0.125 mm).

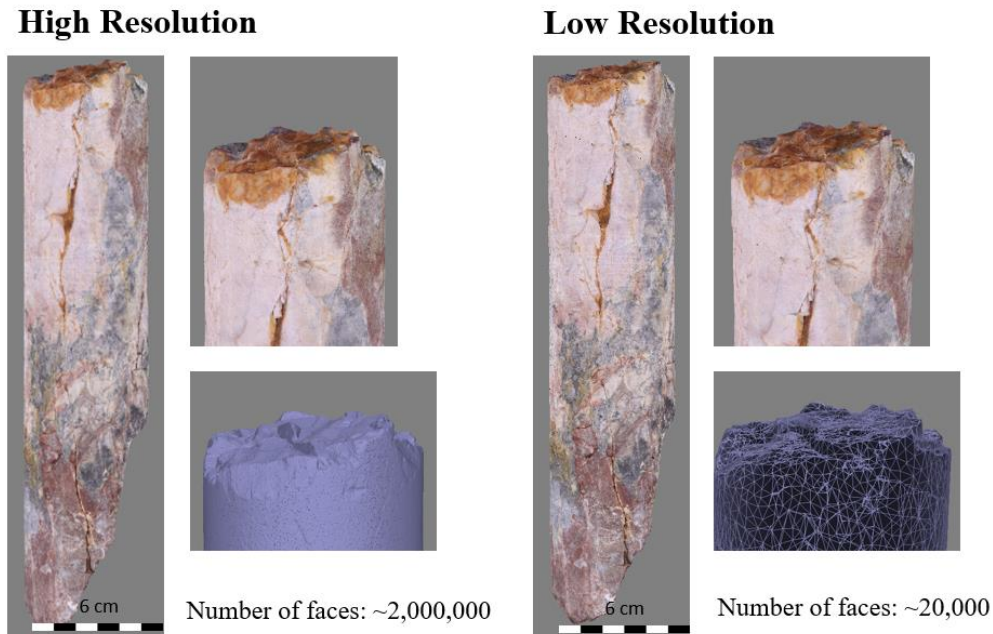


Figure 3.21: Scanning resulted in a highly detailed mesh. For improved rendering the mesh was selectively reduced to only hold 100 times less than the original results (e.g. 1%) without compromising texture or overall model shape.

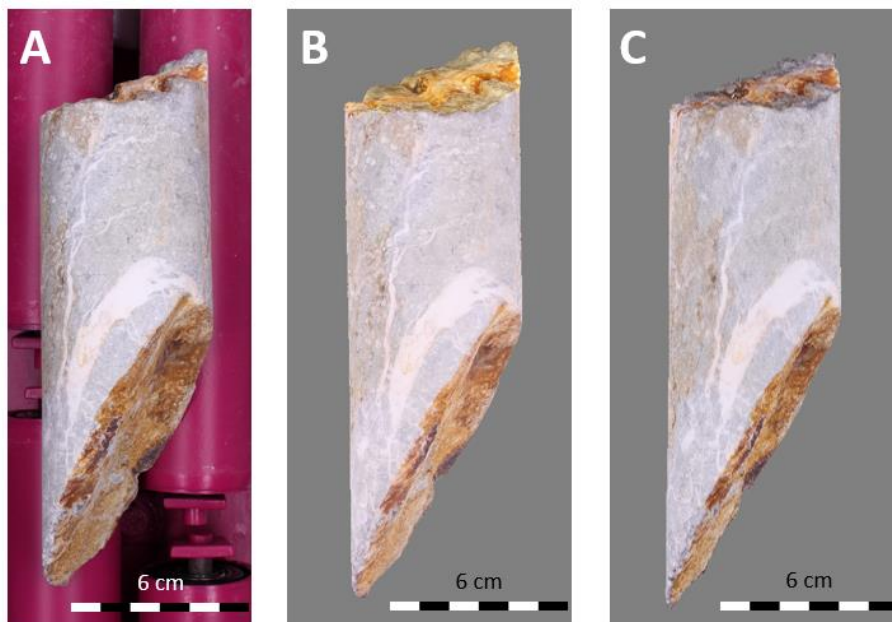


Figure 3.22: TH03 physical and virtual core piece with a slight angle difference (A) Photograph of physical core taken from in-house core scanner (B) 3D model results when three different cameras were used. Differences in camera settings resulted in large contrast difference between the top and the sides of the core. (C) 3D model results when camera settings were homogeneous throughout.

The digitized results were imported into Blender (2021) for further mesh corrections. The Python scripting capabilities of Blender were used to calculate the length of each piece of core by building a 4x4 ray array matrix (with a 0.2 mm separation) that intersects the centre of each virtual core sample (Figure 3.23). The distance between the edges of the core along each intersected ray was computed, and the lowest measurement recorded as the centre line core length (Figure 3.4). A matrix was used instead of a single definier as incorrect lengths were derived if it intersected the mesh at a sharp angle (i.e. intersected a mesh face that was subparallel to the ray). This script also allows indirect calculation of RQD and longest core piece along the core run.

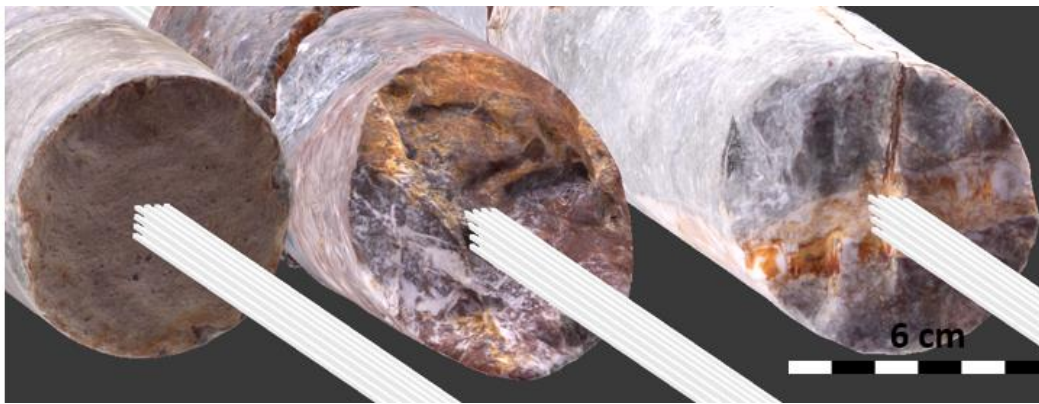


Figure 3.23: 4x4 rectangle matrix used to calculate centre line length of each core piece. A matrix was used because calculation errors were generated along sharp boundaries.

The digitization of core allows texture enhancement by altering contrast, RGB values and brightness from the compiled base images (Figure 3.24). With improved visibility of rock textures, features such as nodules, veining, obscure fabrics, lithological, and modal mineralogy differentiation can be shown with higher precision. Improved observation and geological understanding along each core sample results in improved modelling, and geomechanical characterization (Pérez-Barnuevo et al., 2018).

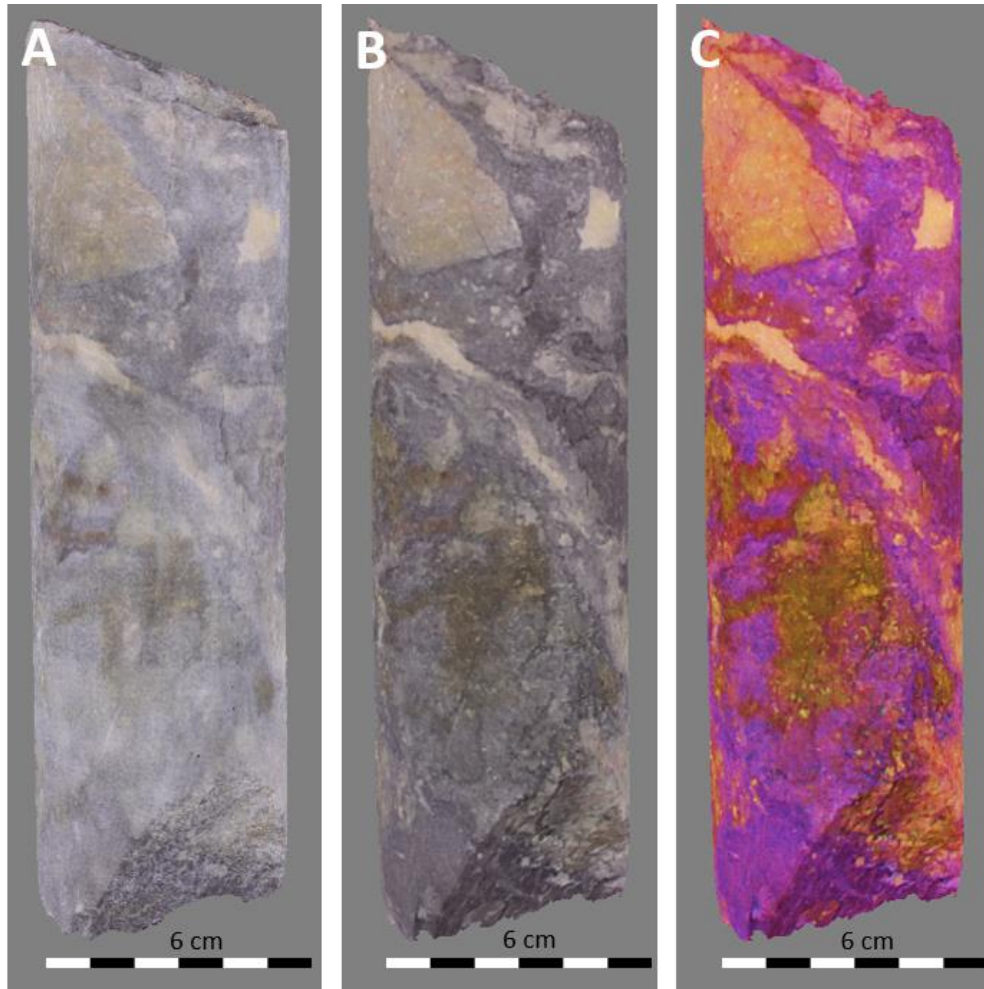


Figure 3.24: 3D digitized core sample (A) Without texture enhancement (B) With texture enhancement. Structures such as brecciated clasts, nodules, and veins are clearly evident (C) False colour.

3.6. Discussion

CoreLogger MR can assist geologists and engineers in improving logging practices by minimizing multi-step procedures and accelerating measuring requirements. Reduced logging time permits larger time investment in quality assurance or complex numerical modelling.

Quantitative classification systems, such as RMR, Q, and GSI, are subjected to ongoing research and have undergone modifications throughout the years (Hoek & Brown, 2018;

Kaiser, 2019; Rehman et al., 2018,). However, engineers and geologists can sometimes be unaware or overlook important changes in these systems. With a modernised interface, such as CoreLogger MR, the geoscientist can ensure that they are using the most up to date, optimized, and adequate classification available for their project site. The digitization of the data also allows rapid recalculation of values, once new changes are made.

When rapidly digitizing data within CoreLogger MR, a clear difference was observed between the Standard RMR assessment and the linear fit approach. It is recognised that RMR ratings are based on extensive empirical database. However, as recommended by Elmo and Stead (2021), there is a need to always consider the limitations in these empirical approaches and its applicability to a given project's site conditions. The linear fit technique available within CoreLogger MR is not intended to be a replacement for the current standard RMR rating assessment, but rather to emphasise the sensitivity of the final RMR rating caused by the sharp rating boundaries and the potential for non-optimal/cost effective support recommendations. Such issues have also been observed in the GSI and discussed by Kaiser (2019).

The successful scanning of core to produce virtual core presents a wide variety of possibilities beyond user interaction demonstrated in CoreLogger MR. The most significant benefit is the ability to observe core data at any time or location. Holographic core allows a referable holographic environment where geologist and engineers can reassess and supervise core logging practice. Other benefits of a 3D core database are that it enables permanent auditability of representative samples prior to splitting or destructive tests. Complete 3D core digitization also ensures minimum occlusion of information evident in 2D core photographs. With detailed texture enhancement, visibility of small structures such as current ripples, oscillation ripples, gold veins, and nodes which can be denoted spatially.

Other benefits of virtual core are related to reducing the physical labour associated with the core handling. Core boxes vary in dimensions but have limited proportions to ensure safe migration, durability, and reduce bulkiness (K7, 2019). An average full core box weights 24 kg (~53 lbs) if we assume it is full of granite core with a density of 2.52 -2.81 kg/m³. If we assume that it is composed of denser rock such as eclogite, it can exceed 30.2 kg (~66.6 lbs). Knowing the exact average weight of a core box is impossible as

weight varies significantly due to mineralogical density, humidity, porosity and other site-specific rock parameters. With the combination of heavy lifting, poor lifting posture, uneasy gripping, undistributed weight, repetitive unnatural movements, and immediate stress in the lower back facilitates susceptibility chronic lower back pain (Nielson et al., 2013). Furthermore, boxes can also fall, have wood splinters, rusty nails protruding, or break while moving, placing not only the worker at risk, but also the core. To put this into perspective, chronic back pain in 2013 reached over US\$50 billion in worker and insurance fees, ranking it as the third most costly expense (Dieleman et al., 2016). By digitizing core, companies could reduce core handling frequency, cost, mismanagement and misplacement, ultimately increasing safety and improving core storage procedures. CoreLogger MR could also be integrated into the virtual core model to allow complete virtual core logging and remote re-assessment of core. This has yet to be implemented.

The virtual core module could also be implemented into VR, allowing higher core resolution and would surpass the limitations of current MR platforms. With VR, the resolution would be mostly restricted by the computational capabilities of the tethered computer. Unity's cross-platform capabilities could also allow the integration of AR devices such as new cell phones, permitting consultation through various mediums for investors, co-workers, public domain, researchers, and students. If investors and external professional have access to virtual samples, they can be more confident in their investments.

3.7. Summary and Conclusion

At the outset of this research, it was evident that current logging practices are susceptible to errors such as: (1) improper digitization of data due to a multi-step standardization, (2) trying to solve a 3D problem via a single 2D image, (3) human bias and error, (4) inconsistency between personnel, and (5) poor handling and cataloguing of samples. Solutions to these issues were investigated through the virtual paradigm capabilities. Incorporating holographic logging procedures and complete 3D digitization of samples within XR platforms, proved that they can serve beyond visualization purposes.

CoreLogger MR showed that MR can be used as a data collection toolbox that can accelerate logging procedures via holographic measuring tools, table

assistance/manipulation, and instant digitization of observations. The in-house developed core scanner provided a remote 3D database that allows referral to drill cores. The ability to see comprehensive and rotatable cores at high resolution permits structural, mineralogical, and other geological/geotechnical observations to be captured virtually. The proposed core hub would be applicable for industries such as mining, civil engineering, geotechnical, and the petroleum industry. The digitization also allows 3D investigations which are not possible during exclusive 2D photographic analysis.

Expensive technical issues that arise from traveling to remote sites, maintaining core shacks, and transporting samples long distances could be significantly reduced by using digitized 3D cores and the development of virtual core sheds. The platform developed during this research provides a basis on which algorithms can be implemented for further analysis, including the characterization of natural/mechanical fracture, and alpha angle (e.g. acute angle between core axis and ellipse long axis (Holcombe, 2013)) measurement scripts. One algorithm developed captured the centreline length measurement value rather than the “tip to tip” or “fully circular” which is normally acquired from 2D images.

CoreLogger MR and the 3D core scanning capabilities have important future implications in engineering, geoscience and geomechanics. These applications are not intended to replace current core logging practices, but rather enhance logging practices with improved QA/QC opportunities. There are some tools, however, that could greatly benefit and even replace current practices. An example that was tested and constructed includes the core measuring tool. Within CoreLogger MR the measurements derived from hand distance had an uncertainty of ± 8 mm that is greater than current conventional ruler measuring tool (i.e. a ruler). This was due to the current limitations of the HoloLens. However, such an approach could be implemented into future accurate hardware enabling faster measurements than a ruler. More importantly, the sample measurement directly obtained from the in-house core scanner are arguably faster and more accurate than conventional ruler measurements as they are able to derive measurements (1) within a tenth of a millimetre, (2) provide centreline measurements, and (3) have more consistency than a conventional ruler. Furthermore, since the core is digitized, referral in how the RQD value was obtained on a site could be referred from all the samples that were scanned.

Large investments are made on drilling and core assessment, yet many common practice procedures remain arguably somewhat primitive. The limited time available for core logging calls for innovative, effective, faster, and more automated methodologies to collect representative data. The 3D core scanner and XR integration can in many environments facilitate this as some required data retrieval can be automated.

New approaches of retrieving quantitative information from core samples have been progressively introduced throughout the last decade, such as hyperspectral scanning (Krupnik & Khan, 2019). However, bridging new practices with old methodologies has not been smoothly assimilated. With holographic core becoming readily available, new quantitative retrieved data can be spatially overlain along the core run visually as will be discussed in the next chapter.

Chapter 4.

Virtual Core Logging for Resource Assessment

4.1. Introduction

Resource modelling and assessment for mining and civil engineering projects relies heavily on subsurface analysis and interpretation. Despite core logging being a foundation of numerous geological and resource models, it is estimated that 70% of core analysis is unreliable (McPhee et al., 2015). Defective data arises from inadequate reporting, poor laboratory procedures, and unrepresentative tests.

If core observations are solely based on visual features, the susceptibility for misinterpreted and ineffective data are greater. To avoid systematic mistakes, quantitative tools that retrieve reliable information ranging from point to four-dimensional (4D) data have been constructed (Tavakoli, 2018). Every procedure excels at extracting specific parameters, and thus, a combination of assessments is normally used (McPhee et al., 2015). The resulting array of complex data sets are rarely observed collectively, despite the fact that they might provide correlating data or information that aids in filtering noise from other datasets.

Virtual paradigm advancement has led to the ability to virtually place complex spatial data along physical and virtual models (i.e. spatially anchor information). Such capabilities were observed to be highly beneficial geologically by overlaying data along physical or virtual drill cores. To successfully achieve physical core overlay, it would require to be in a partly fixed location and image recognition (e.g. Vuforia, 2021) needs to be implemented for adequate importing. MR anchoring along physical core remains novel to date (Figure 4.1). Such an approach was not investigated in this research as it would require the sample to be flushed along the core box which is uncommon for standard logging procedures. However, with the in-house successful 3D core scanner, described in the previous chapter, a parallel project that spatially overlaid complex data sets along holographic core was tested and investigated. In this chapter, various datasets were superimposed along holographic core to enhance in-depth core analysis.



Figure 4.1: Proposed future core module that allows a user to see core data spatially along the core using the virtual paradigm.

The newly constructed quantifiable model represents a significant improvement on the previously examined holographic core as it can help scientists/engineers spatially correlate quantitative anomalies, improve interpretation, retain QA/QC capabilities, and discourage geologist or engineers from solely basing core data on visual features. All scanned core boxes were then brought into a single archive, which formed the foundation of XRCoreShack. This application demonstrated the feasibility of a 3D core database that provides holographic direct comparison and core retention. Current core box storage practices highly discourage direct comparison of rock samples because sorting boxes is extremely laborious, time consuming, and susceptible to misplacement (McPhee et al., 2015). With samples being completely digitized, such a procedure could be securely undertaken digitally.

4.2. Background Information

Core analysis is a crucial and complex practice that involves multi-disciplinary efforts to compile reliable data that defines exploration targets, resource evaluation, development, and constrains production (Tavakoli, 2018). Poor core analysis leads to faulty modelling foundations which will either underestimate or overestimate profitability.

Quantitative measures (e.g. hyperspectral scanning) and qualitative assessments (e.g. mineralogical assessment) are conducted prior, during, and post DDH. Using a suite of tests ensures adequate data constraints and the securing of conclusive results. The type of test undertaken is dependent on the resource type, budget, and time (Tavakoli, 2018). Some analysis procedures can cause certain segments of core to be heavily altered, broken, or sent out to a lab (McPhee et al., 2015). Lack of auditability of the freshly drilled core can cause incorrect assumptions in the future during core re-logging as the sample might have been altered from testing, handling, and storage deficiencies.

4.2.1. One-Dimensional Drill Data

4.2.1.1 Destructive and Geochemical Tests

There are many destructive tests that help characterize the mineralogical and structural integrity of the sample. Since minerals are a naturally occurring crystalline solid composed of atoms and/or ions that are chemically bonded, various geochemical investigations can be undertaken (Nesse, 2011). By crushing the material into powder form, chemical composition can be derived. Some methodologies include X-ray fluorescence (XRF) spectroscopy, mass spectrometry, scanning electron microscopy and electron probe microanalysis (Craigie, 2018). The inorganic and organic geochemical results assist in determining alteration zones, paleotemperature, and estimated ore grades for a region (McPhee et al., 2015).

Other destructive test includes geotechnical procedures such as point load testing, UCS, and triaxial compressive strength (ISRM, 1981). By investigating the mechanical behaviour of intact rock and discontinuities, it is possible to infer the mechanical properties of a rock mass.

The quantity of tests conducted along a core is dependent on budget and time. Larger quantity of samples improves statistical analysis, reduces uncertainty, and improves assumption justifications (Tavakoli, 2018). If budget allows, sampling at regular intervals is recommended (McPhee et al., 2015).

Fundamental data can be retrieved from destructive tests, but the remaining broken samples are usually placed back into their respective core box. If a macroscopic reassessment of a specific interval that has undergone heavy testing is required, this cannot be completed unless images of the original interval were taken. If core images were not captured, the only reliable macroscopic observations are previously recorded logs that can be disproportionally generalized, with potential errors and bias.

4.2.1.2 Non-Destructive Point Data

The inability of destructive tests to return the sample to its previous location after the test completion, has led to many in practice resorting to non-destructive tests. Additionally, non-destructive tests provide faster, cheaper, and more point data collection for improved statistical analysis (Aboutaleb et al., 2018). Several non-invasive handheld devices, such as the TerraSpec Halo (Malvern Panalytical, 2021) or Tracer 5 (Brunker, 2021), helps scientists and technicians quantify elemental composition of analysed regions. Other devices such as the Schmidt Hammer, Equotip (Proceq, 2021) and Ultrasonic testing (Olympus, 2021) can help determine mechanical properties of the rock, without compromising the internal integrity.

Studies have shown minor deviation from non-destructive tests in comparison to destructive tests while inferring both composition and deformability (Gupta, 2009; Kallu & Roghanchi, 2015; Shalabi et al., 2007; Vasanelli et al., 2013). These same studies have also concluded that non-destructive tests provide satisfactory results and increased uncertainties are compensated for by the larger number of tests that can be performed.

4.2.2. Two-Dimensional Drill Data

4.2.2.1 Hyperspectral Scanning

There are many non-invasive and non-destructive 2D imaging techniques and procedures available. An example that has gained large traction in both the petroleum

and mining industries is hyperspectral scanning as it provides fast, effective, and unbiased data (Tusa et al., 2019; Krupnik & Khan, 2019).

Hyperspectral scanning works by obtaining passive spectral information per pixel within an image. The examination retrieves a hypercube where the z-dimension covers radiance data which allow the derivation of absorption, reflectance, and fluorescence values for wavelengths ranging from ultraviolet to infrared (Qin, 2012) (Figure 4.2). The array of waves is derived by uninterruptedly emplacing different band-passes through a passive lens (Valismo, 2015).

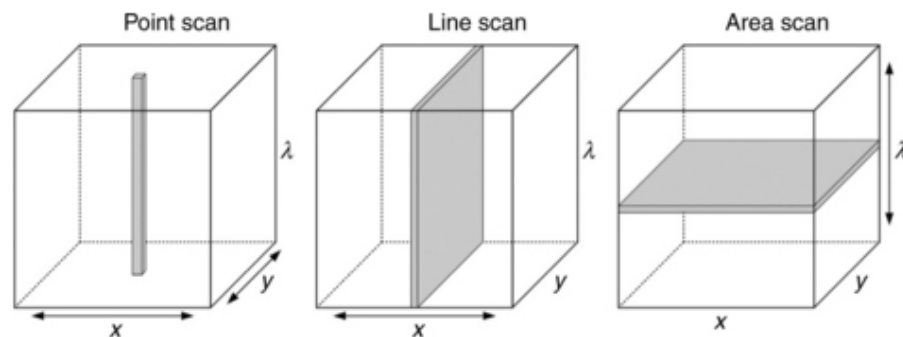


Figure 4.2: 3D hyperspectral cube with spectral data in the z-dimension for a x and y 2D image (Qin, 2012) [Used with permission].

Mineral assemblages absorb wavelength differently due to their crystallographic structures, permitting isolation of grains through diagnostic spectral responses (Nesse, 2011). Untarnished hyperspectral responses can rapidly classify minerals by comparing wavelength responses relative to a mineral spectral library. Wavelength differentiation allows specific types of minerals such as clays, chlorite or muscovite to be easily isolated and classified, a procedure that is challenging in unaided visible core investigation (Krupnik & Khan, 2019).

Computational mineral determination allows rapid classification of alteration zones, modal mineralogical calculation and rock classification (Cracknell et al., 2018; Sahoo & Ray, 2015). Result validation should always be subjected to human oversight because reflectance can be heavily skewed by mineralogical alteration, moisture, improper scanning, and weathering (Krupnik & Khan, 2019).

The wide capabilities of hyperspectral analysis have led companies such as CoreScan (2021), Enersoft (2021), and Specim (2021) to develop multispectral core scanners. The rigs are usually mounted with high-resolution photography and a hyperspectral camera to visually correlate spectral information, capture rock textures, and isolate mineralogical composition (e.g. sericite vs. quartz) (Tiu, 2017). High resolution photography also allows other practices such as confining sulphide minerals for acid rock drainage purpose (Cracknell et al., 2018).

Other instrumentation such as XRF have been implemented on some rigs for additional supplementary pixel comparison and to overcome limitations observed in hyperspectral results (Enersoft, 2021; Cracknell et al., 2018). By combining various mediums, core scanning has become more sophisticated, reliable, and quick. SisuRock claims to have scanned 17, 000 metres of core with a 2 mm resolution in a span of two weeks (Specim, 2021).

Hyperspectral scanning has also been implemented in large scale analysis. Airborne hyperspectral imaging (Kruse et al., 2012; Notesco et al., 2015) and space borne hyperspectral imaging via EO-1-Hyperion satellite (Govil et al., 2018) have been used to map surficial mineralogy. Field spectroscopy within mines has proven to be effective in delineating alteration and mineralization patterns (Krupnik & Khan, 2019).

Like any passive spectra instrumentation, there are increased complications when taken to greater scales. Signal attenuation due to ozone, topography, water vapor, temperature, and emissivity from radiance can distort wavelength responses (Laakso et al., 2018; Notesco et al., 2015). Wave corrections are continuously being investigated and are progressively being refined for improved representative results. Recent machine learning protocols have progressed studies even further because large training data input enables new remedial algorithms to be developed (Acosta et al., 2019).

4.2.2.2 Thin Section Analysis for Petrographic Investigation

Rock and core samples can be sliced into small trims to allow in-depth mineralogical investigation. Mounting it on a glass slide with epoxy, using a diamond saw, and grinding/thinning it to approximately 0.03 mm in height, enables light to transverse through the rock and glass (Nesse, 2011). This results in a thin rock slice known as a “thin section”.

Since light crosses through the mineral specimen differently, microscopic analysis (i.e. petrographic analysis) can be completed. Every mineral has a specific property in polarized, cross-polarized and reflected light allowing petrology studies (Nesse, 2011). Thin sections can help investigate diagenetic processes, mineralogical composition, facies properties, age dating, determining cement type, defining structures, estimating porosity, performing elemental studies and identifying alterations (Tavakoli, 2018). By incorporating other methodologies such as electron microscopy, energy dispersive X-ray (EDX) or backscattered electrons (BSE), more complex and sophisticated information can be obtained.

Micron scale characterization helps understand geological features which can then be propagated into macro or regional scale findings (Nesse, 2011). Data retrieved, however, is heavily dependent on the petrographer's expertise. Such reliance implicates inevitable human bias, and errors from inaccurate interpretation (Tavakoli, 2018). Additionally, the trim that the thin section was developed from can potentially be a poor representation of the whole sequence of focus.

Currently, it is challenging to verify whether the thin section analysis and findings have been conducted adequately or if the location from where it was extracted is representative of the region of interest. Lack of petrographic assurance platform has led to thin section observations to be approved with minor revision, which can have future troublesome implications.

4.2.3. Three-Dimensional Drill Data

4.2.3.1 Imaging of Borehole Walls Through Televiwer and Full Micro Imager (FMI)

If borehole walls are intact after drilling completion, in-situ structures can be directly scanned by numerous types of instrumentation. Detailed explanation of several downhole formation evaluation instruments is included in Gooneratne et al. (2019). The instruments analysed in this thesis include televiwers and fullbore formation microimager (FMI).

Televiwers can be classified into acoustic and optical. Both usually include three axis magnetometers and three accelerometers to capture accurate borehole deviation (Gwynn et al., 2013). An acoustic televiwer (ATV) uses sonic pulses, by rotating a

transducer in a pulse-echo mode. The attenuation and time delay of the pulse differentiates between structures and lithological properties, defining breaks between acquisitions (Gooneratne et al., 2019). The results are then coloured to represent travel time or amplitude reflectance value making a borehole image (Gwynn et al., 2013). Other factors that affect amplitude responses are attenuation of fluids, centralization of the axis, and relative efficiency of the borehole wall (defined by roughness of the wall, lithological properties and structures) (Gwynn et al., 2013; Gooneratne et al., 2019).

Optical televiewers (OTV) use light sensitive cameras to capture high-resolution images of the borehole walls (Mount Sorpris, 2021). OTV works best if the hole is dry and clean because issues arise when the line of sight is murky. Since OTV does not have quantitative data on reflectance, it cannot computationally differentiate between open or filled structures unless image recognition is implemented (Gwynn et al., 2013).

The formation micro-imager (FMI) differs from televiewers as it sends continuous voltage from a lower electrode to an upper electrode receiver. The resistivity that is recorded can then produce an image (Gooneratne et al., 2019). Micro-resistivity will change depending on lithological and petrophysical properties along the formation. The result contains 80% coverage of the borehole walls (Schlumberger, 2021a). FMI is more commonly used within the oil industry as the resistivity can derive bitumen content, geological structures, reservoir geometry, and petrophysical properties.

All borehole imagery produces a permanent auditable record of in-situ oriented measurements, help distinguish natural from induced fractures, and help register appropriate depth (Gwynn et al., 2013). Results are visualized in three common representations: (i) 3D view, (ii) unrolled cylinder, and (iii) azimuthal image (Figure 4.3) (Hurley & Zhang, 2017). The most common observation depiction is via azimuthal image and 3D view.

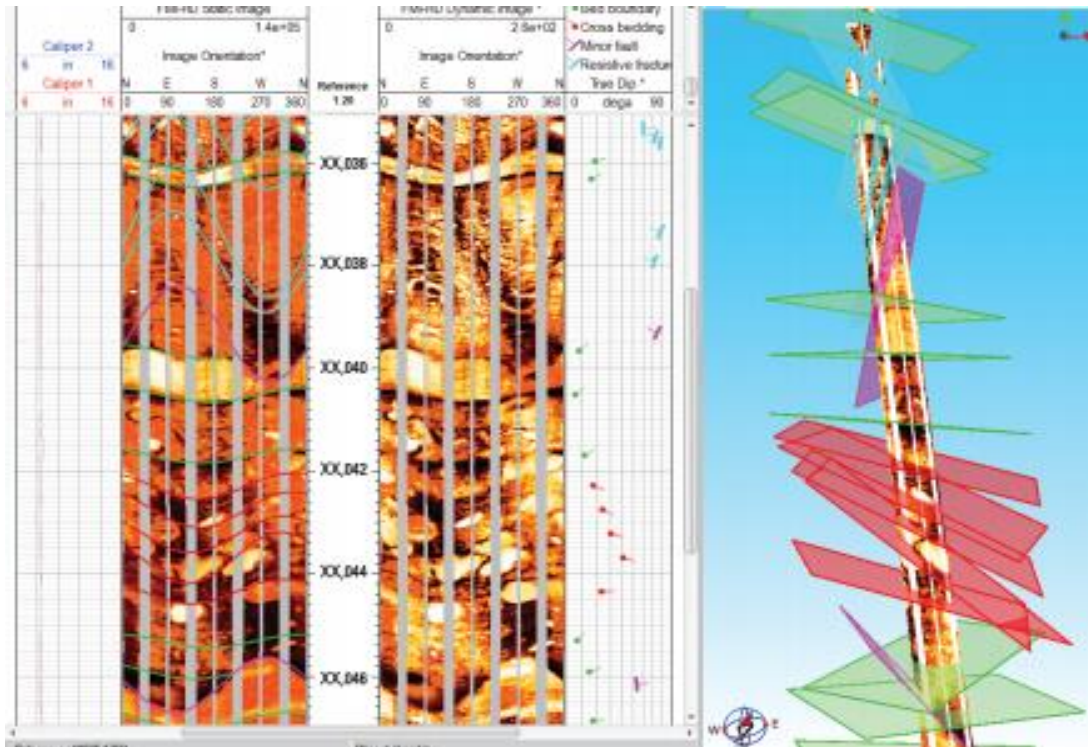


Figure 4.3: Final FMI results seen in both azimuthal and 3D view (Schlumberger, 2021a).

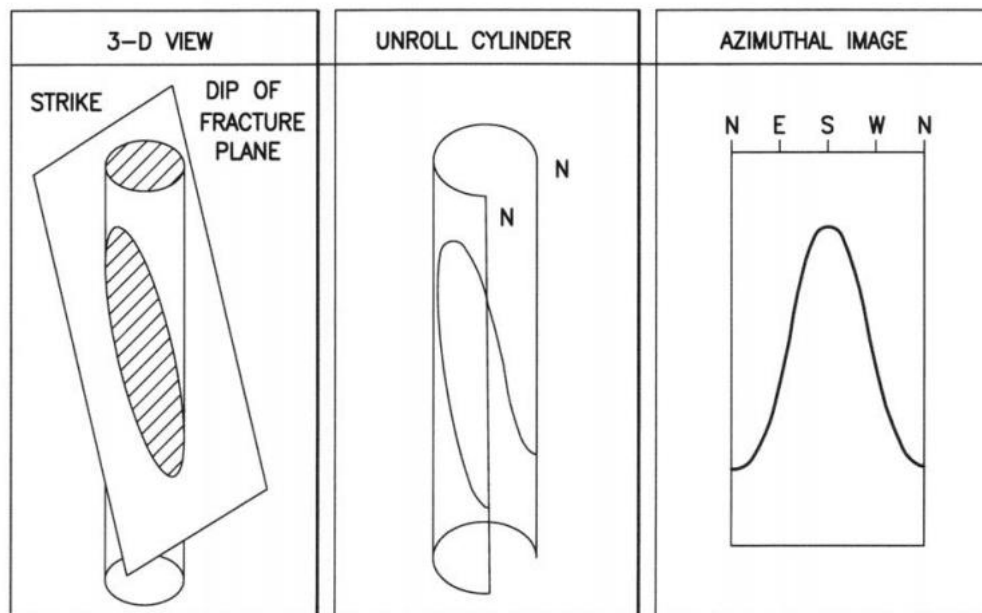


Figure 4.4: Common ways to display borehole imaging. Structures that are observed in 3-D view will appear sinusoidal in azimuthal view (Hurley & Zhang, 2017).

Both televiewer and FMI can be used to delineate structures through visual observation or image recognition (Cruz et al., 2017). The standardized recognition of structure is by a 'sinusoid fit' because structures will commonly appear as a sine wave in azimuthal view (Figure 4.4). By applying numerous filters, structures can become more evident allowing sinuous wave depictions that can calculate parameters such as dip, dip azimuth and width (Fernández-Ibáñez et al., 2018) (Figure 4.5). Visual and computed fits tend to have significant variability due to over interpretation of structures, and image quality (Cruz et al., 2017; Fernández-Ibáñez et al., 2018).

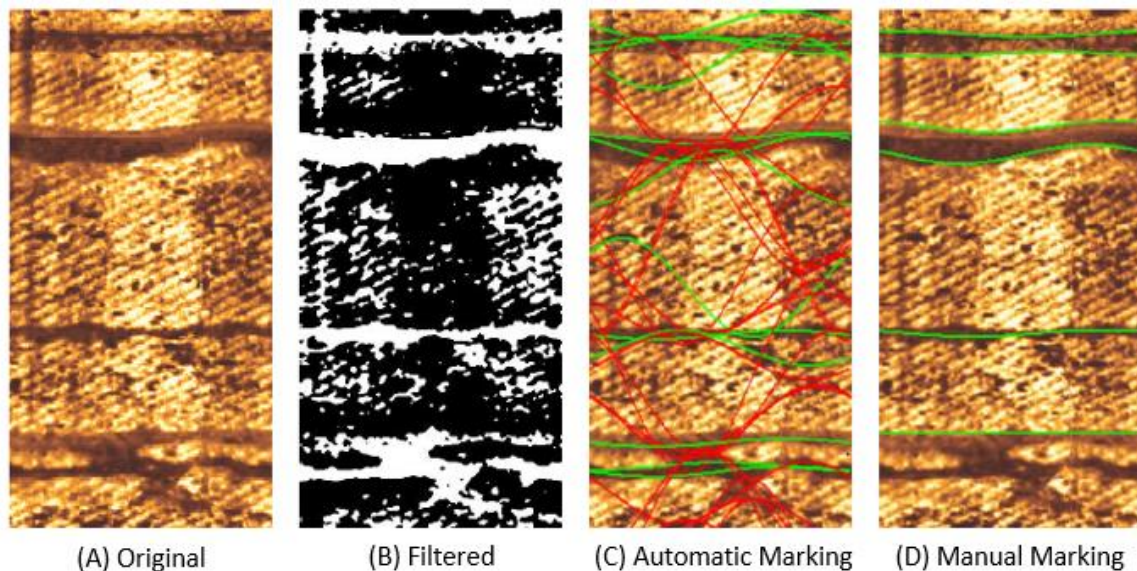


Figure 4.5: Sinuous acoustic image results (A) Original (B) Grayscale filtered (C) Automated marks using machine learning, where red show false positive and green are true positives (D) Manually marked by geologist (Cruz et al., 2017) [Used with permission].

Current lack of a perfected structure picking algorithms requires geologists to manually address whether computed fractures are real or formed from noise (Cruz et al., 2017). By validating structures, faster and less laborious work is achieved when compared to conventional manual sinuous drawing.

To promote accurate and faster structure picking domains, comparing and aligning core-to-log (CTL) studies has proven successful in rejecting more than 50% of the misidentified sinuous fitting (Fernández-Ibáñez et al., 2018). CTL works by correlating and validating distinct features such as layers, boundaries, dissolution, or vugs as tie-

points between the already retrieved core and the images. This methodology has provided more accurate depth registration than the standard porosity or gamma-ray properties alignment (Fernández-Ibáñez et al., 2018).

Borehole images have been proven to be able to measure in-situ structure orientation with an error measurement from 5° to 0.3° (Gwynn et al., 2013). This differs greatly from the alleged accurate orientated drill core that has been verified to have a 20° dip error and 10° to 30° azimuth discrepancy (Holcombe, 2013). Increased incentives to obtain borehole imaging have been recommended as it can retrieve more accurate structure measurements allowing lower waste strip ratios, increased safety, increased reserve, and reduced operation cost (Llewelyn et al., 2018).

The large benefit of borehole imaging, however, is not always achievable because borehole stability is a crucial prerequisite. If there are intense fracture zones or high swelling regions, the instrument may get stuck, damaged, or lost. Additionally, borehole imaging is expensive and with variable hidden costs such as the importing of machinery, supervision, and post processing (Gwynn et al., 2013). Many companies do not conduct such studies as the expenses would exceed budget. Some companies accept the higher cost to ensure optimization of excavation design as borehole imagery can lead to significant financial benefits (Llewelyn et al., 2018).

4.3. Preliminary Complex Virtual Core Model

4.3.1. 2.5 D Core Scan Model

A core drilled by BC Hydro in Stave Falls, British Columbia with distinct discontinuities, different lithologies, and high RQD values was assessed to investigate anomalies that could be captured via hyperspectral, thermal and laser acquisitions (Figure 4.6). It was scanned in 2.5D (Figure 4.7). Unlike the previously investigated 3D core model, a 2.5D model does not allow complete interaction with individual core pieces. The rock type included:

- Unit 1: Melanocratic equigranular biotite phyrlic granite.
- Unit 2: Biotite phyrlic granodiorite with partial chloritization.
- Unit 3: Granite with chloritized veins.

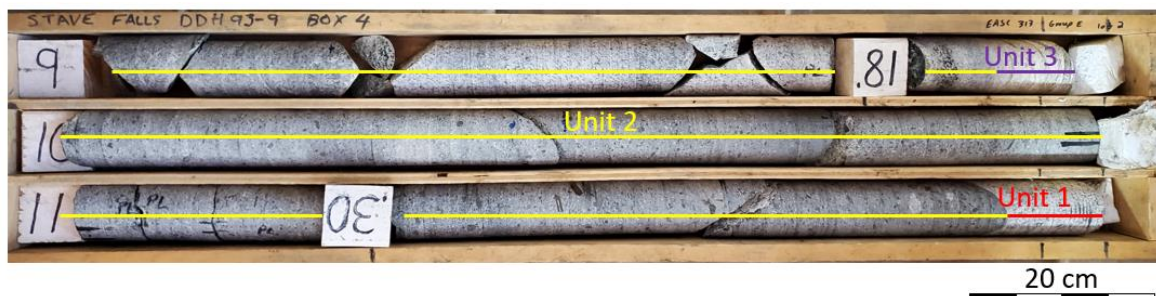


Figure 4.6: Core selected for preliminary 2.5D Core Model. Unit 1: Melanocratic equigranular amphibole biotite phyric granite. Unit 2: Biotite phyric granodiorite. Unit 3: Granite with abundant chloritized veins.

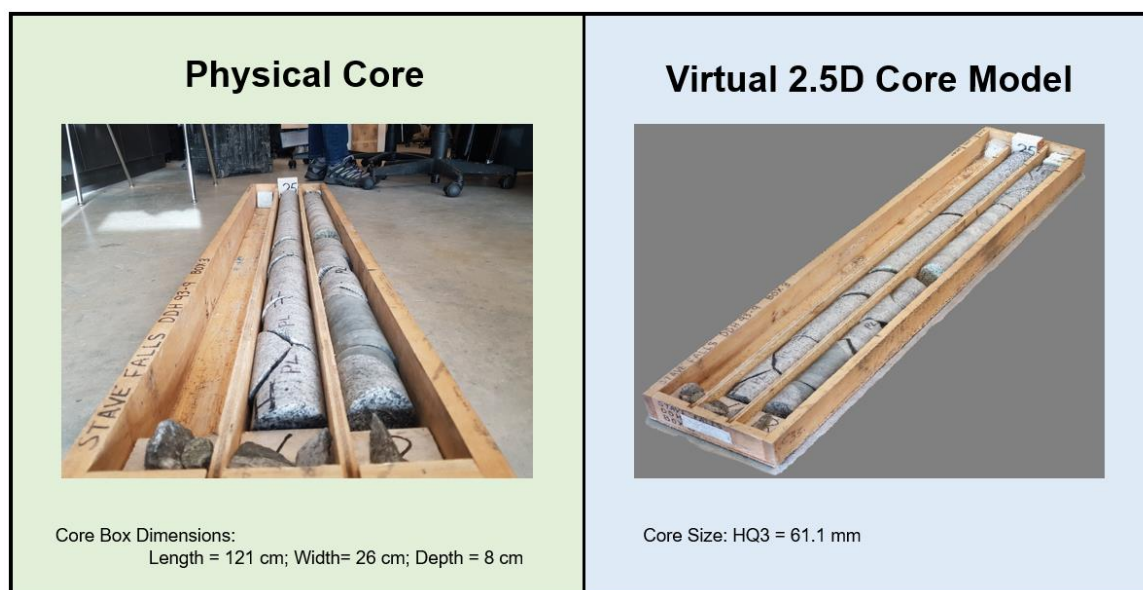


Figure 4.7: Preliminary 2.5D model of a core box. Unlike other 3D core models, individual cores cannot be moved, rotated, or scaled freely.

4.3.2. Thermal Reading Acquisition

The core was left at room temperature for a prolonged period, resulting in a homogeneous temperature. To acquire thermal data, each core piece was heated in an oven at 205 C° (~400 F°) for 3 hours.

Once heated, the core was placed back in the core box and scanned using a thermal camera located 8 m away from the target. The camera used was a FLIR SC7000 with a

standard 50 mm lens that captures pixel temperature between 5 C° to 150 C° with a +/- 1 C° accuracy (FLIR Systems, 2014).

Heat dissipation was captured by acquiring a thermal image every 15 seconds. Time constraint was necessary to minimize memory usage. The core took approximately one hour and thirty-five minutes to equilibrate to room temperature. Since each pixel retained a thermal value, a trace was drawn for five distinct regions to graphically observe heat dissipation (Figure 4.8). It was evident that heat dissipated faster along discontinuities and had slight temperature variances along lithological differences. Discontinuities served as conduits that cooled faster as there was more surface area exposed allowing more heat dissipation. On the other hand, minerals retain heat differently (Nesse, 2011), allowing lithological units to constrain different heat profiles.

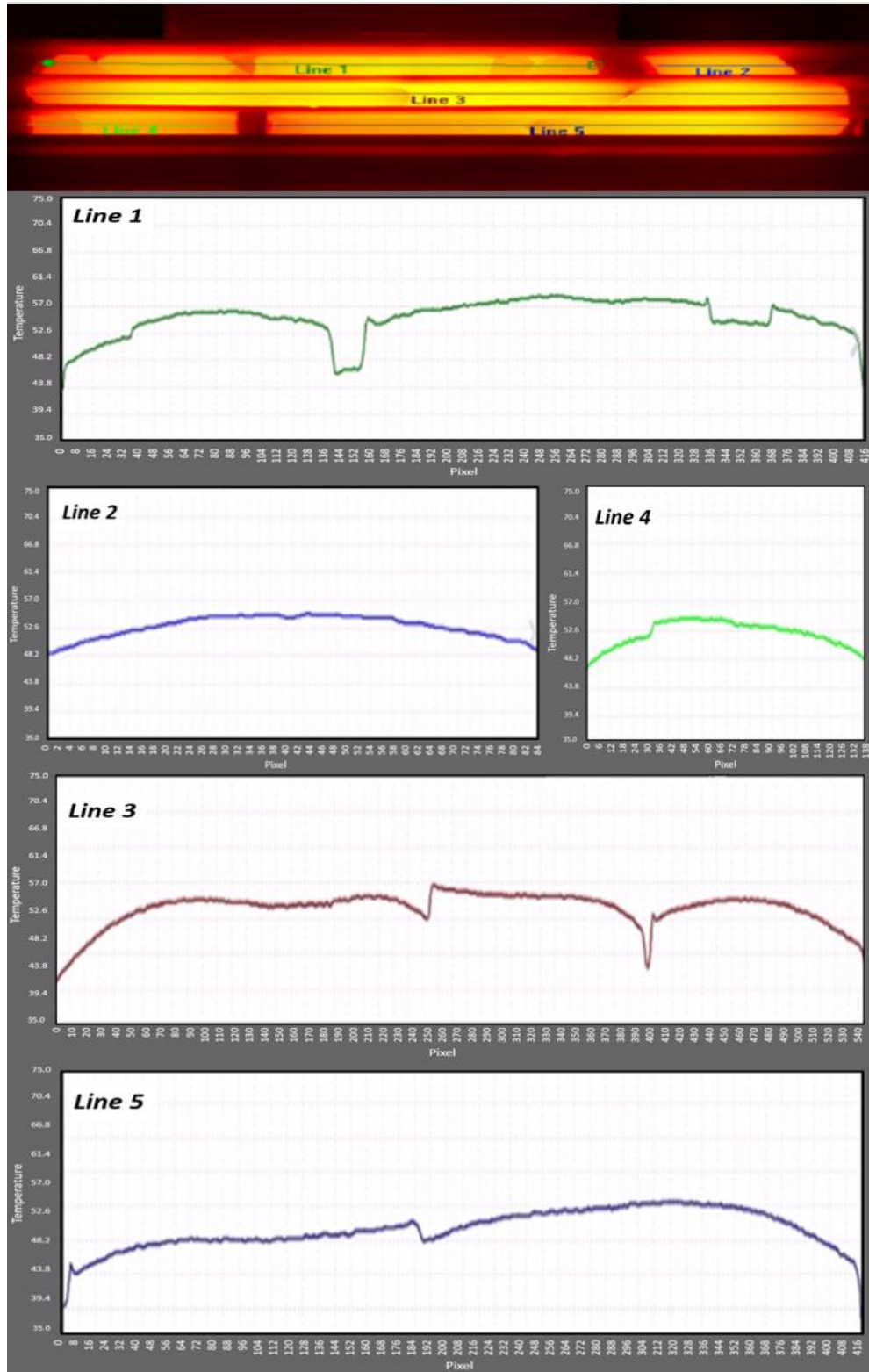


Figure 4.8: Five lines drawn to quantify core heat dissipation per pixel after 33 minutes of cooling. Dips and darker shades show discontinuities or lithological differences.

4.3.3. Laser Reading Acquisition

A Riegl VZ-4000 was used to acquire reflectance pulse amplitude and intensity along the same core box. The laser scanner used has four distinct laser pulse settings of 30 kHz, 50 kHz, 150 kHz, and 300 kHz that are near infrared values. The highest pulse frequency was selected as it gave the best accuracy for close range analysis and apparatus was placed ~25 m away from the target (Riegl, 2020).

Results obtained were unsatisfactory because the pixel resolution per image was too coarse and hosted large noise values (Figure 4.9). Significant difference in reflectance and wave absorption were evident for different composition and textures but the point cloud was too coarse to properly align the results. These errors could be corrected with laser scanner catered for small scale targets (e.g. EinScan HX (Shinning 3D, 2021), or peel 2-s (Peel 3d, 2021).

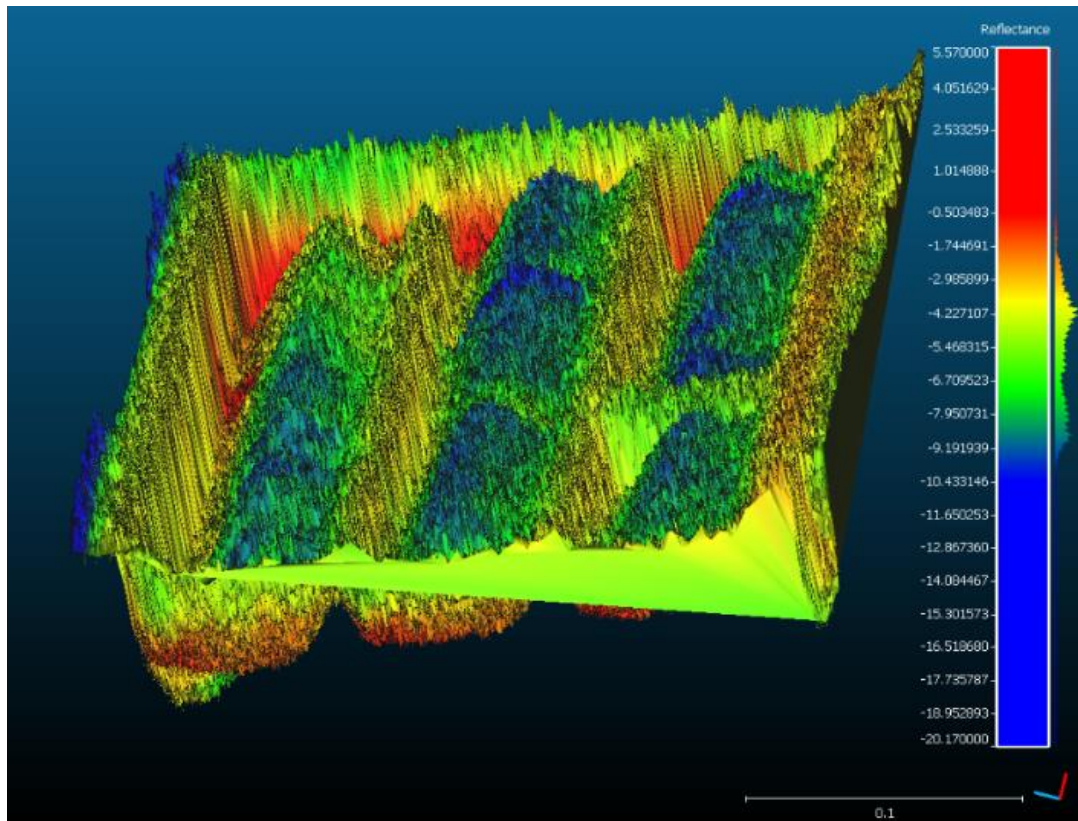


Figure 4.9: Riegl VZ-4000 noisy results of core box.

4.3.4. Hyperspectral Reading Acquisition

A Specim SWIR 3.0 hyperspectral camera that can record wavelengths in the range 1000 – 2500 nm with a spatial resolution of 15 μm (Specim, 2020) was used to scan the selected core box. The camera was placed 10 m from the target. Only simple corrections were applied to the hyperspectral data which include resizing of the data, vertical de-stripping, forward minimum noise fraction (MNF) statistic where Eigenvalue > 2 were selected and inverse MNF rotation. Several combinations of RGB values were used until minerals could be distinguished easily. The array of RGB values used was 15-151-252 and 36-123-218. The value of these codes corresponds to the wavelength of 1052.63 nm – 1813.57 nm – 2375.77 nm and 1171.17 nm – 1657.6 nm – 2186.7 nm, respectively.



Figure 4.10: 1052.63 nm- 1813.57 nm – 2375.77 nm tiff file used to overlay 3D core box model (1) Unit 1 is clearly distinct (2) Bright pixel within the Unit 2 due to large phenocryst (3) Discrepancy within Unit 2 that was not evident during geological analysis (4) Unit 2 gradual change modal mineralogical change (5) Chloritized veins in Unit 3.

4.3.5. Final XR Core Model

The 2.5 D scanning of the core box prevented individual pieces of core from being interactive through XR capabilities. The rigid model enabled all datasets acquired to be synergized spatially, creating a complex holographic core box (Figure 4.11).

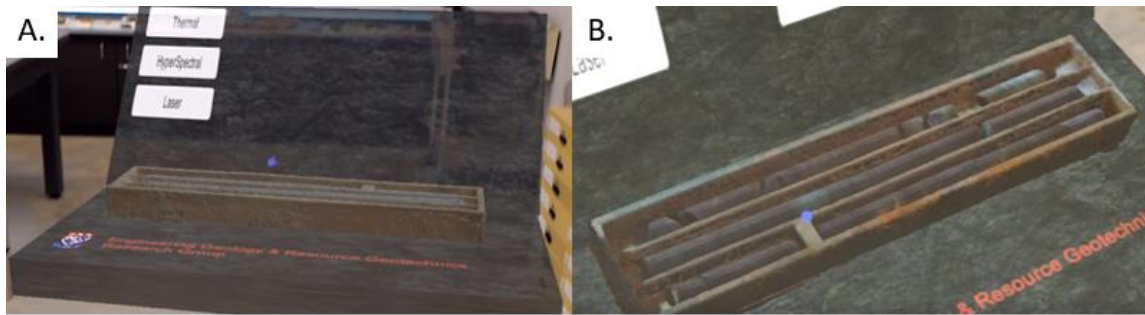


Figure 4.11: Single archive that hosted all the datasets for preliminary core model study (A) Photogrammetry 2.5D model made with a Menu that allows selective overlays (B) Hyperspectral results with RGB value of 15-151-252 on 2.5D model.

Thermal readings were placed along the virtual core as videos (Figure 4.12). Graphical results of each thermal acquisition were also anchored above the virtual core (Figure 4.13). Data overlay along the core effectively delineated modal mineralogical differentiation, discontinuities, and alteration zones.

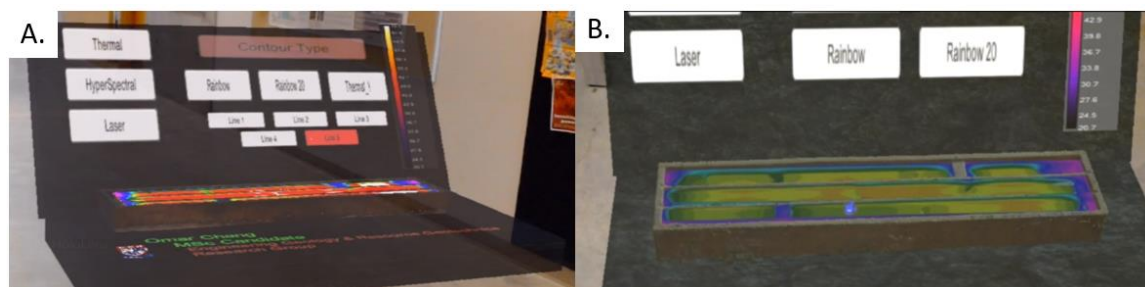


Figure 4.12: Rainbow 24 contour which shows contrast along different rock types and discontinuities. Unit 3 cooled the slowest, while Unit 2 was the fastest.

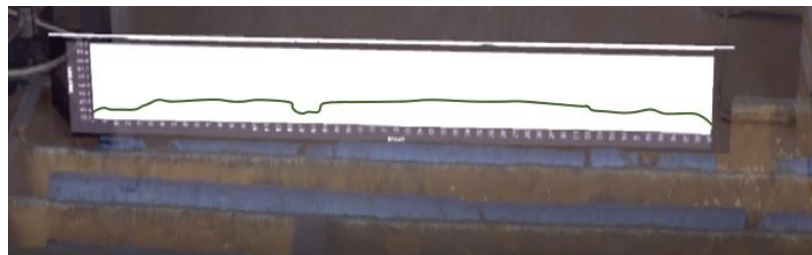


Figure 4.13: Graphical heat dissipation along Line 1 spatially anchored along the core.

4.4. Ore Deposit Virtual Core Model

4.4.1. Hyperspectral Differentiation Along Mining Exploration Core

The successful preliminary assessment led to the investigation of a more sophisticated holographic core model. A split core from an undisclosed location and anonymous early-halo type Cu-Mo-Ag porphyry deposit was digitized in 3D. Texture along the core was not clear unless the physical core was moistened. To effortlessly display scanned textures, the RGB values and contrast were manipulated for permanent contrast along the core (Figure 4.14).

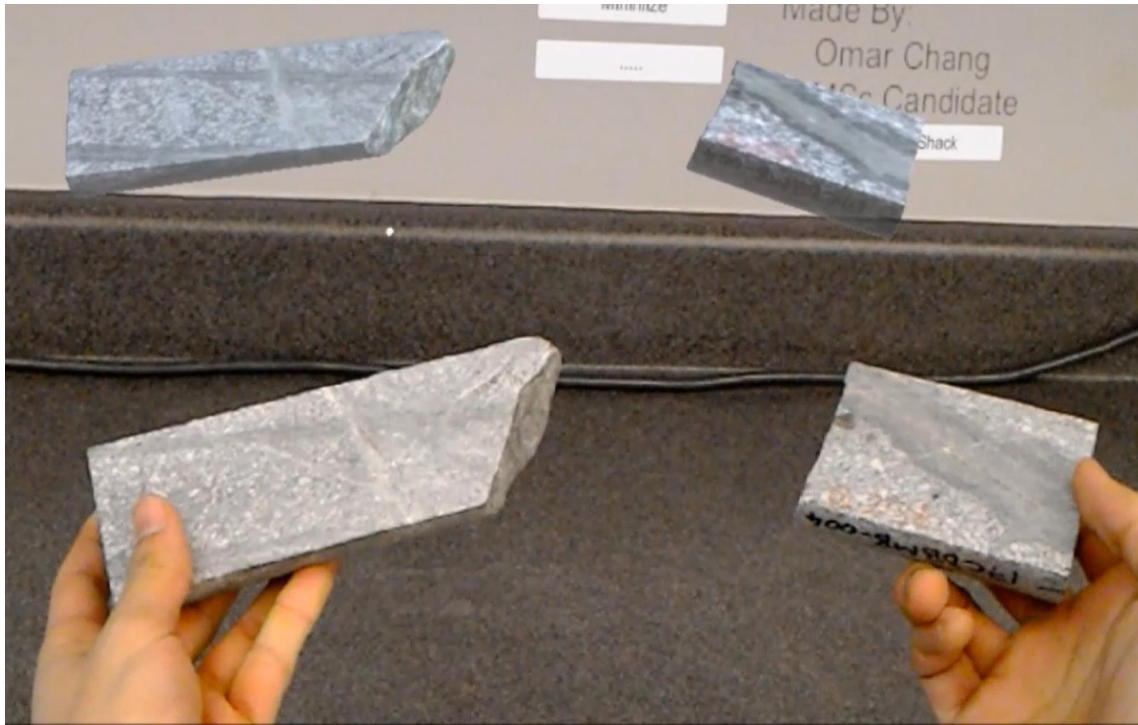


Figure 4.14: Half core run of early halo Cu-Mo-Ag porphyry. Virtual core is floating on the background while physical core is held by the user.

The core was then shipped to Enersoft Inc to be scanned for hyperspectral and infrared analysis. Their results were subsequently overlain along each piece of core (Figure 4.15)

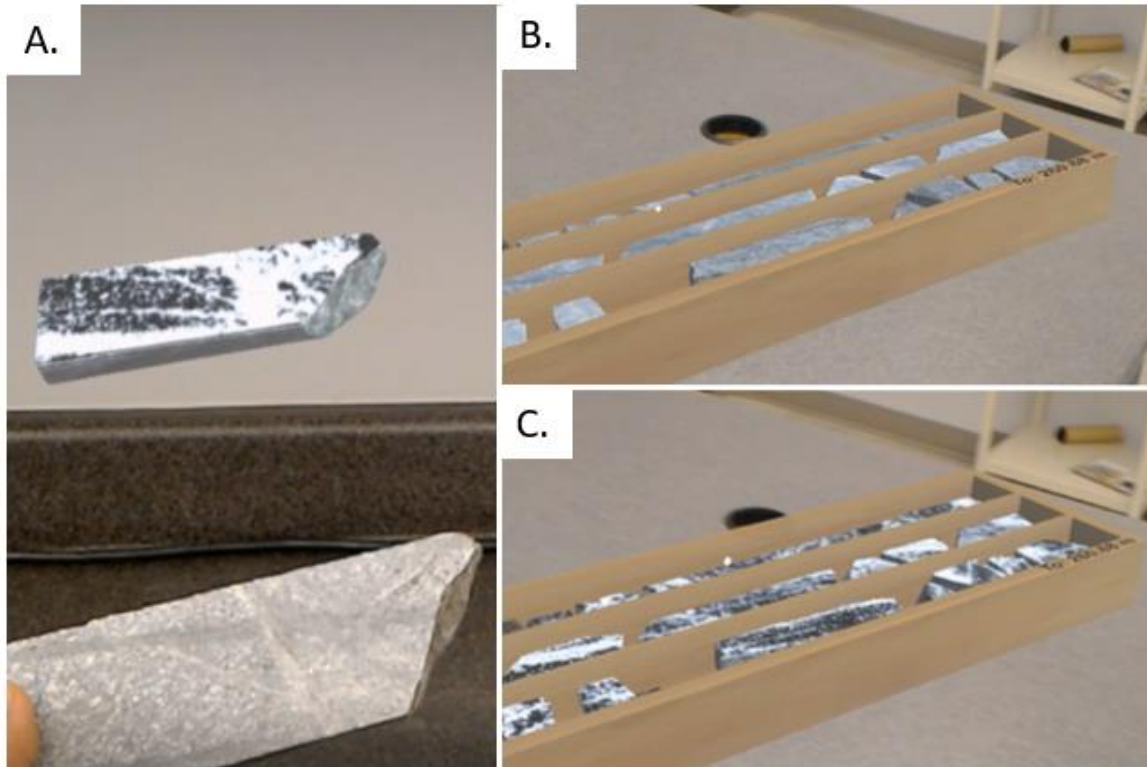


Figure 4.15: Grayscale Enersoft Inc results overlain along the virtual core. (A) Compared to physical core. Virtual core box with (B) raw results versus (C) grayscale overlay.

4.4.2. Thin-Section Analysis

A thin section for the investigated core was available. High-resolution microscopy imagery of the thin section was taken at every 15 degrees in both plain polarized light (PPL) and cross polarized light (XPL) (Figure 4.16). Each micron level image taken had the same dimensions of 4033 x 7524 with 96 dpi.

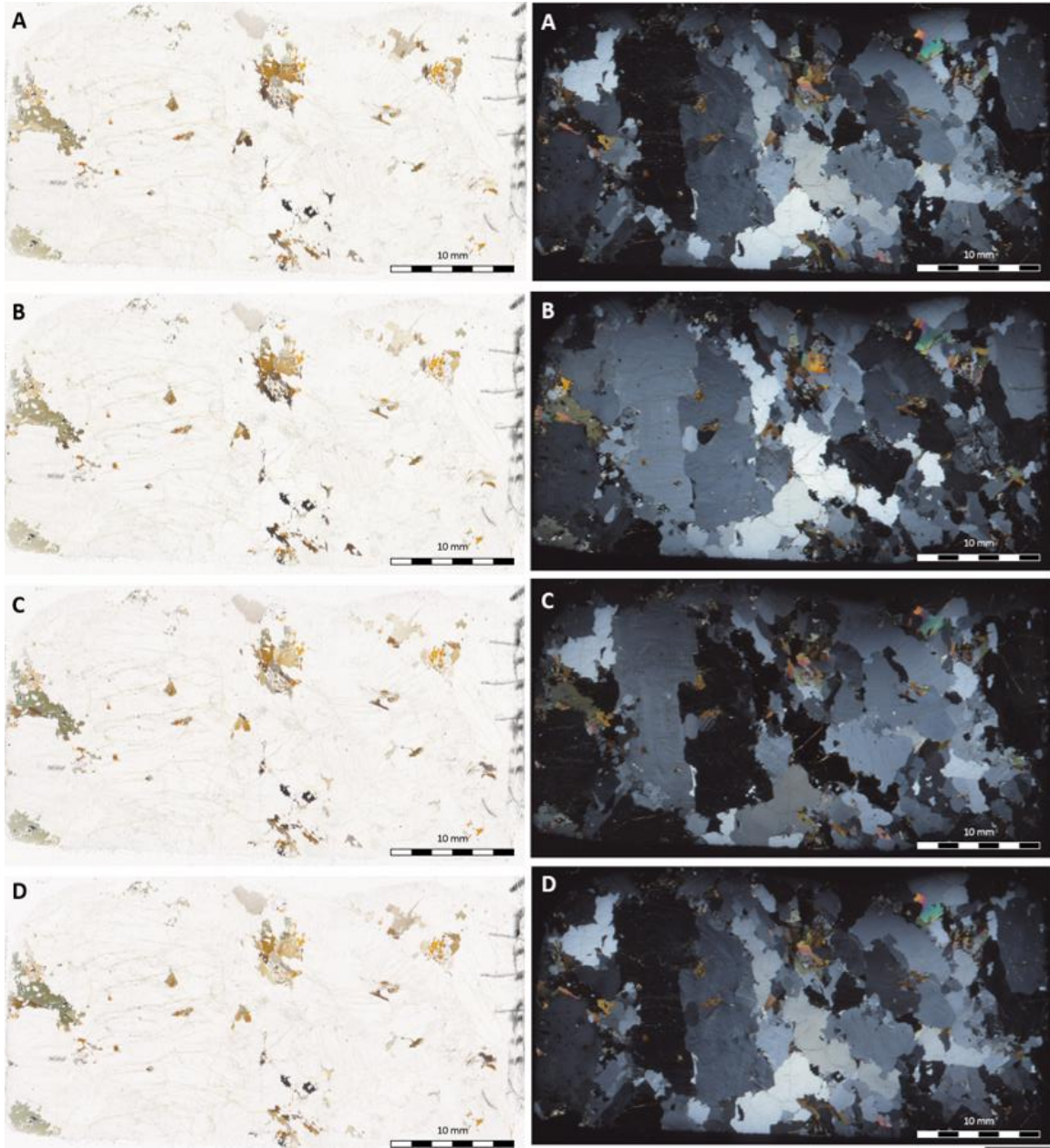


Figure 4.16: Plain polarized light thin section and respective cross polarized region at (A) 0° (B) 30° (C) 60° (D) 90°

The high-resolution imagery required ~11 MB memory space per image. The memory requirement was extremely taxing, resulting in large frame rate drops during VR testing and being inoperable in MR. To regulate the storage necessities, OpenCV (2020) in Python was used to grid and crop every image into 4x4 sequences (Figure 4.17). Each cropped image was then cropped again by a 2x2 grid (Figure 4.18).

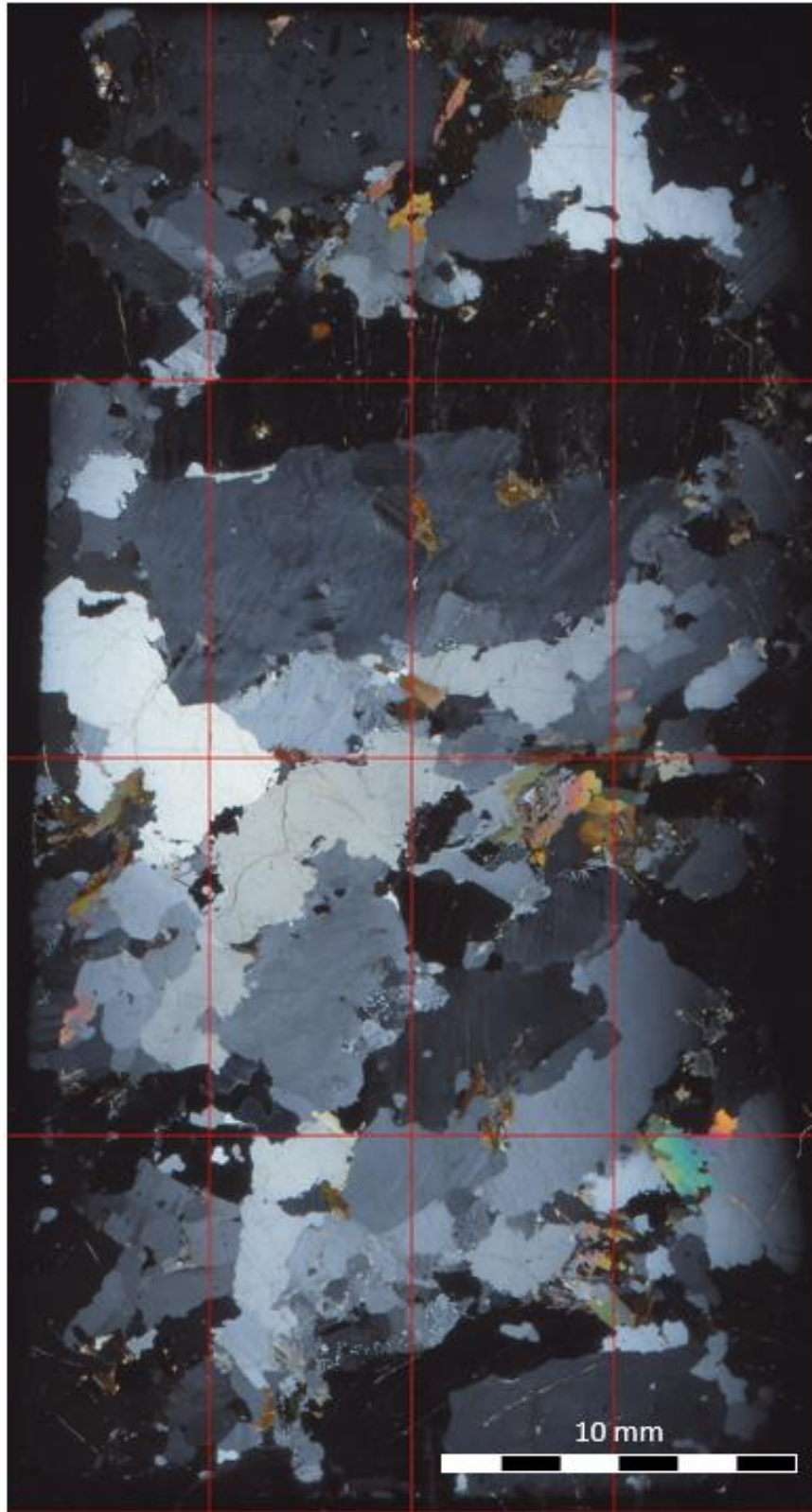


Figure 4.17: Designed thin section broken into a 4x4 grid for cropping purposes

By effectively gridding and cropping each respective image, resolution alteration per zooming sequence was compiled. Each level of image was reduced to ~1 MB. Such reduction allowed users to actively zoom into specific sectors while retaining effective resolution and storage control. By combining the HoloLens external storage within cloud space or designated drivers, selected sequences can be imported into the software with only minor delay. The module was then coded to allow unrestricted 15° rotation and polarization at the user's discretion through a scroll bar adjacent to the holographic thin section (Figure 4.19). The area from where the thin section was retrieved was appropriately indicated as a flag along the core.

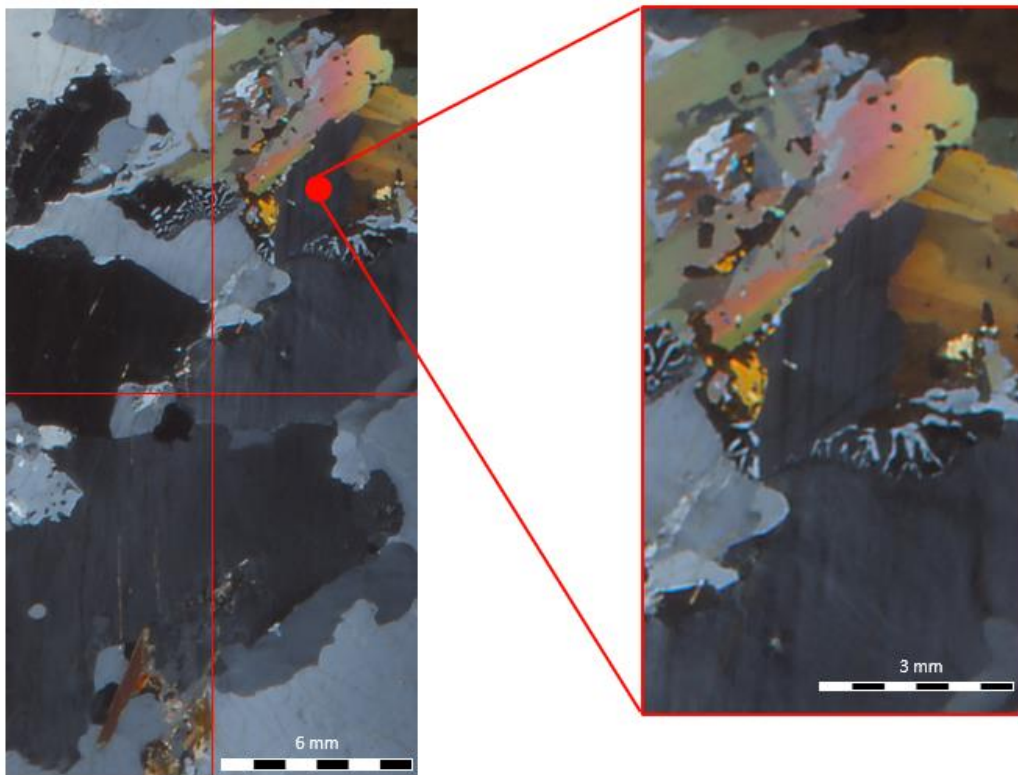


Figure 4.18: Row 3 Column 3 zoomed in and then broken into a 2x2 grid for even more detailed analysis.

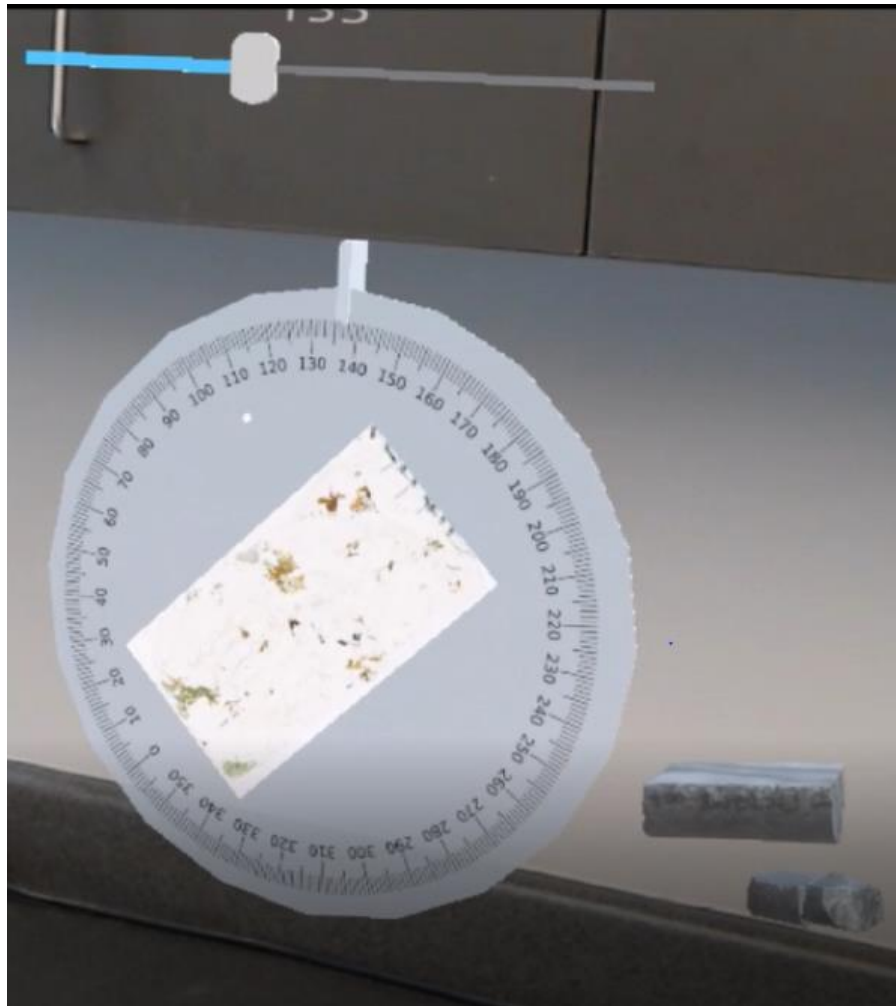


Figure 4.19: Thin section seen through the HoloLens that can be freely rotated by moving the scroller.

4.5. Borehole Imagery in Conjunction with Virtual Core

Anonymized televiewer and FMI data were tested to see whether they could be emplaced within VR and MR environment. Borehole imagery was brought into Unity to permit visual analysis in 3D, unrolled cylinder and azimuthal views (Figure 4.4). The 3D view model was computed to allow scaling proportional to a user's perspective, enabling the user to visualize the results from "inside" or "outside" the borehole in VR and MR (Figure 4.20).

The FMI data investigated also contained raw CSV files which contained discontinuities, bitumen content, lithologies and fracture properties that were derived from the imagery and its respective core. All the CSV files were used to localize information along the model (Figure 4.21); the information imported could then be toggled by the user. Each FMI can also be broken into metre sections for closer VR and MR analysis (Figure 4.22).

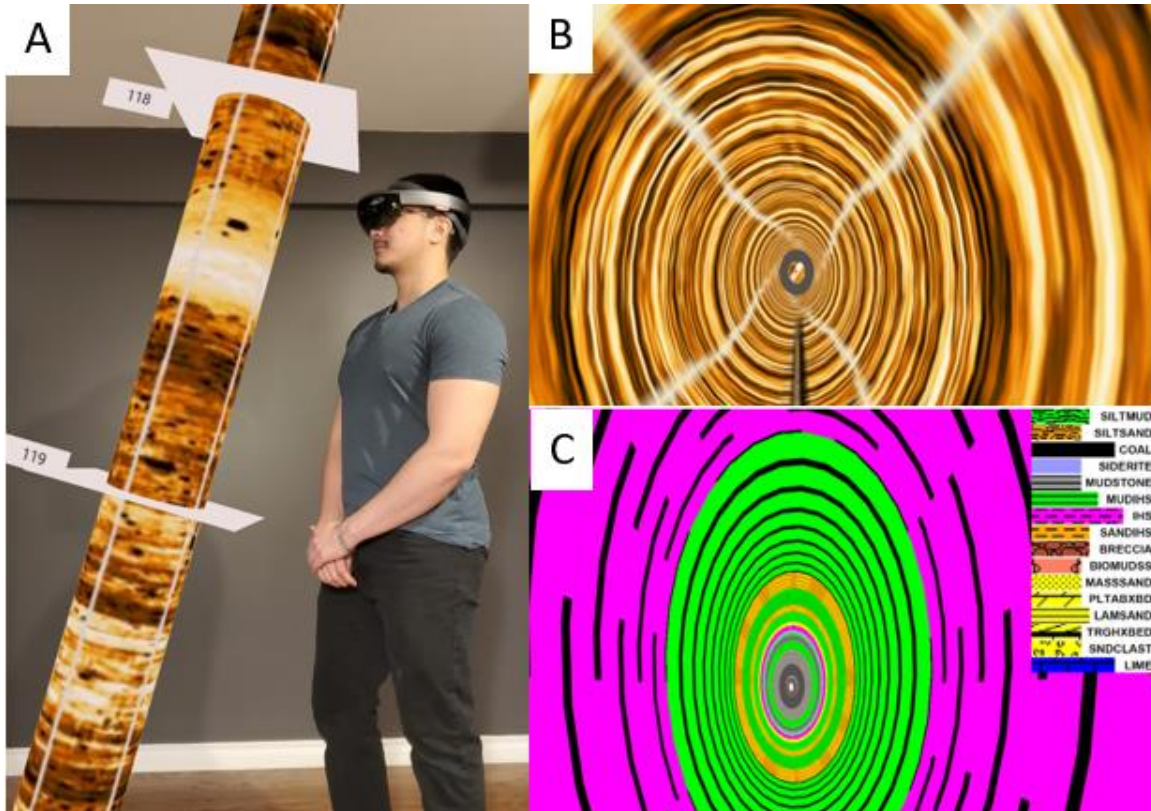


Figure 4.20: Observing borehole imagery in 3D view in (A) MR and (B) VR.

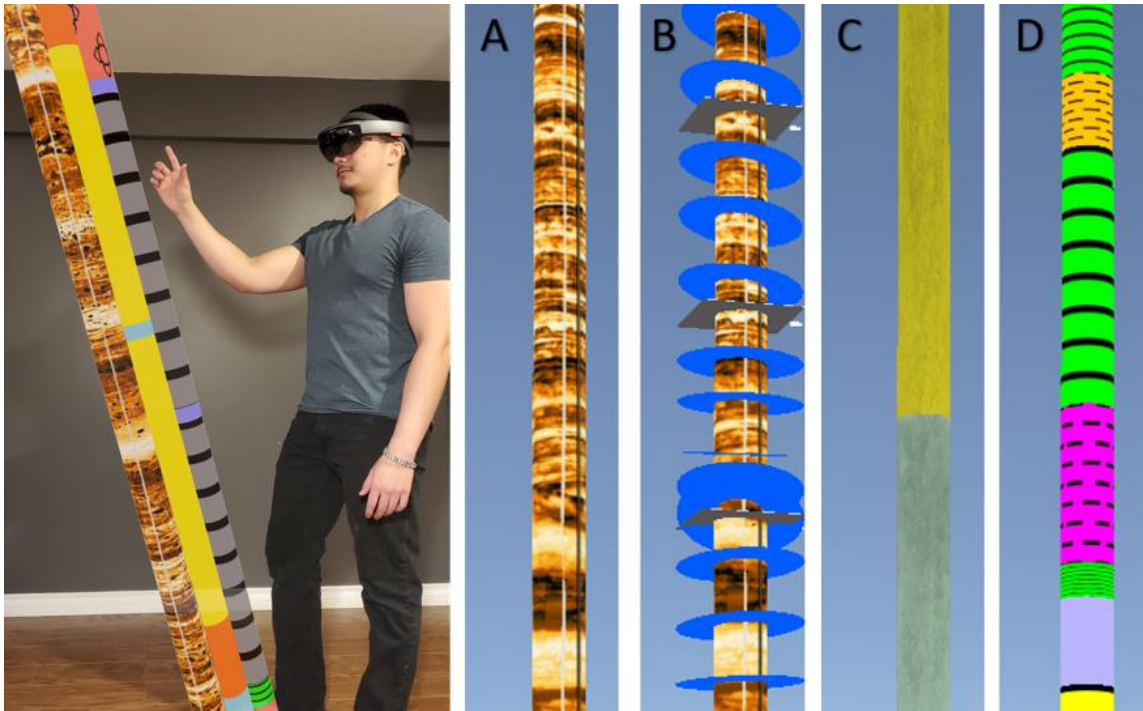


Figure 4.21: 3D FMI MR model (A) Unaltered, (B) Discontinuities with metre breaks, (C) Bitumen content [Light green = No Bitumen; Yellow = Moderate Bitumen], and (D) Lithologies.



Figure 4.22: Analysis of 1 metre FMI segment in MR through Microsoft HoloLens 1.

A virtual core model was then implemented inside of the borehole imagery (Figure 4.23). Since the borehole imagery did not correspond to the scanned core, the example below is presented only as a proof of concept. However, it is evident that by having both respective core model and borehole imagery information, georeferencing of each core piece could be completed by comparing results provided by each input. By having both data sets virtually adjacent to each other improved QA/QC, along with an augmented in-depth analysis (i.e. determining natural versus anthropogenic breaks) is achieved.

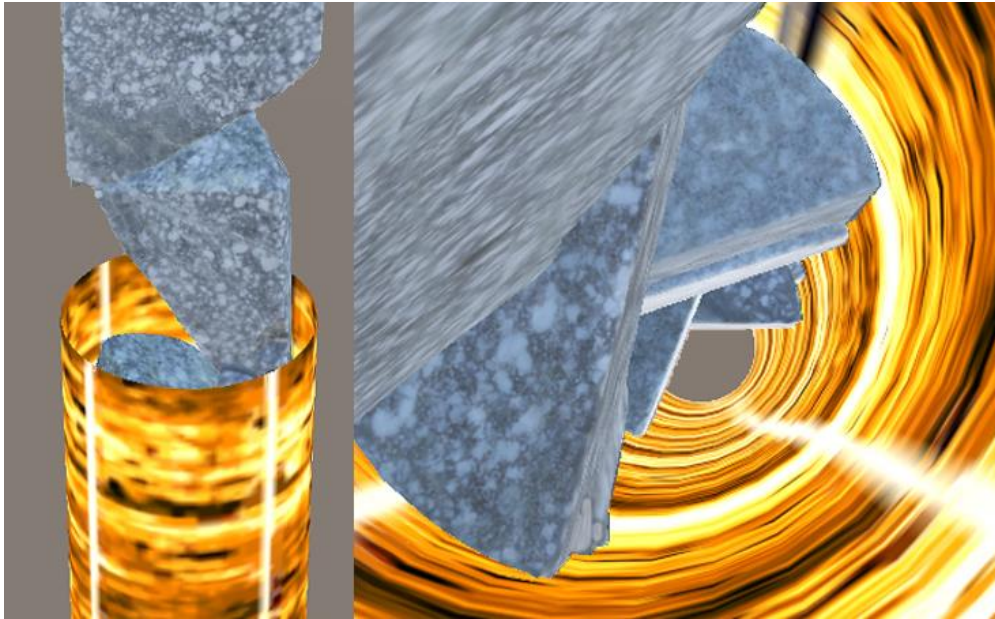


Figure 4.23: 3D FMI model with half core inside it. FMI can be visually toggled.

4.6. XRCoreShack

All three core models were then brought into a single hub simulation, named XRCoreShack. The workflow required to make XRCoreShack operational is shown in Figure 4.25. The most important step is determining whether the target can be scanned in 3D. Depending on the type of scanning (e.g. 2.5D vs. 3D), different methodologies must be used. Once scanned, all the results must be placed into respective folders, and XRCoreShack automatically assigns its UI. Users must then choose which XR methodology they would like to use to observe the results.

4.6.1. XRCoreShack in MR

Due to MR restrictive hardware, only a limited amount of data can be brought into the HoloLens. The MR strand of XRCoreShack, thus, initiates by prompting the user to designate the specific core boxes that need to be imported. Each box that is successfully imported into the HoloLens is automatically linked to the applications UI interaction (Figure 4.24).



Figure 4.24: XRCoreShack MR automatic UI interlinked to every core box imported into module. (A) Shows how hologram can be moved at a user's discretion. (B) List of sites that were available for scanning. (C) User is notified if the specific core box was not scanned or imported.

Core boxes that are successfully imported are linked to an array of different visual interaction for core assessment including:

1. View Continuity: The core can be assessed as a single continuous object that accounts for surveying references, enabling a complete 3D drill hole representation (Figure 4.27A). The whole model can then be moved up or down at a user's discretion. If multiple core boxes for the same region are imported, all boxes can be observed as continuous object.

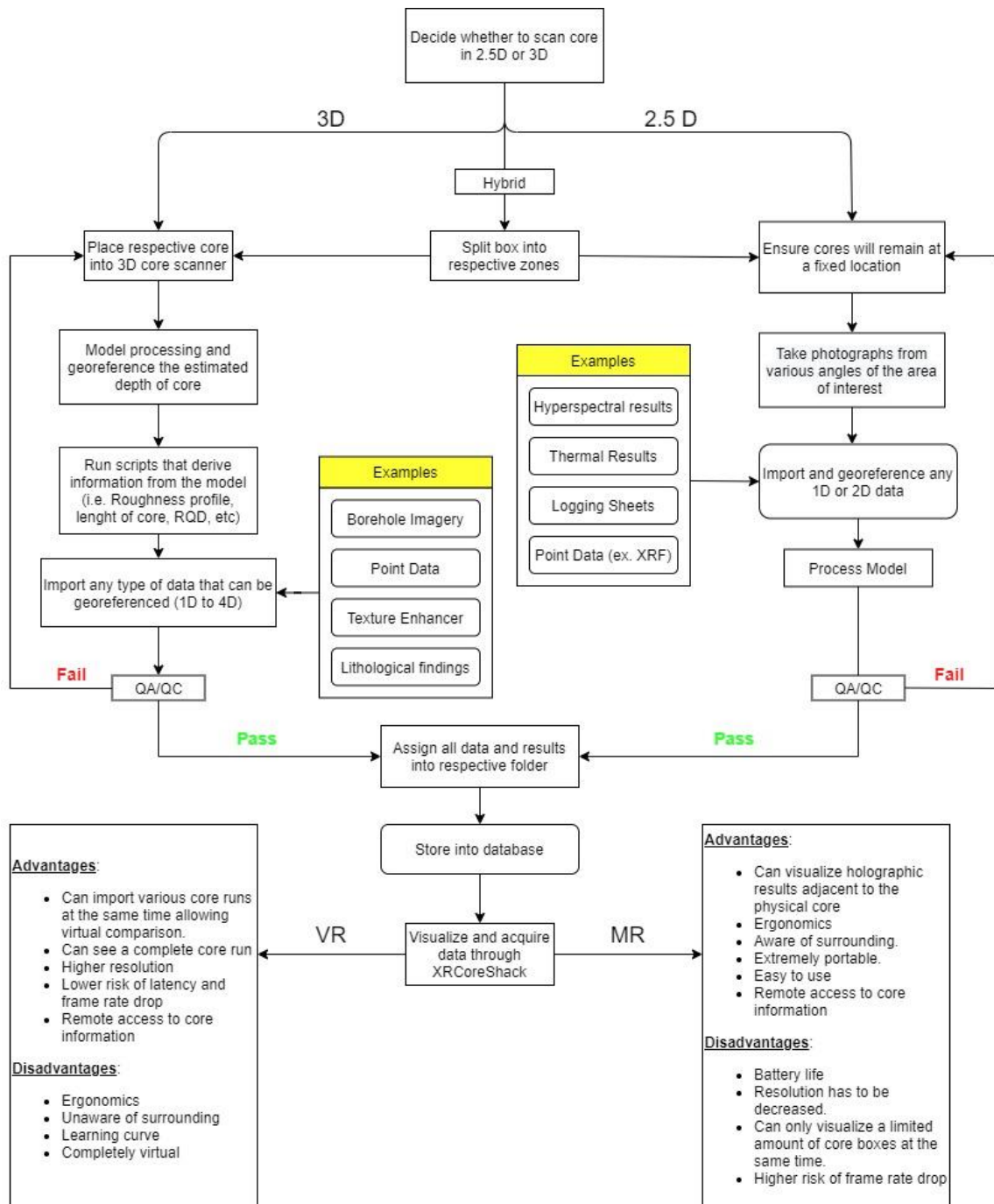


Figure 4.25: XRCoreShack required flowchart

2. Hand draggable: Allows a user to scale, move, and rotate the whole core box model to a desired setting. If the core samples are scaled, the user is informed of the value (Figure 4.27B).
3. Extract core: Moves each individual row up by a predefined scalar distance and rotation. This was completed to allow the user to quickly grab the desired sample (Figure 4.27C).
4. 2.5D or 3D: Toggles the model between 2.5D representation and 3D representation (Figure 3.19 and Figure 4.27D). All other 3D interactions are toggled off during 2.5D analysis.
5. Remove Box: Toggles representative wooden box on and off (Figure 4.27E)

Low RQD areas and portions that could not be scanned are portrayed as red cylinders that have UI interactions. Once clicked, each cylinder independently toggles a corresponding 2.5D representation of the core interval and makes available a collection of representative photographs that can be scrolled through (Figure 4.26). Both representations can also be moved, scaled and rotated freely.



Figure 4.26: Low RQD value regions that were unable to be scanned are represented by red cylinders. If the user clicks on the cylinder it will show a representative 2.5D of the region and collection of representative images that can be scrolled through.

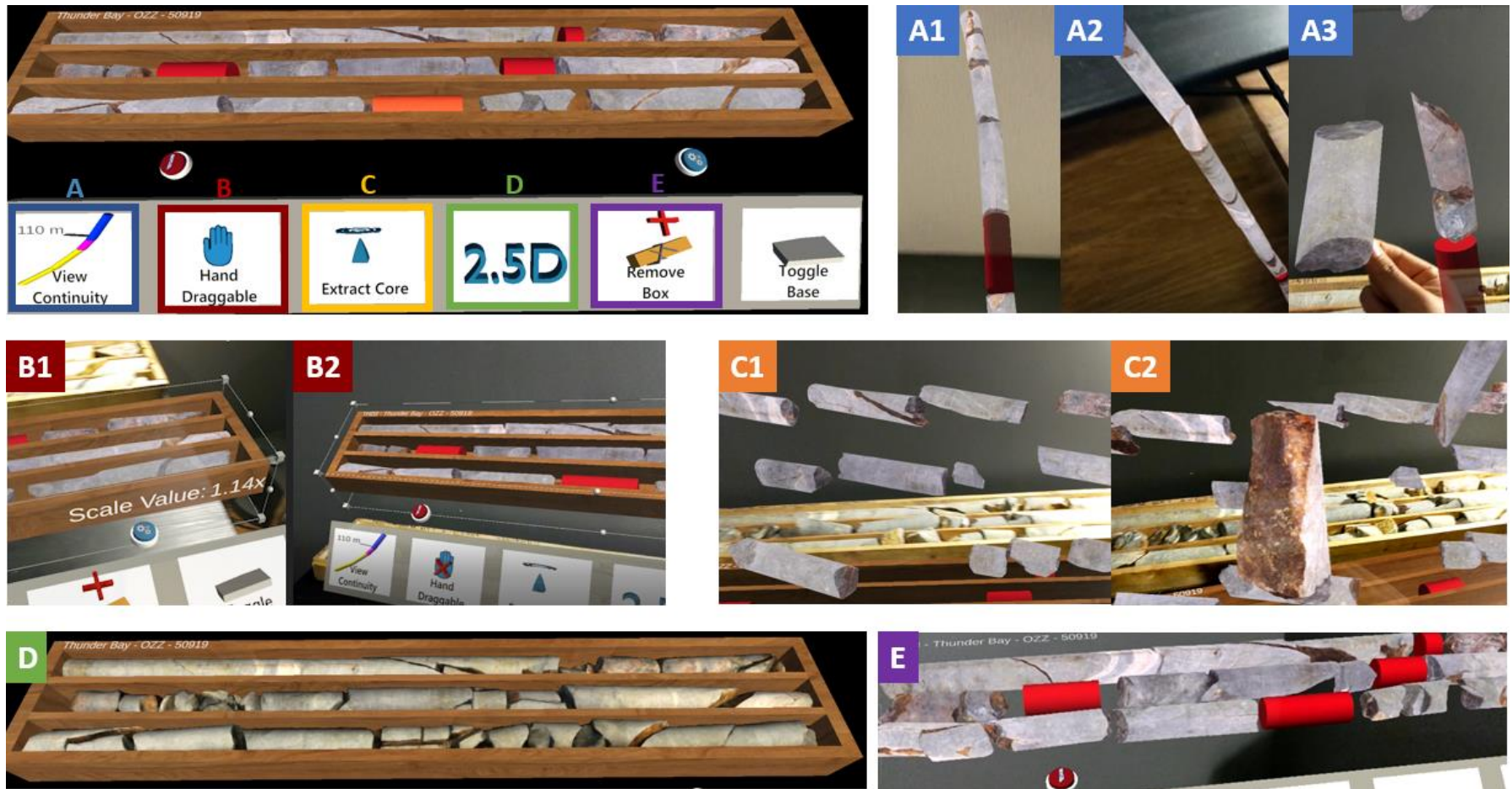


Figure 4.27: Automatic UI interface assigned to every single box in XRCoreShack toggled through setting button. (A) Observe the core box as a single continuity that takes into account surveying, each sample can still be grabbed individually. (B) Hand draggable enables rotation, movement and scaling of the whole model. Scaling degree is stated adjacent to the box. (C) Extract all rows to a predetermined height and rotation. (D) Observe model as a 2.5D model. (E) Toggle box.

Using the diverse hand interaction capabilities of the HoloLens 2, another submenu is displayed once the user shows the palm of their hand thereby minimizing visual cluttering. This submenu can also be dragged, dropped and scaled at user's discretion. The submenu capabilities include description of the sample, texture manipulation, and returning all samples back into their respective zone.

With the samples being completely digitized, the opportunity to assess core remotely is possible. Referencing all 3D scanned cores prior to importing to Unity allows referencing of each sample to a specific CSV file hosting the logging information (Figure 4.28). A user can then “flag” any improper observation by pressing the flag icon that is displayed on the description tab and the appropriate CSV file will be indicated. Other information that is hosted on the “description tab” includes the automated length derived from scanning (Figure 3.23).

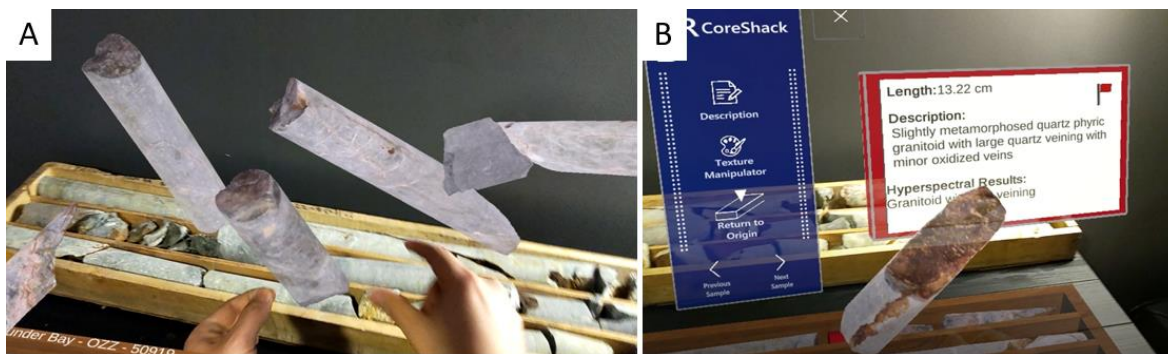


Figure 4.28: XRCoreShack MR (A) Examination of selected samples at the same time at different core box locations without potential misplacement (B) Description tab shown once submenu description is clicked. Information shown is derived from a CSV file and can be flagged for future QAQC.

Once the application is rebooted, all “flagged” samples are highlighted allowing referencing and reassessment. The use of flagging facilitates remote real-time core examination by multiple users. Virtually hosting 3D core data has become easier with Microsoft Mesh (Langston, 2021), which allows multi-platform and multi-user integration within XRCoreShack MR.

Since all core samples were digitized, 3D texture manipulation can actively be juxtaposed to accentuate textures that are not clearly visible with the naked eye (Figure

4.29). Different filters can be used; filter efficiency depends on the specific lithological and structural attributes of the core. With the lens-flip capability of the HoloLens 2 users can rapidly return to un-aided visualization to conduct other operations such as hand-lens analysis without requiring physical removal of the hardware (Figure 4.30). By analysing virtual and physical core contemporaneously, core analysis can be synergized.

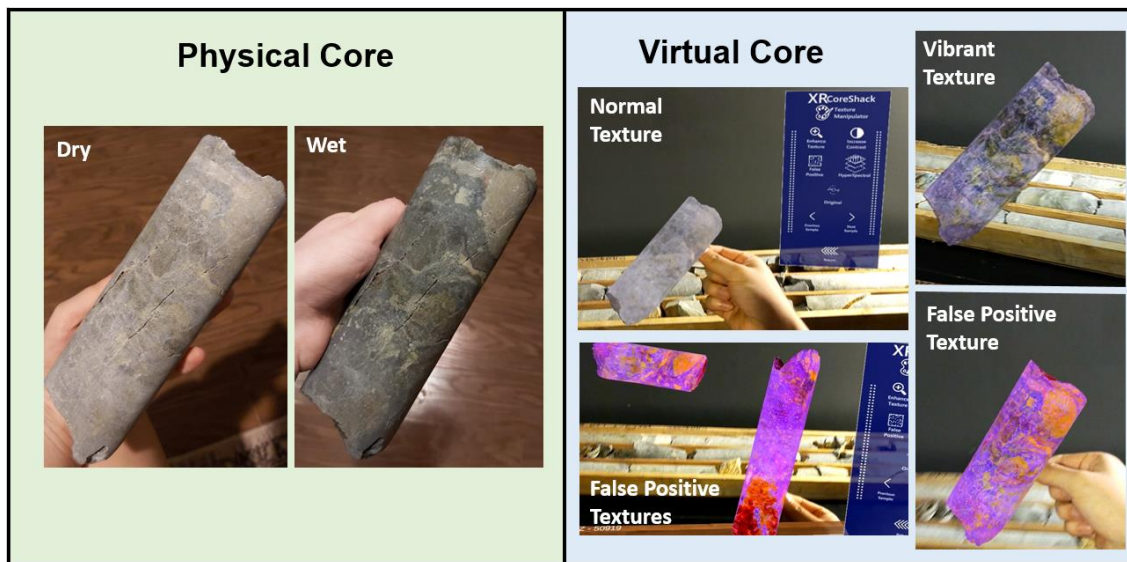


Figure 4.29: Physical core while dry does not display textures effectively. Once wet some textures become prominent but not as clear as when using virtual core texture enhancers such as false positive. Texture enhancers can be applied to all digitized samples



Figure 4.30: Contemporaneous assesment of physical and digital core allows more in-depth analysis of the physical core through standard logging practices.

4.6.2. XRCoreShack in VR

To assist future projects, a VR foundation was designed that allows for a large quantity of core boxes to be scanned and then observed simultaneously (Figure 4.31). As expected, the VR approach has higher resolution and storage capabilities but requires the user to adapt to the unnatural experience of being immersed in a virtual environment.

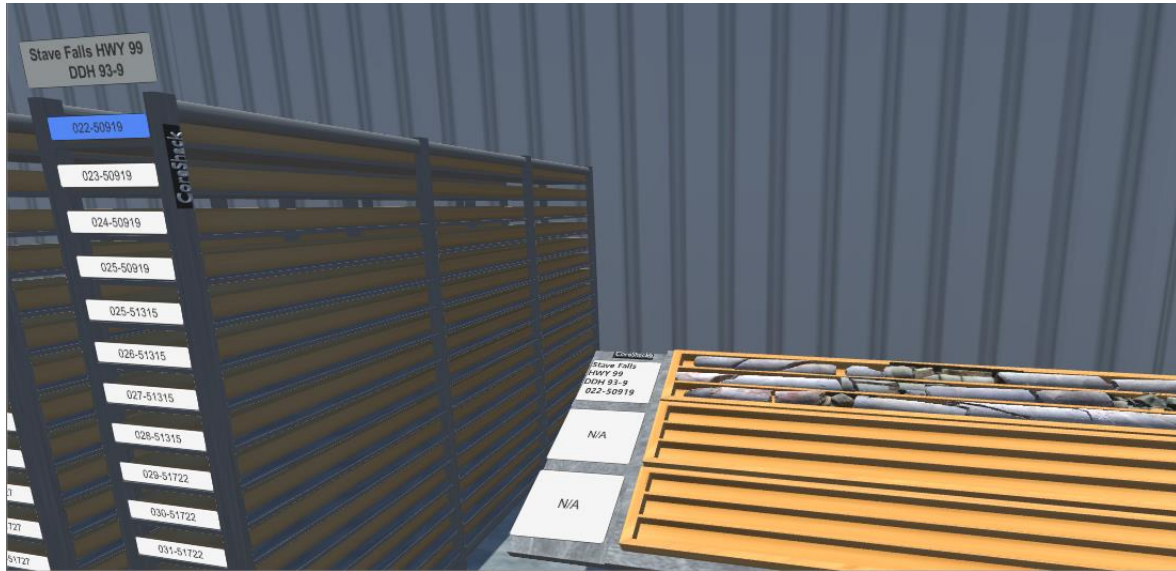


Figure 4.31: XRCoreShack in VR. Core boxes can be scanned and imported into the platform. Samples from different boxes can be directly compared to each other.

4.7. Discussion and Conclusion

Retrieving comprehensive core data is a mandatory process that significantly influences the reliability of mine and engineering design, inherently affecting economic and risk assessment. Lack of coherent data generates future expenses from reassessment of design, re-examination of cores, and preventable drilling projects.

To avoid impractical and incorrect core information, new practices such as hyperspectral scanning, borehole scanning, and geophysical analyses have been developed. Integrating such multi-sensing procedures, however, has become a major challenge in the mining industry (Esmaili, 2020). Lack of conventional core logging procedures,

within new practices, promotes various peers to refute new mediums due to the susceptibility of “black box” geological and engineering classification.

Through rapid development of XR platforms and the previously described in-house 3D core scanner, a new route to combine new and old practices through physical-like overlay of complex numerical analyses was investigated. Quantifiable and visual datasets tested and anchored along the virtual core include thermal, hyperspectral and borehole imagery. It was evident that by digitizing drill core fast, remote and auditability of cores within an office setting or in association with peers is achievable.

By importing various data types within a single hub, improved results can be obtained, avoiding the reliance on a single dataset acquisition which poses high risk of misinterpretations and biased information (Acosta et al., 2019; Roonwal, 2018; Tusa et al., 2019; Krupnik & Khan, 2019; Esmaili, 2020). With in-depth examination of multiple georeferenced datasets along the virtual samples, geologist/engineers can improve designs and avoid inadequate reporting commonly associated with unaided core analysis.

A dataset that was examined in detail focused on petrographic analysis. A new platform that allows thin section observations every 15° in both polarized and unpolarized light was developed. Reliable records of thin section at different stage rotation angles and polarization provide an auditable channel in case the real sample is damaged or misplaced. The module can also be focused on educational purposes as specific mineral grains and regions can be highlighted effectively. To significantly improve the thin section model, images could be taken at every 1° to improve petrographic observations. The virtual petrographic hub is not seen as a replacement for current methodologies, as it lacks the capability of important tests such as reflectance indices. Rather, it provides a novel reviewable medium that can significantly advance single image acquisitions commonly observed to date. The region that the thin section was retrieved from is also marked along the respective core. By indicating the locality of the thin sections, deciding whether the thin section is truly representative of the unit is possible.

In contrast to investigating micro- and nano- scale observations, large scale 3D data was also holographically visualized through borehole imagery. A combination of televiewer data with core observations has been previously investigated and has proven to be

extremely valuable (Gwynn et al., 2013). Borehole imagery within XR allowed a user to observe inside the borehole in VR or externally as a virtual object. The ability to assess imaged in-situ structures adjacent to the equivalent mined rocks helps delineate healed fractures, open discontinuities or anthropogenic damage. Since physical core is the most reliable indicator and method of characterizing fractures in the subsurface, it should be included when deciphering fractures along a borehole image (Fernández-Ibáñez et al., 2018). By applying different media to assess structures, reliable and representative core data can be obtained. Parameters such as computed sinuous fits within borehole imagery can then be marked with higher confidence as acceptable, partial, noise, or negligible improving borehole quality data (Cruz et al., 2017).

Complex holographic core permits management and evaluation at different scales and settings. To organize the model in a more effective manner, virtual cores were hosted in a visual database that was named XRCoreShack. Cataloguing the samples allowed direct comparison of spatially differentiated boxes with no risk of misplacement. In conventional practices, direct comparison is usually not recommended as it poses risk of mixing samples (Roonwal, 2018). However, by directly comparing samples from different locations, differentiation of higher abundance of specific phenocrysts, alteration or fracture abundance can be made with higher detail. By deviating from broad generalization, deeper spatial understanding of rock alteration and mineralogical changes can be achieved.

During the development of XRCoreShack, the limitations of the HoloLens were evident. With exponential improvement in hardware and software, these restrictions are only seen as temporary, and thus, some features although removed from the final model remain available as background scripts for future use. The beneficial ergonomics of the HoloLens, its user friendliness and spatial awareness capabilities make it extremely appealing for geological practice.

Holographic core offers innovative and unique core evaluation capabilities. Its' use can improve both safety and QA/QC procedures as it supports discussion between multi-users of varied experience and background. The availability of holographic core can reduce the costs required for traveling to remote core sheds and allow remote access to core data in an office/boardroom environment. By emplacing core results spatially along virtual core, all levels of management will have more control and access to a suite of

results. XRCoreShack is not envisaged as a replacement for conventional core logging practices as it is unable to measure physical properties required. However, it does permit an auditable platform that can be thoroughly reviewed, refining vital core data. By superimposing computationally derived information spatially within an ergonomic new platform that combines both physical and virtual information, both new and old core logging practices can be interlinked smoothly.

Chapter 5.

Geovisualization of Induced Subsidence at LKAB Kiirunavaara Mine, Sweden

5.1. Introduction

Kiruna, also known as the Kiirunavaara mine, is located in the sub-arctic northern part of Sweden (Lat° 67 50.9; Long° 20 11.7') and is currently the largest underground iron mine in the world (Figure 5.1) (Mining Technology, 2020). It has been operated by Luossavaara-Kiirunavaara Aktiebolag (LKAB) mining company for over 100 years and has mined more than 1.3 billion tonnes of ore (Andersson & Rutanen, 2016). It transitioned from open-pit mining to underground workings in 1952 because the ore became too deep to effectively operate (Mäkitaavola et al., 2016)

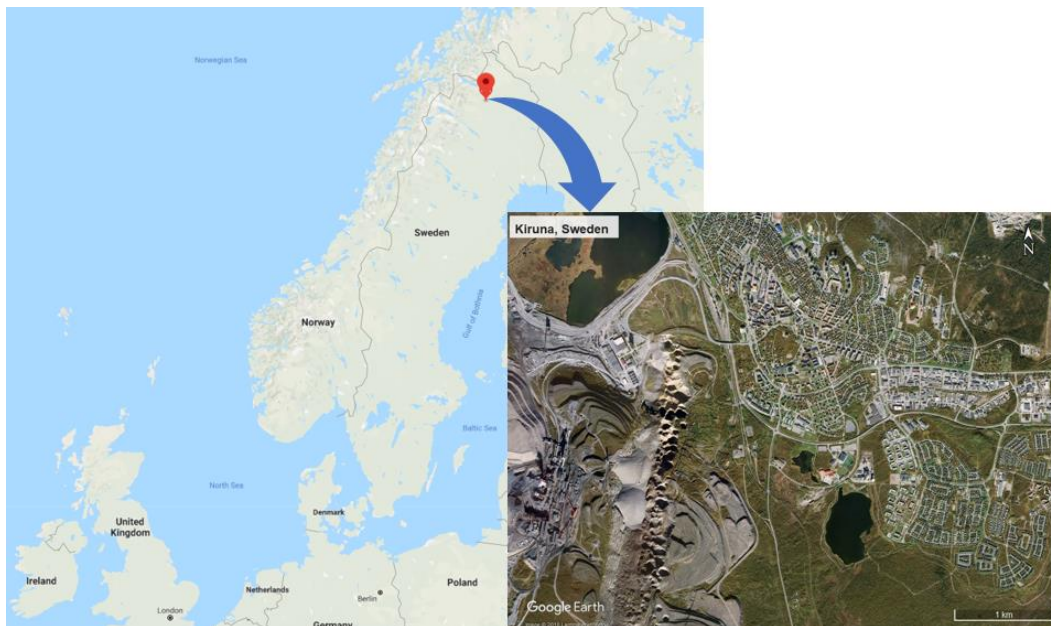


Figure 5.1: Location of LKAB Kiruna mine (Extracted from Google Earth (2021b)).

The steeply dipping competent host rock and ore favoured sublevel caving as the optimum mining procedure. As expected, the progressive non-backfilling caving approach has caused Kiruna's topography to drastically change over the years (Figure 5.2, Figure 5.3).



Figure 5.2: Kirunavaara drastic topographic change from 1920 to 2005 (after Hämäläinen & Furbeck, 2011) [Used with permission].

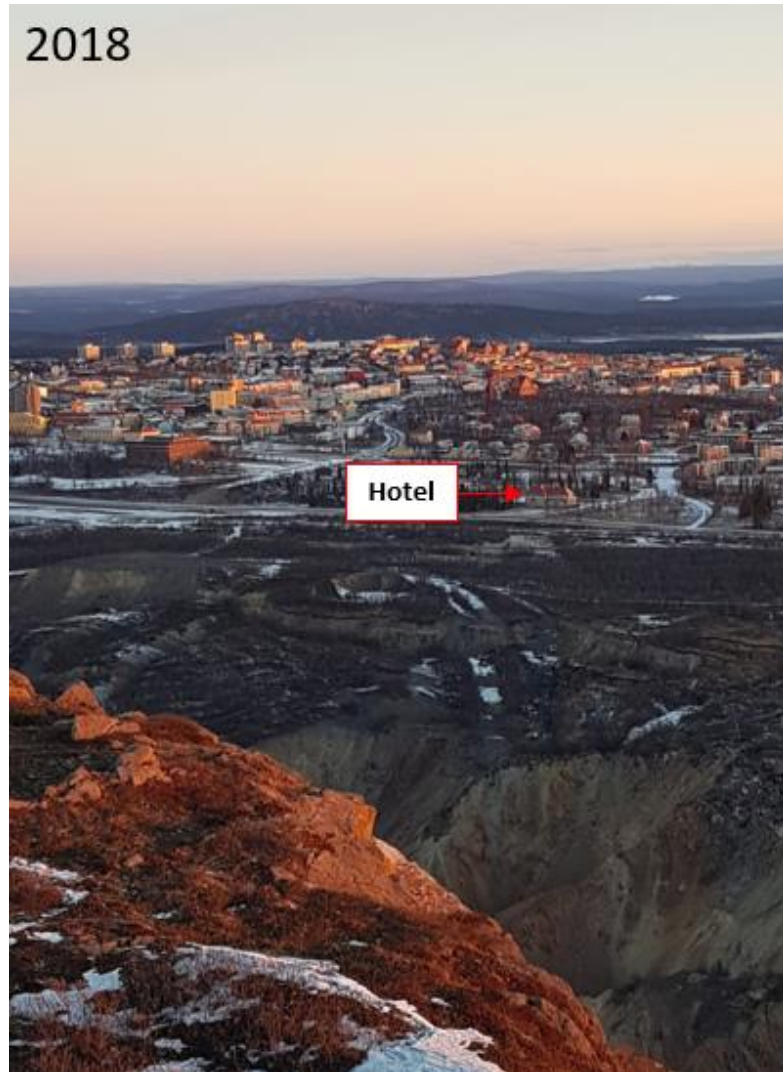


Figure 5.3: Kiruna city observed from mine site lookout point on 2018.

LKAB have installed a world-class monitoring system to ensure maximum safety for both residential and employees' wellbeing. Successfully monitoring the extent of deformation has generated a dynamic boundary that only authorized personal can enter. Any infrastructure enclosed by it (e.g. the city hall, railroads, hotels and various houses) have been relocated (Stöckel et al., 2012). The implications have bestowed significant urban transformation and the testing of new mitigation methodologies that can improve current mine monitoring practice such as InSAR and microseismic analysis (Hämäläinen & Furbeck, 2011; Mäkitaavola et al., 2016).

The wide array of installed monitoring ground deformation methods has led to challenges in data visualization, communications, interpretation, and interlinking of data throughout the years. These issues have progressively become more complex and of increased importance as larger data quantities and interpretations are encountered. With the considerable remaining mine life, optimizing of data analysis and communication is of increasing importance as it affects a wide range of mine personnel and stakeholders.

Since the virtual paradigm has been proven as a conduit for improved communication and visualization, a large-scale mine VR/MR model has been developed as part of this thesis to visualise the LKAB mine site. By juxtaposing and coalescing various data sets within a holographic medium, clarification between peers at different levels can be achieved.

5.2. Background Information

5.2.1. Sublevel Caving

Sublevel caving (SLC) is an underground mining method that involve the extraction of a steeply dipping orebody at regular intervals. The infrastructure is symmetrically constructed by cutting parallel drifts either along or across the ore body with vertical breaks that are approximately 12-35 metres per drift (Shekhar et al., 2017). Blasting starts at the hanging wall and slowly retreats towards the footwall, encouraging gravitational force as a primary driving force (Atlas Copco, 2007).

Mined ore is not backfilled, resulting in ground subsidence at the surface predominantly in the hanging wall but also evident above the foot wall (Brady & Brown, 2006; Hamrin, 1982; Villegas, 2008). (Figure 5.2 -Figure 5.4). Mining induced subsidence differentiates from naturally occurring subsidence as it is usually faster, sometimes promoting significant movement through the reactivation of discontinuities (Borchers et al., 2014). To prevent unforeseen structural failure, continuous caving is essential (Hamrin, 1982).

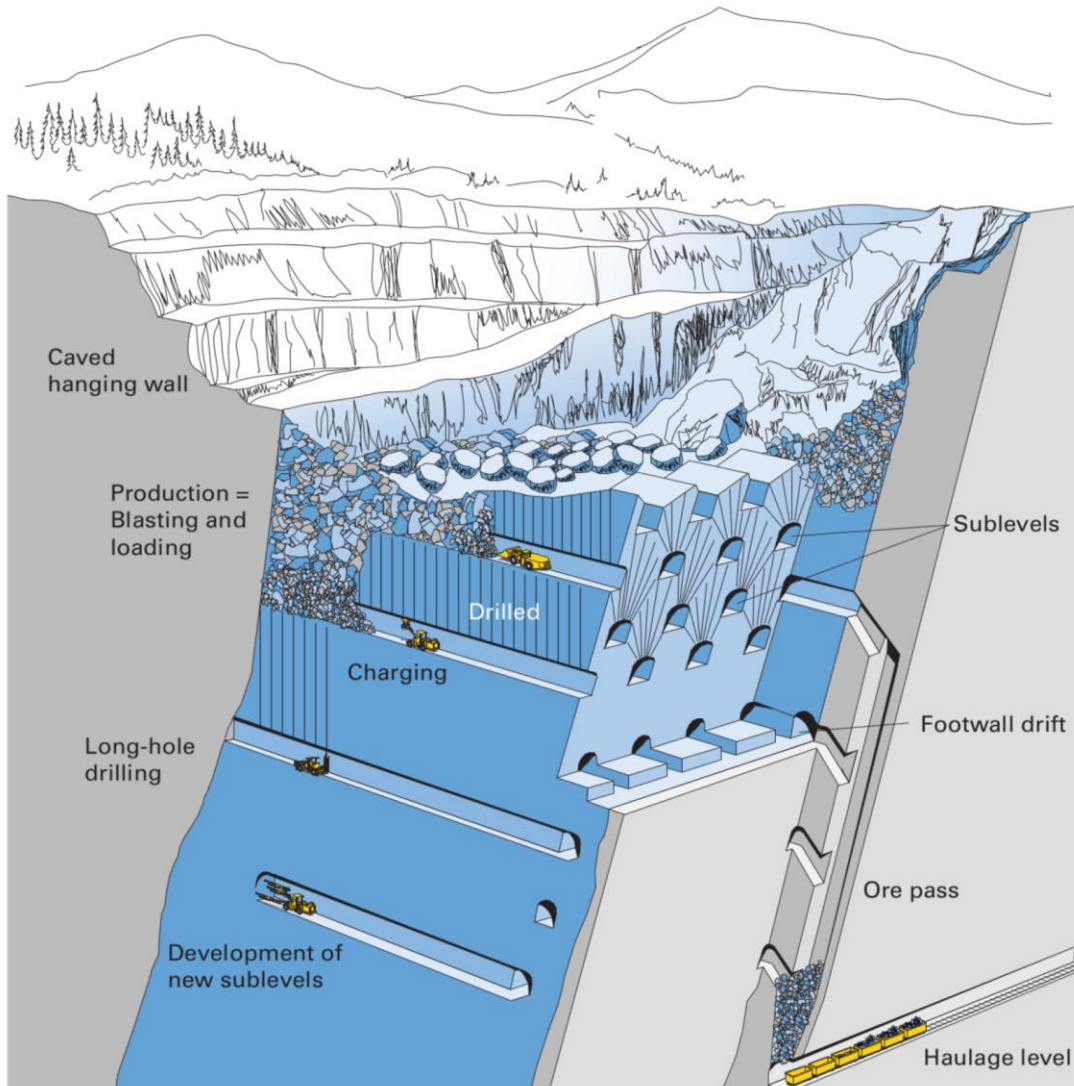


Figure 5.4: Standard Sublevel Caving layout (Atlas Copco, 2007).

5.2.2. Subsidence

Subsidence refers to the sinking of the surface relative to a stable reference point that results from underground resource extraction (Doornhof et al., 2012). Ensuring consistent monitoring of known deformational regions is crucial as major side effects including significant topographical alteration, activation of inactive geological structures, infrastructure deformation, flooding, environmental damage, and economic issues can occur if unmonitored (Harrison, 2011).

Subsidence management is possible due its diagnostic “bowl” shape that can be broken into two major deformation zones known as the continuous and discontinuous deformation zones (Figure 5.5) (Villegas, 2008).

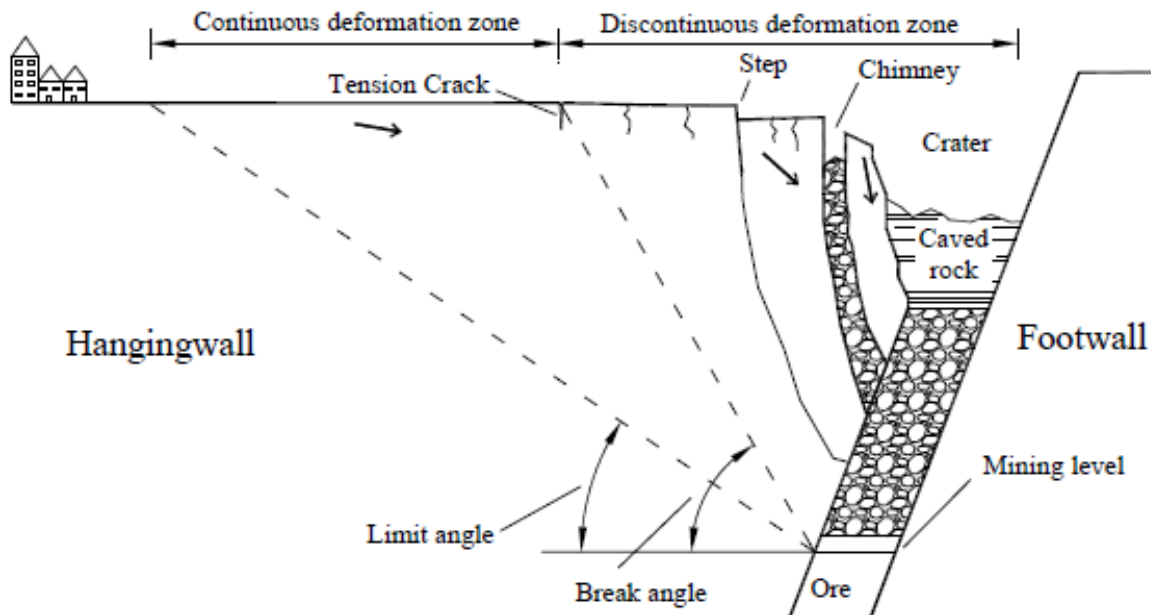


Figure 5.5: Sketch of discontinuous and continuous deformation zone expected in sublevel caving mines (Villegas, 2008) [Used with permission].

5.2.2.1 Continuous Deformation Zone

Deformation in the continuous zone occurs smoothly and is generally more predictable. The zone can be described by the limit of subsidence, limit angle, and critical profile (Figure 5.6). The limit of subsidence is the position where there is zero vertical displacement. The limit angle (also known as angle of draw) is the angle between the limit of subsidence and the edge of the subsurface extraction zone. The critical width is the width in which the vertical displacement is effectively zero. The point at which the limit is reached is proportional to the mining depth and the angle of draw (Harrison, 2011; Holla & Barclay, 2000).

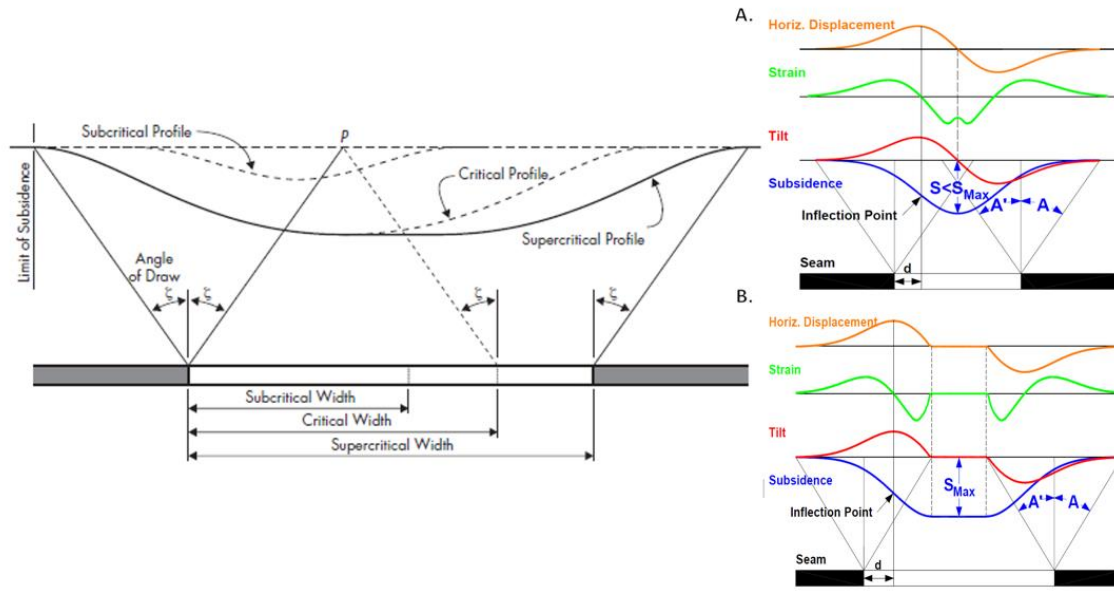


Figure 5.6: Continuous subsidence sketch with diagnostic portions (Modified after Harrison, 2011; Holla & Barclay, 2000). (A) Subcritical profile showing horizontal displacement, stress, and tilt proportional to the extraction amount. (B) Supercritical profile showing the same parameters proportional to a larger extraction width.

Continuous zone deformation stages can also be inferred by three consecutive stages known as regressive, progressive and steady state creep (Zavodni, 2000; Hamdi et al., 2018). The regressive stage encompasses an elastic response of the rock mass to mine excavation that slowly becomes displaced. The progressive stage is characterized by an inflection point, in the time-displacement plot, that identifies an acceleration of the displacement. Formation of tension cracks, and the critical vertical displacement is also intersected. The third and final stage (i.e. steady state creep) is met beyond the critical point, where ground surface moves rapidly at a constant velocity to a super critical profile (Harrison, 2011; Holla & Barclay, 2000; Hamdi et al., 2018).

Such a continuous subsidence bowl profile is more common in areas that have laterally extensive extraction (e.g. longwall coal mining) (Harrison, 2011). SLCs tend to have sharp abundant discontinuity boundaries that serve as interfaces that limit deformation (e.g. foot wall vs. hanging wall), making deformation prominently discontinuous (Villegas, 2008) (Figure 5.5).

5.2.2.2 Discontinuous Deformation Zone

The discontinuous deformation zone is largely controlled by planes of weakness such as faults, discontinuities, and/or veins that can serve as dislocations in the rock mass that allow large offsets as stresses and strains redistribute along them (Brady & Brown, 2006). The degree of displacement magnitude varies depending on their characteristics. These factors, combined with extensive brittle fracturing of intact rock, make modelling and forecasting for the discontinuous deformation zone inappropriate for the application of generic empirical subsidence engineering approaches and thus, geomechanics principles must be applied for each individual case (Harrison, 2011).

Correct modelling requires informative data on discontinuity orientations and characteristics (e.g. roughness, persistence, spacing) at both large and small scales (Villegas, 2008). In SLC, most subsidence effects are seen above the orebody hanging wall, with the extent of the subsidence area progressively increasing with mining depth (Brady & Brown, 2006). Various methods of failure can occur along the discontinuous deformation zone ranging from toppling of persistent subparallel discontinuities with respect to the ore body to planar failure along sliding surfaces (Figure 5.7). Extensive geotechnical rock investigation must be conducted to statistically assess the probability and extent of brittle fracture (Cumming-Potvin, 2018). To ensure that the subsidence model is representative of the site, detailed surface and subsurface monitoring is required.

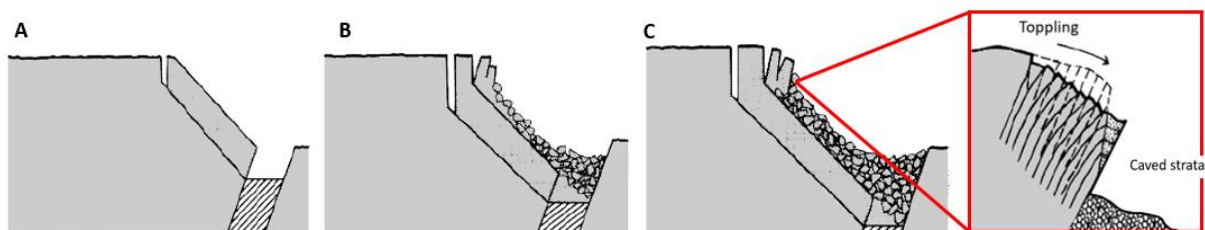


Figure 5.7: Simplified progressive sequence of failure as depth of SLC increases: (a) Initial open pit mine walls fails through bi-planar or wedge failure (b) Failure surfaces and tension cracks develop (c) Continuous development of tension cracks and failures surfaces as mine depth increases. Steeply dipping subparallel discontinuities along the hanging wall strata fail through toppling (Modified after Brady & Brown, 2006; Hoek, 1974).

5.3. Geological and Structural Characteristics Within Kiirunavaara Mine

To effectively mine using SLC methods, several requirements should be met, including: (1) dilution of ore should not be excessive, (2) the ore and host rock are competent, (3) the ore body must be at a significant dip angle, (4) an extensive deposit should exist, (5) minimum hydrological fluctuation exists, and (6) effective fragmentation should be achieved (Brady and Brown, 2006; Shekhar et al., 2017). The dimensions of the tabular Kiruna orebody (4.5 km length, and >250 metre) combined with a depth of more than 1.9 km has made SLC the most suitable approach for mining. Understanding both structural and geological characteristics of the area surrounding the mine is important for understanding surface subsidence.

5.3.1. Geology of Kiirunavaara and Current Mine Works

The ore body at Kiruna is characterized by high iron abundance with magnetite and hematite being the primary mineralized ore. Other iron minerals such as Fe-rich apatite, amphibolite or pyroxene are abundant (Geiher, 1931; Martinsson, 2004). The type of ore is diagnostic by the magmatic and/or hydrothermal mechanism that host abundant iron-oxide apatite (Edfelt, 2007; O. Martinsson, 2004). The peculiar elemental setting has resulted in the precipitated ore setting being classified as its own ore deposit known as “Kiruna type” (Geijer, 1931).

Kiruna type deposits are commonly found in intracratonic basin tectonic settings but have also been found within subduction zones (Frietsch & Perdahl, 1995). Kiruna type formations are associated with alkaline to sub-alkaline magmatic rocks within large fault systems. Partial melting of the old basement rock promotes alkaline-subalkaline and iron-phosphorous bearing magmatic hydrothermal melt to become precipitated concordant to structural conduits that favour inflow. Such large intra-continental requirements explain why only large Kiruna type deposits are found (Frietsch & Perdahl, 1995). The age range of Kiruna type deposit ranges significantly from Paleoproterozoic (e.g. Kiirunavaara ~1.8 Ga) to Pliocene-Pleistocene (e.g. El Laco Mine ~1.6 Ma) (Edfelt, 2007; Frietsch & Perdahl, 1995) (Table 5-1).

Table 5-1: General characteristic of Kiruna type ore setting (Apatite Iron Ore) after Edfelt (2007).

Main Features	Apatite Iron Ore (Kiruna Type)
Age	Paleoproterozoic to Pliocene-Pleistocene [Ex. Kiirunaavara, Sweden and El Laco, Chile]
Tectonic Setting	Emplacement of regional fault zones within intracratonic setting or subduction zones
Host Rock	Calc-alkaline to alkaline volcanic rocks (intermediate to felsic) [Andesite to rhyolite]
Mineralogy Alteration	Magnetite-hematite and apatite-actinolite-diopside. Calcite may also be present Albitization, silification, sericitization, epidotisation and minor carbonate/actinolite. Local alteration is more abundant than extensive.
Ore Genesis	Magmatic intrusive-extrusive, and/or hydrothermal replacement from magmatic fluids

Comparable to any ore body, diagnostic properties of the rock can significantly deform and become overprinted during and subsequent to their ore genesis. The Kiirunaavara origin has remained to some extent disputed as to whether it is 1) Precipitated entirely from a hydrothermal fluid, or 2) A volatile-enriched Fe-P-dominant magma which crystallized and then had high temperature hydrothermal activity within a silicic magmatism in a Fe-rich volcanic system (Edfelt, 2007; Frietsch & Perdahl, 1995; Geijer, 1931; Lund, 2009; Nystrom et al., 2008; Smith et al., 2013; Troll et al., 2019)

Kiirunaavara ore, despite being predominantly tabular, is extremely irregular in shape. Composite mafic granophyric dykes/granite crosscut the ore and some metamorphic processes have deformed the ore body even further (Lund, 2009). The ore also hosts numerous calcite veins that often have pyrite, chalcopyrite, anhydrite, gypsum and quartz. Disseminated pyrite, flow-alignment actinolite crystals, and banded apatite and magnetite are also found in the ore (Andersson & Rutanen, 2016).

The footwall rock is an Fe-rich partially nodular trachyandesite with abundant irregular amphibolite, magnetite and titanite veins. The hanging wall is a rhyodacite with volcanic and ignimbritic texture that sometimes is cut by disrupted bulbous magnetite dykes suggesting coeval magma movement (Andersson & Rutanen, 2016). Intermingling of ore and rhyodacite magma are found in the hanging wall. Evidence of bulbous contact

between magnetite and apatite rich ore suggest a penecontemporaneous liquid interaction between distinct magmatic features (Andersson & Rutanen, 2016).

Local silicification and sericitic alteration with minor boron, fluorine, carbon dioxide and barium were introduced during hydrothermal alteration (Frietsch & Perdahl, 1995). Other alteration comprises of albitization, and epidotization with minor components of actinolite, tourmaline, biotite and carbonate (Edfelt, 2007) (Table 5-1). Abundant heterogeneous clay-altered rock mass affects both hanging and foot wall rock along ore contact.

5.3.2. Major Discontinuities along Kiirunavaara

Kiruna-type deposits require extensive discontinuities to serve as a medium which iron rich magma or hydrothermal material can precipitate in (Edfelt, 2007). Accordingly, Kiirunavaara host several large-scale discontinuities that are brittle with some plastic deformation zones (Figure 5.8) (Magnor & Mattsson, 2000). The major ore precipitated concordant to major discontinuities that dip at 60° East (Villegas, 2008).

Mattsson et al. (2010) compiled a detailed joint map building on a previous map (Magnor & Mattsson, 2000) which was validated against LKAB's aerial data, geophysical information, borehole, and geological database. It was noted that the dominant joint set is oriented NW-SE, parallel to the "Kaptén Fault" located in the southern portion of the mine. Twenty major possible regional deformation zones were also observed (Figure 5.9).

A complete comprehensive structural understanding of the mine site is still unknown (Mattsson et al., 2010; Magnor & Mattsson, 2000). Various structures are well known from detailed geophysical studies (i.e. gravitational and magnetic surveys) (Jensen & Elming, 2012; Jensen, 2011; Mattsson et al., 2010), from surficial deformation (Stöckel et al., 2012), and/or drill data acquisitions obtained over time (Shirzadegan, 2009). However, not all structures have been successfully included in maps, and some disagreement was noted in the results from different structural analysis (Mattsson et al., 2010).

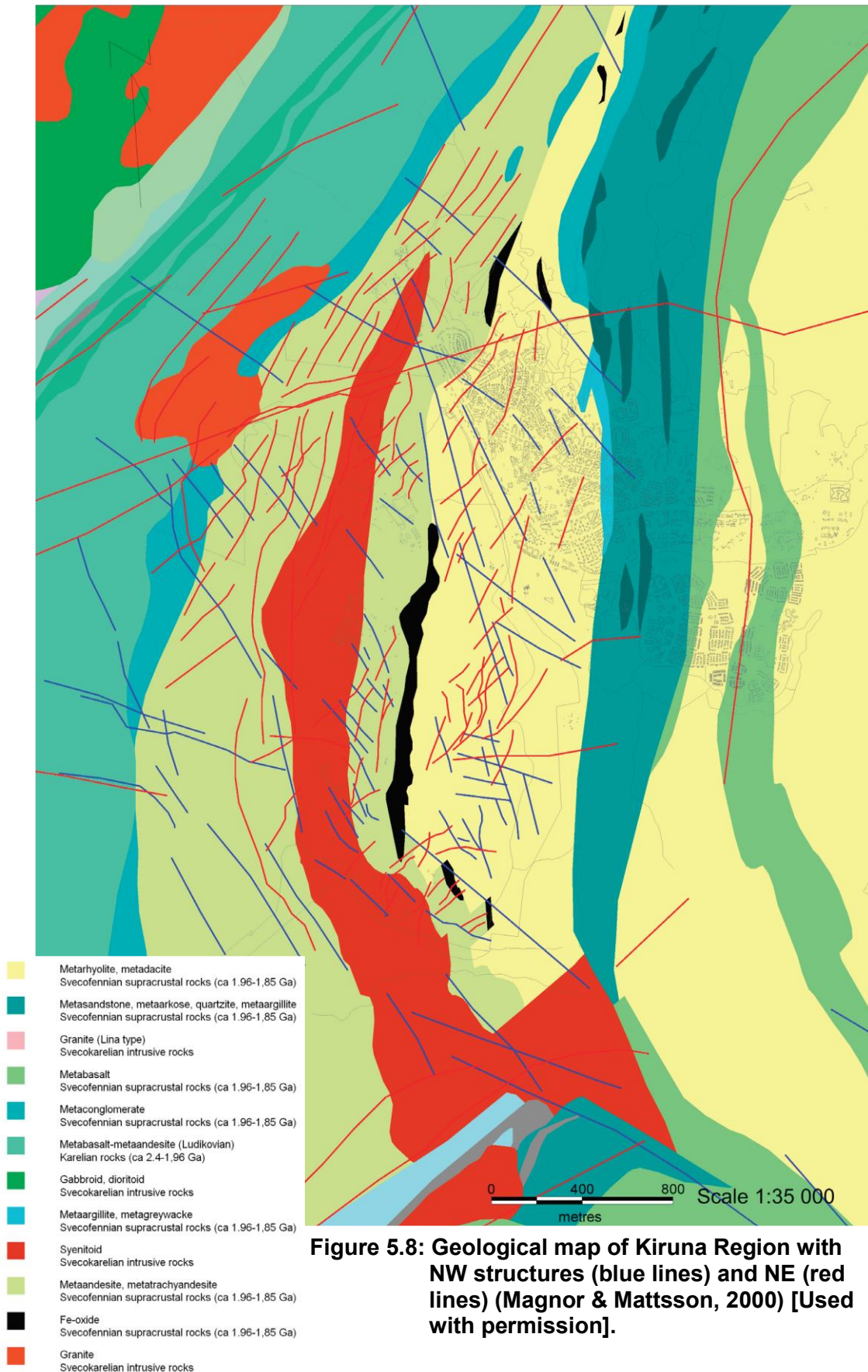


Figure 5.8: Geological map of Kiruna Region with NW structures (blue lines) and NE (red lines) (Magnor & Mattsson, 2000) [Used with permission].



Figure 5.9: Interpreted structural map at LKAB Kiruna (Mattsson et al., 2010) [Used with permission].

By understanding the geological setting, ore body, discontinuities, and rock properties delineation of movement/damage and improved modelling can be achieved. However, modelling cannot forecast movement entirely as there are abundant irregular distributed cavities, porous material, ductile sheared rocks, and clay-altered rock that make the

stress distribution challenging to predict (Andersson & Rutanen, 2016). To minimize unforeseen movement, LKAB has imposed a large array of active monitoring systems.

5.4. Monitoring Mining Induced Subsidence at LKAB Kiruna

Subsidence extent is controlled by the depth of active mining, ore body geometry, mechanical properties of the intact rock, pre-existing discontinuities, and geological structures (Cumming-Potvin, 2018). The proximity of the LKAB Kiirunavaara mine relative to the city has required a comprehensive monitoring program. The monitoring database is extremely advanced and unsurpassed relative to other caving mines in the world (Hamdi et al., 2018). Techniques currently being used for monitoring movement include:

1. Over 400 GPS stations measured annually, except for high alert regions which are measured every quarter (Mäkitaavola et al., 2018; Töyrä, 2013).
2. Extensometers placed at several locations (Stöckel et al., 2012).
3. Documentation and mapping of any evident surface crack since 2008 (Hämäläinen & Furbeck, 2011; Stöckel et al., 2012).
4. Comprehensive understanding of geological history, structures, lithology, and mine layout relative to surface coordinates (Edfelt, 2007; Mattsson et al., 2010)
5. Satellite-based remote sensing (e.g. InSAR) with 12-15 measurements per year. Permanent corner reflectors have been installed throughout the Kiruna region to safeguard accurate backscatter results (Stöckel et al., 2013; Mäkitaavola et al., 2018).
6. Complex matrix of micro-seismic readers at different subsurface and surface locations that allows the pinpointing of rock burst and seismic movement (Svartsjaern, 2015).
7. UAV change detection through surficial point clouds from periodic drone surveys. UAV is also used to investigate major seismic events (LKAB, 2020).

5.4.1. Ground Surface Monitoring GPS

Global Position System (GPS) was developed as an all-weather space-based navigation system that accurately determines the position, velocity and time in reference to a defined system (Wooden, 1985). Despite originating from military purposes, the

wide applications of macro-meter measurements for geodetic surveying caused a rapid civil instrumentation adaptation (Hofmann-Wellenhof et al., 2001). By using a pseudo-range platform between satellite signals and a ground-based device, coordinates to a specific point can be obtained. The value is derived either from the travel time of the signal and multiplying it by the velocity or measuring the phase of the signal (Hofmann-Wellenhof, 2011). Coordinate points host four unknown values which include the three-coordinate locality in true range and clock error. Reading accuracy is directly proportional to the number of satellites available relative to the reference point (Hofmann-Wellenhof et al., 2001).

By placing GPS at a fixed location and measuring periodically, surficial movement can be determined. Subsequently, inferring the extent of subsidence in a region can be monitored by extrapolating a matrix of GPS points. With more than 400 stationary hubs, Kiruna currently maintains a well distributed systematic GPS configuration that spatially enables 3D subsidence judgment (Figure 5.10) (Mäkitaavola et al., 2018; Töyra, 2013). By acquiring measurements annually, deformation against time for each hub can quantify displacement rate (Figure 5.11). Other methodologies to visualize GPS movement include hub X, Y, Z displacements along specific survey lines and contoured displacement plots (Mäkitaavola, 2012) (Figure 5.12).

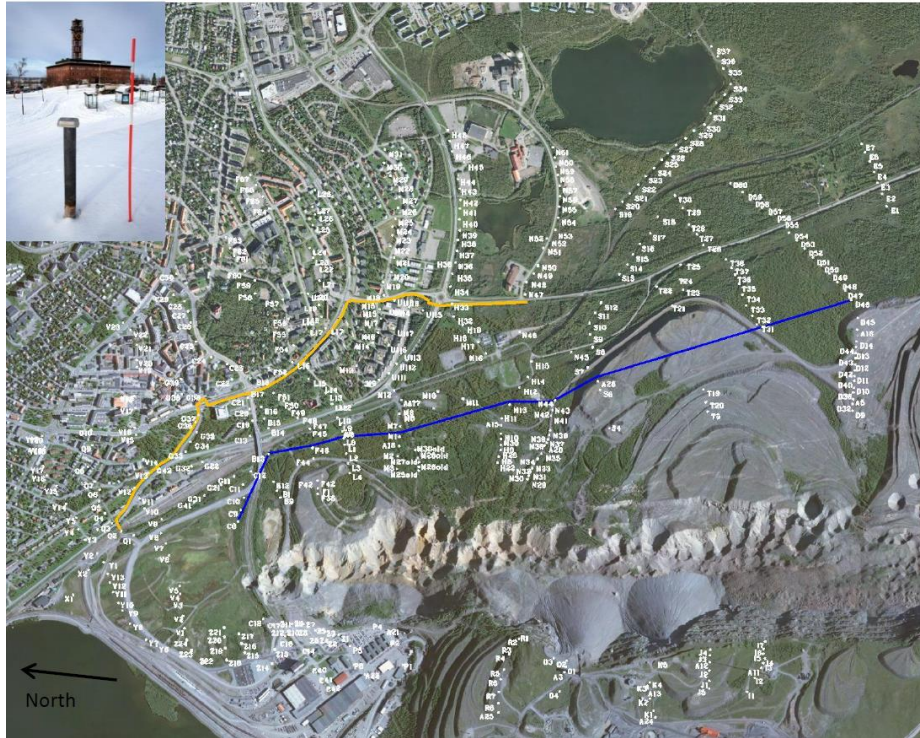


Figure 5.10: GPS lines across the Kiruna mine. The blue and yellow lines outline the limits of the discontinuous zone and continuous deformation, respectively (Töyrä, 2013) [Used with permission].

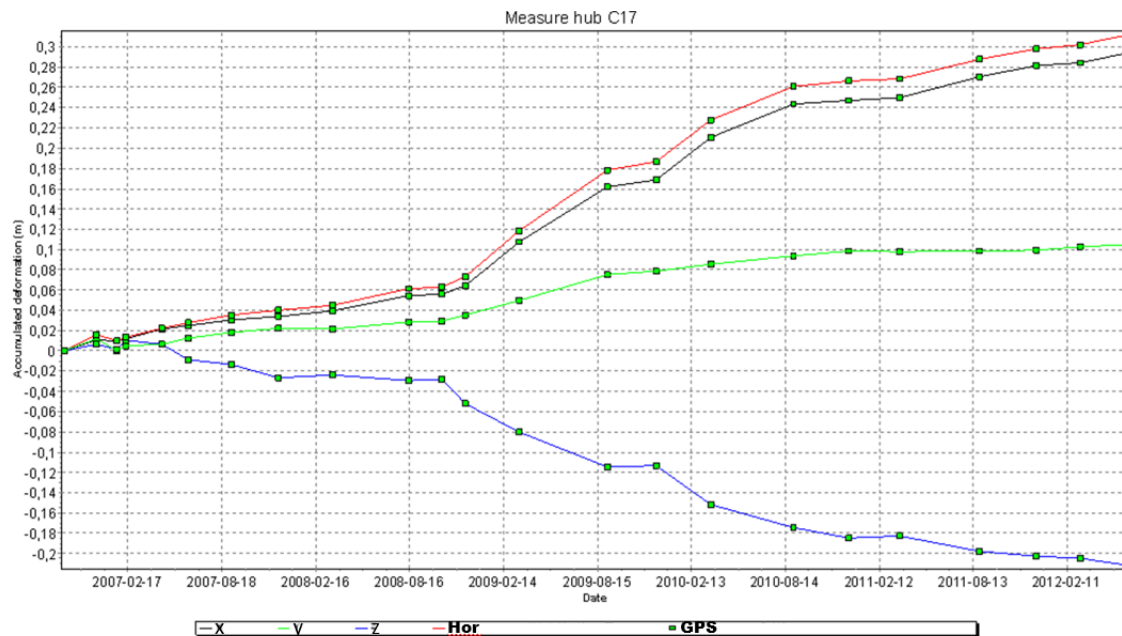


Figure 5.11: Example of cumulative displacement plots for GPS hub C17. Red= total horizontal displacement, Black = Deformation along x-axis direction, Green = Deformation in the y-axis direction, and Blue = Vertical Deformation (Töyrä, 2013) [Used with permission].

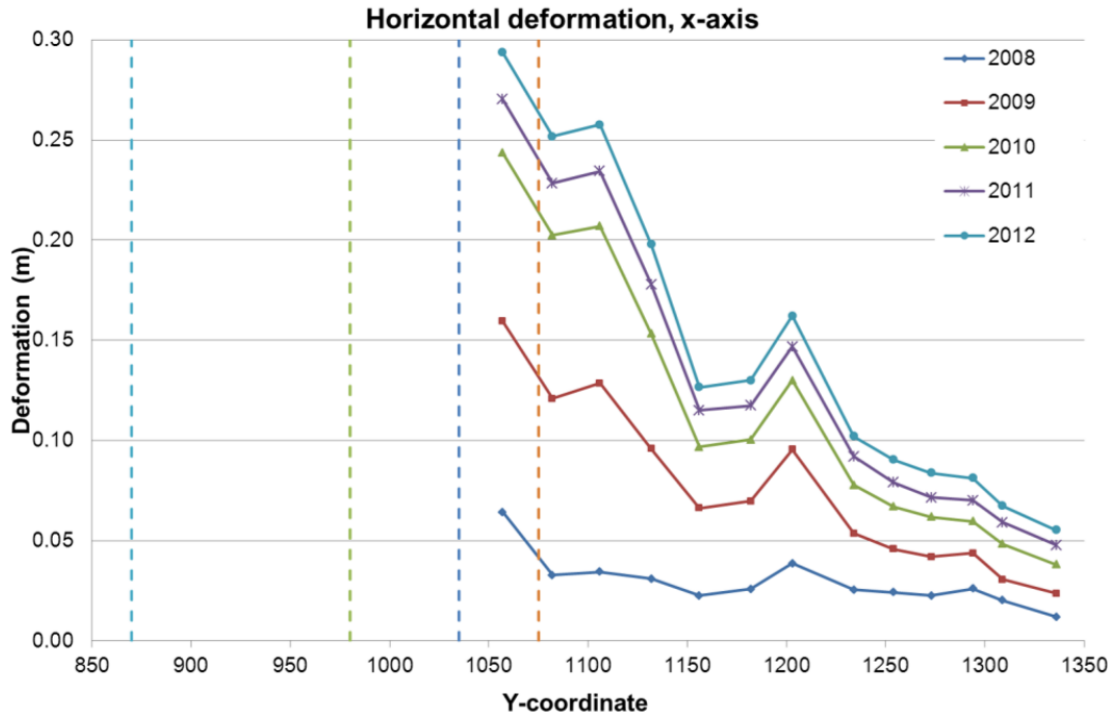


Figure 5.12: Measured horizontal deformation in the x-axis direction for a line roughly perpendicular to the orebody strike (Mäkitaavola, 2012) [Used with permission].

By using various control points, LKAB has estimated they achieve a horizontal precision of 0.7 cm and a vertical precision of 1.3 cm with their GPS measurements (Stöckel et al., 2013). Since Kiirunavaara is an active mine, new permanent GPS stations must be made installed as the mine progressively grows. Additionally, large displacements can cause GPS hubs to become lost or damaged, consequently making the active reference point be inferred as null in successive years (Mäkitaavola et al., 2016).

To ensure the safety of the citizens of Kiruna, the Environmental Court in Sweden imposed a criterion in which people are only able to enter regions where deformation corresponds to a 3% over % horizontal strain and 2% over % vertical strain (Figure 5.13). Areas that exceed this parameter become fenced off and only authorized personnel can enter (Stöckel et al., 2012). Any infrastructure that falls within this criterion is relocated or demolished (Mäkitaavola et al., 2016).

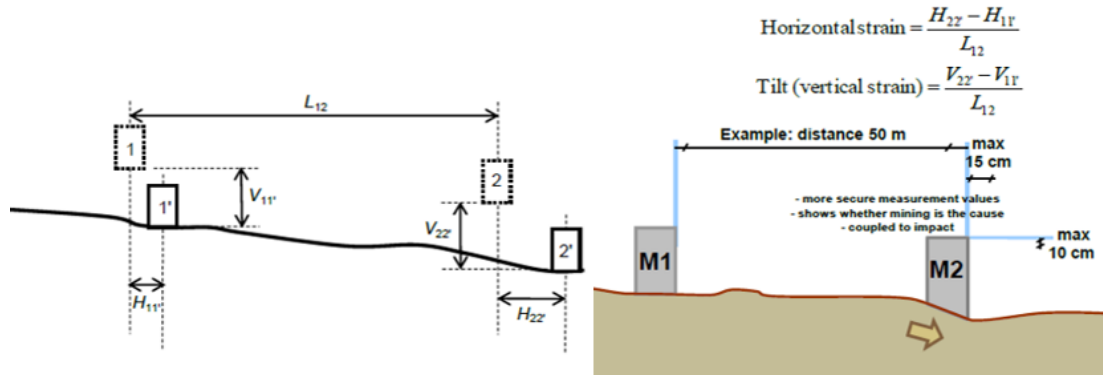


Figure 5.13: Environmental criterion calculation using strain percentage, after Stöckel et al. (2012) [Used with permission].

5.4.2. Ground Surface Monitoring via InSAR

GPS readings can accurately determine displacements relative to reference points. By placing an array of stations, statistical extrapolation of large displacements can be undertaken through the data from discrete measurements (Mäkitaavola et al., 2018). Kiruna's abundant regional deformation zones, geological heterogeneity and unevenly distributed active mining makes continuous extrapolation challenging. Furthermore, the extensive labour required to acquire GPS measurements restricts frequent acquisitions (Mäkitaavola et al., 2016). Such complications make methodologies such as interferometric Synthetic Aperture Radar (InSAR) an attractive option for monitoring induced subsidence.

Synthetic Aperture Radar (SAR) is an active nearly all-weather microwave image sensor that is commonly acquired by either satellite or aircrafts (Curlander & McDonough, 1991). Transmitted waves interact with the surfaces and are either scattered or reflected. The reflected microwaves can then be polarized to infer structural and dielectric properties (Pichierri & Rabus, 2018). To ensure the most accurate SAR images are obtained, various corrections are applied including: (1) surface topography, (2) atmospheric correction due to scattering particles, (3) distance from the source to acquisition, (4) absorption surface differentiation, (5) volume scattering, (6) water content, (7) earth's geodesy, (8) saturation effect on dynamic radar range, and (9) radar model corrections (Bamler & Hartl, 1998; Massonnet & Souyris, 2008; Pepe & Calò, 2017).

Once SAR images are representative of the region of interest, at least two complex value images can be co-registered and differentiated point by point to derive an interferometric SAR (InSAR) image (Pepe & Calò, 2017). By exploiting phase differences, deformation through differential interferometry (D-InSAR) at the Earth surface in cm to mm range can be inferred (Bamler & Hartl, 1998). Since two or more SAR acquisitions are used, new corrections such as variation in viewpoint locality and different atmospheric conditions must be applied (Massonnet & Souyris, 2008). Once successfully corrected and referenced, the resulting image displays interference fringes (Figure 5.14). Such lines do not correspond to altitude as they resemble geometrical differences that are restricted within an amplitude phase of 2π that must be “unwrapped” to infer respective measurements (Bamler & Hartl, 1998; Massonnet & Souyris, 2008). To enable “unwrapping” and seclude displacement, the amplitude phase for movement must be isolated by removing other components within the derived phase variable (Equation 3) (Pepe & Calò, 2017). Some phase variables can be removed by proven equations while others can be attenuated using supplementary data. For instance, to limit topographic phase deviation, a common practice is to use auxiliary DEM information to remove predefined baselines (Massonnet & Souyris, 2008).

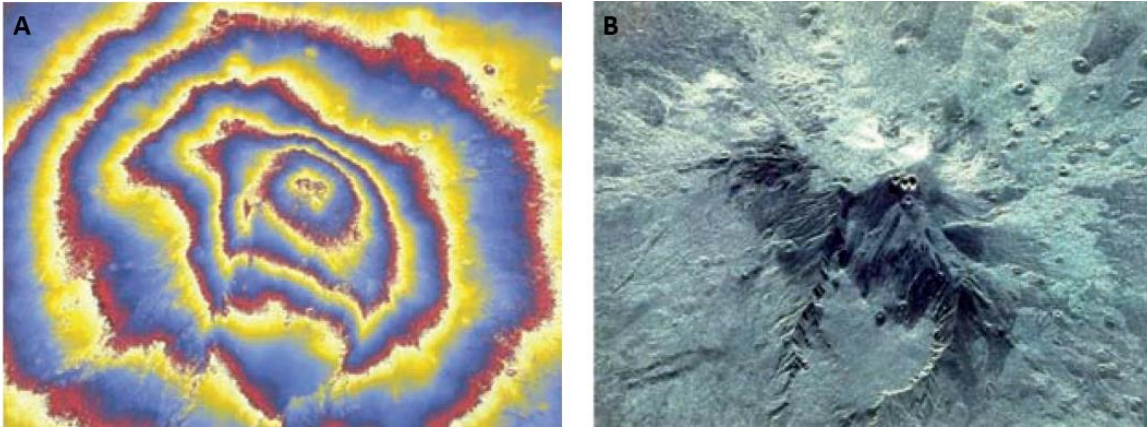


Figure 5.14: Topographic interferogram obtained from SRTM over Mount Etna, Italy (a) Post topographic interferogram after fringes were eliminated (b) mean amplitude image (Massonnet & Souyris, 2008).

$$\Delta\varphi = \Delta\varphi_{displ} + \Delta\varphi_{topo} + \Delta\varphi_{orb} + \Delta\varphi_{atmo} + \Delta\varphi_{scatter} + \Delta\varphi_{noise} \quad (2)$$

To ensure optimum InSAR data, periodic acquisitions are required to capture the progressive deformation phenomena. Depending on the extent of the surface displacements, data collection can be undertaken from a weekly to yearly basis (Pepe & Calò, 2017). Complications in different acquisition periods arise in regions that have heavy snowfall as snow skews backscatter signals due to its volumetric scattering, refraction, and presence of wet snow that prevent radar waves properly interacting with the ground (Martínez, 2008).

With Kiruna's large subarctic seasonal variations and large snowfall periods, coherence has proven to be challenging (Andra Baduge et al., 2016). Other phase complications are caused from the abundant forest areas that have 3 to 4 m tall trees with trunk diameters ranging from 15 cm to 30 cm. Surficial movement on mine waste piles from ore processing also cause complications (Andra Baduge et al., 2016). To minimize and constrain ambiguous reflections, permanent corner reflectors (CR) that output stable anchor pixels have been installed around Kiruna. Some CR have also been co-located with GPS hubs as a means of comparison (Mäkitaavola et al., 2018). CR ensure phase scattering stability and coherent continuity as they are used as reference points that help unwrap and correct noise found on SAR images (Massonnet & Souyris, 2008). With CR input, isolation of 3 mm movement in Kiruna has been successfully captured (Mäkitaavola et al., 2018).

To ensure optimum backscatter data, LKAB has their InSAR measurements made 12-15 times annually by MDA System Ltd. through RADARSAT-2 (Figure 5.15 and Figure 5.16) (Stöckel et al., 2013). To ensure minimum skewing from the winter season, summer images are used as the primary comparison root image (i.e. Master image) to conduct DInSAR investigations (Andra Baduge et al., 2016). Since there are various infrastructure within the mine and the city limits, buildings that have minimum artificial scatter or movement have been used as stable pixels to perform coherent target monitoring (CTM). A benefit of CTM is that CR do not have to be actively installed; however, with Kiruna's progressive subsidence, many of these coherent building targets will be removed or relocated in the future, and thus, CR are considered superior as they are expected to last for more years (Mäkitaavola et al., 2016).



Figure 5.15: Corner reflector (CR) distribution installed in Kiruna with a corresponding image of the reflector (Stöckel et al., 2013) [Used with permission].

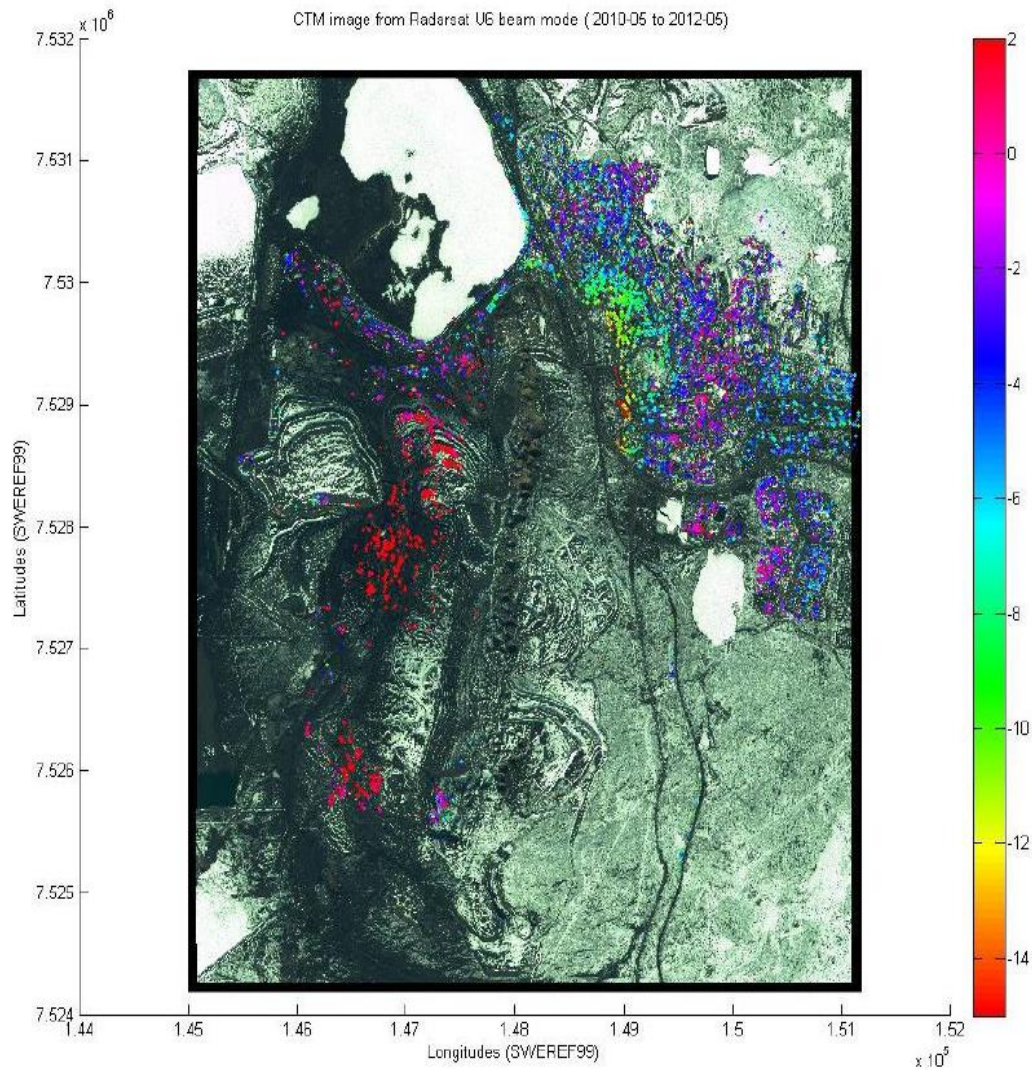


Figure 5.16: Example of InSAR measurements at LKAB Kiruna, colour bar shows the line of sight (LoS) deformation in mm/year (Stöckel et al., 2013) [Used with permission].

InSAR has proven to be extremely useful for topographical measurements but ambiguity can arise from: (1) geometric sensibility proportional to direction of displacement; (2) terrain types can greatly abrupt phases causing underestimation, aliasing, or distorting of unwrapping algorithms; and (3) empirical nature of the corrective formulae leads to uncertainty (Bamler & Hartl, 1998; Massonnet & Souyris, 2008). Displacement direction in spaceborne SAR images lack accuracy when acquiring N-S information because it is parallel to the flight path and perpendicular to the line of sight that is closely constricted to West and East (Bamler & Hartl, 1998; Massonnet & Souyris, 2008). Phenomena

contributing to orientation errors have been investigated in detail at Kiruna by Mäkitaavola et al. (2016) and it was evident that east/west error was within 2 mm, while north/south was approximately 91 mm, and vertical displacement was around 14 mm.

InSAR limitations, however, are outweighed by its capability of high-resolution spatial density morphological measurement of inaccessible areas, and limited cost once the comprehensive system has been emplaced (Massonnet & Souyris, 2008). A comparison of GPS measurement versus InSAR was done by Mäkitaavola et al. (2016) where similar trends and measurements were observed between both data sets. InSAR data was able to acquire more than 23,000 motion estimation points, which covered inaccessible regions and was not limited by the number of GPS points (Mäkitaavola et al., 2016) (Figure 5.17 Figure 5.16).

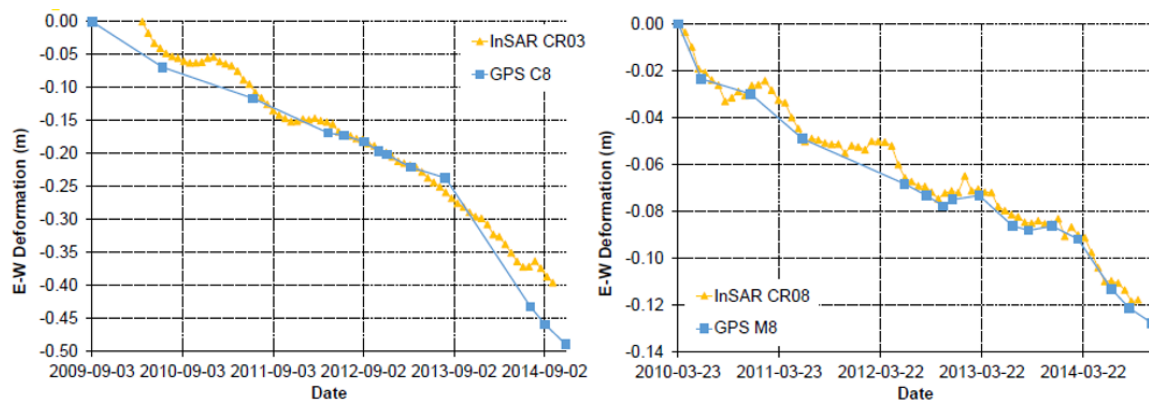


Figure 5.17: Cumulative InSAR deformation measurement for CR03 and CR08, compared to adjacent GPS measurements (C8 and M8), in the east-west direction (Mäkitaavola et al., 2016) [Used with permission]. Jumps are evident in the InSAR data points during every winter period.

Andra Baduge et al. (2015) also assessed InSAR information to see which InSAR methodology worked best by comparing it to known GPS movements. When InSAR CR sequential images (CR-InSAR-SEQ) were used without referring to a coherent threshold, a large difference between both the GPS and InSAR results was evident. However, once a threshold of coherence (COR) and small baseline average subset (SBAS) was utilized, several winter images were discarded. By utilizing all CR, COR, and SBAS (CR-InSAR-SBAS-COR) a mean error correlation of 1.1 mm with a 10.7 mm standard deviation was

calculated with a correlation coefficient of 0.88 relative to the GPS movements (Figure 5.18) proving the importance of coherent images. InSAR skewing effects hosted by subarctic snowfall is also evident in Mäkitaavola et al. (2016) results as clear spikes that occur during winter periods.

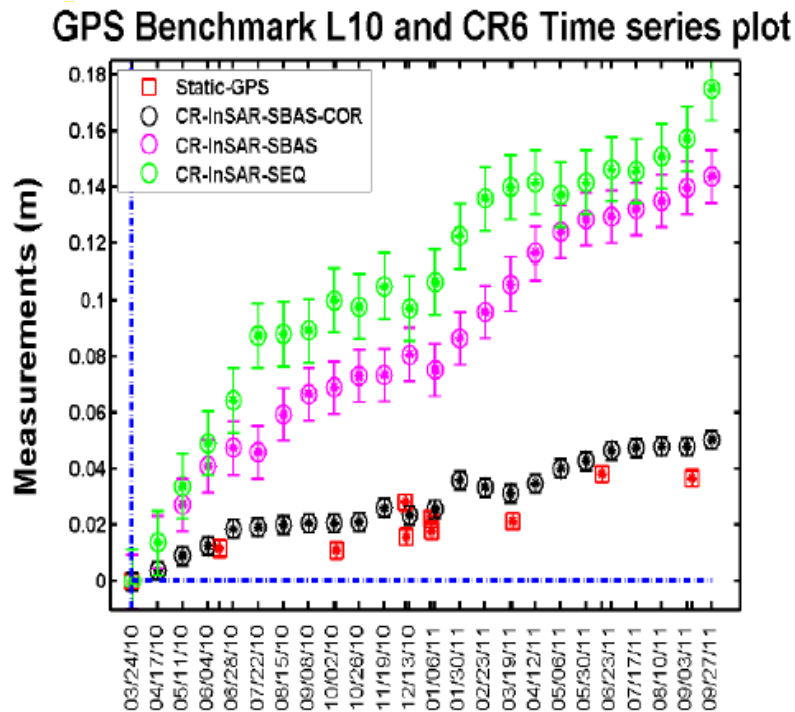


Figure 5.18: Comparison of GPS Benchmarks L10 and CR6, after Mäkitaavola et al. (2016) [Used with permission].

The capability of InSAR frequent measurements and wide area coverage permits LKAB to forecast deformations at higher resolutions than solely using GPS readings. However, the best results are obtained when GPS measurements are complemented with InSAR results as they “ground truth” movement and capture incoherent periods (i.e. poor atmospheric condition or heavy snowfall (Mäkitaavola et al., 2016, 2018)). With the incident angle limitations of satellites resulting in poor recording of movement in the north-south direction, complimentary GPS results ensure all movements are accounted for (Massonnet & Souyris, 2008).

5.4.3. Underground Monitoring using Microseismic Analysis

As a rock mass equilibrates to new stress conditions, energy is released through intact rock failure or reactivation of fractures, faults, stiff dykes, shear zone, or other geological planes of weakness. Abrupt dynamic redistribution of stress causes high frequency seismic wave events that can be recorded (Hedley, 1992; Petersen et al., 2016). Stress redistributes through failure mechanisms that may induce cracks and/or surficial deformation.

Seismic events are inferred by two distinct waves known as the primary wave (P-Wave) and secondary wave (S-Wave) that travel through elastic media as longitudinal and shear stress, respectively. The P-wave is faster, moves through both solid and fluids, and induces stress parallel to the direction of the wave propagation. The S-wave is slower, can only move through solids, and induces stresses that are predominantly orthogonal to the direction of the wave (ESGSolution, 2019). Abrupt rearrangement of rock stresses normally releases minor seismic amplitude and frequency magnitudes smaller than common earthquakes, and thus, are categorized as microseismic events (Brown, 2015; Hudyma, 2008).

Microseismic events are treated as a 4D problem. By progressively tracking seismic clusters and distribution readings through time, properties such as fracture propagation, fracture effectiveness, fluid flow, stress-strain field and discrete fracture network models can be constrained (Langenbruch et al., 2018; Shakiba et al., 2018; Zhu et al., 2017) .

An adequate array of seismic sensors both in locality and wavelength windows is required to pinpoint the hypocentre by synchronizing time delays in both P-wave and S-wave in reference to all points before a velocity model can be derived (Hudyma, 2008). The spatial extent of the required seismic monitoring is directly proportional to the area of interest. The type of sensors (i.e. geophones and/or accelerometers) is also critical as only signals within the instrumentation's bandwidth will be captured. Any frequency that surpasses the range limitations will be truncated and cause a phenomenon known as magnitude saturation (Brown, 2015; Hudyma & Potvin, 2010).

As underground mines reach greater depths and higher stresses, microseismic readings are becoming of greater significance in mining practice (Hudyma, 2008). Safety can be significantly increased as microseismic readings can assess inaccessible areas

indirectly and can even record the effect of reservoir impoundments, waste injection, hydraulic fracture, and mining activity (Petersen et al., 2016). By contouring potential seismic sources, seismic activity can be correlated to known structures or areas prone to failure (Hudyma & Potvin, 2010; Martinsson, 2013; Salvoni et al., 2016). If the seismic source is unidentified, drilling projects can be catered to validate whether it is due to intact rock failure, or from shear release along an unidentified structure (Cumming-Potvin, 2018).

It was previously thought that the S:P energy ratio of microseismicity could directly delineate the dominant failure mechanism type along pre-existing discontinuities (Duplancic, 2001; Tibbett et al., 2016; Hudyma & Potvin, 2010). However, recent work by Cummin-Potvin (2018) has proven that it is not a robust indication. The Duplancic mode of block cave failure (2001) assumes that clusters of seismic events will continuously move outwards within a caving system over time and will dominantly fail due to shear. With borehole imagery available, seismic hot spots were investigated to see whether the Duplancic hypothesis of seismic failure propagation was valid. Microseismicity diffusion proved that seismicity banding phenomenon does not hold true for all cases as discontinuities, rock properties, and stress ratio play an important role in intact rock failure mechanisms, and thus, caving propagation is not continuous nor proportional to the S:P ratio (Cumming-Potvin, 2018).

P and S- wave velocity is also heavily attenuated by various parameters such as: (i) lithology, (ii) heterogeneity in the rock mass, (iii) voids, (iv) geometry, (v) seismic anisotropy, (vi) continuous sliding, (vii) structures, (ix) noise in the data, and (x) cluster resolution (Salvoni, 2017; Brown, 2015; EGSSolution, 2019). To ensure data can be filtered, visualized and interpreted properly, 3D grids provided by software such as mXrap (2021) can generate comprehensive seismic event clustering (CSEC) (Wesseloo, 2018). CSEC can be then broken down into two main subgroups called complete linkage (CLINK) or single linkage (SLINK). Both approaches can help constrain regions that are seismic due to mining activity, stoping activity, failure in fractures or intact rock failure. By filtering seismic noise from the unavoidable mine work, abrupt inelastic stress changes can be isolated.

LKAB Kiruna has an elaborate microseismic system that can rapidly detect underground redistribution of stresses. Its first array of seismic monitoring systems was installed in

2004 and was located around the “Sjömalmén” or Lake Orebody (northern non-daylighting portion of the orebody). During 2008, a larger array was implemented to monitor seismicity in the production area (Stöckel et al., 2013). Detailed analysis of microseismic events using clustering algorithms and applying several corrections has been discussed in detail by Martinsson (2013) and Svartsjaern (2015). Seismic shear events along the footwall have been concentrated in the forefront of the mine excavation where structurally controlled failure has occurred (Svartsjaern, 2015).

Seismicity data in Kiruna is predominantly used in rock burst studies and the tracking of the caving process. Microseismic activity rarely coincides with known regions of clay and weakened rock in Kiruna, likely due to the low strength of the material not permitting tension build up (Mattsson et al., 2010). However, stresses still impact adjacent regions that can cause them to become seismically active and lead to misinterpretation of the true tension source. Such complications result in the need for other complementary data sources to forecast excavation instability and underground movements at LKAB Kiruna. Safety for both workers and civilians can be achieved by constraining an implicit deformation model that mitigates various instrumentation limitations by combining various input sources such as geological models, mine design, known surficial movement, and microseismic results. Thus, a new geovisualization application known as MineViz MR was constructed to investigate the potential of improved 4D assessment and communication with various mine experts using the Microsoft HoloLens headset. Kiruna’s surficial cracking, UAV monitoring, geological findings and extensometer results although possible to include within the MineViz MR application are not presented in this thesis due to both confidentiality and memory capacity issues.

5.5. A New Visualization Approach for Mine Induced Subsidence Results

The extent of ground deformation is controlled by many parameters such as the depth of the active mine, the ore body geometry, mechanical properties of intact rock, pre-existing discontinuities and geological structures. To understand and predict future displacement, various monitoring systems must be synergized to effectively correlate anomalies, noise filtering and elaborate complex numerical analysis. Since various personnel with different expertise are required to evaluate mine-induced subsidence, a common visual medium provides significant advantages. With an impending new era of

visualization, the HoloLens can serve as a medium to host various complex datasets for 4D MR visualisation with improvements in both data interpretation and communication.

The large array of comprehensive information at LKAB Kiruna allows the construction of a complex 4D mine model that can be easily adapted to other mine sites in both MR and VR. The model was first initiated by ensuring a realistic base model of the mine site. A 5 metre LiDAR Kiruna point cloud captured in 2018 was used to develop a mesh with satellite imagery texture. To minimize hardware demands, the mesh was selectively reduced in areas of low importance such as regions with low topographical changes or away from the area of interest. Since Unity does not have scripts that can georeference models adequately, an in-house script was used to georeference any information with respect to the local coordinate system used by LKAB. The results were compared to ArcMap plots and an uncertainty of ± 3 cm was calculated. The error margin was considered negligible as the model is approximately 10.1 km by 10.1 km in scale (Figure 5.19). Various UI options were then implemented into the model for scaling, moving, and rotating both through UI buttons and through the MRTK implementations.

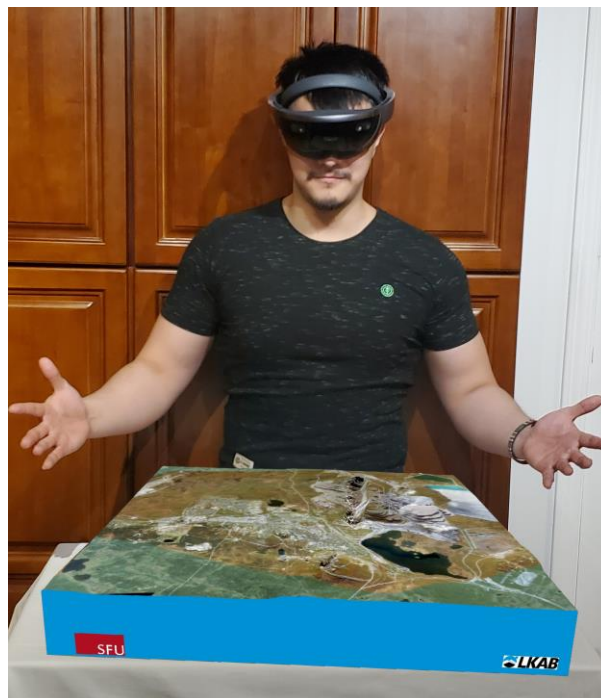


Figure 5.19: MR model of the LKAB Kiruna site observed on MineViz MR. Size of the model can be scaled at the user's discretion.

5.5.1. GPS visualization

All GPS measurements recorded up to 2018 were provided by LKAB. With the topographical base model readily available, all hubs were imported, instantiated and georeferenced along the model from a CSV file. To enhance data interpretation, various methods were used to observe GPS movement, including:

- (i) Linear graphs,
- (ii) 3D hodographic analysis per GPS hub,
- (iii) Line rendered movement in 3D space, and
- (iv) Mesh representation via spatial statistical analysis.

During instantiation, interactability for each GPS station was set up to ensure each hub was assigned its respective linear displacement-time graphs and hodographic results (i.e. displacement vector diagram). If a hub is gazed upon, the specific GPS nametag is displayed above it. To ensure effortless GPS picking, UI interaction that can disable or enable specific GPS lines was developed (Figure 5.20).

If the GPS hub is clicked, its' respective 2D graphical representations x, y, and z displacement through time are displayed. Each 2D graphical analysis per hub was constructed through an in-house python script that outputs the respective graphs in JPG format and are automatically interlinked to the relevant hub in Unity. The 3D vector graph can be toggled by clicking a virtual button adjacent to the 2D graph that enables the graphic representation to appear at a fixed distance away from the user's perspective. To limit the number of objects in the application, each hodographic representation, once prompted, is independently produced from the constituted root CSV. A single axis hodograph could not be used because the magnitude of displacement varied throughout the site. Major and minor gridlines are rendered and the legends updated with respect to the GPS hub (Figure 5.21). The deformation curve for each year has a predefined colour that can easily be manipulated to the user's preference. To ensure optimum assessment, each rendered hodograph can be scaled, rotated, and moved at the user's discretion. If a user gazes at a particular point within the hodograph, the appropriate value is displayed independently.

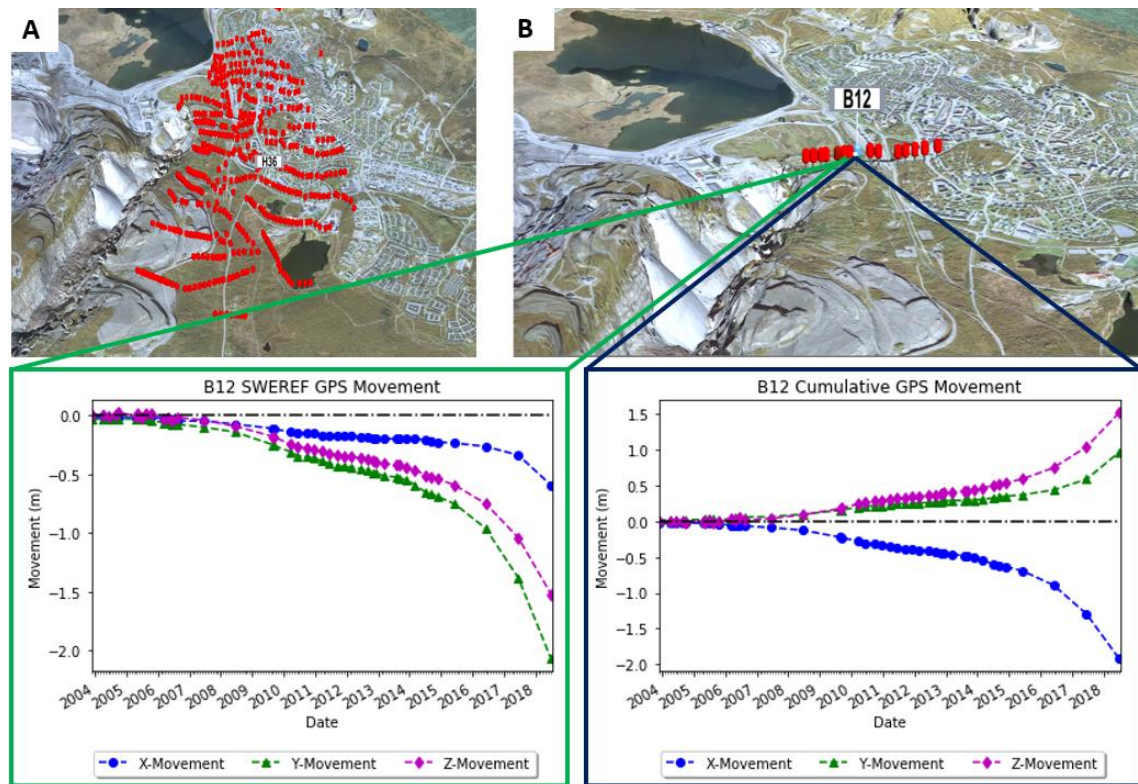


Figure 5.20: Georeferenced GPS hubs along a 3D virtual model. (A) All GPS recorders diaplyed. (B) Only line B displayed. While a user gazes at a GPS hub the specific hub name is displayed. If clicked, the respective displacement-time graph is displayed dependent on coordinate system.

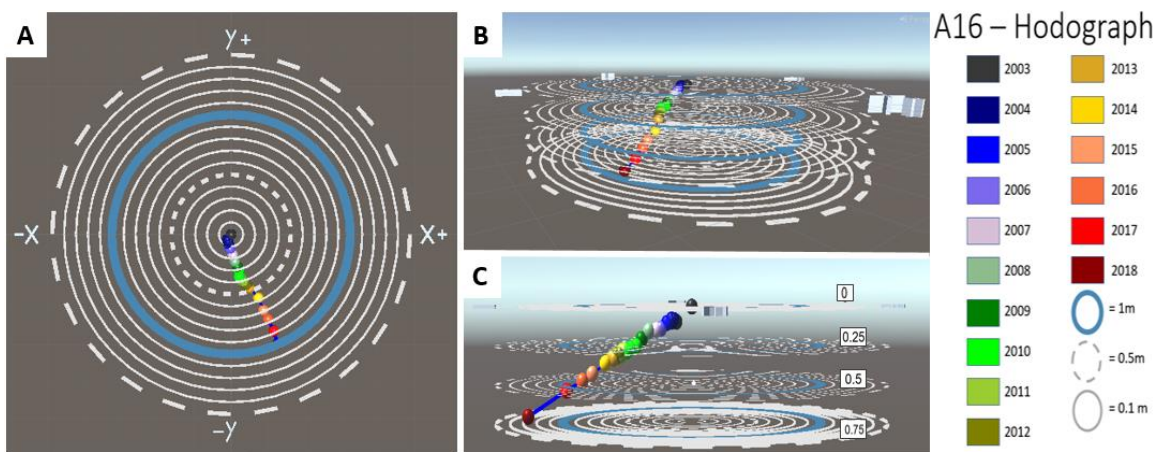


Figure 5.21: Hodograph results observed within the Unity interface in various angles (A) Top view (B) 50° angle and (C) 5° angle.

Both hodographic and conventional displacement-time graphs were effective in graphically displaying GPS movement through time. Another GPS movement methodology that was investigated involved using Unity's line renderer directly on each GPS point along the mesh. Virtually showing how each GPS hub has moved through time by visually showing progressive movement in 3D space relative to their origin enabled a deeper understanding of overall movement. Due to confidentiality, these results are not presented within the thesis.

Surfer Version 16 (Golden Software, 2021) was also used to extrapolate GPS movements via a 3D mesh. The mesh had to be separated into three distinct components of deformation for the x, y and z movement. Constructing these meshes was challenging as an effective batch method to either construct or import the results effectively into Unity is unavailable. Since some movement is less than a metre, the results can be scaled by a scalar multiplier to permit the user to easily observe the movement.

Surfer allows a large suite of statistical gridding and extrapolations that enables efficient contouring. Three methods were tested: kriging, radial basis, and inverse distance. Kriging and radial basis were used as they are the recommended by Surfer (2019) for data sets that range from 250 to 1000 observations. However, the kriging and radial basis packages in Surfer assumes continuity, and thus, do not allow the input of faults or break lines. To consider discontinuities and structures as break lines, inverse distance was investigated. Structures that were described by Mattsson et al. (2010) were georeferenced, imported into Surfer, and treated as break lines. All the Surfer results were then analysed and imported into Unity for deformation assessment through time (4D).

Combining both 4D linear and mesh assessment allowed the identification of areas that required more detailed investigation or hosted potential sources of error. From such an assessment it became apparent that the 3D Surfer mesh interpretations are hindered by the requirements for continuous acquisition over time of all GPS points (Figure 5.22). GPS hubs are, however, lost over time due to large movements, lack of access to the hubs due to safety, hardware malfunctions, or were intentionally skipped during different acquisition periods. These issues make extrapolation and kriging of data in Surfer challenging.

To account for GPS points that were lost over time, an approach to keep those points as a constant variable after being lost was tested. It was found that by keeping reference points constant, meshing could be skewed and can even result in underestimation of GPS displacements in some regions where GPS records ceased at a low value (Figure 5.22).

Statistical interpolation is heavily skewed if previous inputs are removed. Such phenomenon can be easily overlooked when systematically loading data into software such as Surfer where there is only 2D and 3D assessment. By observing data in 4D, drastic changes within the data can be easily observed and problematic regions can be isolated. More detailed observations can then be made by observing each point graphically. As the years have progressed, more GPS monitoring stations have been installed and the effects have become less drastic but remain evident.

Considering break lines and structures within GPS movements is also crucial as large jumps between the continuous and discontinuous zone may severely affect the data. Inferring only points as the main source of movement restricts users' ability to fully visualize all the deformation occurring within the area. Despite the intricate arrays, areas do contain drastic abrupt changes due to structures. Such effects make other acquisitions such as InSAR more reliable for assessing the overall movement of the region.

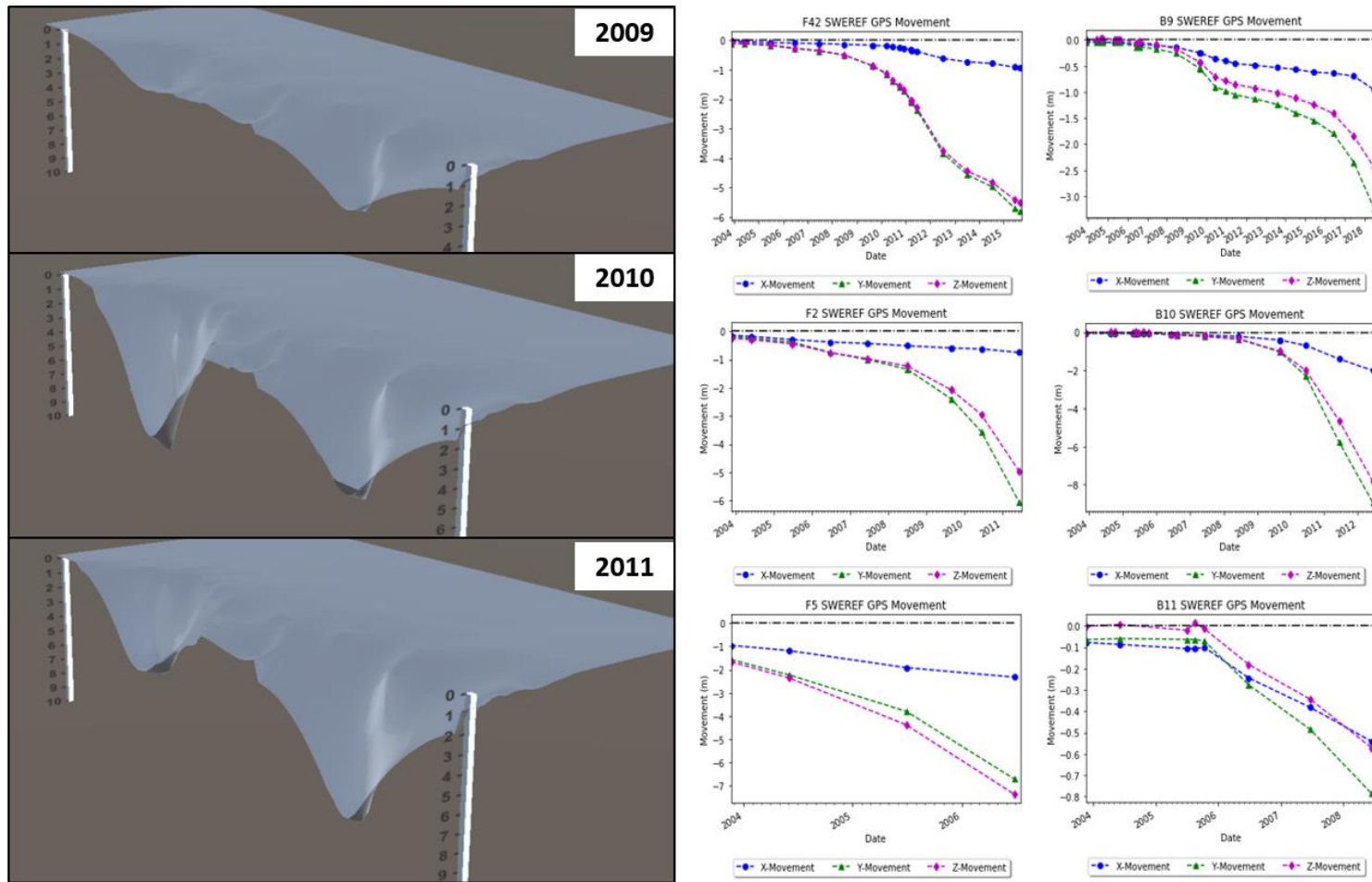


Figure 5.22: Z-Movement mesh derived from Surfer Version 16 imported into Unity. 2009 to 2011 has an evident large rebound but it was not caused geologically, but rather by issues within the data base. Some GPS such as F42 and B9 have repeated acquisition of movement within a year while others such as F2, F5, and B10, became lost due to large offsets. Other data such as B11, stopped being recorded. Losing sources of data caused skewing within the final meshing results.

5.5.2. InSAR visualization

InSAR data provided by LKAB comprised georeferenced PDF files that were processed and assessed by MDA. Since the legend changes through each PDF file, a python script was used to separate the main image from the legend as two separate files that were populated into designated folders. After being registered, each image was imported within the Unity platform allowing an anchored georeferenced InSAR geovisualization module in 2D, 3D and 4D (Figure 5.23 and Figure 5.24).

The raw InSAR, CR, CTM and CR_CTM results were split into different modules. Each acquisition was then enlisted as subgroups that were able to be played through time. Since the InSAR were provided in PDF formats they were unable to be used as effectively as GPS results in terms of quantitatively analysis and visualization.

InSAR applications in 3D space could exponentially become of increased importance if the raw data format were provided by LKAB/MDA. If the 23,000 motion estimation points (Mäkitaavola et al., 2016) were provided as three axis points, a mesh could be constructed in platforms such as Blender or Surfer by treating each point as a vertex. This would enable 3D visualization of InSAR movement as a mesh rather than the limited 2D representation; consequently meshing of the InSAR results has yet to be investigated but holds significant potential. By analysing the results plotted as a 3D mesh, deforming regions can be secluded. With known vertex values, similar graphical analysis seen in GPS results could also be constructed (Mäkitaavola et al., 2016) and played through time. By assessing both GPS and InSAR vertexes, further comparison could be derived.

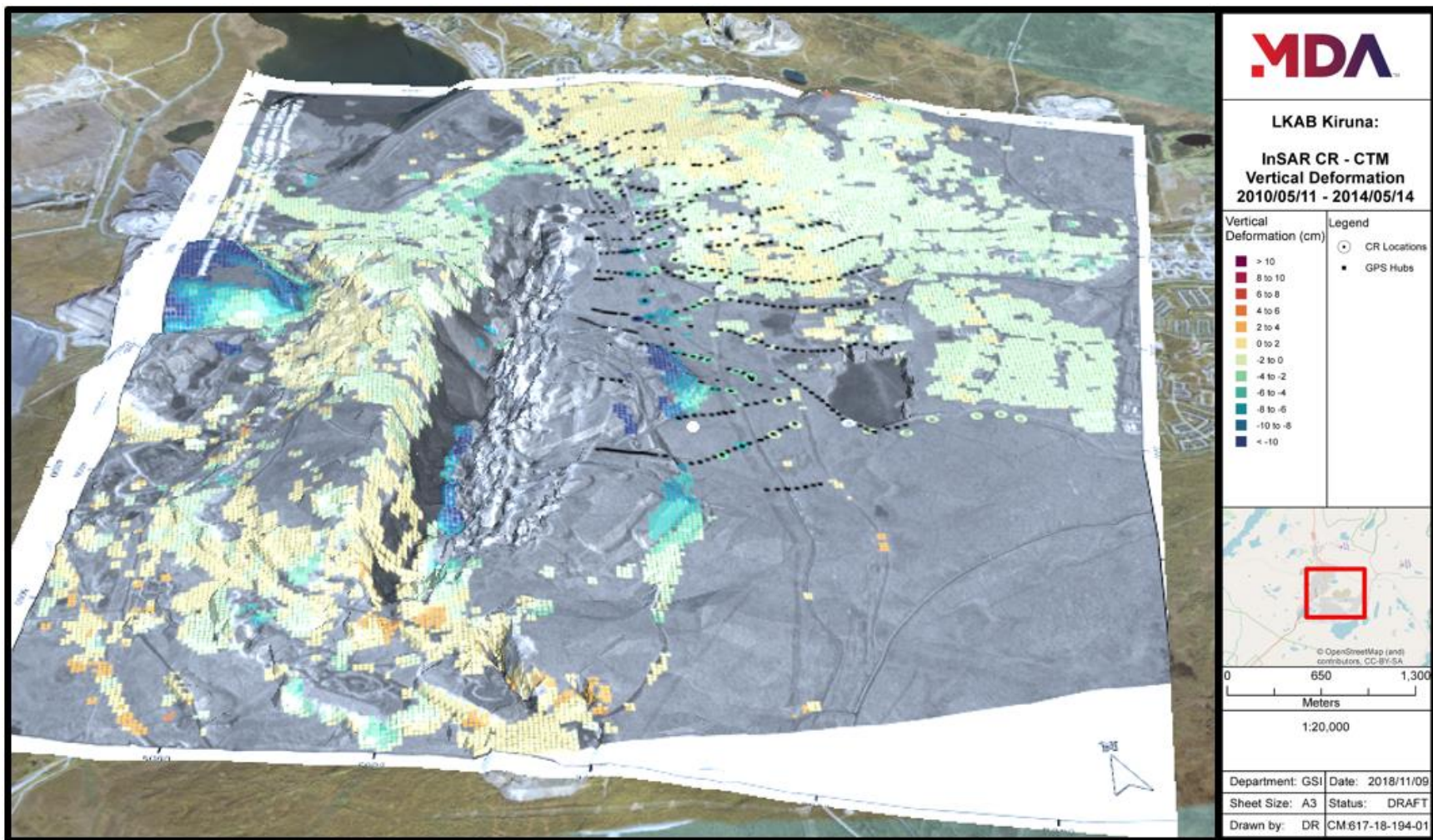


Figure 5.23: InSAR CR-CTM Vertical deformation 2010/05/11 - 2014/05/14 overlain and georeferenced along 3D MineViz MR model.

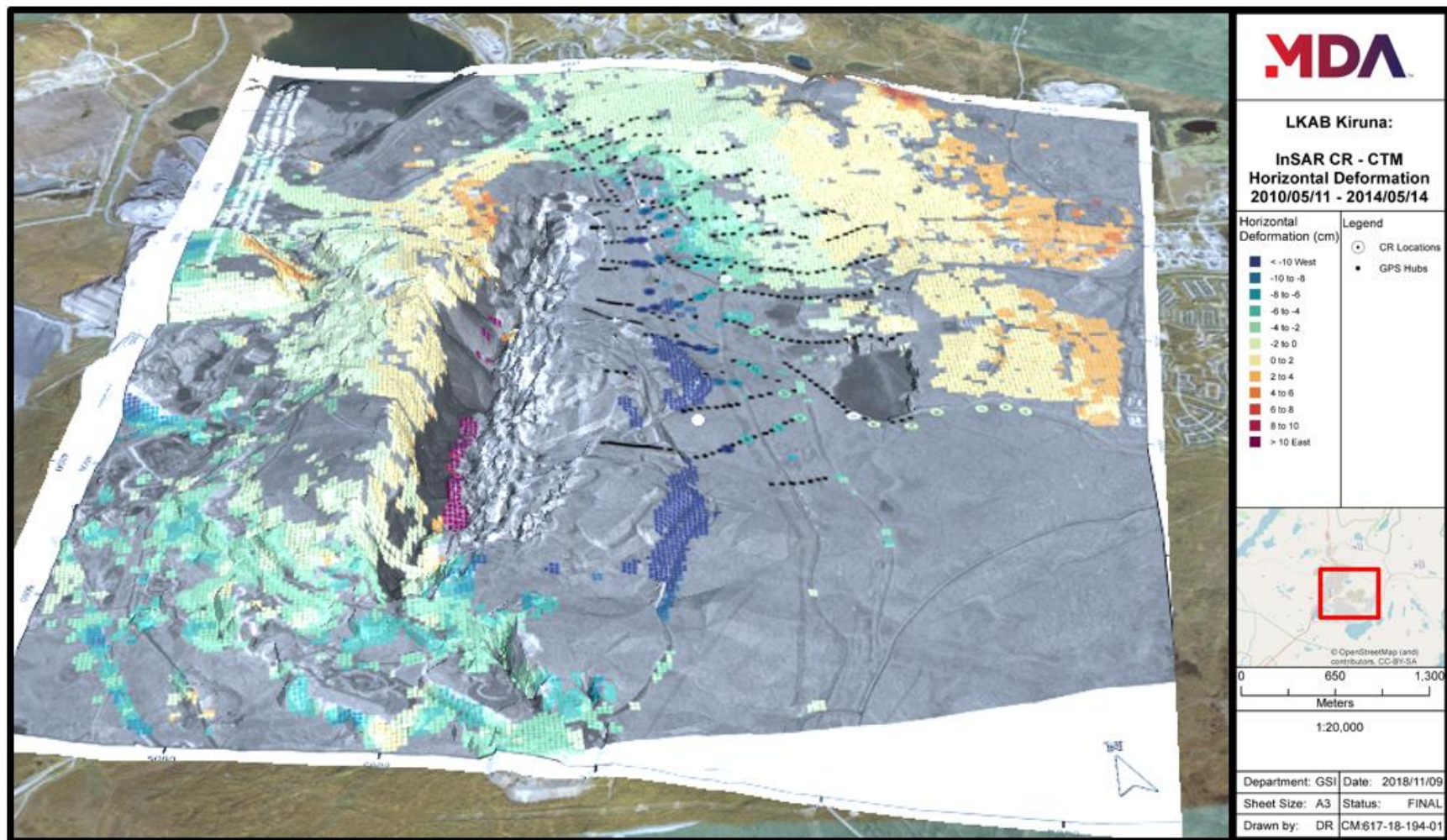


Figure 5.24: InSAR CR-CTM Horizontal deformation 2010/05/11 - 2014/05/14 overlain and georeferenced along 3D MineViz MR model.

5.5.3. Civil and Mining Infrastructure at LKAB Kiirunavaara

Civil infrastructure was obtained through open-source data OpenStreetMap (OSM). More current data evident in Google Maps and Bing was used as reference to correct and modify any outdated results. Both these hubs were not used directly as complete data extraction is impeded by copyrights. Every base imagery was then imported into Unity to allow different mapping texturing of the area of interest (AOI) (Figure 5.25).

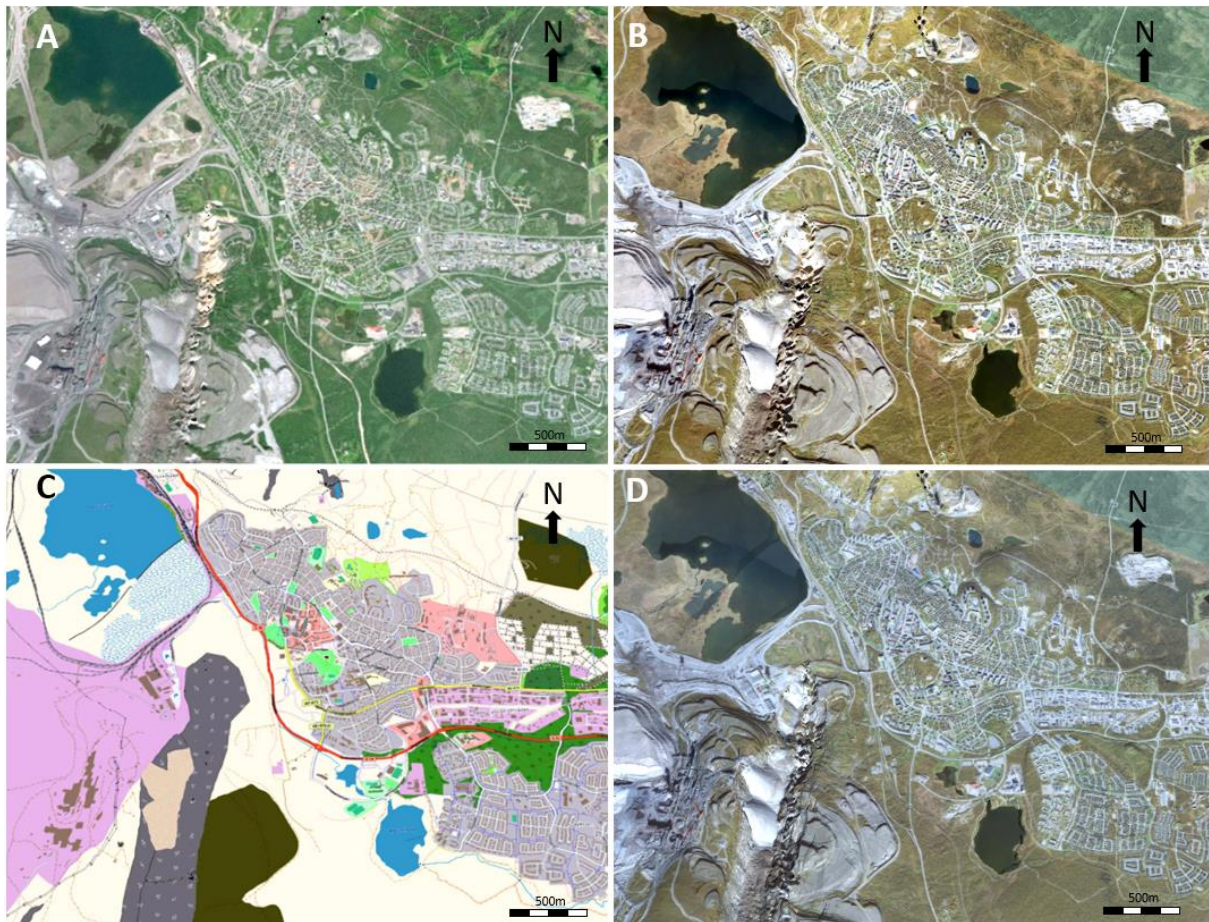


Figure 5.25: Birds-eye view of different textures of map used on Kiruna region that are easily interchangeable between (A) Bing (B) Google Earth (2021b) (C) OpenStreetMap Standard View and (D) Image provided by LKAB

OpenStreetMap limits the amount of export data, and thus, information was retrieved by gridding the map with slight overlaps to ensure that all attributes were retrieved effectively. All files were imported into ArcMap 10.5 to convert into shapefiles (SHP). The SHP files were then computationally filtered to clip data outside of the AOI and remove any redundant information. The attributes were grouped into civil infrastructure parameters, which included buildings, LKAB sector, roads, railways, powerlines and waterbodies.

The georeferenced ArcMap results were exported into Blender for 3D meshing purposes, as simple polylines cannot be rendered effectively in Unity. The results were flushed along the high-resolution DEM mesh of Kiruna to ensure the buildings followed the topography. All results were then exported into Unity (Figure 5.26).

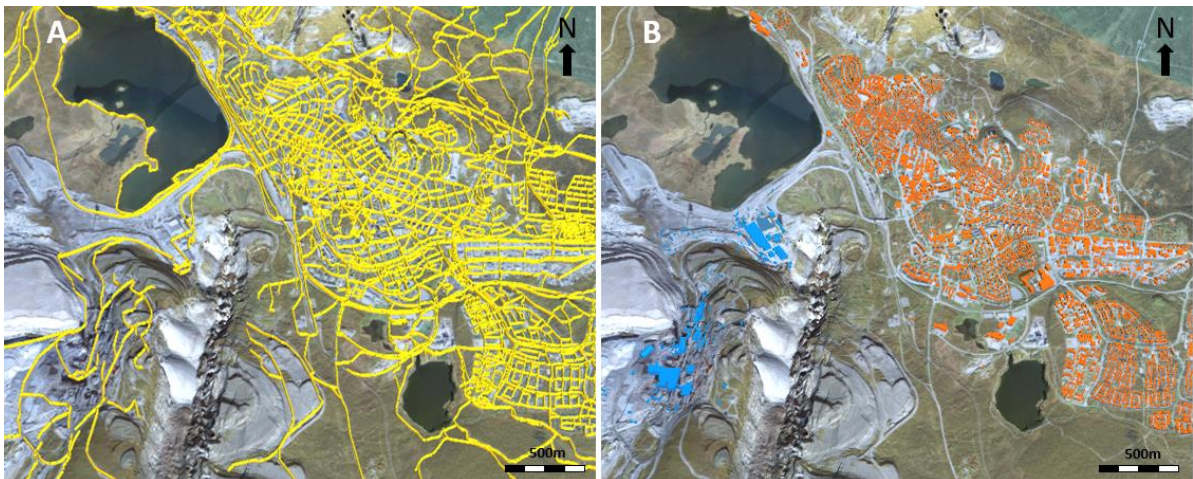


Figure 5.26: 3D model of Kiruna's (A) Road/pathways and (B) infrastructures retrieved from OSM.

OSM only provides a rough estimation of the building's attributes making the resulting shapes simplistic. However, LKAB did provide detailed Computer-Aided Design (CAD) models of the mine site that was exported from Naviswork Software (Autodesk, 2021) and imported into the Kiruna's MineViz MR model (Figure 5.27).

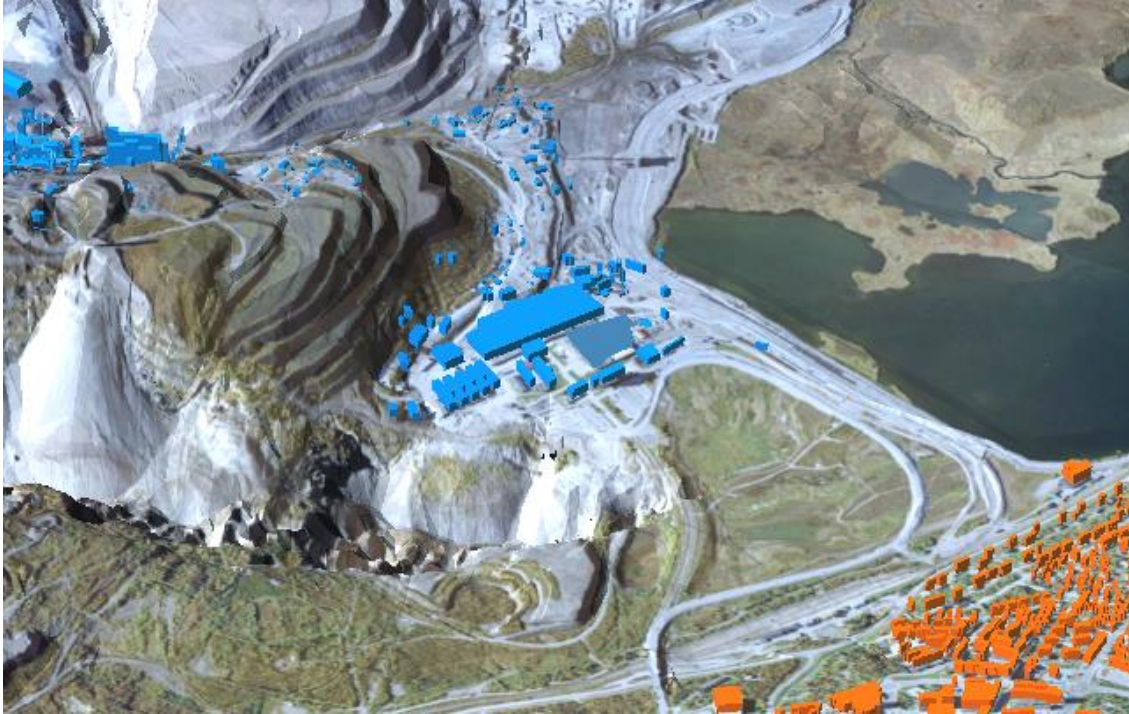


Figure 5.27: LKAB buildings (blue infrastructures) has representative detailed models while OSM models provide satisfactory models but not detailed.

High-resolution mining infrastructure derived from laser scanning and CAD modelling was also provided by LKAB. The high polygon mesh count of such models enforced a targeted model simplification. A complete polygon reduction algorithm was not used as the model became unrepresentative. Any data such as machinery or operating stations were removed due to confidentiality and computational limitations. Reprocessing the mesh reduced the file memory by more than 80%. The final model was then imported into Unity to enable holographic underground analysis of the mine.

5.5.4. Microseismic Analysis

The sophisticated seismic instrumentation network at LKAB Kiruna allows approximated seismic event source location and accurate seismic magnitude measurements (Martinsson, 2013). LKAB provided every recording from -4 to 3 within the magnitude scale measured from late 2008 to late 2018 for geovisualization testing. The data was provided as a single CSV file. To ensure proper quantification, the large CSV file was broken into several CSV files that were restricted to hold a maximum of

1045000 lines. The lines were limited because the Python add-on Panda has a fixed boundary of 1048576 lines due to text file limitations. Since the file was ordered by date, verifying that all data was read was crucial as any data points past the threshold became clipped unbeknown to the user. These requirements were not noticeable while observing the raw CSV file but became clear once geovisualized.

Once the files were adequately split, every reading was represented in 3D space as a corresponding sphere. To limit computing memory demands, a range limit of magnitudes can be specified by the user. Each sphere is then automatically coloured in respect to a default colour ramp that is dynamically picked dependent on the range specified (Figure 5.28).

The CSV file also provides seismic event dates allowing seismic propagation assessment. The CSV files also allows Structured Query Language (SQL) communication or python manipulations to seclude desired readings such as occluding specific dates, remove readings from mine works, or clustering abundant seismic readings into a single unit. By observing microseismic clustering, regions susceptible to intact rock failure can be delineated (Cumming- Potvin, 2018). If more information such as lithological or geotechnical properties are imported, improved determination of seismic sources can be made.

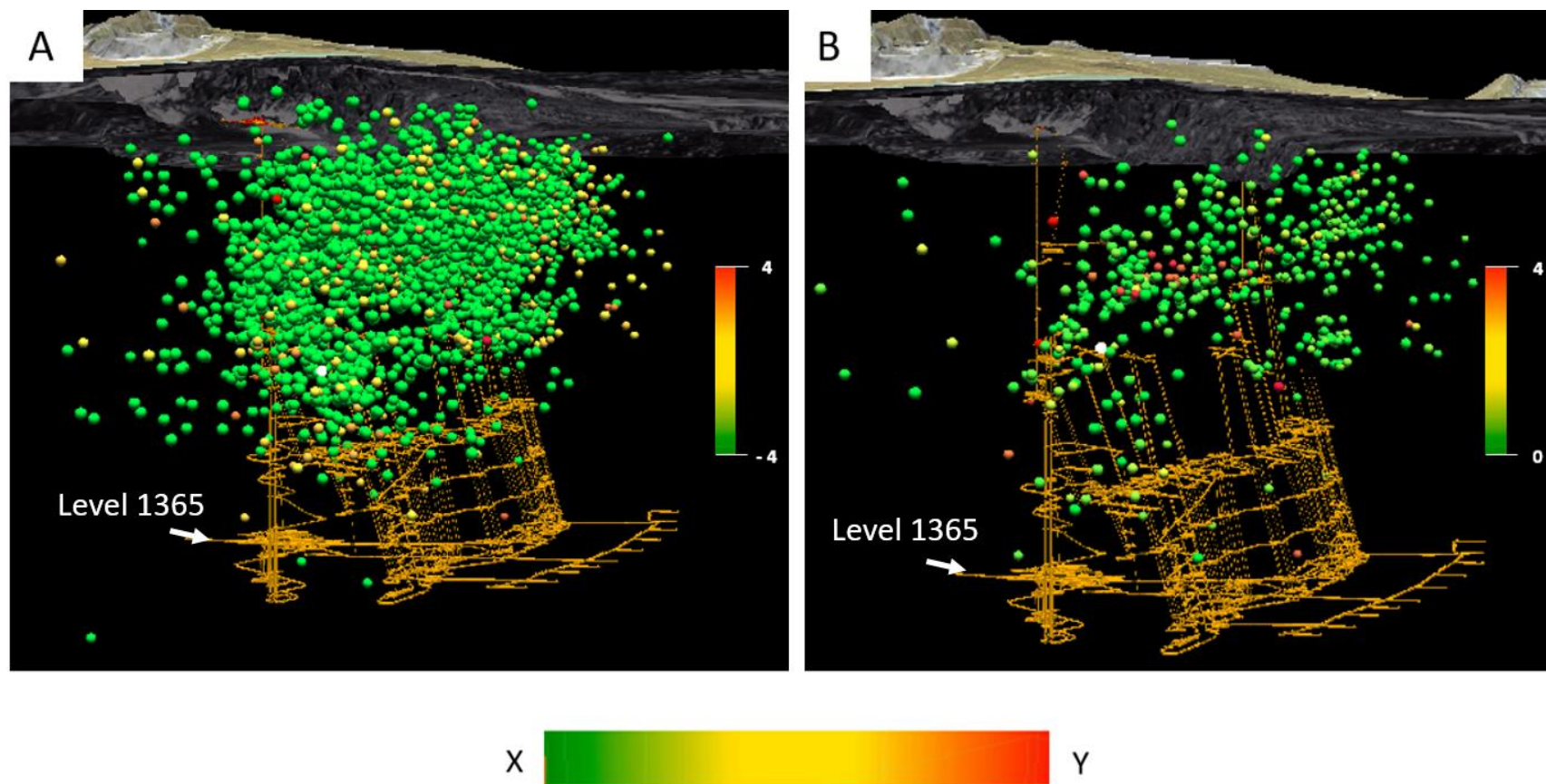


Figure 5.28: Microseismic readings on October 2010 observed with (A) no range limit and (B) with a range limit from 0 – 3 magnitude scale

5.6. Additional Visualization Capabilities

Through the development of each package it became evident that improvements could be gained by direct interaction and visualisation with engineers and geologists very familiar with the varied data sets. Some modifications that could be made to significantly improve analysis include:

1. GPS: Verify the reason why some GPS hubs stopped recording information. GPS lost over time could be re-evaluated and a decision made as to whether they should be completely neglected or reinstalled.
2. InSAR: Import all 23,000 motion estimation points (Mäkitaavola et al., 2016) to generate quantifiable mesh for each respective year allowing 4D movement analysis.
3. Mine Works: Import high-resolution mining infrastructures through the cloud to allow more detailed mine work assessment. Mine works could also be spilt by date to enable a detailed 4D mine model to assist interpreting microseismic readings.
4. Civil Works: Integrating Unity's built-in colliders to every building. Any regions affected by deformation could then be actively observed by changing the colour of the infrastructure once a threshold is surpassed. This would enable better communication with civil engineers and stakeholders by delineating high to moderate risk regions. Additionally, future housing and civil infrastructure plans could be entered in the model to show planned works.
5. Microseismicity: By including geological discontinuities and all known lithological contacts, correlation of seismic events could be investigated in more detail. Additionally, clustering algorithms could be developed through Unity's C# scripting or SQL enabling complex numerical calculations.

There are other data sets that could be implemented for further assessment. Some of these include the incorporation of surficial tension crack records, visual response of current active drilling/blasting zones, and numerical modelling results (Hamdi et al., 2018). With the Kiruna topography being significantly changed each year by subsidence,

new DEM models should also be frequently updated every year. By having a DEM library, differences between observed topographically could also be assessed.

5.7. Potential of MineViz MR

The combination of all the LKAB datasets provided for this thesis allowed the development of a preliminary geovisualization model with significant potential for future modification and extension. All the tools generated were based on the in-house constructed georeferencing package developed for C#, Unity, Blender and Python that enabled information from current geological and engineering practices files such as CSV, DXF, and SHP files to be imported (Figure 5.29). Since Unity and MRTK are not usually used for georeferenced data nor scientific purposes, several routines had to be developed.

By correlating different anomalies together, users can now observe and interpret data that might otherwise have been overseen within different departments. In a mine site where induced displacements are heavily controlled by discontinuity persistence and rock mass anisotropy (Hamdi et al., 2018), 3D and 4D analyses are crucial. As stress concentrations progressively grow, more favourable orientated structures may be involved in failure, forming more abrupt changes in subsidence. Additionally, healed discontinuities commonly observed at Kiruna (Andersson & Rutanen, 2016) might serve as planes of weakness (Day, 2016). Cross communication between different multi-disciplinary experts will become more common and essential as different mine parameters become interlinked. Integrating InSAR, GPS, microseismicity, lithology, structural geology, mine activity, and civil infrastructure into a single MR platform will allow mine site experts to optimize mining geomechanics and subsidence investigation (Figure 5.30 and Figure 5.31). It is important to note that various results are not shared on purpose during this chapter due to a confidentiality agreement, and thus, only surficial base models are shown.

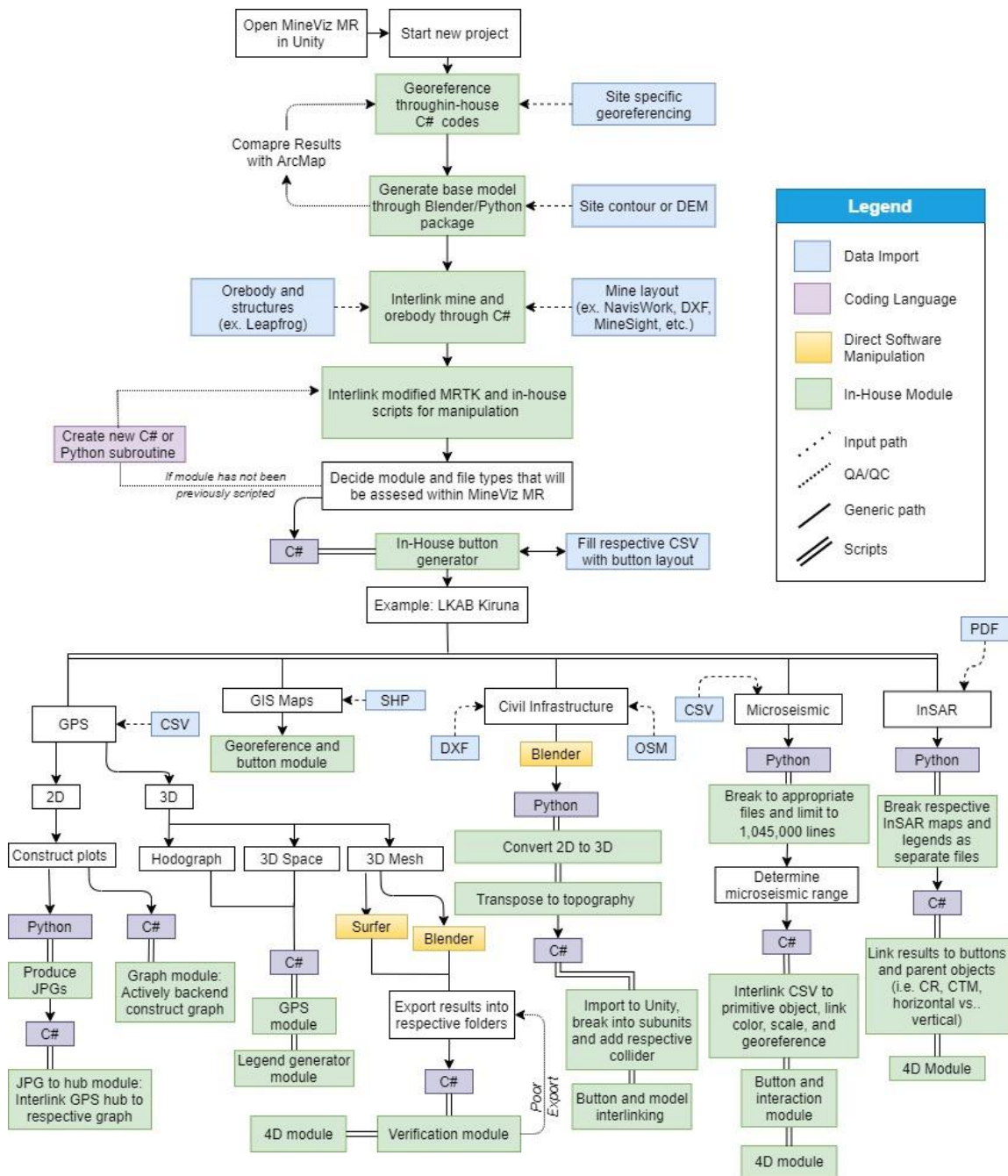


Figure 5.29: Flowchart of MineViz MR with LKAB Kiruna data as an example.

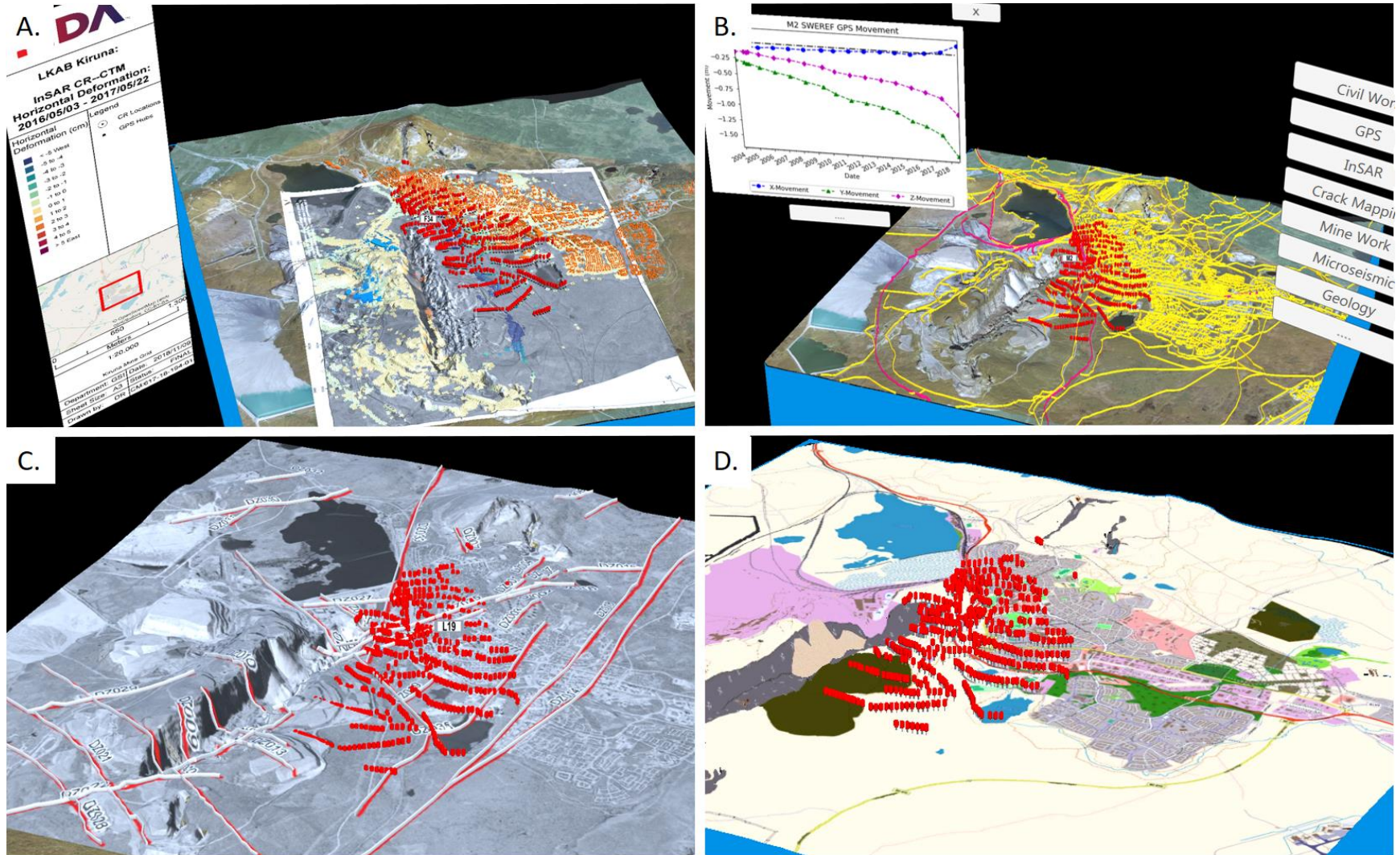


Figure 5.30: MineViz MR with various datasets: (A) GPS hubs, civil infrastructures and InSAR data. (B) Roads, railways, GPS hubs and M2 SWEREF GPS movement. (C) Mattsson et al. (2010) structural map with 3D interpolation. (D) GIS Map retrieved from OSM.

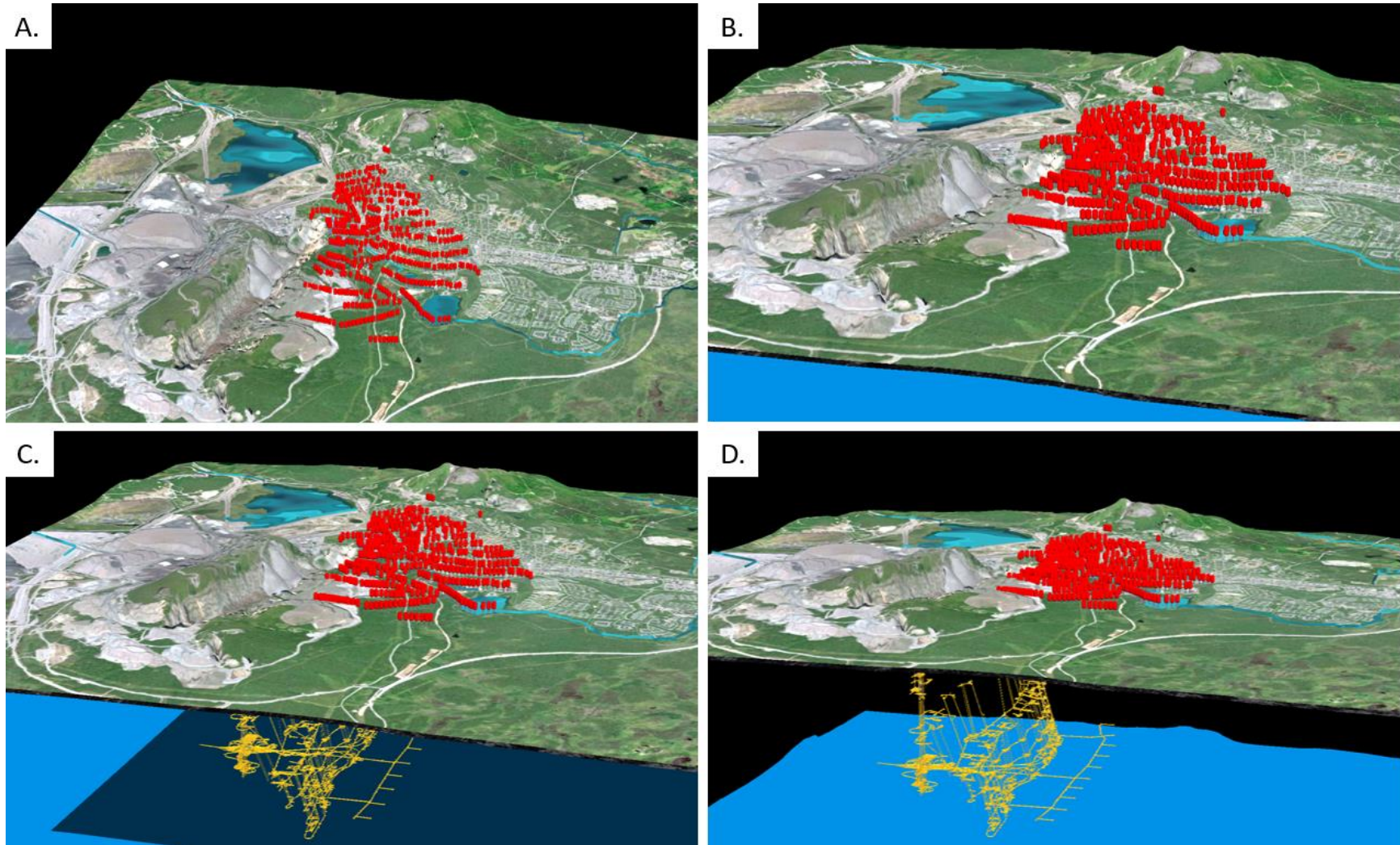


Figure 5.31: MineViz MR with Kiruna datasets. (A) GPS hubs overlaid on a more modern satellite imagery of Kiruna retrieved from Google Earth (2021b) (B) Kiruna observed from a different angle prior to selecting any underground data sets. (C) Once underground data is selected the model expands slowly allowing users to observe underground works clearly. (D) Same point of view as (C) after a few seconds.

Notwithstanding that the results in this research were observed on MR platforms, development of other XR software is possible due the significant versatility of Unity. The export is not only restricted to XR headsets but can also be implemented into cellular devices or can help produce a computer-based application. Being able to easily import ArcMap, PDF, CSV, DEM, OSM, DXF, and many other formats enables the creation of complex models within a single hub. Additionally, with Blender native compatibility, mesh processing and interpretations through python scripts can be integrated.

5.8. Summary and Conclusion

LKAB Kiruna is a complex mine site which has undergone various hydrothermal stages that has weakened the host rock, altered regions to clay minerals, foliated various mineral grains, and host abundant discontinuities (Andersson & Rutanen, 2016; Mattsson et al., 2010). As the mine progressively grows with approximately 28 Mt of crude iron ore mined annually, the extent of mine subsidence effects is progressively becoming larger (Mäkitaavola et al., 2016).

With high anthropogenic activity and the proximity to rural areas, ensuring the safety of infrastructure and personnel is an LKAB priority. By hosting a suite of data ranging from underground to satellite-based instrumentation, LKAB can confidently forecast future deformation and determine optimum response within the Kiruna region. Each type of instrumentation is processed and analysed through different platforms and software packages that facilitate quantifiable and qualitative information. However, such intricate software packages can become rapidly devalued when displaying their results to other experts in mine meetings, as they tend to be simplified to 2D images for PowerPoint presentations or videos that have only minor graphical manipulation capabilities.

A MR model named MineViz MR was developed in this thesis that allows 4D analysis and improve mine experts geovisualization. Through data analysis, active user manipulation of the models, and understanding cross-platform results in a collaborative 3D space improved communication between peers can be achieved. The simplistic rapid updating of the model through only filling respective folders also ensures future user-friendly adaptation of the software. The foundation of MineViz MR can also improves research capabilities within specific departments. For instance, as observed improved

understanding of GPS displacements may be possible when all the point data, 2D, 3D, and 4D data are visualised in a single 3D platform.

By revolutionizing current methodologies of visualization which often undervalue the results of complex instrumentation and numerical models, mines can improve interdepartmental communication. Various levels of the MR model can be made available to different audiences (e.g. dependent on confidentiality, technical content, and stakeholder interest).

The LKAB MR module represents initial steps in the development of an integrated MR/VR module which LKAB Kiruna can freely use in the future work. Like most software, it can continuously be developed, updated, and improved.

Chapter 6.

Conclusions and Recommendations for Future Work

6.1. Introduction

Rapid technological advancement has allowed the virtual paradigm to become a reality, opening new opportunities that improve interpretation and integration of quantitative results. XR platforms can sometimes be perceived only for entertainment and/or restricted to visual application. Through this research it has been demonstrated that XR can also be used for scientific purposes including data acquisition (e.g. CoreLogger MR), QA/QC of 3D information (e.g. Virtual Core), a holographic complex database (e.g. XRCoreShack), and geovisualization between multiple datasets for experts and stakeholders to monitor mining subsidence hazards (e.g. MineViz MR).

All models in this thesis were finalized through Unity, a complex game-engine software. Through the models generated, it is evident that Unity has high potential in providing detailed scientific and numerical analysis that has been overlooked for several years. By integrating Blender, Python, C#, and other geological/engineering software the possibility to create and manipulate models are endless.

6.2. Overall Conclusions

Geoscience and engineering applications within the virtual paradigm have been extremely limited, yet as demonstrated in this research, there is considerable potential for future novel applications. XR can provide improvements in multiple sectors of society such as education, gaming, medical, military, and mining. Remaining aware of how emerging technologies can generate new methodologies that can benefit current practices is imperative for success. MR, VR, and AR capabilities for visual interaction and interpretation in geological and engineering applications within the mining and geological sectors were investigated in this research at different scales.

XR implications for core analysis, which is important for mining and geotechnical investigation, was examined. A MR platform that reduced common errors found in core logging procedures was created using Unity and Blender. An in-house 3D core scanner

was built providing the possibility to archive 3D core information, an important advancement compared to the simplistic 2D images often used in current practice. Through holographic core, high reproducibility of physical core analysis was achieved virtually. Digital representation of the core sample enables a wide array of quantitative geological and geotechnical core data ranging from metre (e.g. borehole imagery) to micron scale (e.g. thin sections) to be georeferenced, superimposed, and integrated along virtual core runs.

With the drilling phase being the most expensive component of mineral exploration, ensuring that both qualitative (i.e. physical core) and quantitative core information (i.e. hyperspectral results) are hosted in a secure and referable platform is crucial. By hosting everything in a single hub (i.e. XRCoreShack), a management framework that reduces the uncertainty commonly observed in unaided traditional core logging is possible. Remote preliminary investigation of the virtual core also allows highlighting of areas that need to be physically assessed or reassessed in greater detail, synergizing core logging evaluation.

Multi-sensor core logging permits remote quality assurance and improves safety not only digitally but also physically. By having a virtual drill core database, revision of logging records and data sets is possible at any time and location. Holographic core observations also certify accountable records prior to destructive core procedures or long periods of poor core handling and storage that can significantly degrade the sample integrity. Laborious physical lifting of core boxes to retrieve necessary samples will also be minimized. Unifying complex core data allows referral for management purposes, information restoration, communal data assessment, and information transfer for disclosure for mineral projects (e.g. Standard 43-101) or selling of property which can have great implications within the mining and oil industry.

The second section of this thesis focused on an XR application (i.e. MR/VR) based on LKAB Kiruna sublevel cave mine, in Sweden, allowing improved communication between multi-disciplinary experts for collective mine site judgment and interpretation. Distinct data sets such as InSAR, GPS, microseismicity, civil planning, and mine works were integrated and transferred within a 4D platform. By observing time dependent mine-induced subsidence in 3D space, a deeper understanding of the causes, outcomes, precautions, and future investigation zones was possible. Such an XR

methodology is also cheaper, more reproducible, and easily transportable compared to physical 3D models.

Technological applications and development has become a necessity for various geological and engineering applications. With XR platforms representing one of the next major technological advancement, remaining at the forefront of this technology is essential. In the aftermath of the COVID-19 pandemic, virtual meetings, social distancing, and remote assessment have all become the new normal, and more companies are noticing that remote work has significant implications and benefits.

The foundation for various XR applications was developed in this research and clearly illustrates the potential benefits that could be incorporated with numerous engineering and geological practices. As with any new application, a testing phase needs to be implemented, and software must be progressively updated to ensure optimal results.

6.3. Research Contributions

An important contribution of this research, at a larger scale, was to demonstrate means to allow the engineer/geoscientist to see beyond the preconceived notion that the virtual paradigm only serves for entertainment. It has been clearly shown through the methodologies developed in this research that XR diverse applications can significantly aid geologists and engineers:

1. Collect data through a non-intrusive holographic interface as observed in CoreLogger MR. With the ability to type data with a Bluetooth or MR keyboard, acquire RQD through MR capabilities (i.e. hand to hand measurements or spatial mapping), and holographic table input (i.e. RMR, GSI, and Q-system) loggers can improve data collection. MR models can be placed anywhere in the user's field of view, at their discretion, enabling effective placement of models. Core logging tailored software also ensures loggers use the most up to date classifications and systems.
2. Improve engineering investigation through enhanced QA/QC, data interpretation, and communication capabilities, observed in this research through the development of XRCoreShack and virtual thin-sections. The use of a digital petrographic platforms reduces the risk of information being lost if

the fragile thin-section is broken or misplaced. The ability to rotate and zoom a virtual thin-section allows petrographic digital mineral grain delineation and analysis. A 3D core scanner that exceeds resolutions of fine lower grain size (>0.125 mm) and enable visual texture enhancers through scripts provides an excellent digital repository for core information.

3. 2D investigations can misrepresent 3D problems, ranging from incorrect data itself to complex models being oversimplified by 2D representation. Minimizing miscommunication between experts can optimize and safeguard information sharing. XR platforms can improve communication between different experts as complete 3D models can be observed in virtual space providing a 3D solution for 3D problems (e.g. XRCoreShack and MineViz MR). With a platform such as MineViz MR, rapid adaptation of 3D mine data can be shared with various users allowing cross-collaboration between peers. Moreover, 3D representation of core characterizes a significant advance compared to current 2D representations that contain large areas of occlusion and prevent proper core measurement. The ability to superimpose geological information ranging on virtual core samples including point data (i.e. thin-section extraction location), 2D data (i.e. thermal, hyperspectral, and laser scanning) and 3D data (i.e. FMI, lithology, discontinuities, and bitumen content) has been demonstrated in this thesis.
4. A 4D approach allows geologist and engineers to isolate potential sources of error or noisy regions that can easily be missed by simplistic 2D or 3D analysis. XR is a excellent conduit for 4D investigation as observed both graphically and through mesh assessment on MineViz MR. The interlinking of InSAR, GPS, microseismicity, civil infrastructure, mine works and different mapping results (i.e. structural, and GIS) in 4D space has been shown to improve multi-disciplinary communication.

During this thesis various scripts have been developed to allow importing of file types commonly used in geological, geotechnical, and engineering practices but not normally applicable for game development. Since Unity and Blender were not designed for geological nor engineering means, both software root scripting languages (e.g. C# and Python) were used to develop tools that enable their resourceful toolbox to be used for

scientific purposes. Some of these scripts include but are not limited to: (i) Mine mesh simplification; (ii) RQD calculator; (iii) Georeferencing; (iv) CSV reader for GPS and microseismic tracking; (v) PDF mesh texturing; (vi) Legend, scaling, and texture development in Unity from input files; and (vii) UI development through XR platform. Once scripted, adaptation of new powerful platform for visualization and interpretation (e.g. XR) was able to be interlinked with common geological and engineering file types such as SHP, DXF, and CSV. For example, by using Blender versatile toolbox, Python scripts were generated to assist with raw OSM and SHP files to construct respective building, roads, railways, and other infrastructures. Since OSM and SHP files are normally 2D, scripts were developed to generate representative 3D models that are levelled and georeferenced with the specified topography.

All the packages built in this research required UI interaction. All UIs were constructed through C# rather than Unity's API to enable dynamic data imports. Such an approach allows different meshes and data sets to be imported without requiring major updating or corrections to the packages. For instance, through the input of a CSV file that contains GPS movement an output of georeferenced GPS models, 2D graphs, hodographs, GPS line breakages, and corresponding UI are all automatically generated once the coordinate system is specified. By having most of the MineViz MR scripted, implementation to other mines sites is available if appropriate files are provided.

Scripting all models enables geoscientist and engineers to easily import models from other complex modelling software without requiring major knowledge of either coding or Unity, allowing easy future adaptation and improvements. If models were solely generated through Unity's API, dynamic adaptation would have been limited as new UI's would have to be generated for each project.

Another major contribution of this research is the construction of an in-house core scanner that enables complete 3D representation, 2.5D scanning, and archiving of crucial core data. 3D core models allow remote core analysis and even calculate parameters that are normally time consuming to quantify (i.e. RQD). Core digitization also allows rapid roughness measurement, depth updating, structural delineation, lithological breaks, and various other measurements allowing significant potential for future novel work that synergizes core logging. By easily importing CSV files that are automatically interlinked to the respective sample, advanced QA/QC is possible. Any

information that is evidently misinterpreted or potentially wrong can be flagged and then observed with greater detail on site. Additionally, with the implementation of the texture enhancers and manipulator scripts, specific mineral and structural attributes that are not evident with the naked eye can be highlighted easily. With the HoloLens 2 ergonomic dismantling that allows the flipping of the lenses, physical and virtual core samples can be assessed contemporaneously. XRCoreShack can also enable synchronous sample comparison of cores from different localities, especially when implemented in VR, when multiple samples are brought into the user's perspective.

Computer code and procedures for complex drill core dataset analysis has been tested and developed in this thesis through the superposition of hyperspectral, thermal, and borehole imagery in MR. By archiving a 3D drill database in a virtual platform, such as XRCoreShack, geologists and engineers can log and assess core remotely.

It is important to emphasise that the basis of the various tools developed and XR implementation during this thesis was originally as a proof of concept but clearly there is major potential for future work which will be discussed in below. The challenges that were faced are minimal relative to the potential for future work. The roots of Unity and XR might have been in the gaming industry; this thesis, however, has demonstrated the versatility it offers in scientific investigations and the potential for game-changing mediums that augment geological and engineering work.

6.4. Current Challenges

6.4.1. Overall Challenges within the Virtual Paradigm

During development, hardware restrictions were evident within all XR platforms. By optimising and reprocessing each imported model (e.g. decimating and “baking” the texture) most geological models became feasible. However, some textures in the HoloLens 1 were still undervalued due to the limited pixel quantity. In applications such as XRCoreShack where texture is fundamental, such a limitation was of concern. The significant improvement introduced by the HoloLens 2, has addressed these issues.

Another limitation within the virtual paradigm is the heavy dependence on user experience. Despite VR being able to display the virtual core and mine models in higher detail, the need to wear VR headsets may discourage many users. During presentations

of the research to some stakeholders and peers it was also noted that there is considerable reluctance by some to adopt new practices, as their tendency is to continue with accustomed procedures. This issue has also been observable with the introduction of new data sources such hyperspectral scanning into core logging procedures despite being proven to be effective (Esmaili, 2020). It is thought that refusal of new practices is not only due to the learning curve but also because many new practices tend to remove standard methodologies entirely. With MR being a platform with intuitive commands that can interlink new and old practices, future adaptation of these mediums might be introduced more effortlessly.

Issues while filming videos within the HoloLens were also encountered as videos and images are only captured from a single lens, causing the resulting media to not capture the complete MR experience where models coexist with the physical world. Furthermore, the resolution of the captured video is also lower than what a user observes. This belittled the true resolution a user observes while running the developed applications.

It is emphasised that many of the limitations described in this thesis are only seen as momentary obstacles and will be undoubtedly overcome in the future. As hardware improves, software will adjust to new capabilities, and thus, developers must stay vigilant to remain at the forefront of the application market. Technological advancement within the XR platforms is observed as the new technological “gold rush” that is comparable to the rapid cell phone development growth over recent decades. Cell phones started solely as portable phone two decades ago and now smart phones host hardware capabilities greater than early computers and even offer higher photographic resolution than many digital cameras. For instance, the iPhone 12 Pro now has LiDAR capabilities that also enables AR interaction and rapid camera focus (Apple, 2021).

6.4.2. Challenges in Virtual Core Development

The biggest issue faced in this research during the CoreLogger development was that it was developed for the HoloLens 1 but once finalized, the HoloLens 2 was released. Luckily, most of the codes and UI developed can be easily imported and updated to the new hardware. However, some other scripts were integrated within the previous HoloToolkit, which has been significantly adjusted, requiring more laborious updating, and debugging.

In XRCoreShack core scanning mesh resolution was also purposely decreased to fit the HoloLens specifications and to reduce unnecessary complexity. To ensure optimum meshing while scanning, a blueprint for a new core scanner and software corrections have been built and planned for future work. Some of the limitations that will be addressed include:

1. Metashape's built-in masking tool can sometimes ineffectively isolate the core samples from a consistent background. An in-house masking code that secludes the subject more effectively from known photographic properties will be developed.
2. Ensuring the right number of images are taken is essential. Too many photographs resulted in increased processing time, while few photographs caused errors to arise. More testing is required to assess the adequate number.
3. Metashape has a more equilateral mesh decimation algorithm than Blender. Therefore, resolution reduction should be conducted in Blender as it can be implemented in focused regions. An automated Python script which isolates and simplifies cylindrical and flat portions of the mesh would reduce vertex quantity.
4. Test other software packages that can conduct photogrammetry.
5. Test whether close-range laser scanner can generate improved results. Photogrammetry was used in this project due to high importance of texturing.

The XRCoreShack module applicability was limited due to the quantity of data that was available and inaccessibility of a complete complex core run (e.g. physical core that contained a suite of quantitative (e.g. previous made logs) and qualitative data (e.g. hyperspectral, assay results, etc.)). Additionally, only three core boxes were scanned preventing the observation of a whole core run virtually or the systematic comparison of two different core boxes with different localities but similar attributes.

6.4.3. Challenges within the Kiruna MineViz MR Model

The largest limitation of the Kiruna MineViz MR model is the constant increase of complex information. Currently, the final model mostly serves as a communication

platform in which various data types can be easily introduced and updated by simply populating specific folders. However, only a selected amount of information can be imported due to the memory limitation of the HoloLens. Data resolution was also reduced to fit MR capabilities, but such a reduction was controlled and monitored.

Another challenge was that the model was developed on the HoloLens 1. Microsoft is now only selling HoloLens 2, which enforces a required update on the model.

6.5. Recommendations for Future Work

All applications built for this thesis can be significantly enriched in a variety of ways. CoreLogger MR could be improved by integrating XR dictation scripts into the application allowing people to verbally describe their observation rather than typing it. Geological and geotechnical terminology would have to be implemented to ensure dictation captures every word effectively. CoreLogger MR could also exploit the HoloLens capability of interlinking multiple lenses at once to allow multiple inputs in real-time. This would allow team logging, which has proven to be more than twice as effective as a single logger (Gwynn et al., 2013). This application is currently not a commercially feasible application as it still requires rigorous field testing and debugging. Nonetheless, this application served as a proof of concept to show how the virtual paradigm can be used beyond visualization in geoscience and engineering.

Two major plans to improve the core scanners for more automated scanning that is more efficient and detailed are planned. The first proposed improvement is an on-site rig that allows scanning of freshly drilled core with no or limited post-drilling damage from handling or alteration. The other is designed to scan cores that have been already stored and require archiving into a complex 3D database.

Perfecting both the rigs and the software portion of core scanning is crucial to make the procedure reproducible at a larger scale. Metashape and Blender both run through Python, and thus, a complex script that completely automates the backend portion could be developed. Once the rig has been perfected, various software improvements could be developed including:

1. Combine both CoreLogger MR and XRCoreShack to permit complete remote preliminary assessment.

2. Since all the core boxes are digitized, new depth measurements can be systematically updated along all respective core boxes.
3. Constrain similar observations of different core runs, to host visual lithological continuity.
4. Install other cameras such as hyperspectral, XRF or other quantitative mediums on the rig to enable improved 3D quantifiable analysis (i.e. 3D hyperspectral analysis).
5. Automated modal mineralogy, grain size distribution, and shape recognition have been investigated by several researchers and industry (Acosta et al., 2019; Mine & Tiu, 2017; Partio et al., 2002; Tessier et al., 2007). Recent studies by Pérez-Barnuevo et al. (2018) used grey scale intensity and spatial organization of pixels from 245 core images to categorize six major patterns diagnostic to their field of study. Pérez-Barnuevo et al. (2018) based his findings on 30 x 40 mm focused area with 39 μ m resolution. If a similar approach was completed with the in-house core scanner developed in this research, an array of images would improve automated assumptions because there are more pixels to use in the assessment and the entire 3D sample would be captured. Similar micron level resolution could be achieved if the camera were anchored at either a closer setting, smaller focal length, or the lens was changed.
6. Interlinking pixel values from various cameras can support a machine learning platform that compares pixels to pixel annotations. The user could then review the machine learning results through MR, VR, AR, or directly through a computer application and then determine whether the computed results are representative. By considering the users personal evaluation, a complete “black box” approach would be diminished.
7. Digitized holographic core also permits discontinuity roughness estimation in each core end to be measured through mesh assessment. The in-house roughness profile demonstrated by Onsel et al. (2018) can be used to compute various roughness coefficients. Since this procedure can be computationally intensive, it would be undertaken during the core digitization

stage. The results and profile of each discontinuity could then be used to potentially distinguish natural and mechanical fractures (Olson, 2013).

8. By assessing each core end, the alpha angle can also be measured by interpolating a plane along each discontinuity surface. A similar methodology has been used to measure discontinuity orientation in virtual outcrops (Sturzenegger & Stead, 2009). If correctly used, the algorithm has the potential to significantly reduce the required time to measure alpha angles via geotechnical protractor arms or transparent protractor templates (Holcombe, 2013). By implementing a systematic scan core feedback, logging would be accelerated, allowing other time consuming parameters, such as CGSI (Day, 2016) to become more feasible to record.

If alpha angles are computed effectively, they could then be fitted to match any derived angles obtained from borehole imagery. This would enable a similar approach to core-to-log (CTL) alignment (Fernández-Ibáñez et al., 2018) but would be a virtual-core-to-log (VCTL) instead. To date, CTL has helped validate image log structures to core structures. Issues arise when confirming whether written core information is accurate and representative because poor representation of structures can sometimes be interpreted (Tavakoli, 2018). VCTL validation would also significantly assist current time-consuming methodologies for depth correlation between the rock mass and image log (Gwynn et al., 2013). Correct VCTL alignment would also derive orientated core with the same error window observed in borehole imagery. In order to assess VCTL development, raw data on both borehole imagery and the respective core would be required. Such a concept was indirectly demonstrated in this thesis by placing the virtual cores inside borehole imagery.

Reference to the physical core remains primitive as it based only on 2D images, a log, and/or requires the personnel to retrieve the physical sample from the core shack. With a 3D core scanner, core referral would be routine in practice. The large database that would inevitably be formed from the complex core scanner would eventually require a large cloud storage. Users would then simply have to import the respective temporary files onto their computer or XR headset to enable editing or assessment. Hosting all information in cloud storage further enhances the proposed machine learning platform because there would be more training data available from various sites while maintaining

confidentiality. As more cores are scanned and assessed, a library of predefined textures could be produced. With MR capabilities, appropriate visualization that can bridge data-driven machine learning and human theoretical driven research can effectively coexist (Turkay et al., 2017).

Virtual core is only successful if displayed correctly, and thus, platforms like XRCoreShack must be perfected to ensure optimum outcomes. If it is adapted to other software packages, data could be retrieved more effectively. For instance, a user could be allowed to dynamically click on a complex 3D model map, such as Leapfrog Geo (2021) or MineSight (2021), to retrieve the referenced core box within XRCoreShack.

Unlike both core modules, the prospect on how to advance the MineViz MR model is highly subjected in improving user experience. To complete such a goal, continuous user feedback would have to be implemented to ensure dynamic construction of software. With further contribution, other mine features that can benefit analysis and communication within LKAB Kiruna could be added. For example, the possibility to take advantage of their high-resolution tunnel scans obtained from laser scanning virtual mapping or analysis. If the results were hosted in cloud space or if the hardware was changed to VR, where memory is not a limiting factor, referencing to each sector could be made. A program that enables a user to click an AOI, and immediately visualize the section at a higher resolution could be made. A similar approach of retrieving information from other platforms was investigating during thin-section analysis (Section 4.4.2).

It is emphasized that XR capabilities are not restricted to only core or mine analysis as it can be applied to various geoscience applications (Table 6-1). In a science such as earth science where both quantitative and qualitative information are essential, extending realities through MR, VR, and AR applicability can only improve current platforms that are being used.

Table 6-1: Examples of possible XR geoscience/engineering applications.

Site Assessment	<ul style="list-style-type: none"> - <u>VR mapping</u>: Structural and lithological mapping of inaccessible areas. Currently being investigated by SRK Vancouver and SFU through EasyMap MR (Onsel et al., 2019). - <u>Geological history</u>: Time lapse of geological history of a site through XR
Teaching	<ul style="list-style-type: none"> - <u>Sample identification</u>: Helps student visually observe where specific mineral grains or fossils parts are located in a sample. The petrographic microscope module created could also be used for more in-depth petrographic education - <u>Structure</u>: Improved visualisation and teaching of stereonet and other visually challenging structural geological concepts.
Mining Engineering	<ul style="list-style-type: none"> - <u>Dispatch and excavator</u>: Overlay short term planning results or dispatch requests on the excavator operators FOV for direct visual response. - <u>Planner</u>: Host short term plan meeting in XR to provide a better understanding of the blasting, excavation, and targets (mine operating cycle) for the day or week.
Landslide Mapping	<ul style="list-style-type: none"> - <u>Terrain mapper</u>: Virtual 3D mapping in MR or VR, allowing polygon reconstruction that are exported as georeferenced model. - <u>Holographic landslide database</u>: A landslide database that include site investigation/monitoring for various sights (Mysiorek, 2019b).
Geophysics	<ul style="list-style-type: none"> - <u>Geophysics Viewer</u>: Analyse geophysics results in 3D space with other complementary data sets. - <u>Augmented geophysical viewer</u>: Link the HoloLens to a GPS to anchor geophysics and exploration results in the field for augment field assessment.
Hydrogeology	<ul style="list-style-type: none"> - <u>Fluvial assessment</u>: Using Blender's realistic water and other viscous like material rendering capabilities to assess surficial water movement. Results can then be brought into XR for further analysis. - <u>Ground water assessment</u>: Observe ground water contamination plume migration, and cones of drawdown development.
Rock Engineering	<ul style="list-style-type: none"> - <u>Discrete fracture network (DFN) model</u>: Observe complex numerical modelling, such as DFN models, for further assessment. - <u>Laboratory tests</u>: Observe laboratory test along the physical or virtual sample. Models construction of the prior and after destructive tests can be conducted to verify result legitimacy.

References

- Abay, T. B. (2017). Diversity of Petroleum in terms of Source Rock Properties and Secondary Alteration Processes A study of source rocks, migrated petroleum, oils and condensates from the Norwegian Continental Shelf. PhD Thesis. University of Oslo Norway. ISSN 1501-7710.
- Agisoft (2021) Discover Intelligent Photogrammetry with Metashape. Retrieved from: <https://www.agisoft.com/>
- Alberta Energy Regulator (2021) Directives: Directives Set Out Requirements or Process that Energy Companies Operating in Alberta Must Follow. Alberta Energy Regulator (AER). Retrieved from: <https://www.aer.ca/regulating-development/rules-and-directives/directives.html>
- Aboutaleb, S., Behnia, M., Bagherpour, R., & Bluekian, B. (2018). Using non-destructive tests for estimating uniaxial compressive strength and static Young's modulus of carbonate rocks via some modeling techniques. *Bulletin of Engineering Geology and the Environment*, 77(4), 1717–1728. <https://doi.org/10.1007/s10064-017-1043-2>
- Acosta, I. C. C., Khodadadzadeh, M., Tusa, L., Ghamisi, P., & Gloaguen, R. (2019). A Machine learning framework for drill-core mineral mapping using hyperspectral and high-resolution mineralogical data fusion. *IEEE Journal of Selected Topics in Applied Earth Observations and Remote Sensing*, 12(12), 4829–4842. <https://doi.org/10.1109/JSTARS.2019.2924292>
- Allcoat, D., & von Mühlenen, A. (2018). Learning in virtual reality: Effects on performance, emotion and engagement. *Research in Learning Technology*, Vol. 26 Num. 2140. <https://doi.org/10.25304/rlt.v26.2140>
- American Petroleum Institute (1998) Recommender Practices for Core Analysis [Second Edition]. American Petroleum Institute (API).
- Andersson, U., & Rutanen, H. (2016). *Geological features in and around the Kiirunavaara ore body, northernmost Sweden, and some implications*. 2015, 2989. <https://doi.org/10.13140/RG.2.2.30031.89769>
- Andra Baduge, A. W., Henschel, M. D., Hobbs, S., Buehler, S. A., Ekman, J., & Lehrbass, B. (2016). Seasonal variation of coherence in SAR interferograms in Kiruna, Northern Sweden. *International Journal of Remote Sensing*, 37(2), 370–387. <https://doi.org/10.1080/01431161.2014.915435>
- Andrienko, G., Andrienko, N., Jankowski, P., Keim, D., Kraak, M. J., MacEachren, A., & Wrobel, S. (2007). Geovisual analytics for spatial decision support: Setting the research agenda. *International Journal of Geographical Information Science*, 21(8), 839–857. <https://doi.org/10.1080/13658810701349011>

- Apple (2021) iPhone 12 Pro: It's a Leap Year. Retrieved from:
<https://www.apple.com/ca/iphone-12-pro/>
- Atlas Copco. (2007). Mining methods in underground mining. *Second Edition*, 7–10.
- Autodesk (2021) Navisworks: 3D model review software for architecture, engineering and construction. Retrieved from:
<https://www.autodesk.ca/en/products/navisworks/overview?plc=NAVSIM&term=1-YEAR&support=ADVANCED&quantity=1>
- Bamler, R., & Hartl, P. (1998). *Synthetic aperture radar interferometry*. In Inverse Problem Vol.14 R1-R54.
- Bar, N., & Barton, N. (2017). The Q-Slope method for rock slope engineering. *Rock Mechanics and Rock Engineering*, 50(12), 3307–3322.
<https://doi.org/10.1007/s00603-017-1305-0>
- Bardeen L. (2017) Ford Bring Microsoft HoloLens to Design Studio; Drives speed, Creativity and Collaboration. Microsoft. Retrieved from:
<https://blogs.windows.com/devices/2017/09/20/ford-brings-microsoft-hololens-to-design-studio-drives-speed-creativity-and-collaboration/#FM4BqfezgjssPXP.97>
- Barton, N., Lien, R., Lunde, J., Barton, L., & Lunde. (1974) Engineering Classification of Rock Masses for the Design of Tunnel Support. *Rock Mechanics Felsmechanik mecanique des Roches* (Vol. 6 , Issue 106, pp. 189-236). DOI: 10.1007/BF01239496
- BGC (2020) Clarity Through Holographic Visualization: BGC Introduces the Ada Platform. BGC Engineering Inc. Retrieved from:
<https://www.bgcengineering.ca/3d-visualization.html>
- Bhatnagar, A., Khandelwal, M., & Rao, K. U. M. (2011). Laboratory investigations for the role of flushing media in diamond drilling of marble. *Rock Mechanics and Rock Engineering*, 44(3), 349–356. <https://doi.org/10.1007/s00603-011-0144-7>
- Bieniawski, Z. T. (1973) Engineering Classification of Jointed Rock Masses. *Transaction of the South African Institution of Civil Engineers*, 15, 335-344
- Bieniawski, Z. T. (1989) *Engineering Rock Mass Classifications: A Complete Manual for Engineers and Geologist in Mining, Civil, and Petroleum Engineering*. Wiley-Interscience. ISBN: 0-471-60172-1
- Bieniawski, Z.T. (1976) Rock Mass Classification in Rock Engineering. In Bieniawski Z. T. (Ed.) *Symposium on Exploration for Rock Engineering*, Balkema: Rotterdam, pp. 97-106.
- Blender (2021) Download Blender. Retrieved from: <https://www.blender.org/download/>

- Boneworks (2021) Stress Level Zero Boneworks. Valve Corporation. Retrieved from: <https://store.steampowered.com/app/823500/BONEWORKS/>
- Borchers, J. W., Grabert, V. K., Carpenter, M., Dalgish, B., & Cannon, D. (2014). Land Subsidence from Groundwater Use in California. *California Water Foundation*, Vol. 4
- Brady, B. H., & Brown, E. T. (2006) *Rock Mechanics for Underground Mining*. (3rd edition). Springer. ISBN: 978-1-4020-2116-9
- Brown E.T. (1981) Rock Characterization, Testing and Monitoring – ISTM suggested methods, 171 – 183. Oxford, Pergamon
- Brown, L. G. (2015). Seismic Hazard Environment Using Apparent Stress Ratio for Mining-Induced Seismic Events. *Seismic Hazard Evaluation Using Apparent Stress Ratio for Mining-Induced Seismic Event, Mater Thesis. Laurentian University, Ontario, Canada.*
- Brunker (2021) Tracer 5 Family of Portable XRF Spectrometer. Brunker. Retrieved from: <https://www.bruker.com/products/x-ray-diffraction-and-elemental-analysis/handheld-xrf/tracer-5-family/overview.html>
- Brunner (2020) Simulation Products: Precision, Performance, and Quality. Brunner Elektronik AG. Retrieved from: <https://www.brunner-innovation.swiss/products-technologies/simulation-products/>
- Canada Mines (2020) Core Logging 101: The Basics of Logging Core for Exploration. Canada Mines. Retrieved from: <https://canadamines.ca/basics-of-logging-core-samples-for-mineral-exploration/>
- Cannon, S. (2016). *Petrophysics: A Practical Guide*. John Wiley & Sons Ltd. ISBN: 1-118-74672-4
- Cartwright, W., & Peterson, M. P. (2007). Multimedia Cartography. In *Multimedia Cartography*. <https://doi.org/10.1007/978-3-540-36651-5>
- CBInsight (2016) Google Goofs: 23 of the Company's Biggest Product Flops. BC Information Services Inc. Retrieved from: <https://www.cbinsights.com/research/google-product-flops/>
- Chan, M. A., Bowen, B. B., Corsetti, F. A., Farrand, W. H., Law, E. S., Newsom, H. E., Spear, J. R., & Thompson, D. R. (2019). Exploring, mapping, and data management integration of habitable environments in astrobiology. *Frontiers in Microbiology* (Vol. 10 Num. 147). <https://doi.org/10.3389/fmicb.2019.00147>
- CloudCompare (2021) CloudCompare: 3D Point Cloud and Mesh Processing Software. Retrieved from: <https://www.danielgm.net/cc/>

- Corescan (2021) Automated Mineralogy and Texture. Corescan. Retrieved from:
<http://www.corescan.com.au/>
- Çöltekin, A., Bleisch, S., Andrienko, G., & Dykes, J. (2017). Persistent challenges in geovisualization—a community perspective. *International Journal of Cartography*, Vol. 3, 115–139. <https://doi.org/10.1080/23729333.2017.1302910>
- Cracknell, M. J., Parbhakar-Fox, A., Jackson, L., & Savinova, E. (2018). Automated acid rock drainage indexing from drill core imagery. *Minerals*, 8(12), 1–11. <https://doi.org/10.3390/min8120571>
- Craigie, N. (2018) Principles of Elemental Chemostratigraphy: A Practical User Guide. Advances in Oil and Gas Exploration & Production. Springer. ISBN: 978-3-319-71215-4
- Cruz, R. A. Q., Cacau, D. C., Dos Santos, R. M., Pereira, E. J. R., Leta, F. R., & Clua, E. G. (2017). Improving Accuracy of Automatic Fracture Detection in Borehole Images with Deep Learning and GPUs. *Proceedings - 30th Conference on Graphics, Patterns and Images, SIBGRAPI 2017*, 345–350. <https://doi.org/10.1109/SIBGRAPI.2017.52>
- Cui, N., Kharel, P., & Gruev, V. (2017). Augmented reality with Microsoft HoloLens holograms for near infrared fluorescence based image guided surgery. *Molecular-Guided Surgery: Molecules, Devices, and Applications III*, Vol. 1004. <https://doi.org/10.1117/12.2251625>
- Cumming-Potvin, D. (2018). *An Extended Conceptual Model of Caving Mechanics*. PhD Thesis. The University of Western Australia.
- Cummings, R. A, Kendorski, F. S. and Bieniawski, Z. T. (1982) Caving Rock Mass Classification and Support Estimation. U.S. Bureau of Mines Contract Report #J01000103 Chicago: Engineers International.
- Curlander, J. C. and McDonough R. N. (1991) Synthetic Aperture Radar – Systems and Signal Processing, John Wiley & Sons Inc.
- Davies, C. (2019) HoloLens 2: The Four Big Improvements. SlashGear. Retrieved from:
<https://www.slashgear.com/microsoft-hololens-2-four-key-improvements-comfort-fov-holograms-25567353/>
- Day, J. J. (2016). The influence of healed intrablock rockmass structure on the behaviour of deep excavations in complex rockmasses. *PhD Thesis. Queen's University. Kingston, Ontario, Canada.*
- Deere D. U. (1963) Technical Description of Rock Cores for Engineering Purpose, Rock Mechanics and Engineering Geology, Vol. 1, No. 1, pp. 16 – 22

- Deere D.U., Hendron A. J., Patton F. D. and Cording E. J. (1967) Design of Surface and Near Surface Construction in Rock. In Fairhurst C. (Ed.) Failure and Breakage of Rock, Proceedings of the 8th U.S. Symposium on Rock Mechanics. New York: SME-AIME
- Deere D.U. and Deere D.W. (1989) Rock Quality Designation (RQD) After 20 Years. U.S. Army Corps of Engineers Contract Report GL-89-1. Vicksburg, MS: Waterways Experimental Station
- Dieleman, J. L., Baral, R., Birger, M., Bui, A. L., Bulchis, A., Chapin, A., Hamavid, H., Horst, C., Johnson, E. K., Joseph, J., Lavado, R., Lomsadze, L., Reynolds, A., Squires, E., Campbell, M., DeCenso, B., Dicker, D., Flaxman, A. D., Gabert, R., ... Murray, C. J. L. (2016). US spending on personal health care and public health, 1996-2013. *JAMA - Journal of the American Medical Association*, 316 (24), 2627–2646. <https://doi.org/10.1001/jama.2016.16885>
- DJI (2021) DJI Googles: See a Different World. DJI. Retrieved from: <https://www.dji.com/ca/dji-goggles>
- Doornhof, D., Kristiansen, T. G., Nagel, N. B., Pattillo, P. D., & Sayers, C. (2012). Compaction and subsidence. *Environmental Science and Engineering (Subseries: Environmental Science)*, 9783642291036, 343–363. https://doi.org/10.1007/978-3-642-29104-3_15
- Duplancic P. (2001) Characterisation of Caving Mechanisms Through Analysis of Stress and Seismicity, PhD thesis, The University of Western Australia, Perth.
- Edfelt, Å. (2007). *The Tjårrojåkka Apatite-Iron and Cu (-Au) Deposits, Northern Sweden*. PhD Thesis. Luleå University of Technology, Luleå, Sweden.
- Elmo, D.; & Stead, D. (2021) The Role of Behavioural Factors and Cognitive Biases in Rock Engineering. *Rock Mechanics and Rock Engineering*. <https://doi.org/10.1007/s00603-021-02385-3>.
- Enersoft (2021) Introducing Geological Artificial Intelligence. Retrieved from: <https://enersoft.ca/>
- Epic Games (2021) Unreal Engine: Make Something Unreal. Epic Games Inc. Retrieved from: <https://www.unrealengine.com/en-US/>
- Esmaili K. (2020) Improving the Quality and Quantity of Geotechnical Core Logging Data. In Fontoura S., Rocca R. J., Mendoza J. F. (Ed.) Rock Mechanics for Natural Resources and Infrastructure Development. Proceeding in Earth and Geoscience Vol. 6. ISRM. ISBN: 978-0-367-42284-4
- ESRI (2021) ArcMap. Retrieved from: <https://desktop.arcgis.com/en/arcmap/>

- Facey, N. (2019) Leveraging Technology in Mining. Finger Food Studios. Retrieved from: <https://www.fingerfoodatg.com/articles/leverage-tech-optimize-mining-operation/>
- Fernández-Ibáñez, F., DeGraff, J. M., & Ibrayev, F. (2018). Integrating borehole image logs with core: A method to enhance subsurface fracture characterization. *AAPG Bulletin*, 102(6), 1067–1090. <https://doi.org/10.1306/0726171609317002>
- Fink C. (2019) Qaladrom Converges XR Tech with New Snapdragon XR2. Forbes. Retrieved from: <https://www.forbes.com/sites/chariefink/2019/12/05/qualcomm-converges-xr-tech-with-new-snapdragon-xr2/#7c1dcadc39b4>
- FLIR Systems (2014) FLIR SC7000 Series: State-of-the-art Infrared Technology for R&D/Science. FLIR Systems Inc. Retrieved from: http://www.flirmedia.com/MMC/THG/Brochures/RND_017/RND_017_US.pdf
- Forster D. (2015) Classification of Rock Masses for Dam Engineering: A New System-Rock Condition Number. Proceedings of the Australian Commission on Large Dams Symposium. Brisbane.
- Fox K. (2017) The Usefulness of NI 43-101 technical reports for Financial Analysts. Elsevier. Resources Policy Vol. 51 pp. 225-233.
- Fresia, B., Ross, P. S., Gloaguen, E., & Bourke, A. (2017). Lithological discrimination based on statistical analysis of multi-sensor drill core logging data in the Matagami VMS district, Quebec, Canada. *Ore Geology Reviews* 80: pp. 552–563. <https://doi.org/10.1016/j.oregeorev.2016.07.019>
- Frietsch, R., & Perdahl, J. A. (1995). Rare earth elements in apatite and magnetite in Kiruna-type iron ores and some other iron ore types. *Ore Geology Reviews*, 9(6), 489–510. [https://doi.org/10.1016/0169-1368\(94\)00015-G](https://doi.org/10.1016/0169-1368(94)00015-G)
- Galeon D. (2017) Ford is Using Microsoft's HoloLens to Design Cars in Mixed Reality: AR/VR Technology Offers Designers a New World to Tinker With. Futurism. Retrieved from: <https://futurism.com/ford-is-using-microsofts-hololens-to-design-cars-in-mixed-reality>
- Geijer, P. (1931) The iron ores of the Kiruna type, geographical distribution, geological. Geological Survey of Sweden Serie C (367): 1-39.
- GitHub (2020) Mixed Reality Toolkit (MRTK) – Unity. Retrieved from: <https://github.com/microsoft/MixedRealityToolkit-Unity>
- Golden Software (2021) Golden Software Products: Choose the Right Product. Golden Software LLC. Retrieved from: <https://www.goldensoftware.com/products>
- Google (2021a) Discover Glass Enterprise Edition: A Hands-free Device for Smarter and Faster Hand-on Work. Retrieved from: <https://www.google.com/glass/start/>

- Google (2021b) The World's Most Detailed Globe. Retrieved from:
<https://www.google.com/earth/>
- Gooneratne, C. P., Li, B., Deffenbaugh, M., & Moellendick, T. (2019). *Instruments, Measurement Principles and Communication Technologies for Downhole Drilling Environments* (Vol. 32). <http://link.springer.com/10.1007/978-3-030-04900-3>
- Govil, H., Gill, N., Rajendran, S., Santosh, M., & Kumar, S. (2018). Identification of new base metal mineralization in Kumaon Himalaya, India, using hyperspectral remote sensing and hydrothermal alteration. *Ore Geology Reviews*, 92, 271–283. <https://doi.org/10.1016/j.oregeorev.2017.11.023>
- Gownder, J. P. (2016). *Breakout Vendors : Virtual And Augmented Reality*. Forrester Research Inc.
- Gupta, V. (2009). Non-destructive testing of some Higher Himalayan Rocks in the Satluj Valley. *Bulletin of Engineering Geology and the Environment*, 68(3), 409–416. <https://doi.org/10.1007/s10064-009-0211-4>
- Gwynn X. P., Brown M. C., and Mohr P. J. (2013) Combined Use of Traditional Core Logging and Televiwer Imaging for Practical Geotechnical Data Collection. In Dight P. M (Ed.) *Slope Stability 2013*, Australian centre for Geomechanics, Perth, ISBN: 978-0-9870937-5-2
- Hämäläinen, S., & Furbeck, A. (2011). *Mining in Harmony with the Society*. Kiruna Kommun. Kiruna Municipality.
- Hamdi P. (2015) Characterization of Brittle Damage in Rock from the Micro to Macro Scale. PhD Thesis. Simon Fraser University, Burnaby, Canada.
- Hamdi, P., Stead, D., Elmo, D., & Töyrä, J. (2018). Use of an integrated finite/discrete element method-discrete fracture network approach to characterize surface subsidence associated with sub-level caving. *International Journal of Rock Mechanics and Mining Sciences*, 103(February), 55–67. <https://doi.org/10.1016/j.ijrmms.2018.01.021>
- Hamrin H. (1982) Choosing an Underground Mining Method. In Hustruid W. (Ed.) *Underground Mining Methods Handbook*, SME-AIME, New York, pp: 88-112
- Harrison J. (2011) Mine Subsidence, In Darling P. (Ed.) *SME Mining Engineering Handbook*, Third Edition, pp 627-644 (Society for Mining Metallurgy and Exploration: Littleton)
- Haselton T. (2019) How the Army Plans to Use Microsoft's High-tech HoloLens Goggles on the Battlefield. CNBC LLC. Retrieved from:
<https://www.cnbc.com/2019/04/06/microsoft-hololens-2-army-plans-to-customize-as-ivas.html>

- Hedley, D.G.F. (1992) Rockburst handbook for Ontario hardrock mines. CANMET Special. Report SP92-1E.
- Hoek, E. (1974) Progressive caving induced by mining an inclined orebody. *Trans. Instn Min. Metall.*, 83: A133–9.
- Hoek E. (1994) Strength of Rock and Rock Masses. *ISRM News Journals* Vol. 2 Num. 2 pp. 4-16
- Hoek E. (2007) Rock Mass Classification. *Practical Rock Engineering*. RocScience. Retrieved from: <https://www.rocscience.com/assets/resources/learning/hoek/Practical-Rock-Engineering-Chapter-3-Rock-Mass-Classification.pdf>
- Hoek, E., & Brown, E. T. (1980). Empirical strength criterion for rock masses. In *Journal of the Geotechnical Engineering Division, ASCE* (Vol. 106, Issues GT9, Proc. Paper, 15715, pp. 1013–1035). [https://doi.org/10.1016/0148-9062\(81\)90766-x](https://doi.org/10.1016/0148-9062(81)90766-x)
- Hoek, E., & Brown, E. T. (2018). The Hoek–Brown failure criterion and GSI – 2018 edition. *Journal of Rock Mechanics and Geotechnical Engineering*, 11(3), 445–463. <https://doi.org/10.1016/j.jrmge.2018.08.001>
- Hoek, E., Carter, T. G., & Diederichs, M. S. (2013). Quantification of the geological strength index chart. *47th US Rock Mechanics / Geomechanics Symposium 2013*, 3, 1757–1764.
- Hoek, E. , & Marinos, P. (2000). Predicting tunnel squeezing problems in weak heterogeneous rock masses. *Tunnels and Tunnelling International, Part 1-2*(2), 1–20. <http://www.rocscience.com/hoek/references/H2000d.pdf>
- Hofmann-Wellenhof B., Lichtenegger H., and Collins J. (2001), *Global Positioning System: Theory and Practice*, 5th ed. New York: Springer Verlag Wien.
- Holcombe, R. (2013). *Oriented Drillcore : Measurement , Conversion , and Qa / Qc Procedures for Structural and Exploration Geologists*. Oriented Core Manual. Holcombe, Coughlin and Oliver Consultants.
- Holla L., and Barclay E. (2000) Mine Subsidence in the Southern Coalfield, NSW, Australia. Sydney: Department of Mineral Resources.
- HoloGroup (2020) HoloGroup: Experts in Mixed Reality. HoloGroup Ltd. Retrieved from: <https://holo.group/en/>
- Hopkins C. (2019) Virtual Reality Geology Field Trips: Bringing world-class Geological Gield Locations into Classroom Using Virtual Reality Technology. *GeoExpro* Vol. 16, No. 1

- Horwitz J. (2019) Qualcomm Announces Snapdragon XR2, The World's First 5G XR Platform. Venture Beat. Retrieved from: <https://venturebeat.com/2019/12/05/qualcomm-announces-snapdragon-xr2-the-worlds-first-5g-xr-platform/>
- HP Development Company (2020) HP Windows Mixed Reality Headset with Controllers. Retrieved from : <https://www8.hp.com/us/en/campaigns/mixedrealityheadset/overview.html>
- Hudson Institute of Mineralogy (2020) Harrison Gold Mine (RN; Abo; GEO), Bear Mountain, Harrison Lake, New Westminster Mining Division, British Columbia Canada. Retrieved from: <https://www.mindat.org/loc-18456.html>
- Hudyma, M., & Potvin, Y. H. (2010). An engineering approach to seismic risk management in hardrock mines. *Rock Mechanics and Rock Engineering*, 43(6), 891–906. <https://doi.org/10.1007/s00603-009-0070-0>
- Hudyma, M. R. (2008). *Analysis and interpretation of clusters of seismic events in mines*. PhD Thesis. University of Western Australia.
- Huntington, J., Whitbourn, L. B., Mason, P., Berman, M. and Schodlok, M. C. (2010) HyLogging – Voluminous Industrial-Scale Reflectance Spectroscopy of the Earth's Subsurface. Art, Science and Applications of Reflectance Spectroscopy Symposium, Boulder
- Hurley N. F., and Zhang T. (2017) Method for Characterizing a Geological Formation Traversed by a Borehole. US Patent No. 9581723 B2
- IKEA (2021) IKEA Mobile Apps. Inter IKEA Systems. Retrieved from: <https://www.ikea.com/ca/en/customer-service/mobile-apps/>
- Imago (2021) Geological Image Management Software for Geologist. Imago Inc. Retrieved from: <https://www.imago.live/>
- Itasca (2020) Software Products. Itasca Consulting Group. Retrieved from: <https://www.itascacg.com/software>
- ISRM (1978): Suggested Methods for the Quantitative Description of Discontinuities in Rock Masses. *International Journal of Rock Mechanics, Mining Sciences & Geomechanics Abstract* 16(3): 319-368
- [ISRM \(1981\) Rock Characterization, Testing, and Monitoring. Pergamon, Oxford. International Society for Rock Mechanics \(ISRM\).](#)
- Jang, J., Tschabrunn, C. M., Barkagan, M., Anter, E., Menze, B., & Nezafat, R. (2018). Three-dimensional holographic visualization of high-resolution myocardial scar on HoloLens. *PLoS ONE*, 13(10), 1–14. <https://doi.org/10.1371/journal.pone.0205188>

- Jensen, M. B., & Elming, S. Å. (2012). A correlation of AMS and rock quality in crystalline and sedimentary rocks in the Kiirunavaara hanging wall, Sweden. *Journal of Applied Geophysics*, 86, 54–69. <https://doi.org/10.1016/j.jappgeo.2012.07.006>
- Jensen, M. M. (2011). *Geophysical Tools for Prognosis of Deformation in Hardrock Environments*. PhD Thesis. Luleå University of Technology.
- Jiang, T., Yu, D., Wang, Y., Zan, T., Wang, S., & Li, Q. (2020). HoloLens-Based Vascular Localization System: Precision Evaluation Study with a Three-Dimensional Printed Model. *Journal of Medical Internet Research*, 22(4), 1–9. <https://doi.org/10.2196/16852>
- K7 Corebox (2020) K7 Corebox: Canada's Largest Supplier of Core Boxes. Corebox K7. Retrieved from: <http://www.k-7.ca/en/>
- Kaiser, P. K. (2019) From Common to Best Practice in Underground Rock Engineering. 8th Mueller lecture presented at the 14th ISRM Congress, Brazil, CRC Press, pp. 141-182.
- Kallu, R., & Roghanchi, P. (2015). Correlations between direct and indirect strength test methods. *International Journal of Mining Science and Technology*, 25(3), 355–360. <https://doi.org/10.1016/j.ijmst.2015.03.005>
- Keating M. and Bricaud P. (2002) Reuse Methodology Manual for System-on-a-Chip Designs (Third Edition), Kluwer Academic Publishers. ISBN: 978-1-4020-7141-6
- Keim D. A., Panse C., and Sips M. (2005) Information Visualization: Scope, Techniques and Opportunities for Geovisualization. In Dykes J., MacEachren A. M., and Kraak M. (Ed.) Exploring Geovisualization (pp. 23 – 52). Elsevier Ltd. ISBN: 978-0-08-044531-1
- Kendroski F.S., Cummings R. A., Bieniawski Z.T. and Skinner E. H. (1983) Rock Mass Classification for Block Caving Mine Drift Support. International Society of Rock Mechanics and Rock Engineering (ISRM). Proceedings of the 5th ISRM Congress.
- Kremers, N. A. H., Detournay, E., & Van De Wouw, N. (2016). Model-Based Robust Control of Directional Drilling Systems. *IEEE Transactions on Control Systems Technology*, 24(1), 226–239. <https://doi.org/10.1109/TCST.2015.2427255>
- Krupnik D. and Khan S. (2019) Close-Range, Ground-Based Hyperspectral Imaging for Mining Applications at Various Scales: Review and Case Studies. *Earth-Sciences Reviews* Vol. 198: 102952. DOI: 10.1016/j.earscirev.2019.102952
- Kruse, F. A., Bedell, R. L., Taranik, J. V., Peppin, W. A., Weatherbee, O., & Calvin, W. M. (2012). Mapping alteration minerals at prospect, outcrop and drill core scales using imaging spectrometry. *International Journal of Remote Sensing*, 33(6), 1780–1798. <https://doi.org/10.1080/01431161.2011.600350>

- Kuhlemann, I., Kleemann, M., Jauer, P., Schweikard, A., & Ernst, F. (2017). Towards X-ray free endovascular interventions - Using HoloLens for on-line holographic visualisation. *Healthcare Technology Letters*, 4(5), 184–187. <https://doi.org/10.1049/htl.2017.0061>
- Laakso, K., Middleton, M., Heinig, T., Bärs, R., & Lintinen, P. (2018). Assessing the ability to combine hyperspectral imaging (HSI) data with Mineral Liberation Analyzer (MLA) data to characterize phosphate rocks. *International Journal of Applied Earth Observation and Geoinformation*, 69, 1–12. <https://doi.org/10.1016/j.jag.2018.02.018>
- Langenbruch, C., Weingarten, M., & Zoback, M. D. (2018). Physics-based forecasting of man-made earthquake hazards in Oklahoma and Kansas. *Nature Communications*, 9(1), 1–10. <https://doi.org/10.1038/s41467-018-06167-4>
- Langston, J. (2021) “You can actually feel like you’re in the same place”: Microsoft Mesh powers shared experience in mixed reality. Microsoft Innovative Stories. Retrieved from: <https://news.microsoft.com/innovation-stories/microsoft-mesh/>
- Laramée, R. S., & Kosara, R. (2007). Challenges and unsolved problems. *Lecture Notes in Computer Science (Including Subseries Lecture Notes in Artificial Intelligence and Lecture Notes in Bioinformatics)*, 4417 LNCS, 231–254. https://doi.org/10.1007/978-3-540-71949-6_5
- Laubscher D. H. and Jakubec J. (2001) The MRMR Rock Mass Classification for Jointed Rock Masses. In Hustrulid W.A and Bullock R. L. (Eds.) *Underground Mining Methods: Engineering Fundamentals and International Case Studies*. Littleton, CO: Society for Mining, Metallurgy, and Exploration, Inc., pp. 475–481
- Lehman, J. A. (1999). The Bre-X Stock Debacle: Why the Enactment of Canadian Federal Securities Legislation Would Be Good as Gold. *Brooklyn Journal of International Law*, 24(3), 823–853.
- Lemy, F., Hadjigeorgiou, J., Côté, P., & Maldague, X. (2001). Image analysis of drill core. *Institution of Mining and Metallurgy. Transactions. Section A: Mining Technology*, 110(SEPT/DEC). <https://doi.org/10.1179/mnt.2001.110.3.172>
- LKAB (2020) One Month after the Seismic Event in Kiruna Mine. LKAB. Retrieved from: <https://www.lkab.com/en/news-room/news/one-month-after-the-seismic-event-in-the-kiruna-mine/?aid=5232>
- Llewellyn, K., Mccracken, A., & Brown, M. (2018). Core Orientation: Comparison of televiewer and traditional methods to highlight inaccuracies in old data. *SRK Presentation in International Symposium in Slope Stability in Open Pit Mining and Civil Engineering at the XIV International Congress for Energy and Resource Mining*. Retrieved from: <https://www.srk.com/sites/default/files/file/slope-stability-2018-core-orientation-comparison-of-televiewer-and-traditional-methods-to-highlight-inaccuracies-in-old-data.pdf>

- Lowe's (2020) 3D Product Visualization. Lowe's Innovation Labs. Retrieved from: <http://www.lowesinnovationlabs.com/lowes3d>
- Lund, C. (2009). Mineralogical, chemical and textural properties of the Malmberget iron deposit : a process mineralogically characterisation. In *Licentiate thesis / Luleå University of Technology*. <http://ltu.diva-portal.org/smash/get/diva2:990666/FULLTEXT01.pdf%0Ahttp://urn.kb.se/resolve?urn=urn:nbn:se:ltu:diva-17661>
- Lv, D., & Zhang, Y. (2018). Numerical simulation of chipping formation process with smooth particle hydrodynamic (SPH) method for diamond drilling AlN ceramics. *International Journal of Advanced Manufacturing Technology*, 96(5–8), 2257–2269. <https://doi.org/10.1007/s00170-018-1724-4>
- MacEachren, A. M., & Kraak, M.-J. (2001). Research Challenges in Geovisualization. *Cartography and Geographic Information Science*, 28(1), 3–12. <https://doi.org/10.1559/152304001782173970>
- MacLagan, E. A., Walton, E. L., Herd, C. D. K., & Rivard, B. (2020). Hyperspectral imaging of drill core from the Steen River impact structure, Canada: Implications for hydrothermal activity and formation of suevite-like breccias. *Meteoritics and Planetary Science*, 55(7), 1564–1580. <https://doi.org/10.1111/maps.13388>
- Magnor B. and Mattsson, H. J. (2000) Struktureologisk Model over Kirunavaara, CTMG Report 00001. Center for Applied Ore Studies (CTMG), Luleå University of Technology, 2000.
- Mäkitaavola K. (2012) Prognosis of Large-Scale Footwall Surface Deformations in Kiruna. LKAB Report 12-807
- Mäkitaavola, K., Stöckel, B.-M., Savilahti, T., Sjöberg, J., Dudley, J., McParland, M. A., & Morin, R. (2018). *InSAR as a practical tool to monitor and understand large-scale mining-induced ground deformations in a caving environment*. 661–674. https://doi.org/10.36487/acg_rep/1815_51_sjoberg
- Mäkitaavola, K., Stöckel, B., Hobbs, S., Henschel, M., & Wickramanyake, A. (2016). Application of InSAR for Monitoring Deformations at the Kiirunavaara Mine. *3rd International Symposium on Mine Safety Science and Engineering*, 73, 1–6.
- Malvern Panalytical (2021) Mineral Analysis – ASD TerraSpec Halo Mineral Identifier. AzoNetwork. Retrieved from: <https://www.azom.com/equipment-details.aspx?EquipID=2953>
- Marck, J., Detournay, E., Kuesters, A., & Wingate, J. (2014). Analysis of spiraled-borehole data by use of a novel directional-drilling model. *SPE Drilling and Completion*, 29(3), 267–278. <https://doi.org/10.2118/167992-PA>

- Marinos, P., Marinos, V., & Hoek, E. (2007). Geological Strength Index (GSI). A characterization tool for assessing engineering properties for rock masses. *Underground Works under Special Conditions - Proceedings of the Workshop (W1) on Underground Works under Special Conditions, January 2015*, 13–21. <https://doi.org/10.1201/noe0415450287.ch2>
- Marinos, V. (2019). A revised, geotechnical classification GSI system for tectonically disturbed heterogeneous rock masses, such as flysch. *Bulletin of Engineering Geology and the Environment*, 78(2), 899–912. <https://doi.org/10.1007/s10064-017-1151-z>
- Marshall D., Anglin C. D. and Mumin H. (2011) Ore Mineral Atlas (2nd ed.). Geological Association of Canada – Mineral Deposits Division. ISBN: 978-0-86491-318-0
- Martínez, A. (2008). Snow cover monitoring techniques with gb-SAR. *Tesisenxarxa.Net*, October. <http://www.thesisenxarxa.net/TDX-0312109-134141>
- Martinsson, J. (2013). Robust bayesian hypocentre and uncertainty region estimation: The effect of heavy-tailed distributions and prior information in cases with poor, inconsistent and insufficient arrival times. *Geophysical Journal International*, 192(3), 1156–1178. <https://doi.org/10.1093/gji/ggs067>
- Martinsson, O. (2004). Geology and Metallogeny of the Northern Norrbotten Fe-Cu-Au Province. in Allen, R. L., Martinsson, O., and Weihed, P. (eds.), *Svecofennian Ore-Forming Environments: Volcanic-Associated Zn-Cu-Au-Ag, Intrusion-Associated Cu-Au, Sediment-Hosted Pb-Zn, and Magnetite-Apatite Deposits of Northern Sweden*, Society of Economic Geologists, Guidebook Series, 33., p. 131-148
- Massonnet, D., & Souyris, J.-C. (2008). *Imaging With Synthetic Aperature Radar* (1st Edition). EPFL Press. <https://doi.org/10.1201/9781439808139>
- Mattsson, H., Berglund, J., & Magnor, B. (2010). *Strukturgeologisk modell över Kiruna gruvområde* (in Swedish). Internal report (10-874). LKAB.
- McPhee C, Reed J, and Zubizarreta I (2015) *Core Analysis: A Best Practice Guide*. Elsevier, Science. ISBN: 9780444636577
- Merriam-Webster (2021) Definition of Virtual Reality. Retrieved from: <https://www.merriam-webster.com/dictionary/virtual%20reality>
- MeshLab (2021) MeshLab. Retrieved from: <https://www.meshlab.net/>
- Microsoft (2021a) VR Headsets for PC: Virtual Reality Gaming. Microsoft. Retrieved from: <https://www.microsoft.com/en-ca/store/collections/vrheadsetsandaccessories>

- Microsoft (2021b) Microsoft HoloLens. Microsoft. Retrieved from:
<https://docs.microsoft.com/en-us/hololens/>
- Microsoft (2021c) Microsoft Excel: Get it now with a Microsoft 365 subscription. Retrieved from: <https://www.microsoft.com/en-ca/microsoft-365/excel>
- Milgram, P., & Kishino, F. (1994). A taxonomy of mixed reality. *IEICE Transactions on Information and Systems*, 77(12), 1321–1329.
- Mine, A., & Tiu, S. G. (2017). *Classification of Drill Core Textures for Process Simulation in Geometallurgy*.
- Mining Technology (2020) Kiruna Iron Ore Mine. Verdict Media Limited. Retrieved from:
<https://www.mining-technology.com/projects/kiruna/>
- Mount Sopris Instruments (2021) Mount Sopris Instruments: Home. Retrieved from:
<https://mountsopris.com/>
- Müller, D., Bruns, F. W., Erbe, H., Robben, B., & Yoo, Y. (2007). Mixed reality learning spaces for collaborative experimentation: A challenge for engineering education and training. *International Journal of Online Engineering (IJOE)*, 3(4), 15–19.
- Mysiorek, J., Onsel, I. E., Stead, D., & Rosser, N. (2019a). Engineering geological characterization of the 2014 Jure Nepal landslide: An integrated field, remote sensing-virtual/mixed reality approach. *53rd U.S. Rock Mechanics/Geomechanics Symposium*.
- Mysiorek, J. (2019) Engineering Geological Characterization of the 2014 Jure Nepal Landslide: An Integrated Field, Remote Sensing and Virtual/Mixed Reality Approach. Master Thesis. Simon Fraser University, Burnaby, Canada.
- mXrap (2021) What is mXrap?. Australian Centre for Geomechanics. Retrieved from:
<https://mxrap.com/>
- Nesse W. D. (2012) Introduction to Mineralogy (2nd Edition). Oxford University Press. ISBN: 978-0-19-982738-1
- Newfoundland Labrador Canada (2020) Natural Resources: Drill Core Information. Government of Newfoundland and Labrador. Retrieved from:
<https://www.gov.nl.ca/nr/mines/geoscience/drill/>
- Newman D. (2018) Mining Law of Canada. LexisNexis Canada Inc. ISBN: 978-0-433-49006-7
- NGI (2015). Using the Q-system: rock mass classification and support design. *Norwegian Geotechnical Institute*.

- Nielson, W. R., Jensen, M. P., Karsdorp, P. A., & Vlaeyen, J. W. S. (2013). Activity pacing in chronic pain: Concepts, evidence, and future directions. *Clinical Journal of Pain*, 29(5), 461–468. <https://doi.org/10.1097/AJP.0b013e3182608561>
- Nikafshan Rad, H., & Jalali, Z. (2019). Modification of rock mass rating system using soft computing techniques. *Engineering with Computers*, 35(4), 1333–1357. <https://doi.org/10.1007/s00366-018-0667-6>
- Notesco, G., Ogen, Y., & Ben-Dor, E. (2015). Mineral classification of makhtesh ramon in israel using hyperspectral longwave infrared (LWIR) remote-sensing data. *Remote Sensing*, 7(9), 12282–12296. <https://doi.org/10.3390/rs70912282>
- Nystrom, J. O., Billstrom, K., Henriquez, F., Fallick, A., & Naslund, H. R. (2008). Oxygen isotope composition of magnetite in iron ores of the Kiruna type in Chile and Sweden. *Gff*, 130(4), 177–188. <https://doi.org/10.1080/11035890801304177>
- O'Brien A. (2017) Thyssenkrupp Claims Up to 4x Faster Workflow with HoloLens. Next Reality. Retrieved from: <https://hololens.reality.news/news/thyssenkrupp-claims-up-4x-faster-workflow-with-hololens-0177209/>
- Oculus (2021) Oculus: VR Headset & Equipment. Facebook Technologies LLC. Retrieved from: <https://www.oculus.com/>
- Olson, L. (2013). *The 3-D Imaging of Drill Core for Fracture Mapping*. Master Thesis. Carleton University, Ottawa, Ontario Canada. <http://library1.nida.ac.th/termpaper6/sd/2554/19755.pdf>
- Olympus (2021) Ultrasonic Velocity and Attenuation Measurements in Geological Samples. Olympus Corporation. Retrieved from: <https://www.olympus-ims.com/en/applications/ultrasonic-velocity-and-attenuation-measurements-in-geological-samples/>
- Onsel, E., Chang, O., Mysiorek, J., Donati, D., Stead, D., Barnett, W., & Zorzi, L. (2019). *Applications of mixed and virtual reality techniques in site characterization*. 26th Vancouver Geotechnical Society Symposium.
- Onsel, I. E., Donati, D., Stead, D., & Chang, O. (2018). Applications of virtual and mixed reality in rock engineering. *52nd U.S. Rock Mechanics/Geomechanics Symposium*.
- OpenCV (2021) Open Computer Vision Library. OpenCV team. Retrieved from: <https://opencv.org/>
- Orpen, J. L. (2014). Best practice and new technology in core drilling , logging and fracture analysis. *Dfne 2014*, ii.
- Palmström A. (1995): RMI - a system for characterization of rock masses for rock engineering purposes. Ph.D. thesis, University of Oslo, Norway.

- Palmström, A. (2005). Measurements of and correlations between block size and rock quality designation (RQD). *Tunnelling and Underground Space Technology*, 20(4), 362–377. <https://doi.org/10.1016/j.tust.2005.01.005>
- Partio, M., Cramariuc, B., Gabbouj, M., & Visa, A. (2002). Rock texture retrieval using gray level co-occurrence matrix. *The Proceedings of the 5th Nordic Signal Conference, June 2014*, 1–5.
<http://citeseerx.ist.psu.edu/viewdoc/download?doi=10.1.1.161.1056&rep=rep1&type=pdf%0Ahttp://scholar.google.com/scholar?hl=en&btnG=Search&q=intitle:Rock+texture+retrieval+using+gray+level+co-occurrence+matrix#0>
- Peel 3d (2021) Peel 2-S 3D Scanner. Peel 3d. Retrieved from: <https://peel-3d.com/products/3d-scanner-peel-2-s?variant=33041483202583>
- Pells, P. J., Bieniawski, Z. T., Hencher, S. R., & Pells, S. E. (2017). Rock quality designation (RQD): Time to rest in peace. *Canadian Geotechnical Journal*, 54(6), 825–834. <https://doi.org/10.1139/cgj-2016-0012>
- Pepe, A., & Calò, F. (2017). A review of interferometric synthetic aperture RADAR (InSAR) multi-track approaches for the retrieval of Earth's Surface displacements. *Applied Sciences (Switzerland)*, 7(12).
<https://doi.org/10.3390/app7121264>
- Perkins T., Quirein J., and Parker T. J. (2009) Wireline and Lwd Borehole Image Log Dip and Azimuth Uncertainty. Society of Petrophysical and Well-Log Analysis (SPWLA) 50th Annual Logging Symposium No. 21847
- Pérez-Barnuevo, L., Lévesque, S., & Bazin, C. (2018). Automated recognition of drill core textures: A geometallurgical tool for mineral processing prediction. *Minerals Engineering*, 118(January), 87–96. <https://doi.org/10.1016/j.mineng.2017.12.015>
- Perneder, L., Marck, J., & Detournay, E. (2017). A Model of Planar Borehole Propagation. *SIAM Journal on Applied Mathematics*, 77(4), 1046–1060.
- Petersen, M. D., Mueller, C. S., Moschetti, M. P., Hoover, S. M., Rukstales, K. S., McNamara, D. E., Williams, R. A., Shumway, A. M., Powers, P. M., Earle, P. S., Llenos, A. L., Michael, A. J., Rubinstein, J. L., Norbeck, J. H., & Cochran, E. S. (2016). 2016 one-year seismic hazard forecast for the central and eastern United States from induced and natural earthquakes. *U. S. Geologic Survey Open-File Report 2016 -1035*, 1049–1061.
<https://doi.org/http://dx.doi.org/10.3133/ofr2016035>
- Pichierri, M., & Rabus, B. (2018). Applications of SAR Remote Sensing in the Arctic: A Review. *Proceedings - ANTEM 2018: 2018 18th International Symposium on Antenna Technology and Applied Electromagnetics, 2018-August*, 5–8.
<https://doi.org/10.1109/ANTEM.2018.8573026>

- Piringer, H., Berger, W., & Krasser, J. (2010). HyperMoVal: Interactive visual validation of regression models for real-time simulation. *Computer Graphics Forum*, 29(3), 983–992. <https://doi.org/10.1111/j.1467-8659.2009.01684.x>
- Prensky, S. (2010). Recent advances in well logging and formation evaluation. *World Oil Online*, 231(6).
- Proceq (2021) Equotip portable hardness testers – Leeb, Rockwell & UCI. Retrieved from: [https://www.proceq.com/compare/equotip-portable-hardness-testing/#:~:text=Proceq's%20Equotip%20enables%20portable%20hardness,Contact%20Impedance%20\(UCI\)%20method.](https://www.proceq.com/compare/equotip-portable-hardness-testing/#:~:text=Proceq's%20Equotip%20enables%20portable%20hardness,Contact%20Impedance%20(UCI)%20method.)
- Qin J. (2012) Hyperspectral and Multispectral Imaging in the Food and Beverage Industries. In Sun D. (Ed.) *Computer Vision Technology in the Food and Beverage Industries*. pp 27 – 63. Cambridge: Woodhead Publication. ISBN: 0-85709-577-3
- Rad H. N. and Jalali Z. (2019) Modification of Rock Mass Rating System Using Soft Computing Techniques. *Engineering with Computers Vol 35*: 1333-1357. DOI: 10.1007/s00366-018-0667-6
- Rathi, C. (2015). Outsource Drill Core Storage To Increase Oil & Gas Operational and Financial Efficiency. *Frost & Sullivan*.
- Rehman, H., Ali, W., Naji, A. M., Kim, J. J., Abdullah, R. A., & Yoo, H. K. (2018). Review of rock-mass rating and tunneling quality index systems for tunnel design: Development, refinement, application and limitation. *Applied Sciences (Switzerland)*, 8(8). <https://doi.org/10.3390/app8081250>
- Rekha Sahoo, S., & Champati Ray, P. K. (2015). Hyperspectral Image Analysis for Iron Ore Discrimination in Keonjhar District, Odisha. *International Journal of Remote Sensing & Geoscience*, 4(2), 28–34. www.ijrsg.com
- RideOn (2019) RideOn Ski Goggle. RideOn Ltd. Retrieved from: <https://www.rideonvision.com/new/>
- Rider, M. H. and Kennedy, M. (2011) *The geological Interpretation of Well Logs* (3rd edition), Rider French Consulting Limited.
- RockWare (2021) RockWare Geoscience Software Consulting and Training. RockWare Inc. Retrieved from: <https://www.rockware.com/>
- RocScience (2021a) Find the Geotechnical Tools that Work for you. RocScience Inc. Retrieved from: <https://www.rocscience.com/software>
- RocScience (2021b) Grid Data Oriented Core Borehole Data in Dips. RocScience Inc. Retrieved from: https://www.rocscience.com/help/dips/dips/Borehole_Orientation_Data_Pairs.htm

- Romana, M. (1985) New Adjustment Rating for Application of Bieniawski Classification to Slopes. Proceedings of International Symposium on the Role of Rock Mechanics in Excavations for Mining and Civil Works, ISRM, pp. 49-53
- Romana, M., Tomás, R., & Serón, J. B. (2015). Slope Mass Rating (SMR) geomechanics classification: Thirty years review. *13th ISRM International Congress of Rock Mechanics, 2015-MAY*(November), 1–10.
- Roonwal, G. (2018). Mineral Exploration: Practical Application. *Springer*.
<https://link.springer.com/content/pdf/10.1007/978-981-10-5604-8.pdf>
- Rossler, K. L., Sankaranarayanan, G., & Duvall, A. (2019). Acquisition of Fire Safety Knowledge and Skills with Virtual Reality Simulation. *Nurse Educator*, 44(2), 88–92. <https://doi.org/10.1097/NNE.0000000000000551>
- Salvoni, M., Morkel, I., & Dight, P. (2016). *Microseismic data — a comparison between routine trigger method and continuous data processing*. March 2017, 639–655. https://doi.org/10.36487/acg_rep/1604_43_salvoni
- Schlumberger (2021a) FMI: Fullbore Formation Microimager. Schlumberger Limited. Retrieved from: <https://www.slb.com/reservoir-characterization/surface-and-downhole-logging/wireline-openhole-logging/fmi-fullbore-formation-microimager>
- Schlumberger (2021b) Petrel E&P Software Platform. Schlumberger Limited. Retrieved from: <https://www.software.slb.com/products/petrel>
- Schodlok, M. C., Whitbourn, L., Huntington, J., Mason, P., Green, A., Berman, M., Coward, D., Connor, P., Wright, W., Jolivet, M., & Martinez, R. (2016). HyLogger-3, a visible to shortwave and thermal infrared reflectance spectrometer system for drill core logging: functional description. *Australian Journal of Earth Sciences*, 63(8), 929–940. <https://doi.org/10.1080/08120099.2016.1231133>
- Seequent (2021) Leapfrog: Setting the Standard in Geological Modeling. Seequent Limited. Retrieved from: <https://www.leapfrog3d.com/>
- Shakiba, M., Cavalcante Filho, J. S. de A., & Sepehrnoori, K. (2018). Using Embedded Discrete Fracture Model (EDFM) in numerical simulation of complex hydraulic fracture networks calibrated by microseismic monitoring data. *Journal of Natural Gas Science and Engineering*, 55(June 2017), 495–507. <https://doi.org/10.1016/j.jngse.2018.04.019>
- Shalabi, F. I., Cording, E. J., & Al-Hattamleh, O. H. (2007). Estimation of rock engineering properties using hardness tests. *Engineering Geology*, 90(3–4), 138–147. <https://doi.org/10.1016/j.enggeo.2006.12.006>
- Shekhar, G., Gustafson, A., & Schunnesson, H. (2017). *Draw Control Strategy and Resource Efficiency in Sublevel Caving*. Luleå University of Technology. Research Report ISBN: 1402-1528.

- Shinning 3D (2021) EinScan HX: Hybrid Blue Laser & LED Light Source Handheld 3D Scanner. 3D Shinning. Retrieved from: <https://www.einscan.com/handheld-3d-scanner/einscan-hx/>
- Shirzadegan, S. (2009). *Effect of geological structures on the subsidence of the Kiirunavaara hangingwall*. Master Thesis, Luleå University of Technology.
- Smit J. (2013) Africa's First Virtual Reality Mine Design Center. University of Pretoria. Features Innovative 8.
- Smith, M. P., Gleeson, S. A., & Yardley, B. W. D. (2013). Hydrothermal fluid evolution and metal transport in the Kiruna District, Sweden: Contrasting metal behaviour in aqueous and aqueous-carbonic brines. *Geochimica et Cosmochimica Acta*, 102, 89–112. <https://doi.org/10.1016/j.gca.2012.10.015>
- Sony Interactive Entertainment (2021) PlayStation VR: Immerse yourself in Incredible Virtual Reality Games and Experience. Retrieved from: <https://www.playstation.com/en-ca/ps-vr/>
- Specim (2021) Hyperspectral Imaging in Geology. Specim, Spectral Image Ltd. Retrieved from: <https://www.specim.fi/hyperspectral-imaging-in-geology/>
- StereoCore (2021) StereoCore PhotoLog. Ground Modelling Technologies Ltd. Retrieved from: <https://www.stereocore.net/>
- Stöckel, B.-M., Mäkitaavola, K., & Sjöberg, J. (2013). 'Hangingwall and footwall slope stability issues in sublevel caving', in Dight P.M. (Ed.), Proceedings of the 2013 International Symposium on Slope Stability in Open Pit Mining and Civil Engineering, Australian Centre for Geomechanics, Perth, pp. 1045 – 1060, https://doi.org/10.36487/ACG_rep/1308_73_Makitaavola
- Stöckel, B. M., Sjöberg, J., Mäkitaavola, K., & Savilahti, T. (2012). Mining-induced ground deformations in Kiruna and Malmberget. *ISRM International Symposium - EUROCK 2012*, i, 1–14.
- Stocking A. (2018) 4 Ways to Leverage Mixed Reality for Smarter Infrastructure Design. Redshift by Autodesk. Retrieved from: <https://www.autodesk.com/redshift/mixed-reality-for-infrastructure/>
- Sturzenegger, M., & Stead, D. (2009). Quantifying discontinuity orientation and persistence on high mountain rock slopes and large landslides using terrestrial remote sensing techniques. *Natural Hazards and Earth System Science*, 9(2), 267–287. <https://doi.org/10.5194/nhess-9-267-2009>
- Sugiura, J., & Jones, S. (2008). The use of the near-bit vibration sensor while drilling leads to optimized rotary-steerable drilling in push- and point-the-bit configurations. *SPE Asia Pacific Oil and Gas Conference and Exhibition 2008 - "Gas Now: Delivering on Expectations,"* 2(1), 816–825. <https://doi.org/10.2118/115572-ms>

- Svartsjaern, M. (2015). Predominant failure mechanisms at the Kiirunavaara mine footwall. Doctoral Dissertation. *Luleå University of Technology*. ISSN 1402-1757.
- Tavakoli, V. (2018). *Geological Core Analysis: Application to Reservoir Characterization*. Springer International Publishing. ISBN 978-3-319-78026-9
- Terzaghi, R.D. (1965). "Sources of errors in joint surveys". *Geotechnique*. 15(3): 287-30
- Tessier, J., Duchesne, C., & Bartolacci, G. (2007). A machine vision approach to on-line estimation of run-of-mine ore composition on conveyor belts. *Minerals Engineering*, 20(12), 1129–1144. <https://doi.org/10.1016/j.mineng.2007.04.009>
- The Franklin Institute (2021) History of Virtual Reality. Retrieved from: <https://www.fi.edu/virtual-reality>
- Tibbett J. D., Suorineni F. T., and Hebblewhite B. K. (2015) Understanding Damage Source Mechanisms in a Caving System Using Virtual Reality Scientific Visualization. Proceedings of the 7th International Conference & Exhibition on Mass Mining. The Australian Institute of Mining and Metallurgy, Melbourne, pp. 439-452.
- Tiu G. (2017) Classification of Drill Core textures for Process Simulation in Geometallurgy - Aitik Mine, Sweden. Master Thesis. Luleå University of Technology
- Töyrä J. (2013) Mining-Induced Ground Deformation in Kiruna and Malmberget. LKAB Presentation. Performance in Ironmaking
- Trimble (2021) Trimble XR10 with HoloLens 2: Trimble Inc. Retrieved from: <https://mixedreality.trimble.com/>
- Troll, V. R., Weis, F. A., Jonsson, E., Andersson, U. B., Majidi, S. A., Högdahl, K., Harris, C., Millet, M. A., Chinnasamy, S. S., Kooijman, E., & Nilsson, K. P. (2019). Magmatic origin of 'Kiruna-type' apatite-iron-oxide ores revealed by Fe-O isotope correlations. *Nature Communications*, 10(1), 1–12. <https://doi.org/10.1038/s41467-019-09244-4>
- Turkay, C., Slingsby, A., Lahtinen, K., Butt, S., & Dykes, J. (2017). Supporting theoretically-grounded model building in the social sciences through interactive visualisation. *Neurocomputing*, 268, 153–163. <https://doi.org/10.1016/j.neucom.2016.11.087>
- Tusa, L., Andreani, L., Khodadadzadeh, M., Contreras, C., Ivascanu, P., Gloaguen, R., & Gutzmer, J. (2019). Mineral mapping and vein detection in hyperspectral drill-core scans: Application to porphyry-type mineralization. *Minerals*, 9(2). <https://doi.org/10.3390/min9020122>

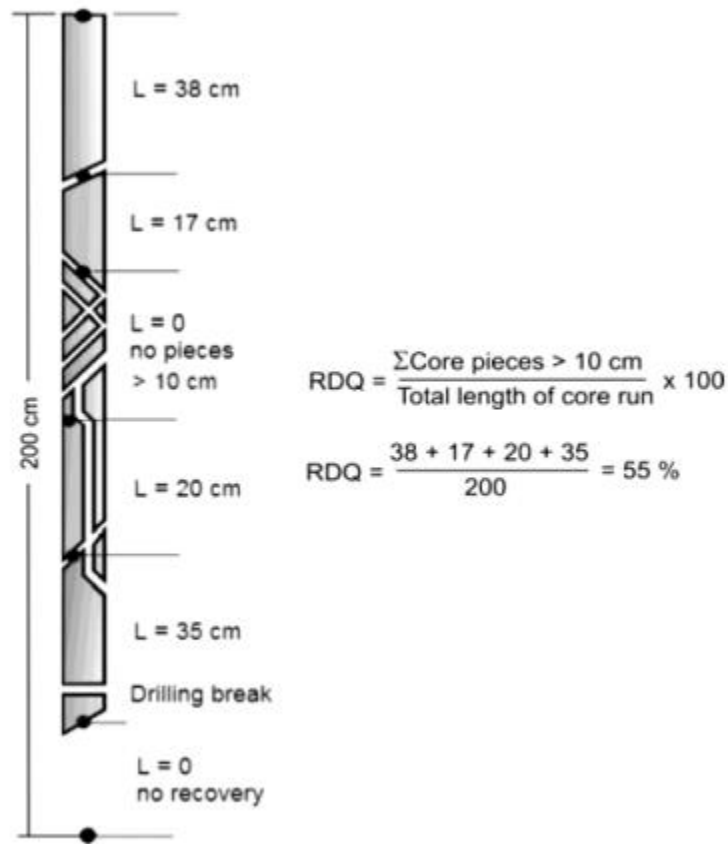
- Ultraleap (2021) Digital Worlds that Feel Human. Retrieved from:
<https://www.ultraleap.com/>
- Unity Technologies (2021) This is Why Creators Choose Unity. Retrieved from:
<https://unity.com/our-company>
- vGIS (2021) BIM and GIS Data in Augmented Reality. vGIS Inc. Retrieved from:
<https://www.vgis.io/>
- Valismo P. (2015) Optical Methods for Assessing Skin Flap Survival. In Meglinski I. (Ed.) Biophotic for Medical Application. Elsevier. ISBN: 978-0-85709-662-3
- Valve Corporation (2021) Valve Index – The best way to experience VR. Valve Corporation. Retrieved from: <https://www.valvesoftware.com/en/index>
- Vasanelli, E., Sileo, M., Calia, A., & Aiello, M. A. (2013). Non-destructive Techniques to Assess Mechanical and Physical Properties of Soft Calcareneitic Stones. *Procedia Chemistry*, 8, 35–44. <https://doi.org/10.1016/j.proche.2013.03.006>
- Villegas, T. (2008). Numerical analyses of the hangingwall at the Kiirunavaara mine. *Geotechnical Engineering*, 11. <http://epubl.ltu.se/1402-1757/2008/11/index-en.html>
- Virrantaus, K., Fairbairn, D., & Kraak, M. J. (2009). ICA research agenda on cartography and GI science. *Cartographic Journal*, 46(2), 63–75.
<https://doi.org/10.1179/000870409X459824>
- Virtuix (2021) Run Around in VR: Active VR and Esports for Your Venue. Retrieved from:
<https://www.virtuix.com/>
- Vuforia Engine (2021) Vuforia Engine: Developer Portal. PTC Inc. Retrieved from:
<https://developer.vuforia.com/>
- Waltham T., Bell F., and Culshaw M. (2005) Sinkholes and Subsidence: Karst and Cavernous rocks in Engineering and Construction. Springer-Praxis Publishing Ltd. ISBN 3-540-20725-2.
- WayRay (2021) We Create Windows into Virtual Worlds. WayRay AG. Retrieved from:
<https://wayray.com/>
- Wang, X., & Mauldon, M. (2006). Proportional errors of the Terzaghi correction factor. *Proceedings of the 41st U.S. Rock Mechanics Symposium - ARMA's Golden Rocks 2006 - 50 Years of Rock Mechanics, December*.
- Wesseloo, J. (2018). The Spatial Assessment of the Current Seismic Hazard State for Hard Rock Underground Mines. *Rock Mechanics and Rock Engineering*, 51(6), 1839–1862. <https://doi.org/10.1007/s00603-018-1430-4>

- Wickham G. E., Tiedemann H. R., and Skinner E. H. (1972) Support Determination Based on Geologic Prediction. In: Lane K.S., and Garfield L. A. (Eds) Proceeding North American Rapid Excavation Tunneling Conference Chicago. American Institute of Mining, Metallurgical, and Petroleum Engineering (AIME) Pp. 43-46
- Wickham G. E., Tiedemann H. R., and Skinner E. H. (1974) Ground Support Prediction Model -RSR Concept. In: Pattison H. C. and D'Appolonia E. (Eds.) Proceedings Rapid Excavation and Tunneling Conference (2nd Edition) San Francisco. American Institute of Mining, Metallurgical, and Petroleum Engineering (AIME). Pp. 691-707
- Wooden W.H., (1985). Navstar Global Positioning System. Proceedings of the first International Symposium on Precise Positioning with Global Positioning System, Rockville, Maryland, April 15-19, vol. 1, pp 23-32
- Woods, T. L., Reed, S., Hsi, S., Woods, J. A., & Woods, M. R. (2016). Pilot study using the augmented reality sandbox to teach topographic maps and surficial processes in introductory geology labs. *Journal of Geoscience Education*, 64(3), 199–214. <https://doi.org/10.5408/15-135.1>
- Zavodni, Z.M. (2000) Time-dependent movements of open-pit slopes, Slope stability in surface mining, Society for Mining, Metallurgy, and Exploration Inc., eds W.A. Hustrulid, M.K. McCarter, and D.J.A. Van Zyl, Littleton, USA, Chap. 8.
- Zhu, Q., Feng, Y., Cai, M., Liu, J., & Wang, H. (2017). Interpretation of the extent of hydraulic fracturing for rockburst prevention using microseismic monitoring data. *Journal of Natural Gas Science and Engineering*, 38, 107–119. <https://doi.org/10.1016/j.jngse.2016.12.0344>

Appendix A.

Rock Quality Designation (RQD)

Graphical procedure of calculating RQD according to RocScience (2021b) after Deere and Deere (1989) for any core size bigger than NW size (547 mm or 2.15 inches in diameter).



RQD gives an estimate of rock mass quality, and thus, it is important to ensure that breaks are natural occurring and not anthropogenic. If the sum of number of joints per unit lengths (J_v) is known for a clay-free rock mass, the suggested equation is (Palmström, 2005):

$$RQD = 110 - 2.5 * J_v$$

Appendix B.

Q-System (NGI, 2015):

Joint Set Number (J_n)

Joint set number rating value for Q-value after NGI (2015):

Joint Set Number		J_n
A	Massive, no major joint sets	0.5 - 1.0
B	One Joint Set	2
C	One Major Joint Set plus a few other joints	3
D	Two Major Joint Set	4
E	Two Major Joint Sets plus a few other joints	6
F	Three Joint Sets	9
G	Three Joint Sets plus a few other joints	12
H	Four or More Major Joint Sets	15
J	Crushed Rock	20

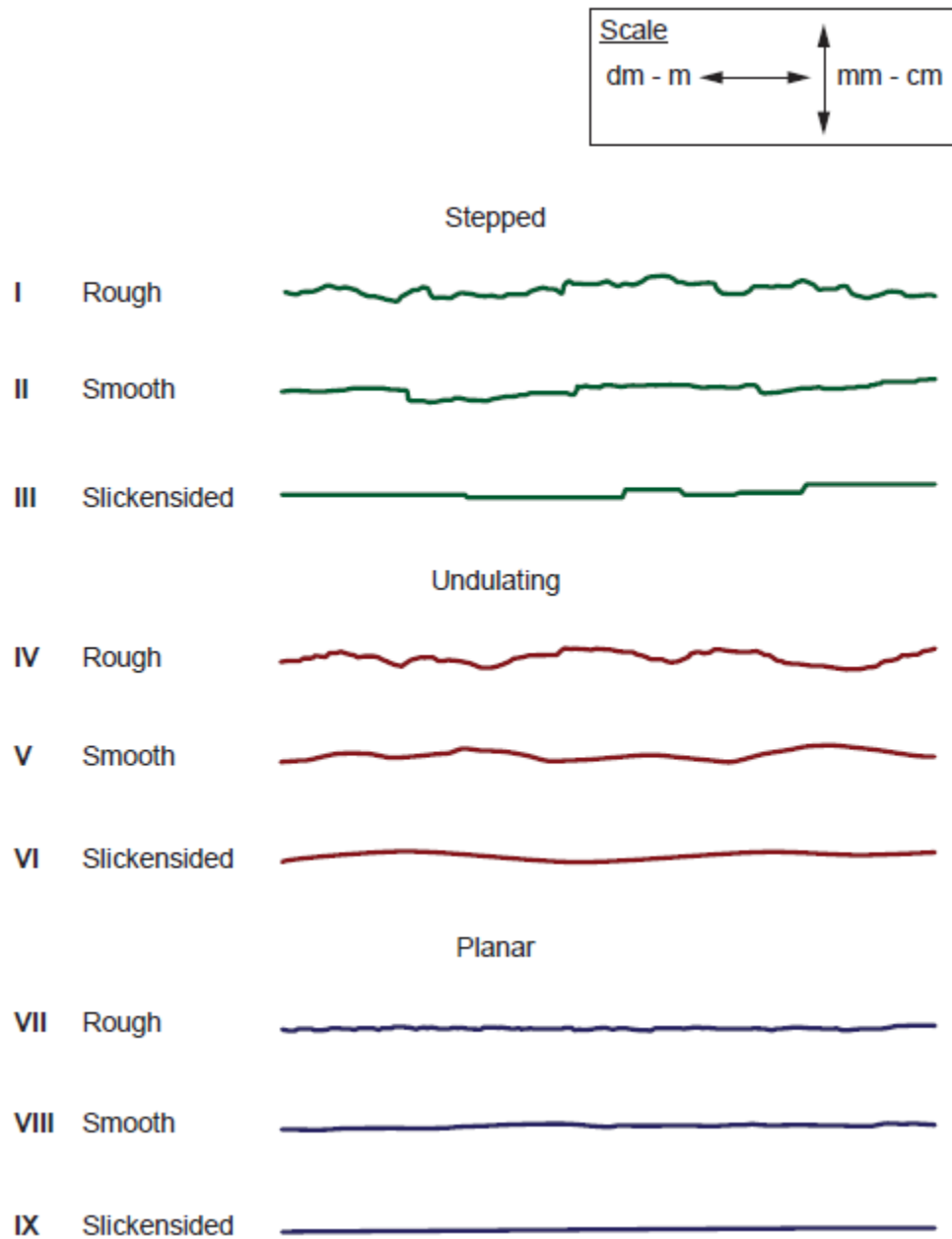
Major joint sets are joints that display similar characteristics, spacing and are nearly parallel to each other. Note that J_n is a rating and not a representation of the number of joint sets.

Joint roughness Number (J_r)

Joint roughness number represents the nature of joint condition quantitatively (NGI, 2015). The rating are as follows for small to intermediate scale feature:

Joint Roughness Number		J_r
A	Discontinuous Joint	4
B	Rough or irregular, undulating	3
C	Smooth, Undulating	2
D	Slickensided, Undulating	1.5
E	Rough, Irregular, Planar	1.5
F	Smooth, Planar	1
G	Slickensided, Planar	0.5
H	Zone Containing Clay Minerals Thick Enough to Prevent Rock-Wall contact when sheared	1

The profile of each individual joint roughness attribute was also modified in NGI (2015) from the ISRM (1978) diagram that represents 1 -10 roughness where the vertical and horizontal are equal.



Joint Alteration Number (J_a)

Quantification rating of significance of joint infill and its contribution to friction. The thickness and strength (mineral composition) are crucial. Broken into three major categories within the classification scheme. The simplified table after NGI (2012) is as follows:

Joint Alteration Number		Φ_f Approx.	J _a
Rock-Wall Contact (No mineral filling, only coating)			
A	Tightly healed, hard, non-softening, impermeable filling (ex. Quartz or epidote)		0.75
B	Unaltered joint wall, surface staining only	25-35	1
C	Slightly altered joint walls. Non-softening mineral coating; sandy particles, clay-free disintegrated rock, etc.	25-30	2
D	Silty or sandy clay coating, small clay fraction (non-softening)	20-25	3
E	Softening or low friction clay mineral coatings. (ex. Kaolinite or mica)	8-16	4
Rock-wall contact before 10 cm shear (thin mineral fillings)			
F	Sandy particles, clay-free disintegrated rock.	25-30	4
G	Strongly over-consolidated, non-softening clay minerals (continuous, but <5mm thickness)	16-24	6
H	Medium or low over-consolidation, softening, clay mineral fillings (continuous but <5mm thickness).	12-16	8

J	Swelling-clay filling i.e. montmorillonite (continuous, but <5mm thickness). Value varies depending on swelling clay %	6-12	8-12
No rock-wall contact when sheared (thick mineral filling)			
K	Zones or bands of disintegrated or crushed rock. Strongly over-consolidated	16-24	6
L	Zones or bands of clay, disintegrated, or crushed rock. Medium or low over-consolidation or softening fillings	12-16	8
M	Zones or bands of clay, disintegrated, or crushed rock. Swelling clay. Value varies depending on swelling clay %	6-12	8-12
N	Thick continuous zones or bands of clay. Strongly over-consolidated	12-16	10
O	Thick continuous zones or bands of clay. Medium to low over-consolidated	12-16	13
P	Thick, continuous zones or bands with clay. Swelling clay. Value varies depending on swelling clay %	6-12	13-20

*For complete table refer to NGI, 2015

Joint Water Reduction Factor (J_w)

Water within joint reduces friction as it will soften or washout mineral infill. The water pressure properties also counteract normal stress causing them to move more freely. The rating is subdivided by:

Joint Water Reduction Factor		J_w
A	Dry or minor inflow (humid or a few drips)	1.0
B	Medium inflow, occasional outwash or joint filling ("rain like")	0.66
C	Jew inflow or high pressure in competent rock with unfilled joints	0.5
D	Large inflow or high pressure, considerable outwash of joint filling	0.33
E	Exceptionally high inflow or water pressure decaying with time. Causes outwash of material and perhaps cave in	0.2 – 0.1
F	Exceptionally high inflow or water pressure continuing without noticeable decay. Causes outwash of material and perhaps cave in	0.1 – 0.05

Assessing inflow can be challenging due to seasonal and anthropogenically altered environments such as grouting. Thus, this parameter should be taken with great caution.

Stress Reduction Factor (SRF)

Quantitative representation of the degree and type of stress occurring along an underground opening. Effects can be, slabbing, rock burst, spalling squeezing, dilatancy and deformation. The SRF value can be calculated from the uniaxial compressive strength (σ_c) and the major principal stress (σ_1) or the maximum tangential stress (σ_θ) and compressive strength (σ_c). SRF is split into four major categories:

Stress Reduction Factor (SRF)				
Weak Zones intersecting the underground opening , which may or may not transfer stresses to surrounding rock mass				SRF
A	Multiple weak zones within a short section containing clay or chemically disintegrated, very loose, surrounding rock.	10		
B	Multiple shear zone within a short section in competent clay-free rock with loose surrounding	7.5		
C	Single weak zones with or without clay or chemical disintegrated rock (depth <50m)	5		
D	Loose, open joints heavily jointed (ex. "sugar cube")	5		
E	Single weak zone with or without clay or chemical disintegration rock (depths > 50m)	2.5		
Competent rock with stability problems due to high stresses or lack of stresses.		σ_c / σ_1	σ_θ / σ_c	SRF
F	Low Stress, near surface, open joints	>200	<0.01	2.5
G	Medium stress, favourable stress condition	200-100	0.01-0.3	1
H	High stress, very tight structure. Unfavourable relative to orientation of stresses compared to joints	10- 5	0.3-0.4	0.5- 5

I	Moderate spalling and/or slabbing after >1hour	5-3	0.5 – 0.65	5-50
J	Spalling or rock burst after a few minutes	3-2	0.65 -1	50-200
K	Heavy rock burst and immediate dynamic deformation	<2	>1	200-400
Squeezing rock with plastic deformation of incompetent rock under the influence of moderate or high rock stresses			σ_θ / σ_c	SRF
L	Mild squeezing rock pressure		12-16	8
M	Heavy squeezing rock Pressure		6-12	8-12
Swelling rock ; chemical swelling activity depending on the presence of water.				SRF
N	Mild swelling rock pressure			5-10
O	Heavy swelling rock pressure			10-15

Stress release can occur immediately after excavation while slower plastic or joint development can vary in time from days to months to form. Thus, SRF values can vary significantly through time.

Appendix C.

Rock Mass Rating System (RMR) (Bieniawski, 1989)

1

A. CLASSIFICATION PARAMETERS AND THEIR RATINGS									
Parameter			Range of values						
1	Strength of intact rock material	Point-load strength Index	>10 MPa	4 - 10 MPa	2 - 4 MPa	1 - 2 MPa	For this low range - uniaxial compressive test is preferred		
		Uniaxial comp. strength	>250 MPa	100 - 250 MPa	50 - 100 MPa	25 - 50 MPa	5 - 25 MPa	1 - 5 MPa	< 1 MPa
	Rating		15	12	7	4	2	1	0
2	Drill core Quality RQD		90% - 100%	75% - 90%	50% - 75%	25% - 50%	< 25%		
	Rating		20	17	13	8	3		
3	Spacing of		> 2 m	0.5 - 2 m	200 - 500 mm	60 - 200 mm	< 60 mm		
	Rating		20	15	10	6	5		
4	Condition of discontinuities (See E)		Very rough surfaces Not continuous No separation Unweathered wall rock	Slightly rough surfaces Separation < 1 mm Slightly weathered walls	Slightly rough surfaces Separation < 1 mm Highly weathered walls	Slackened surfaces or Gouge < 5 mm thick or Separation 1-5 mm Continuous	Soft gouge > 5 mm thick or Separation > 5 mm Continuous		
	Rating		30	25	20	10	0		
5	Groundwater	Inflow per 10 m tunnel length (lit)	None	< 10	10 - 25	25 - 125	> 125		
		(Joint water pressure) (Major principal stress)	0	< 0.1	0.1 - 0.2	0.2 - 0.5	> 0.5		
		General conditions	Completely dry	Damp	Wet	Dripping	Flowing		
	Rating		15	10	7	4	0		
B. RATING ADJUSTMENT FOR DISCONTINUITY ORIENTATIONS (See F)									
Strike and dip orientations			Very favourable	Favourable	Fair	Unfavourable	Very Unfavourable		
Ratings	Tunnels & mines		0	-2	-5	-10	-12		
	Foundations		0	-2	-7	-15	-25		
	Slopes		0	-5	-25	-50			
C. ROCK MASS CLASSES DETERMINED FROM TOTAL RATINGS									
Rating			100 ← 81	80 ← 61	60 ← 41	40 ← 21	< 21		
Class number			I	II	III	IV	V		
Description			Very good rock	Good rock	Fair rock	Poor rock	Very poor rock		
D. MEANING OF ROCK CLASSES									
Class number			I	II	III	IV	V		
Average stand-up time			20 yrs for 15 m span	1 year for 10 m span	1 week for 5 m span	10 hrs for 2.5 m span	30 min for 1 m span		
Cohesion of rock mass (kPa)			> 400	300 - 400	200 - 300	100 - 200	< 100		
Friction angle of rock mass (deg)			> 45	35 - 45	25 - 35	15 - 25	< 15		
E. GUIDELINES FOR CLASSIFICATION OF DISCONTINUITY CONDITIONS									
Discontinuity length (persistence)			< 1 m	1 - 3 m	3 - 10 m	10 - 20 m	> 20 m		
Rating			6	4	2	1	0		
Separation (aperture)			None	< 0.1 mm	0.1 - 1.0 mm	1 - 5 mm	> 5 mm		
Rating			6	5	4	1	0		
Roughness			Very rough	Rough	Slightly rough	Smooth	Slackened		
Rating			6	5	3	1	0		
Infiling (gouge)			None	Hard filling < 5 mm	Hard filling > 5 mm	Soft filling < 5 mm	Soft filling > 5 mm		
Rating			6	4	2	2	0		
Weathering			Unweathered	Slightly weathered	Moderately weathered	Highly weathered	Decomposed		
Ratings			6	5	3	1	0		
F. EFFECT OF DISCONTINUITY STRIKE AND DIP ORIENTATION IN TUNNELLING**									
Strike perpendicular to tunnel axis					Strike parallel to tunnel axis				
Drive with dip - Dip 45 - 90°			Drive with dip - Dip 20 - 45°		Dip 45 - 90°		Dip 20 - 45°		
Very favourable			Favourable		Very unfavourable		Fair		
Drive against dip - Dip 45-90°			Drive against dip - Dip 20-45°		Dip 0-20 - irrespective of strike*				
Fair			Unfavourable		Fair				

* Some conditions are mutually exclusive. For example, if infilling is present, the roughness of the surface will be overshadowed by the influence of the gouge. In such cases use A.4 directly.
 ** Modified after Wickham et al (1972).

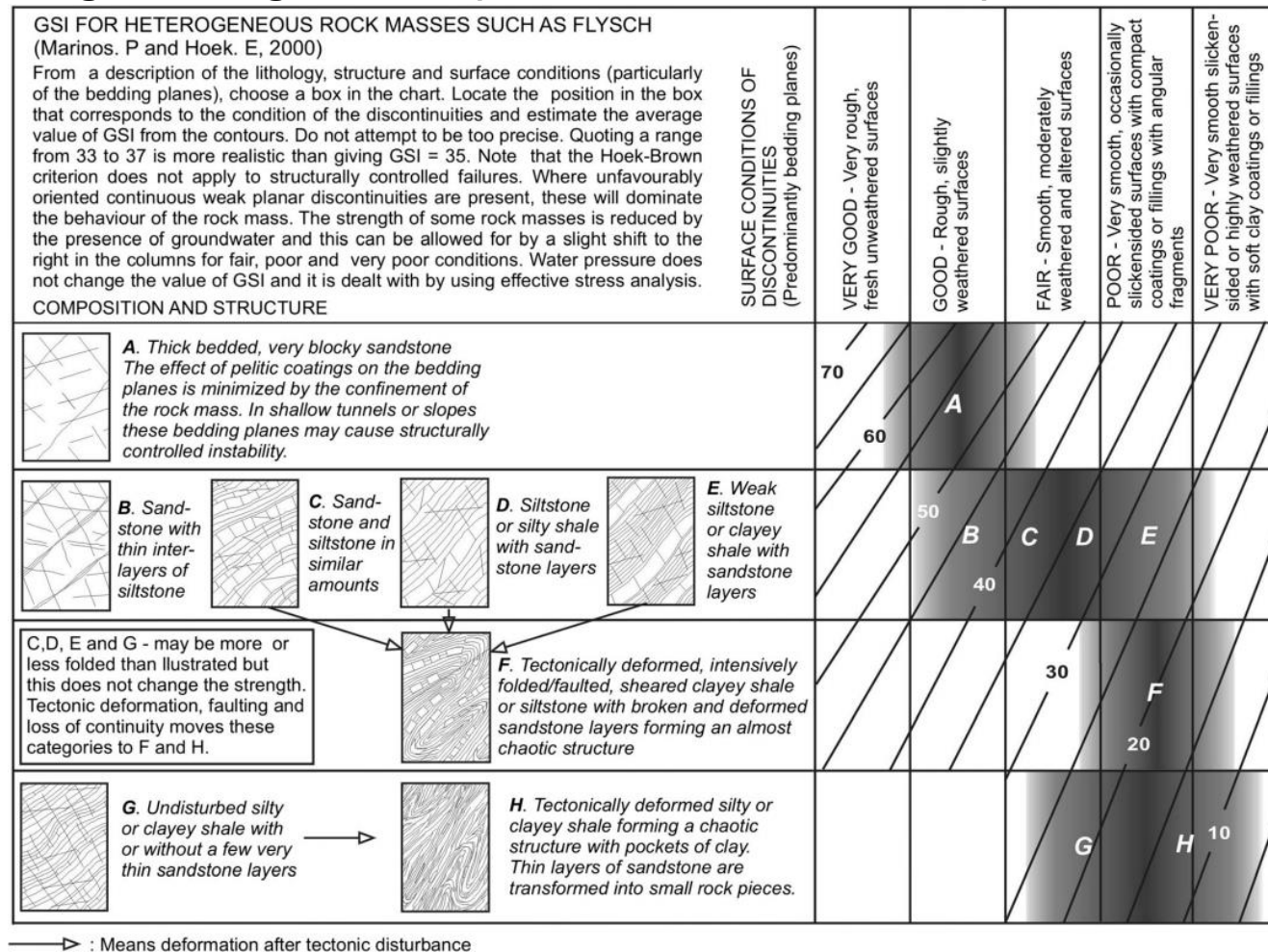
*** [Used with permission]

Geologic Strength Index (GSI) (Hoek and Marinos, 2000)



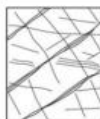
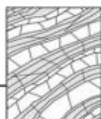
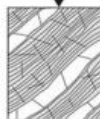
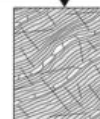



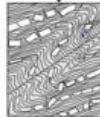

195

Appendix E.

Flysch Geologic Strength Index (Marinos and Hoek, 2001)

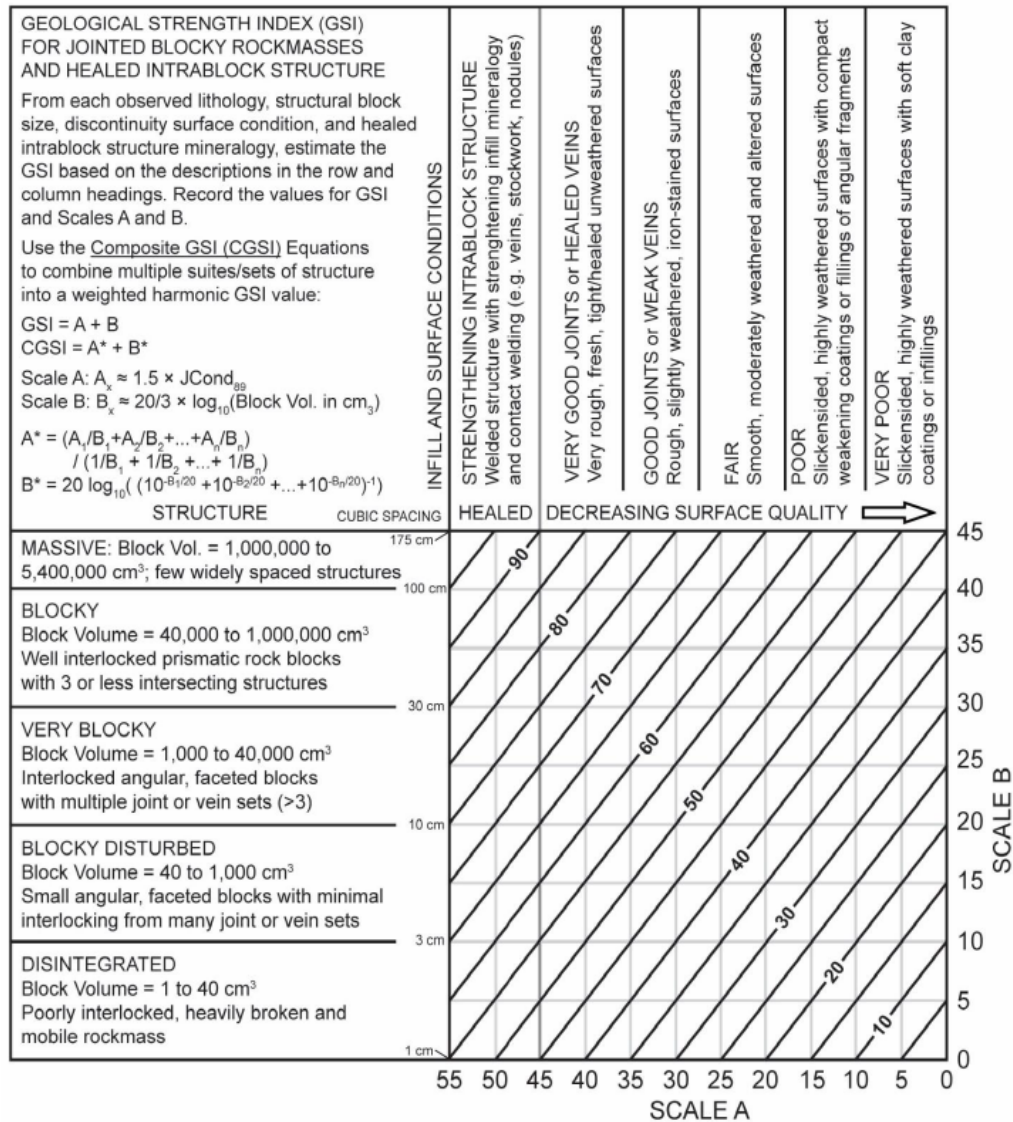


Flysch Geologic Strength Index (Marinos, 2019)

GEOLOGICAL STRENGTH INDEX (GSI) FOR HETEROGENEOUS ROCK MASSES SUCH AS FLYSCH		SURFACE CONDITIONS OF DISCONTINUITIES (Predominantly bedding planes)				
Chart modified and extended by V. Marinos from the P.Marinos & E.Hoek (2001) original one		VERY GOOD Very rough, fresh unweathered surfaces	GOOD Rough, slightly weathered or oxyllised surfaces	FAIR Smooth, moderately weathered and altered surfaces	POOR Very smooth, occasionally slickensided surfaces with compact coatings or fillings with angular fragments	VERY POOR Very smooth, slickensided or highly weathered surfaces with soft clay coating or fillings
Heterogeneous rockmasses are meant those with alternating layers of clearly different lithology types with significant differences in their strength properties. For flysch, a typical formation with heterogeneous rock masses, these alternations are consisting of sandstones and siltstones. Clay shales may be present. From a description of the lithology, structure and surface conditions of discontinuities (particularly of the bedding planes), choose a box in the chart. The selection of the structure should be based on the tectonic disturbance (undisturbed, slightly disturbed, strongly disturbed - folded, desintegrated, sheared), the proportion of siltstones against sandstones and the expressed or not stratification inside the siltstone layers. In the type IV and V when the thickness of sandstone beds exceed 50cm an increase of the GSI value by 5 is suggested. From type IV and the following types, the stratification planes are perceptible inside the siltstone mass. Locate the position in the box that corresponds to the conditions and estimate the average value GSI from the contours. The determination of the structure and the condition of discontinuities may range between two adjacent fields. Note that the Hoek - Brown criterion does not apply to structurally controlled failures. Where unfavourably oriented continuous weak planar discontinuities are present, these will dominate the behaviour of the rock mass. The strength of some rock masses is reduced by the presence of groundwater and this can be allowed for by a slight shift to the right in the columns for fair, poor and very poor conditions. Water pressure does not change the value of GSI and it is dealt with by using effective stress analysis.		DECREASE OF THE QUALITY OF DISCONTINUITIES →				
STRUCTURE AND COMPOSITION						
	TYPE I. Undisturbed, with thick to medium thickness sandstone beds with sporadic thin films of siltstone. In shallow tunnels or slopes where confinement is poor the mode of the failure has a kinematic character controlled by the bedding planes and GSI is meaningless					
	TYPE II. Undisturbed massive siltstone (stratification planes are imperceptible) with sporadic thin interlayers of sandstones	80	I	II	N/A	N/A
	TYPE III. Moderately disturbed sandstones with thin films of interlayers of siltstone	70				
	TYPE IV. Moderately disturbed rockmass with sandstone and siltstone similar amounts	60	III	IV	V	VI
	TYPE V. Moderately disturbed siltstones with sandstone interlayers	50				
	TYPE VI. Moderately disturbed siltstones with sparse sandstone interlayers					
	TYPE VII. Strongly disturbed, folded rockmass that retains its structure, with sandstone and siltstone in similar extend		N/A	40	VII	VIII
	TYPE VIII. Strongly disturbed, folded rockmass, with siltstones and sandstone interlayers. The structure is retained and deformation - shearing is not strong			30		
	TYPE IX. Desintegrated rockmass that can be found in wide zones of faults or/and of high weathering. In this type mainly brittle material is present with some disturbed siltstones between rock pieces		N/A		20	IX
	TYPE X. Tectonically deformed intensively folded/ faulted siltstone or clay shale with broken and deformed sandstone layers forming an almost chaotic structure				10	X
	TYPE XI. Tectonically strongly sheared siltstone or clayey shale forming a chaotic structure with pockets of clay. Thin layers of sandstone are transformed into small rock pieces. Ultimately the ground behavior is that of a soil		N/A	N/A		XI

Appendix F.

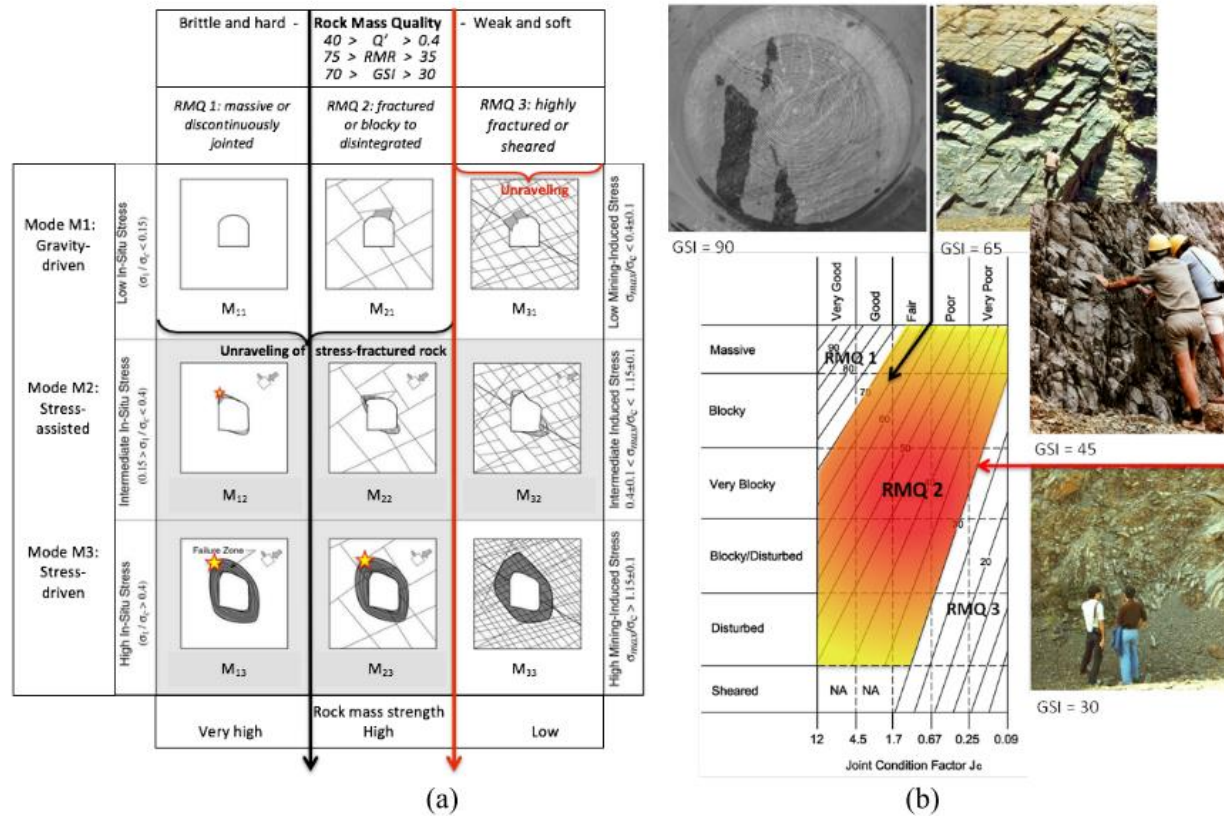
Composite Geologic Strength Index (Days, 2016)



CGSI chart used to derive complex rock masses with intrablock structures, such as healed fractures with quartz infill (Days, 2016).

Appendix G.

RMQ in respect to GSI (Kaiser, 2019)



(a) Rock mass quality (RMQ) vs. in-situ stress and mining induced stresses. (b) GSI chart with corresponding RMQ

Appendix H.

Field Estimate of Uniaxial Compressive Strength (Brown, 1981)

Grade*	Term	Uniaxial Comp. Strength (MPa)	Point Load Index (MPa)	Field estimate of strength	Examples
R6	Extremely Strong	> 250	>10	Specimen can only be chipped with a geological hammer	Fresh basalt, chert, diabase, gneiss, granite, quartzite
R5	Very strong	100 - 250	4 - 10	Specimen requires many blows of a geological hammer to fracture it	Amphibolite, sandstone, basalt, gabbro, gneiss, granodiorite, limestone, marble, rhyolite, tuff
R4	Strong	50 - 100	2 - 4	Specimen requires more than one blow of a geological hammer to fracture it	Limestone, marble, phyllite, sandstone, schist, shale
R3	Medium strong	25 - 50	1 - 2	Cannot be scraped or peeled with a pocket knife, specimen can be fractured with a single blow from a geological hammer	Claystone, coal, concrete, schist, shale, siltstone
R2	Weak	5 - 25	**	Can be peeled with a pocket knife with difficulty, shallow indentation made by firm blow with point of a geological hammer	Chalk, rocksalt, potash
R1	Very weak	1 - 5	**	Crumbles under firm blows with point of a geological hammer, can be peeled by a pocket knife	Highly weathered or altered rock
R0	Extremely weak	0.25 - 1	**	Indented by thumbnail	Stiff fault gouge

* Grade according to Brown (1981).

** Point load tests on rocks with a uniaxial compressive strength below 25 MPa are likely to yield highly ambiguous results.